

University of Southampton Research Repository

Copyright © and Moral Rights for this thesis and, where applicable, any accompanying data are retained by the author and/or other copyright owners. A copy can be downloaded for personal non-commercial research or study, without prior permission or charge. This thesis and the accompanying data cannot be reproduced or quoted extensively from without first obtaining permission in writing from the copyright holder/s. The content of the thesis and accompanying research data (where applicable) must not be changed in any way or sold commercially in any format or medium without the formal permission of the copyright holder/s.

When referring to this thesis and any accompanying data, full bibliographic details must be given, e.g.

Thesis: Author (Year of Submission) "Full thesis title", University of Southampton, name of the University Faculty or School or Department, PhD Thesis, pagination.

Data: Author (Year) Title. URI [dataset]

University of Southampton

Faculty of Environmental and Life Sciences

School of Biological Sciences

**Droplet Microfluidic and Microcrystal Strategies for
Time-Resolved Serial Crystallography of Enzymes at
Synchrotron and XFEL Sources**

by

Jack Robert Stubbs

ORCID 0000-0002-3788-1687

Thesis for the degree of Doctor of Philosophy

November 2025

University of Southampton

Abstract

Faculty of Environmental and Life Sciences

School of Biological Sciences

Thesis for the degree of Doctor of Philosophy

Droplet Microfluidic and Microcrystal Strategies for Time-Resolved Serial Crystallography of Enzymes at Synchrotron and XFEL Sources

by

Jack Robert Stubbs

Observing transient structural intermediates remains a central challenge in enzymology. Little is known about these despite their pivotal role in catalytic function. Time-resolved serial crystallography at synchrotron and X-ray free electron laser (XFEL) sources offers a promising avenue to capture these dynamic events. However, experimental success hinges on rigorous control of crystallisation, ligand delivery, and integration with beamline infrastructure. This thesis explores the use of droplet microfluidic and microcrystal strategies to address these bottlenecks and establish pipelines for future time-resolved studies.

A high-throughput crystallisation system was developed to generate uniform microcrystals within discrete aqueous droplets, leveraging a seeding strategy to overcome the low probability of nucleation at diminishing volumes. In parallel, a droplet micromixing device was engineered to initiate ligand-triggered reactions on millisecond timescales by exploiting convection within droplets as a means for rapidly mixing microcrystals with ligands. Flow parameters and mixing efficiency were characterised, followed by iterative design and fabrication of a X-ray transmissible device suitable for deployment at a synchrotron beamline.

Arabidopsis thaliana Pyridoxal 5'-phosphate synthase subunit 1.3 (AtPdx1.3) microcrystal slurries were validated for time-resolved studies using static serial femtosecond crystallography (SFX) at the SPring-8 angstrom compact free electron laser (SACLA). High-resolution radiation damage-free structures of apo and ligand-bound AtPdx1.3 were obtained at room temperature, representing the first XFEL structures of this enzyme. Diffraction from 20 μm crystals yielded resolution comparable to or better than previous larger crystals at cryogenic temperatures. Notably, only minimal structural differences were observed relative to cryotrapped structures, indicating strong conformational consistency. Soaking protocols enabled rapid ligand incorporation, capturing R5P, PLP and the crucial I320 intermediate within 15 minutes. These results establish robust workflows for intermediate state trapping and future dynamic studies. Taken together, the platforms developed in this thesis represent a significant step towards realising dynamic structural studies of enzymes at synchrotron and XFEL sources.

Table of Contents

Table of Contents	3
Table of Tables	7
Table of Figures	9
List of Accompanying Materials	14
Research Thesis: Declaration of Authorship.....	15
Acknowledgements.....	16
Definitions and Abbreviations.....	18
Chapter 1 Introduction	21
 1.1 Macromolecular Crystallography.....	21
1.1.1 The evolution of macromolecular crystallography	21
1.1.2 Core crystallographic principles.....	24
1.1.2.1 Crystal lattice, unit cell and asymmetric unit	25
1.1.2.2 Bragg's Law and diffraction geometry.....	26
1.1.2.3 Structure factors, Fourier transforms and the phase problem	28
 1.2 Serial crystallography.....	29
1.2.1 Serial femtosecond crystallography (SFX)	30
1.2.2 Serial synchrotron crystallography (SSX).....	32
1.2.3 Sample preparation.....	33
1.2.3.1 Protein crystallisation phase diagram	33
1.2.3.2 Seeding.....	35
1.2.3.3 Scaling up from vapour diffusion to batch.....	37
1.2.4 Sample delivery	38
1.2.4.1 Fixed-targets	41
1.2.4.2 Injectors	42
1.2.4.2.1 Liquid injectors.....	42
1.2.4.2.2 Viscous injectors.....	44
1.2.4.2.3 Droplet injectors	44

Table of Contents

1.2.4.3 Hybrid methods	45
1.2.4.4 Microfluidics	46
1.2.5 Time-resolved serial crystallography	48
1.2.5.1 Mix-and-inject serial crystallography (MISC)	49
1.3 Motivation for time-resolved studies: AtPdx1.3	50
1.4 Droplet microfluidics in macromolecular crystallography	54
1.4.1 Principles of droplet microfluidics	55
1.4.2 Droplet microfluidics in sample preparation	58
1.4.3 Droplet microfluidics in sample delivery	60
1.5 Aims	61
Chapter 2 Materials and Methods	62
2.1 Transformation of AtPdx1.3 for protein expression	62
2.2 Transformation of AtPdx1.3 for plasmid amplification	63
2.3 AtPdx1.3 protein expression	63
2.4 AtPdx1.3 protein purification	64
2.5 SDS-PAGE	65
2.6 Protein crystallisation	65
2.6.1 Lysozyme	65
2.6.2 AtPdx1.3	66
2.6.3 Trypsin	67
2.6.4 Chlorite dismutase	67
2.6.5 Thaumatin	67
2.7 Phase diagrams	68
2.7.1 Vapour diffusion phase diagram	68
2.7.2 Microbatch-under-oil phase diagram	68
2.8 Serial synchrotron crystallography	69
2.8.1 Sample delivery and data collection	69
2.8.2 Data processing	69

Table of Contents

2.8.3 Structure solution and refinement.....	70
2.9 Serial femtosecond crystallography.....	71
2.9.1 Sample delivery and data collection	71
2.9.2 Data processing.....	71
2.9.3 Structure solution and refinement.....	72
2.10 Droplet Microfluidics	73
2.10.1 Device fabrication	73
2.10.2 Microfluidic experimental setup and flow conditions	74
2.10.3 Crystal retrieval and analysis	76
2.10.4 Mixing in droplets and image analysis	77
Chapter 3 Towards time-resolved studies of AtPdx1.3.....	78
3.1 From single crystals to microcrystals of AtPdx1.3	79
3.2 Serial femtosecond crystallography (SFX) of AtPdx1.3.....	90
3.3 Kinetic crystallography of AtPdx1.3	99
3.4 Discussion	106
Chapter 4 Droplet microfluidics for crystal size engineering.....	110
4.1 Crystal size control by droplet miniaturisation.....	111
4.1.1 Lysozyme	111
4.1.2 Thaumatin	114
4.2 Microseeding strategies to overcome low nucleation rates at small scales	116
4.2.1 AtPdx1.3.....	116
4.2.2 Chlorite dismutase.....	118
4.3 Serial synchrotron crystallography (SSX) for testing diffraction quality of microcrystals grown in batch and droplet conditions	123
4.3.1 Lysozyme	124
4.3.2 Thaumatin	126
4.3.3 AtPdx1.3.....	130

Table of Contents

4.3.4 Chlorite dismutase.....	132
4.4 Considerations for crystallisation in microfluidic droplets	136
4.4.1 Axial ratio	136
4.4.2 Viscosity.....	137
4.4.3 Minimum crystal size.....	137
4.5 Discussion	139
Chapter 5 Droplet microfluidics for rapid micromixing	143
5.1 Mixing in droplets	144
5.2 Fabrication of an X-ray transmissible droplet microfluidic device	148
5.2.1 Material feasibility testing of PDMS.....	148
5.2.2 Fabrication of a thin-film PDMS droplet microfluidic device for in-flow experiments at a beamline.....	154
5.3 N-Acetylglucosamine (GlcNac) binding to lysozyme, a proof-of-principle experiment for time-resolved mixing	161
5.3.1 Validation of time-resolved GlcNac binding using a tapedrive-based sample delivery system	162
5.3.2 Effect of GlcNac concentration on ligand occupancy.....	165
5.4 PDMS droplet microfluidic device commissioning beamtime	168
5.5 Discussion	174
Chapter 6 Conclusions and future work	178
Appendix A Supplementary crystallographic tables	180
Appendix B Publication 1	188
Appendix C Publication 2	201
Bibliography.....	220

Table of Tables

Table 1. Comparison of sample delivery methods for serial crystallography.	40
Table 2. Crystal structures of <i>Arabidopsis thaliana</i> Pyridoxal 5'-phosphate synthase subunit 1.3 (AtPdx1.3).	51
Table 3. Targets for time-resolved serial crystallography of AtPdx1.3.	54
Table 4. Flow conditions for preparing Lysozyme crystals in droplets.....	75
Table 5. Flow conditions for preparing AtPdx1.3 crystals in droplets.	75
Table 6. Flow conditions for preparing Trypsin crystals in droplets.....	75
Table 7. Flow conditions for preparing Chlorite Dismutase crystals in droplet.	75
Table 8. Flow conditions for preparing Thaumatin crystals in droplets.	76
Table 9. Data collection and refinement statistics for AtPdx1.3.	94
Table 10. Data collection and refinement statistics for Lysozyme crystals growth under batch and droplet conditions.	124
Table 11. Data collection and refinement statistics for thaumatin crystals grown under batch and droplet conditions.	127
Table 12. Data collection and refinement statistics for AtPdx1.3 crystals grown under batch and droplet conditions.	130
Table 13. Data collection and refinement statistics for chlorite dismutase crystals grown under batch and droplet conditions.	133
Table 14. Calculated X-ray interaction distances and corresponding timepoints for selected flow rates in the droplet microfluidic device.	156
Table 15. Droplet diameter measurements from the droplet microfluidic devices. .	157
Table 16. Data collection statistics for static SSX data collection of lysozyme microcrystals in the PDMS droplet microfluidic device and the mylar chipless chip.	172
Table 17. Data collection and initial refinement statistics for I320 cryo-trapping experiments.....	180

Table of Tables

Table 18. Data collection and initial refinement statistics for PLP cryo-trapping experiments.....	181
Table 19. Data collection and initial refinement statistics for tapedrive experiments with lysozyme microcrystals and 50 mg/mL GlcNac.....	182
Table 20. Data collection and initial refinement statistics for static equilibrium soaks of lysozyme microcrystals with 1 to 20 mg/mL GlcNac on SOSOS chips at ESRF.	183
Table 21. Data collection and initial refinement statistics for static equilibrium soaks of lysozyme microcrystals with 30 to 50 mg/mL GlcNac on SOSOS chips at ESRF.	184
Table 22. Data collection and initial refinement statistics for single crystal lysozyme GlcNac soaking experiments from 0 to 10 mg/mL.	185
Table 23. Data collection and initial refinement statistics for single crystal lysozyme GlcNac soaking experiments from 20 to 50 mg/mL.	186

Table of Figures

Figure 1. The evolution of macromolecular crystallography.....	23
Figure 2. Eadweard Muybridge's <i>The Horse in Motion</i>.....	24
Figure 3. Assembly of a protein crystal.	26
Figure 4. Bragg's Law.....	26
Figure 5. Geometric construction of the Ewald sphere.....	27
Figure 6. The difference between conventional rotation crystallography and serial crystallography.....	30
Figure 7. X-ray generation at synchrotron and XFEL facilities.....	31
Figure 8. Diffraction before destruction.....	32
Figure 9. A protein crystallisation phase diagram.....	34
Figure 10. Iterative seeding improves crystal quality of a helicase.....	36
Figure 11. Effect of seed stock concentration on crystal size and number of a tyrosine kinase.	36
Figure 12. Serial crystallography sample delivery methods.	39
Figure 13. Fixed-target data collection strategies.....	41
Figure 14. Examples of liquid injectors.	43
Figure 15. Droplet injector from the Ros lab.	45
Figure 16. Hybrid methods.....	46
Figure 17. A 3D flow-focusing microfluidic device on the beamline.....	47
Figure 18. Time-resolved methods and their corresponding timescales.....	48
Figure 19. Crystallographic snapshots of the AtPdx1.3 reaction cycle.	53
Figure 20. Effect of Taylor dispersion in microfluidic channels.	56
Figure 21. Microfluidic device fabrication by photolithography and soft lithography. 58	
Figure 22. Microfluidic experimental setup for droplet generation.....	74

Table of Figures

Figure 23. Breaking the emulsion.....	76
Figure 24. Nickel His-Tag purification of AtPdx1.3.	79
Figure 25. Crystallisation workflow for transitioning from single crystals to large volumes of microcrystals.....	80
Figure 26. Effect of sodium citrate concentration on AtPdx1.3 crystal size under vapour diffusion conditions.....	81
Figure 27. Vapour diffusion phase diagram of AtPdx1.3.....	83
Figure 28. A simple and rapid microbatch-under-oil setup for generating phase diagrams.	85
Figure 29. A microbatch-under-oil phase diagram of AtPdx1.3.....	86
Figure 30. Experimental setup for scaling up of batch conditions on the Oryx8 crystallisation robot.	88
Figure 31. Effect of volume scaling on crystal size and density in microcrystal slurries.	89
Figure 32. Optimised AtPdx1.3 microcrystal slurry produced via seeded-batch cditions.	90
Figure 33. Oxford fixed-target chip for SFX sample delivery.	91
Figure 34. Oxford fixed-target chip sample delivery system at the SACLA XFEL.	92
Figure 35. SFX crystal structure of wildtype AtPdx1.3 at a resolution of 1.83 Å.....	93
Figure 36. SFX crystal structure of AtPdx1.3 with R5P bound at a resolution of 1.83 Å.....	96
Figure 37. SFX crystal structure of AtPdx1.3 with PLP bound at a resolution of 1.94 Å.....	97
Figure 38. SFX crystal structure of AtPdx1.3 with the I320 intermediate formed at a resolution of 1.98 Å.....	98
Figure 39. The experimental setup for <i>in crystallo</i> UV-Vis spectroscopy.	100
Figure 40. <i>In crystallo</i> UV-Vis absorption spectra tracking I320 intermediate formation in AtPdx1.3.....	101
Figure 41. Time-resolved structural snapshots of I320 formation in AtPdx1.3 crystals.102	

Figure 42. <i>In crystallo</i> UV-Vis absorption spectra of AtPdx1.3 following incubation with PLP.	103
Figure 43. Time-resolved structural snapshots of PLP binding to AtPdx1.3 crystals.	105
Figure 44. Droplet miniaturisation for lysozyme crystallisation.	111
Figure 45. Rapid growth of lysozyme microcrystals under batch conditions.	112
Figure 46. Control of lysozyme crystal size through droplet volume scaling.	113
Figure 47. Trade-offs associated with droplet volume miniaturisation.	114
Figure 48. Droplet confinement enhances crystal size uniformity in thaumatin.	115
Figure 49. Effect of seed stock dilution on seeded-batch crystallisation of AtPdx1.3.	117
Figure 50. Droplet volume scaling enables crystal size uniformity in AtPdx1.3 crystallisation.	118
Figure 51. Effect of seed stock dilution on seeded-batch crystallisation of chlorite dismutase.	119
Figure 52. Influence of chlorite dismutase seed stock on droplet flow stability.	120
Figure 53. Effect of seed stock filtering on crystal size distribution in chlorite dismutase crystallisation under seeded-batch conditions.	121
Figure 54. Droplet confinement of chlorite dismutase with filtered seed stock.	122
Figure 55. The sheet-on-sheet on spine (SOSOS) chip for SSX experiments at ESRF ID29.	123
Figure 56. Structural comparison of Lysozyme from batch-grown and droplet-grown crystals.	126
Figure 57. Structural comparison of thaumatin from batch-grown and droplet-grown crystals.	129
Figure 58. Structural comparison of AtPdx1.3 from batch-grown and droplet-grown crystals.	132
Figure 59. Structural comparison of chlorite dismutase from batch-grown and droplet-grown crystals.	135
Figure 60. The effect of droplet confinement on crystal axial ratio.	136

Table of Figures

Figure 61. The effect of viscosity on droplet throughout.	137
Figure 62. The production of femtolitre-sized droplets for <i>AtPdx1.3</i> crystallisation.	138
Figure 63. Rapid connective-diffusive mixing in droplets.	143
Figure 64. The presence of crystals does not affect mixing times in droplets.....	145
Figure 65. The ratio of components being mixed effects mixing times in droplets.	146
Figure 66. Increasing droplet velocity leads to faster mixing times.	147
Figure 67. Effect of PDMS film thickness and X-ray energy on background scattering.	149
Figure 68. Control measurements of background scattering for air and 6 μm thick mylar.	150
Figure 69. PDMS-induced background scattering as a function of film thickness and X-ray energy.	150
Figure 70. Peak background scattering from PDMS across varying film thicknesses and varying X-ray energies.	151
Figure 71. X-ray diffraction testing of lysozyme microcrystals embedded in PDMS thin-film assemblies.	152
Figure 72. Effect of PDMS thickness and X-ray energy on diffraction data quality.	153
Figure 73. Droplet microfluidic device design for time-resolved serial crystallography.	155
Figure 74. Effect of channel widening on droplet velocity and spacing.	157
Figure 75. Assessment of droplet residence time uniformity across eleven widened incubation cells.	158
Figure 76. Thin-film PDMS microfluidic assembly for synchrotron experiments.	160
Figure 77. Supplementary equipment for enhanced beamline functionality.	161
Figure 78. Time-resolved crystallographic snapshots of GlcNac binding to lysozyme using drop-on-demand sample delivery.	162
Figure 79. Experimental configuration of the tapedrive-based sample delivery system at ESRF ID29.	163
Figure 80. Time-resolved GlcNac binding via the ESRF tapedrive.	164

Table of Figures

Figure 81. Electron density, polder, and omit maps of GlcNac binding to single lysozyme crystals soaked with increasing ligand concentrations under cryogenic conditions.....	166
Figure 82. Electron density, polder, and omit maps of GlcNac binding to lysozyme microcrystal slurries soaked with increasing ligand concentrations under room temperature conditions.....	167
Figure 83. Refined GlcNac occupancy values across concentration and data collection modality.....	168
Figure 84. Integration of the PDMS droplet microfluidic device into the Diamond I24 beamline.....	169
Figure 85. Evaluation of PDMS droplet microfluidic device performance under beamline conditions at I24.	170
Figure 86. Static SSX data collection using PDMS microfluidic device and a mylar chipless chip.....	171
Figure 87. Comparison of diffraction quality between a PDMS droplet microfluidic device and a mylar chipless chip.	173

List of Accompanying Materials

Crystal structures presented in this thesis have been deposited in the Protein Data Bank (PDB) for public access and reference:

1. SSX structure of lysozyme grown in batch conditions (PDB: 8S2U)
2. SSX structure of lysozyme grown in microfluidic droplets (PDB: 8S2V)
3. SSX structure of *Arabidopsis thaliana* Pdx1.3 grown in seeded batch conditions (PDB: 8S2W)
4. SSX structure of *Arabidopsis thaliana* Pdx1.3 grown in microfluidic droplets (PDB: 8S2X)
5. SSX structure of thaumatin grown in batch conditions (PDB: 9QXW)
6. SSX structure of thaumatin grown in microfluidic droplets (PDB: 9QXY)

The SFX structures of *Arabidopsis thaliana* Pdx1.3 and the SSX structures of *Cyanothece sp.* PCC 7425 chlorite dismutase remain confidential and therefore have not been deposited.

Research Thesis: Declaration of Authorship

Print name: Jack Robert Stubbs

Title of thesis: Droplet Microfluidic and Microcrystal Strategies for Time-Resolved Serial Crystallography of Enzymes at Synchrotron and XFEL Sources

I declare that this thesis and the work presented in it are my own and has been generated by me as the result of my own original research.

I confirm that:

1. This work was done wholly or mainly while in candidature for a research degree at this University;
2. Where any part of this thesis has previously been submitted for a degree or any other qualification at this University or any other institution, this has been clearly stated;
3. Where I have consulted the published work of others, this is always clearly attributed;
4. Where I have quoted from the work of others, the source is always given. With the exception of such quotations, this thesis is entirely my own work;
5. I have acknowledged all main sources of help;
6. Where the thesis is based on work done by myself jointly with others, I have made clear exactly what was done by others and what I have contributed myself;
7. Parts of this work have been published as:

Stubbs, J., Hornsey, T., Hanrahan, N., Esteban, L.B., Bolton, R., Malý, M., Basu, S., Orlans, J., De Sanctis, D., Shim, J., Shaw Stewart, P.D., Orville, A.M., Tews, I., West, J., 2024. Droplet microfluidics for time-resolved serial crystallography. *IUCrJ* 11, 237–248.

<https://doi.org/10.1107/S2052252524001799>

Tremlett, C.J.‡, Stubbs, J.‡, Stuart, W.S., Stewart, P.D.S., West, J., Orville, A.M., Tews, I. and Harmer, N.J., 2025. Small but mighty: the power of microcrystals in structural biology. *IUCrJ*, 12(3), 262-279.

<https://doi.org/10.1107/S2052252525001484>

Signature: Date:.....

Acknowledgements

First and foremost, I would like to thank my primary supervisors, Ivo Tews, Allen Orville, and Jonathan West whose insight, encouragement, and unwavering support have been instrumental throughout this journey. Their willingness to embrace new ideas has shaped not only this thesis but also my approach to scientific research.

I'm especially grateful to Ivo and Allen for teaching me all things crystallography, and for allowing me to explore the world through 35 beamtimes across synchrotron and XFEL facilities amounting to over 1000 hours of beamtime (big thanks to Phil and Pauline for transporting me to the airport). I consider myself incredibly fortunate for these opportunities. To Jonathan, thank you for illuminating the world of microfluidics and introducing me to the wonders of droplets. To Patrick Shaw Stewart and Stefan Kolek, thank you for supporting the industrial placement, your guidance in crystallisation and for troubleshooting alongside me with the Oryx robot, which I now strongly advocate. I'm also grateful to Pierre Aller and Mark Roe for being part of the supervisory team and for supporting training and opportunities wherever possible. At Diamond, I would like to thank Robin Owen and Danny Axford for their continued support with access to beamtime at I24, and for their openness to new instrumentation. I also thank James Beilsten-Edmands for his help with serial data processing. My appreciation extends to those who made the long nights at ID29 more enjoyable: Courtney Tremlett, Lewis Williams, Eloisa Wheatley, and Abi Balakrishnan. I also want to acknowledge the undergraduates I've had the pleasure of supervising during the BIOL3034 project, as well as Darwin Tu and Abigail Waitman, whom I was fortunate to mentor during their master's projects.

I'm thankful for the funding provided by the Biotechnology and Biological Sciences Research Council (BBSRC), South Coast Biosciences Doctoral Training Partnership (SoCoBio DTP, BB/T008768/1), University of Southampton, Diamond Doctoral Studentship Programme, Wellcome Investigator Award (210734/Z/18/Z awarded to Allen Orville) and Royal Society Wolfson Fellowship (RSWFR2 awarded to Allen Orville), which made this work possible.

To my labmates in Southampton, Abigail Sudol, Charlotte Cordery, Martin Maly, Rachel Bolton, Hayden Fisher, Anjala Gammanpila, Elodie Wells, Isabel Elliott, Kieran Basavaraja, Malek Hawela, Daniel Burns and Kinga Niedobecka, your humour and support made even the most demanding experiments memorable. Special thanks to those who offered insight and encouragement beyond the lab. To Abigail and Charlotte who were there from the start and guided me throughout the PhD, I'm beyond grateful. And to Martin I say ahoj, your infectious enthusiasm and crystallographic knowledge will stay with me throughout my career.

Acknowledgements

To my collaborators and colleagues, particularly those at the University of Southampton, Diamond Light Source, and the European Synchrotron Radiation Facility, thank you for your expertise, enthusiasm, and camaraderie. Your discussions, patience, and generosity helped transform challenging moments into meaningful progress. I'm also indebted to the mentors and lecturers who first inspired my passion for structural biology and crystallography.

To my family, thank you for your unconditional love and support. To my girlfriend Kat, whose patience, positivity, and unwavering presence has guided me through every high and low, thank you for being my rock throughout the PhD. I truly can't thank you enough.

Lastly, to the memory of Alan, Sam, and Christine, whose presence is missed but whose influence quietly endures, you are never far from thought.

Definitions and Abbreviations

ADE	Acoustic droplet ejection
ASU	Asymmetric unit
ASU	Arizona state university
AtPdx1.3	<i>Arabidopsis thaliana</i> pyridoxal 5'-phosphate synthase subunit 1.3
BITS	Combination of inject-and-transfer system
CAD	Computer-aided design
COC	Cyclic olefin copolymer
coMESH.....	Concentric-flow electrokinetic holder
CV	Coefficient of variation
DFFN	Double flow-focusing nozzle
DoD	Droplet on demand
ESRF.....	European synchrotron radiation facility
FID.....	Free interface diffusion
G3P	Glyceraldehyde-3-phosphate
GDVN	Gas dynamic virtual nozzle
GlcNac	N-Acetylglucosamine
GPCRs	G-protein coupled receptors
HARE	Hit-and-return
HVE	High-viscosity extruder
icOS.....	In crystallo optical spectroscopy
ID	Internal diameter
IMAC.....	Immobilised metal affinity chromatography
K166	Lysine 166
K98	Lysine 98
K_{cat}	Median enzyme turnover rate
LAMA.....	Liquid application method for time-resolved analyses
LCLS.....	Linac coherent light source

Definitions and Abbreviations

LCP	Lipidic cubic phase
MBM	Microbatch mixing
MDI	Modular droplet injector
MESH	Microfluidic electrokinetic sample holder
MicroED	Microcrystal electron diffraction
MISC	Mix-and-inject serial crystallography
MISP	Micro-structured polymer
MME	Monomethyl ether
MPD	2-methyl-2,4-pentanediol
MR	Molecular replacement
MX	Macromolecular crystallography
O/W	Oil-in-water
O/W/O	Oil-in-water-in-oil
OAV	On-axis viewing
OD	Outer diameter
PDB	Protein data bank
PDE	Piezoelectric droplet ejection
PDMS	Polydimethylsiloxane
PEG	Polyethylene glycol
PFO	1 <i>H</i> ,1 <i>H</i> ,2 <i>H</i> ,2 <i>H</i> -perfluoro-1-octanol
PLP	Pyridoxal 5'-phosphate
PSI	Photosystem I
R5P	Ribose-5-phosphate
<i>Re</i>	Reynolds number
<i>R</i> _{free}	Free R-factor
rMMS	Random microseed matrix screening
RMSD	Root mean square deviation
<i>R</i> _{work}	Working R-factor

Definitions and Abbreviations

SAA.....	Sulfanilic acid azochromotrop
SACLA	SPring-8 angstrom compact free electron laser
SASE.....	Self-amplifying spontaneous emission
SD	Standard deviation
SDS-PAGE.....	Sodium dodecyl sulphate-polyacrylamide gel electrophoresis
SFX.....	Serial femtosecond crystallography
SNR	Signal-to-noise ratio
SOS	Sheet-on-sheet
SOSOS.....	Sheet-on-sheet-on-spine
SSX.....	Serial synchrotron crystallography
TR-SX.....	Time-resolved serial crystallography
VMXm	Versatile macromolecular crystallography microfocus
W/O	Water-in-oil
W/O/W.....	Water-in-oil-in-water
XES.....	X-ray emission spectroscopy
XFEL	X-ray free electron laser

Chapter 1 Introduction

Enzymes serve as nature's catalysts, driving the biochemical reactions essential for life. This remarkable proficiency is largely attributed to dynamic conformational changes that occur during catalysis, processes which are difficult to capture with conventional static imaging techniques. X-ray crystallography has yielded high-resolution data on the ensemble averaged structure of a protein. However, these static snapshots often mask transient states that are critical to understanding enzymatic mechanisms. In response to this challenge, time-resolved serial crystallography has emerged as a transformative approach, offering insights into protein dynamics by capturing successive structural snapshots of enzymatic systems. This approach has the potential to bridge the gap between static structural data and the dynamic nature of biological function. In doing so, it deepens our understanding of enzyme mechanisms and informs future drug discovery and enzyme engineering strategies. The broad aim of this thesis is to develop droplet microfluidic and microcrystal strategies for advancing time-resolved serial crystallography by enabling precise crystal size engineering and rapid defined mixing.

Some of the figures shown in this chapter appear in the following publication: Tremlett, C.J.‡, Stubbs, J.‡, Stuart, W.S., Stewart, P.D.S., West, J., Orville, A.M., Tews, I. and Harmer, N.J., 2025. Small but mighty: the power of microcrystals in structural biology. *IUCrJ*, 12(3), 262-279. The publication is included within the Appendix for reference.

1.1 Macromolecular Crystallography

1.1.1 The evolution of macromolecular crystallography

Macromolecular crystallography (MX), established in the early 20th century, laid the groundwork for modern structural biology by enabling atomic-level visualisation of biological macromolecules. Its emergence marked a transformative moment in our ability to interrogate the molecular architecture of life. A landmark achievement came in 1958 when Kendrew and colleagues determined the first 3D structure of a protein, myoglobin using X-ray diffraction methods (1). This breakthrough not only demonstrated the feasibility of protein structure determination but also precipitated a wave of discoveries that would shape biochemistry, molecular biology, and drug design for decades to come.

In its early stages, MX was constrained by significant technical limitations. Crystals suitable for diffraction had to exceed 100 µm in all dimensions to ensure sufficient scattering volume, and data collection required prolonged exposure times due to the relatively low brilliance of

available X-ray sources (2) (**Figure 1**). These challenges necessitated meticulous crystal growth protocols to grow such large crystals and often limited the scope of structural studies to highly stable, abundant proteins. Despite these hurdles, the foundations of MX remained robust, forming the basis for successive innovations in synchrotron instrumentation, detector technology and computational algorithms. The introduction of synchrotron radiation in the 1980s marked a major turning point. First-generation synchrotrons originally designed for particle physics, were repurposed to deliver more focused X-ray beams that dramatically improved resolution and throughput (3–5). Subsequent generations brought dedicated beamlines, enhanced monochromaticity, and microfocus capabilities. Today, third and especially fourth-generation synchrotrons offer diffraction-limited storage rings, enabling highly precise interrogation of protein crystals just a few micrometres in size (6) (**Figure 1**). These advances have not only reduced sample requirements but also expanded the scope of MX to previously inaccessible targets.

As the field matured, it became clear that static cryogenically trapped structures offered only a limited view of biological function, particularly for enzymes whose activity depends on dynamic conformational changes and transient intermediate states. To address this, time-resolved crystallography emerged in the late 20th century, allowing scientists to capture short-lived intermediates within enzymatic reaction cycles (7–10). This approach expanded the temporal dimension of MX, enabling snapshots of molecular motion and reactivity. More recently, the development of X-ray free electron lasers (XFELs) has further transformed the landscape. These sources deliver femtosecond pulses with extreme brilliance, allowing single-shot diffraction from microcrystals and facilitating studies of irreversible or radiation-sensitive processes (11,12). In parallel, the rise of room-temperature data collection has gained momentum, offering a more physiologically relevant view of protein dynamics by preserving native conformational ensembles and reducing cryo-induced artefacts (13,14).

Complementing these hardware advances, serial crystallography has emerged as a powerful strategy for collecting complete datasets from thousands of microcrystals (15,16). This approach has enabled high-resolution structure determination under near-native conditions and is particularly well-suited to time-resolved experiments and ligand screening. In parallel, microcrystal electron diffraction (MicroED) has expanded the structural toolkit by enabling atomic-resolution data collection from nanocrystals, less than 1 μm in size (17,18). This is possible due to the strong interaction between electrons and biological matter (19). Bridging the gap between electron-based and X-ray based microcrystal methods, beamlines such as Versatile Macromolecular Crystallography microfocus (VMXm) at Diamond Light Source now enable *in situ* diffraction from crystals as small as 1–2 μm (20,21). VMXm operates *in vacuo* to minimise air scatter and employs a high energy, nanofocused X-ray beam to optimise data

quality from small-volume samples benefitting from enhanced photoelectron escape and reduced radiation damage (22). Together these developments represent a convergence of precision, speed, and biological relevance. The evolution of MX can be traced not only through its expanding methodological repertoire from static single crystal diffraction to time-resolved, serial, and electron-based techniques, but also through the dramatic reduction in crystal size from millimetre to nanometre scales (**Figure 1**). From the early days of large static crystals to today's dynamic, micro and nanocrystal workflows, MX continues to evolve. The boundaries of what can be visualised, understood, and engineered at the molecular level are being pushed further than ever before.

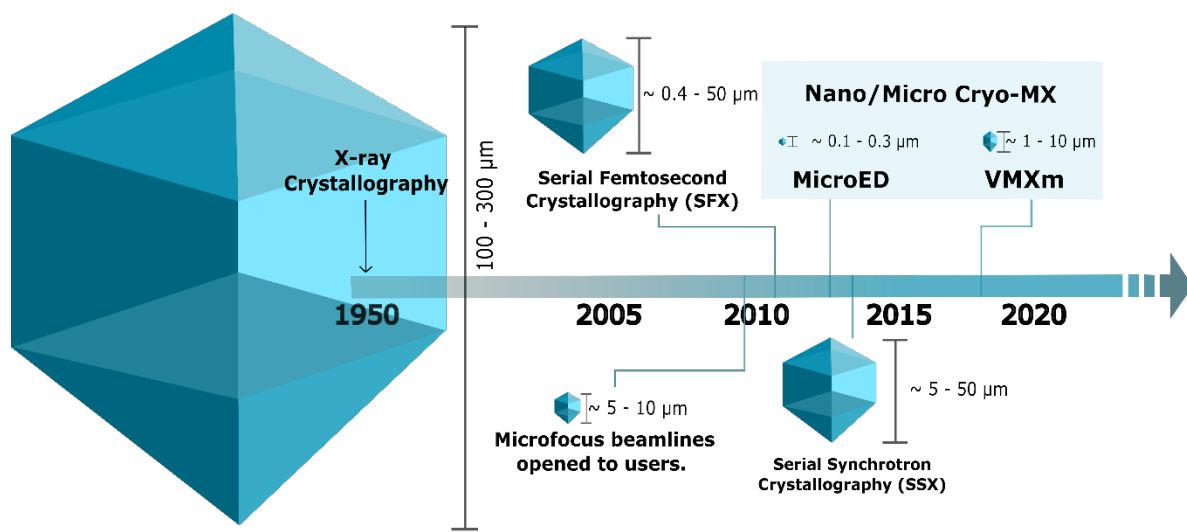


Figure 1. The evolution of macromolecular crystallography. Macromolecular crystallography (MX) gave rise to the first 3D protein structure of myoglobin in the 1950s but at the time, large crystals ($>100\text{ }\mu\text{m}$) were required to generate enough signal. The emergence of synchrotron radiation in the late 1980s led to an increase in the number of structures solved by X-ray crystallography. In the early 2000s, improvements in instrumentation and sources led to the development of microfocus beamlines, allowing data collection from much smaller crystals. More recently, a rise in room temperature data collection along with the integration of serial crystallography has led to an uptake in experiments at synchrotrons and XFELs. Ongoing source, detector and method developments will result in data collection from crystals as small as a few microns, for example at the VMXm beamline, or even a few hundreds of nanometres via the use of MicroED. Image taken from Tremlett *et al.* (23).

All MX experiments yield ensemble averaged measurements, meaning that the resulting structure represents an average over many molecular conformations present within the protein crystal. This is conceptually similar to Muybridge's 1887 'horse in motion' experiment (24), where a composite image captures multiple phases of movement simultaneously (**Figure 2A**). In MX, the crystal contains a population of molecules in various conformational or chemical states, and the diffraction data reflects a spatial and temporal average of these states. As a result, transient intermediates and dynamic changes are often obscured, leading to a loss of structural resolution and dynamic insight (**Figure 2B**). Historically, intermediate states were probed by soaking ligands into preformed crystals and arresting the reaction at specific

timepoints using mechanistic or kinetic trapping (25). These approaches typically capture static snapshots on timescales ranging from seconds to minutes and are limited by the feasibility of trapping, and the stability of the intermediate. Such methods are inherently restrictive when the goal is to observe transitions between states or capture fleeting conformations. The emergence of XFEL sources and serial crystallography has transformed this landscape. These approaches enable time-resolved experiments that capture molecular motion in real time (26). Pump-probe strategies allow for the synchronised initiation of a reaction follow by rapid data collection at defined time delays. Depending on the X-ray source, it is possible to achieve temporal resolutions down to the femtosecond timescale. This is several orders of magnitude faster than traditional trapping experiments and offers unprecedented insights into the structural dynamics of biological systems (27).

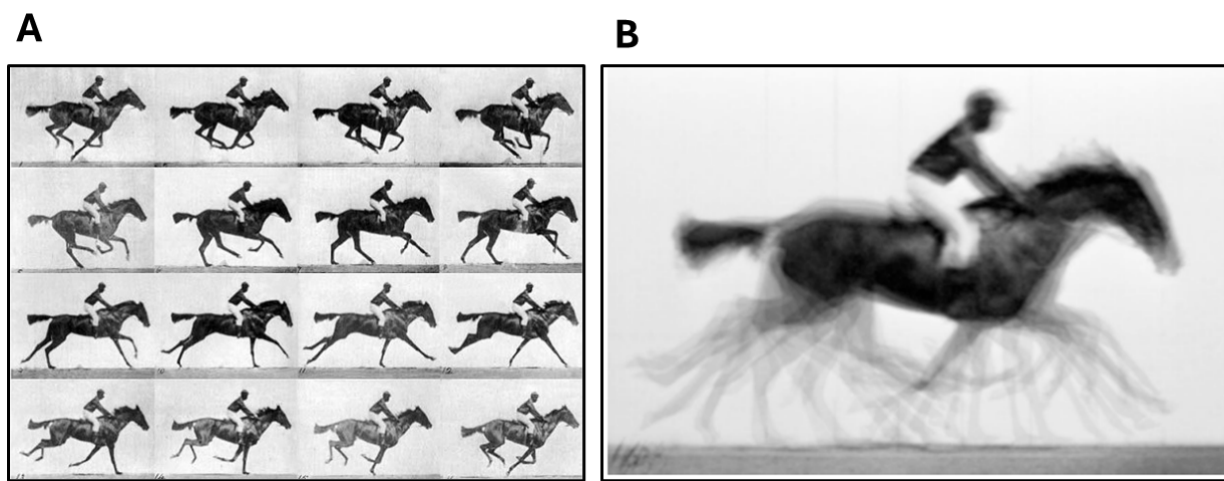


Figure 2. Eadweard Muybridge's *The Horse in Motion*. (A) A series of films observing snapshots of the horse's movement and action, akin to all the conformations of a macromolecule being probed in a macromolecular crystallography experiment. (B) An averaged out image of the horse's movement over time, akin to an averaged ensemble which is collected during an MX experiment, resulting in the loss of dynamic information. Images adapted from Stillman and Muybridge (28).

1.1.2 Core crystallographic principles

All crystallographic workflows, be that single crystal, serial or time-resolved, are governed by physical and mathematical principles that define how molecular structure is derived from X-ray diffraction data. These concepts shape experimental design, data collection strategies and structure solution pipelines, but remain central regardless of crystal format or beamline modality. The primary goal of any X-ray diffraction experiment is to reconstruct the electron density map of the unit cell from the information encoded in the diffracted X-rays. This map reveals the spatial distribution of electrons within the crystal. This enables the construction of an atomic model by fitting individual atoms into regions of electron density that correspond to the molecular structure of the protein. A full treatment of crystallographic theory is beyond the scope of this thesis, but core crystallographic principles are briefly introduced.

1.1.2.1 Crystal lattice, unit cell and asymmetric unit

Protein crystals are highly ordered, three-dimensional arrays of macromolecules capable of diffracting incident X-rays into discrete reflections. These crystals form through the self-assembly of protein molecules into repeating units, stabilised by non-covalent interactions such as hydrogen bonding, van der Waals forces, and electrostatic contacts. For diffraction to be measurable, the crystal lattice must exhibit sufficient order; an especially critical requirement in serial crystallography, where data are collected from micron-sized crystals. In such cases, the integrity and stability of the lattice are paramount, as the reduced number of molecules limit the amplification of signal relative to background noise. The quality of the crystal lattice directly affects the sharpness of diffraction patterns. If the lattice is well-ordered, X-rays scatter coherently, producing sharp reflections. However, lattice disorder or high mosaicity where the crystal is composed of many small domains that are slightly misaligned, causes reflections to broaden and lose intensity. This lowers the signal-to-noise ratio and reduces the resolution of the resulting electron density map, compromising the accuracy of atomic modelling.

At the core of the crystal lattice is the unit cell, the smallest repeating unit defined by six parameters: three edge lengths (a, b, c) and three interaxial angles (α, β, γ). Contained within the unit cell is the asymmetric unit (ASU), the smallest portion of the structure from which the entire crystal can be reconstructed using symmetry operations (**Figure 3**). These operations, including translations, rotations, screw axes, and mirror planes are collectively described by the space group, which governs how the ASU is propagated throughout the crystal lattice and how diffraction reflections are related. The complete set of symmetry combinations yields 230 unique space groups, of which only 65 are compatible with chiral molecules. This restriction arises because chirality precludes symmetry elements such as mirror planes and inversion centres, which would violate the handedness of the molecular structure. Accurate determination of the space group is essential for the key steps in crystallographic data processing, including indexing, integration, and model building.

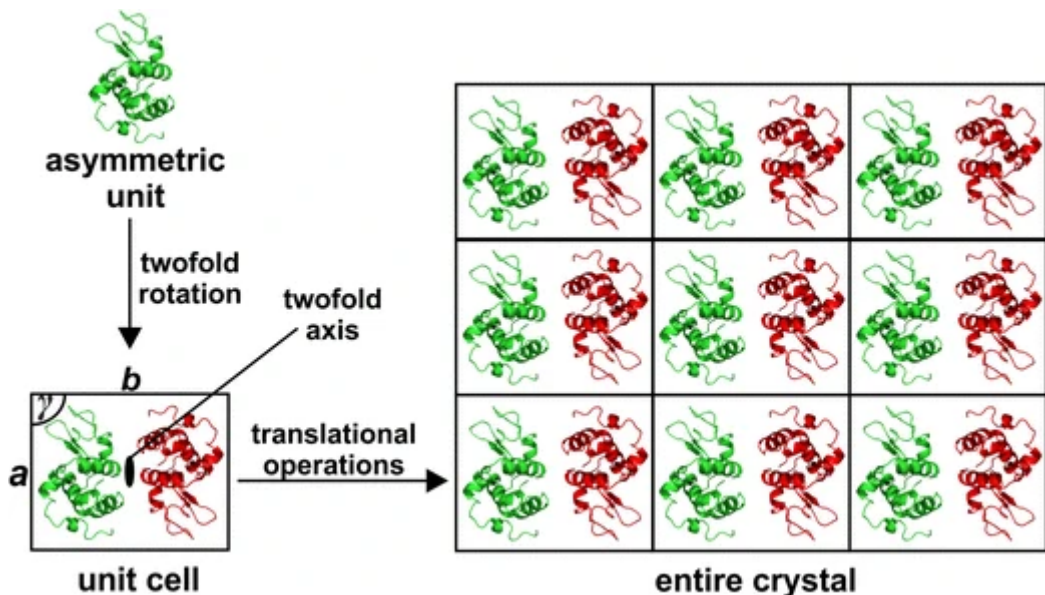


Figure 3. Assembly of a protein crystal. The asymmetric unit consists of one molecule of lysozyme (green). The unit cell is generated by applying a two-fold rotation to produce a copy of the molecule known as a symmetry mate (red). By applying translational operations to the unit cell, the entire crystal can be built. Image taken from Bijelic and Rompel (29).

1.1.2.2 Bragg's Law and diffraction geometry

When X-rays are directed at a protein crystal (incident on its surface), they are scattered by the electrons within its ordered lattice. For these scattered waves to interfere constructively and thus produce detectable diffraction spots, the path difference between reflections from adjacent lattice planes must be an integer multiple of the X-ray wavelength (**Figure 4**). Constructive interference occurs only when the scattered waves from multiple planes remain in phase, resulting in discrete diffraction signals. This fundamental condition is governed by Bragg's Law (**Equation 1**), which defines the relationship between the wavelength, the angle of incidence, and the spacing between lattice planes within the protein crystal.

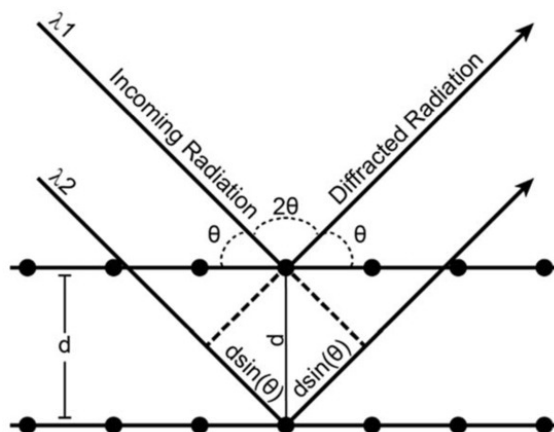


Figure 4. Bragg's Law. Incoming X-rays of wavelength λ interact with crystallographic planes spaced by distance d at angle θ . Constructive interference of diffracted X-rays occurs when the path difference between the X-rays ($2ds\sin\theta$) equals an integer multiple of the wavelength ($n\lambda$). This results in the formation of measurable diffraction spots. Image taken from Stan *et al.* (30).

$$n\lambda = 2d_{hkl} \sin \theta$$

Equation 1. Bragg's Law. Where λ is the incident X-ray wavelength, d is the spacing between lattice planes within a crystal, θ is the angle of incidence and n is the reflection order.

Bragg's law defines the angular conditions under which reflections occur and determines the geometry of the diffraction pattern. Reflections are measured in reciprocal space, which is defined by reciprocal lattice vectors, and is distinct from the real space crystal lattice. A geometric construction known, as the Ewald sphere, is used to visualise which reciprocal lattice points satisfy Bragg's condition for a given crystal orientation and X-ray wavelength (Figure 5). The Ewald sphere is drawn as a circle within reciprocal space, with a radius equal to $1/\lambda$ (the inverse of the X-ray wavelength). The crystal's reciprocal lattice is placed inside the sphere and each lattice point represents a possible reflection. Reciprocal lattice points that intersect the surface of the sphere satisfy Bragg's condition and produce detectable reflections.

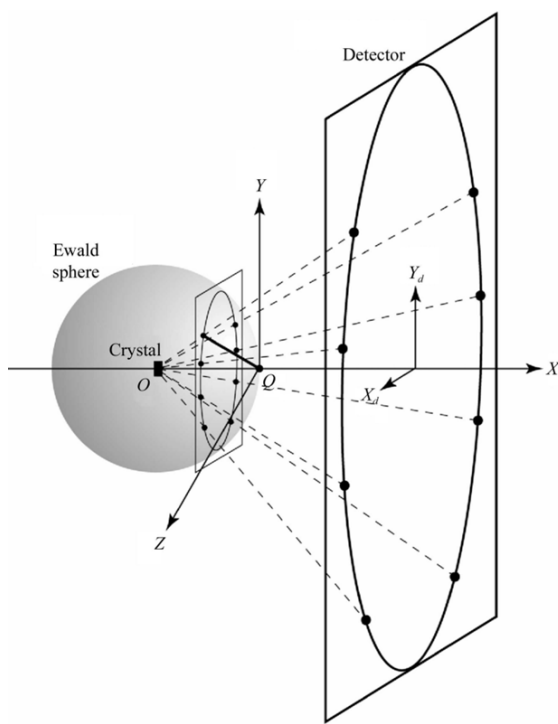


Figure 5. Geometric construction of the Ewald sphere. The X-ray beam travels on the X axis, while the crystal rotates around the Z axis. The crystal sits at the centre of the Ewald sphere (O), with its axis aligned to the X axis. The reciprocal lattice origin (Q) is positioned where the beam exits the sphere. The $h=1$ reciprocal plane is shown, with each diffraction spot corresponding to a scattering vector in reciprocal space. This is highlighted with a bold line extending from Q to the sphere's surface. Image taken from Leslie (31).

To ensure comprehensive sampling of reciprocal space, conventional crystallography rotates a single crystal during data collection, sequentially aligning different lattice planes to satisfy Bragg's Law. Serial crystallography, by contrast collects single exposures from randomly oriented microcrystals, each capturing only a small, unique slice of reciprocal space. Comprehensive coverage, therefore, relies on merging of data from thousands of crystals to reconstruct a complete dataset.

1.1.2.3 Structure factors, Fourier transforms and the phase problem

Each diffraction spot arises from the collective scattering of X-rays by all atoms within the unit cell and is mathematically described by the structure factor, $F(hkl)$, which represents the sum of individual atomic wave contributions. This wavefunction encompasses both the amplitude (related to intensity) and the phase of the scattered waves, while the frequency (or wavelength) is determined by the incident X-ray and contributes to the spatial resolution of the diffraction pattern. The positions of the diffraction spots on the detector provide frequency-related information and define the geometry of the crystal in reciprocal space. Each reflection appears as a discrete spot corresponding to a specific set of crystallographic planes. These reflections must be indexed to assign corresponding Miller indices (h, k, l) , which describe the orientation and spacing of the diffracting lattice planes. The measured intensity of each reflection $I(hkl)$ is directly proportional to the square of the structure factor amplitude $|F(hkl)|^2$. The structure factor, $F(hkl)$ encapsulates both the amplitude and phase information of the scattered X-rays and is fundamental to reconstructing the electron density map. The electron density at a given point (x, y, z) within the unit cell, denoted $\rho(x, y, z)$ is calculated via an inverse Fourier Transform of the measured diffraction data (**Equation 2**). This transformation translates reciprocal space data into a real space representation of the atomic structure. It relies on the structure factor amplitudes $|F(hkl)|$, which are obtained as the square root of the observed reflection intensities. However, to fully reconstruct the electron density, the corresponding phase angles ($\alpha_{(hkl)}$) are required. These phases are not directly measured during a diffraction experiment and must instead be estimated through phasing methods such as molecular replacement (MR) or experimental phasing.

$$\rho(x, y, z) = \frac{1}{V} \sum |F_{(hkl)}| e^{-2\pi i (hx + ky + lz - \alpha_{(hkl)})}$$

Equation 2. The electron density equation. Where V is the volume of the unit cell, hkl are the Miller indices for each reflection, $|F(hkl)|$ is the structure factor amplitude and $\alpha_{(hkl)}$ is the phase of the corresponding reflection.

In macromolecular crystallography, phase information is usually obtained through MR. This technique uses a homologous structure as a starting model to estimate phases for a new crystal. Increasingly, these models are derived from computational predictions, such as those generated by AlphaFold or alternative structure prediction software. MR is only effective when the initial model shares sufficient structural similarity with the target, allowing calculated structure factors to approximate the observed reflection intensities. This method involves determining the optimal orientation and position of the model within the unit cell to best match the experimental data. Although initial MR solutions often contain substantial inaccuracies due to imperfect model fitting, these are gradually corrected through iterative cycles of model

building, real space refinement, and reciprocal space refinement. As refinement progresses, the agreement between calculated and observed data improves, leading to more accurate phase estimates and ultimately a well-resolved electron density map suitable for atomic model interpretation.

Model quality is quantitatively assessed using two key residual metrics: the working R-factor (R_{work}) and the free R-factor (R_{free}). These values reflect the degree of agreement between the observed (F_{obs}) and calculated (F_{calc}) structure factor amplitudes. The working R-factor is computed over the reflections actively during refinement (**Equation 3**). A low R_{work} value typically indicates improved fit to the data, however it is inherently susceptible to overfitting.

$$R_{\text{work}} = \frac{\sum ||F_{\text{obs}}| - |F_{\text{calc}}||}{\sum |F_{\text{obs}}|}$$

Equation 3. The working R-factor (R_{work}) equation. Where F_{obs} is the observed structure factor amplitudes and F_{calc} is the calculated structure factor amplitudes.

Overfitting occurs when a structural model is overly adjusted to match the observed diffraction data, including noise and random fluctuations. In crystallography, this can produce a model that fits the data numerically but fails to generalise, misrepresenting the true molecular structure. In several cases, this leads to unrealistic sidechain conformations or incorrect ligand placement. To guard against overfitting, a subset of the reflections (usually 5 – 10%) is excluded from the refinement process and used to calculate the free R-factor (using the same formula as provided in **Equation 3**). Because these reflections remain unaltered during refinement, the R_{free} provides an unbiased assessment of model accuracy. A small difference between R_{work} and R_{free} reflects a well refined structure with minimal overfitting, whereas large differences would suggest modelling errors or excessive parameterisation.

1.2 Serial crystallography

Serial crystallography involves the collection of diffraction data from a series of thousands of microcrystals (15,32,33). Conventional rotation crystallography uses a goniometer to rotate a large (10 – 100 μm) cryocooled single crystal, collecting a full set of Bragg reflections on the Ewald sphere (**Figure 6A**). In contrast, serial crystallography collects single diffraction images, known as ‘stills’ from thousands of microcrystals, each with a randomly oriented lattice (**Figure 6B**). These stills contain partial reflections, and together they sample different regions of reciprocal space (34). Diffraction stills from large crystal numbers are computationally integrated, merged and scaled (**Figure 6C**). Two commonly used terms during serial crystallography data processing are hit rate (the ratio of hits to overall collected images) and indexing rate (the ratio of indexed images to hits) (**Figure 6D**) (35).

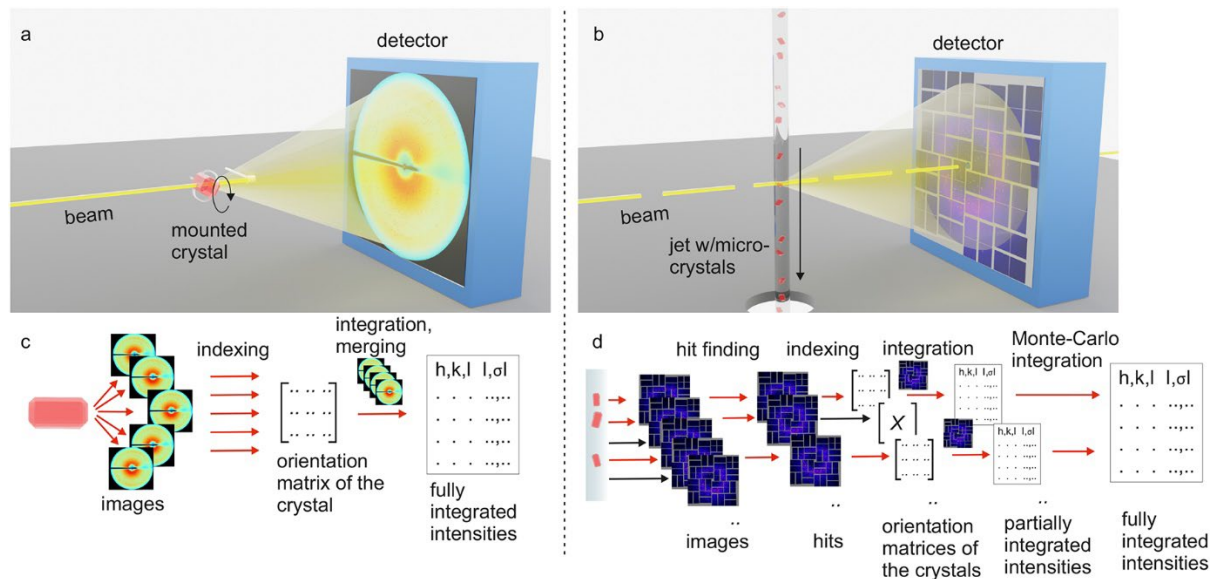


Figure 6. The difference between conventional rotation crystallography and serial crystallography. (A) In conventional rotation crystallography, a single crystal is mounted in a loop maintained at 100 K by a cryogenic stream before being rotated on a goniometer allowing consecutive X-ray exposures. (B) In serial crystallography, thousands of microcrystals are delivered in a stream into the X-ray beam at random orientations. (C) Rotation crystallography data processing involves indexing of many images from a single crystal, generating an orientation matrix before integration and merging results in fully integrated intensities. (D) Serial crystallography data processing involves processing images from individual crystals, with initial hit finding of Bragg diffraction patterns with partial intensities. The rest of the workflow is like rotation crystallography despite the final step where partial intensities must be merged by Monte-Carlo integration to generate fully integrated intensities. Image taken from Barends *et al.* (34).

1.2.1 Serial femtosecond crystallography (SFX)

Serial crystallography is performed at either synchrotron sources known as serial synchrotron crystallography (SSX) or XFELs, referred to as serial femtosecond crystallography (SFX). Both facilities generate X-rays by accelerating electrons through undulators: arrays of alternating magnets that cause electrons to oscillate and emit radiation (Figure 7A). The key distinction lies in beam properties, XFELs use multiple undulators and a linear accelerator to produce tightly packed electron bunches (~10 fs), whereas synchrotrons generate broader pulses (~100 ps) via circular storage rings (36). SFX leverages ultrashort, high-energy photon pulses to collect diffraction data before radiation damage can manifest (11,15,32). These pulses are produced via self-amplifying spontaneous emission (SASE), where X-ray photons interact with relativistic electrons in the undulator, inducing microbunching and amplifying the beam (Figure 7B) (37,38). The result is a highly brilliant, coherent X-ray pulse capable of capturing molecular snapshots on the femtosecond timescale (39,40). Its high brilliance delivers sufficient photon flux to produce measurable diffraction from microcrystals in single-shot exposures, whilst spatial coherence enhances data quality by minimising background noise. Together, these properties make XFEL pulses uniquely suited for time-resolved crystallography and the study of transient molecular states.

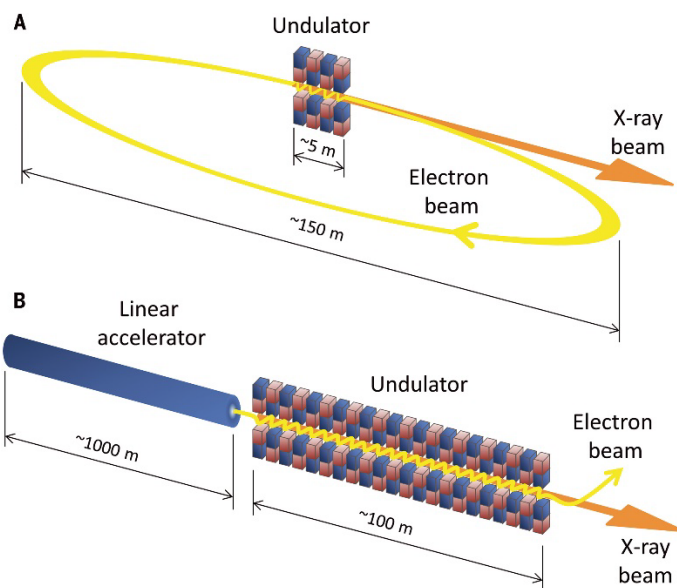


Figure 7. X-ray generation at synchrotron and XFEL facilities. At X-ray facilities, electrons are accelerated through periodic arrays of magnets known as undulators. The magnets are aligned in opposite directions, resulting in electron oscillation and the generation of X-rays. (A) At synchrotrons, electrons travel in a circular storage ring and pass through short undulators producing continuous X-ray pulses. (B) In contrast, XFELs utilise long linear accelerators generating electron bunches which pass through long undulators. This results in a feedback mechanism which leads to a coherent and compact electron bunch, with subsequently ultrafast X-ray pulses. Image taken from Brändén and Neutze (36).

The femtosecond pulse duration of an XFEL enables the collection of diffraction data before radiation damage compromises the crystal, a principle coined ‘diffraction before destruction’ (11,15). This was first proposed by Hajdu and colleagues through molecular dynamics simulations of T4 lysozyme exposed to a 2 fs XFEL pulse (12). Upon interaction, atoms within the protein are rapidly ionised, leading to a Coulomb explosion driven by electrostatic repulsion, typically occurring within 10 – 20 fs of exposure (Figure 8). Crucially, the XFEL pulse duration governs the extent of site-specific radiation damage in protein crystals: pulses shorter than 10 fs preserve atomic coordinates, while longer pulses (>10 fs) induce bond disruption, ionisation and loss of resolution (41–46).

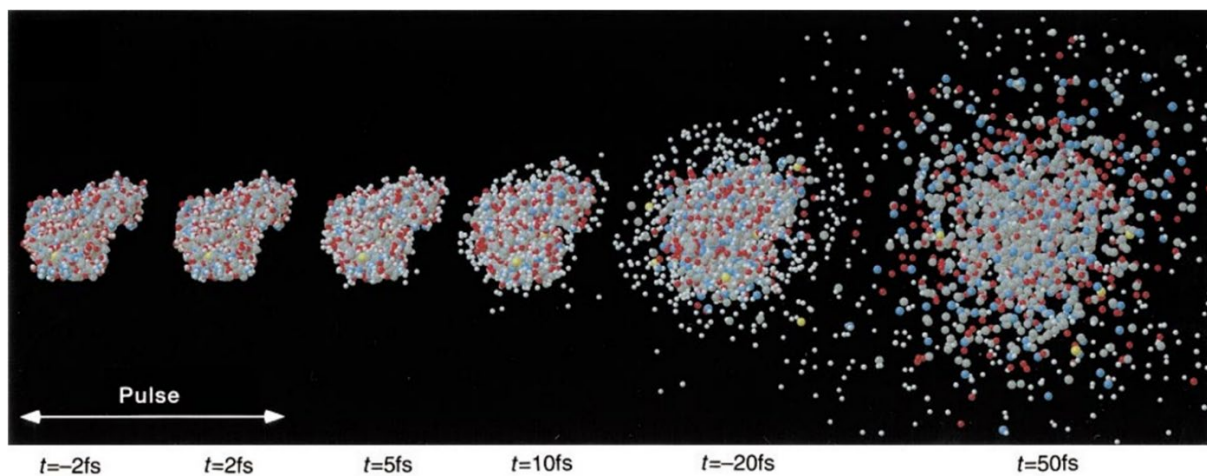


Figure 8. Diffraction before destruction. A molecular dynamics trajectory of T4 lysozyme bombarded with a 2 fs X-ray pulse, resulting in a Coulomb explosion between 10 – 50 fs. The simulation assumes a single coherent pulse of 50 fs in duration. Image from Neutze *et al.* (12).

The first SFX experiment was conducted by Chapman and colleagues in 2011 at the Linac Coherent Light Source (LCLS) in the United States (15). This landmark study provided the first experimental evidence that a hard X-ray XFEL could be used for macromolecular structure determination, successfully reconstructing photosystem I (PSI) to 8.5 Å by merging over three million individual diffraction patterns (15). Early SFX efforts focused predominantly on light-sensitive systems and membrane proteins, particularly G-protein coupled receptors (GPCRs), which naturally yield large quantities of microcrystals suitable for serial data collection. Their intrinsic conformational flexibility also makes them ideal candidates for time-resolved studies (47). More recently, XFELs have enabled structure determination from sub-micron sized crystals naturally grown *in cellulo*, expanding the scope of crystallographic analysis to include native crystals formed within insect and bacterial cells (48–51).

1.2.2 Serial synchrotron crystallography (SSX)

Due to the limited access to highly competitive XFEL beamtime, the use of synchrotron sources for collecting serial crystallographic data at room temperature has grown rapidly in recent years. This shift reflects both logistical constraints and the increasing maturity of SSX as a viable alternative for high-throughput structural studies. However, most SSX beamlines remain highly specialised, often requiring extensive prior planning, particularly when collecting room temperature data or designing time-resolved experiments. Unlike XFELs, synchrotrons deliver lower photon flux, necessitating longer X-ray exposure times (typically $\sim 100 \mu\text{s}$ to 10 ms), which are largely dictated by detector frame rates and sample delivery speeds (52,53). As a result, SSX is not inherently radiation damage free, but instead mitigates damage by distributing the X-ray dose across multiple crystals (54). In some cases, this property is leveraged intentionally through dose series experiments, which allow for the investigation of radiation-sensitive systems such as metalloproteins under incrementally increasing dose conditions (55). Time-

resolved SSX experiments, while limited to slower timescales than those achievable at XFELs, enable kinetic studies of catalysis, ligand exchange, and conformational rearrangements using pump-probe or mix-and-diffuse approaches.

Given the high degree of methodological overlap between SSX and SFX, synchrotron-based screening experiments are frequently employed ahead of XFEL beamtime. This strategy enables optimisation of key experimental parameters including crystal size, hit rate, and preferential orientation, thereby minimising dead time and sample consumption during precious XFEL beamtime. Many aspects of the experimental pipeline, such as sample delivery systems, data collection strategies, and processing workflows are common between SSX and SFX, allowing users to adopt a complementary approach that maximises both efficiency and data quality.

1.2.3 Sample preparation

Sample preparation for serial crystallography relies heavily on a thorough understanding of the protein's phase diagram to guide crystallisation conditions towards reproducible microcrystal formation. Seeding is often employed to generate large amounts of small, uniform crystals and scaling up of these optimised conditions is essential to generate sufficient sample volumes for serial sample delivery systems. Experimental success depends critically on the consistency and quality of microcrystal slurries.

1.2.3.1 Protein crystallisation phase diagram

Protein crystallisation is the inherently rare and complex process by which irregular macromolecules self-assemble into a highly ordered, periodic lattice that separates from a metastable solution as a distinct ordered phase. Successful crystallisation depends on three main factors: the protein's intrinsic ability to form crystal contacts, the thermodynamic favourability of lattice formation, and the kinetic accessibility to enable the transition from soluble state to crystalline form (56). At the heart of protein crystallisation is the concept of supersaturation: the driving force that governs both nucleation and subsequent crystal growth. Supersaturation defines a dynamic and condition specific landscape, that can be segmented into distinct physiochemical zones, referred to as a phase diagram (**Figure 9A**) (56,57). These include the undersaturated zone where no crystallisation occurs, the nucleation zone where critical nuclei spontaneously form, the metastable zone where slow growth may occur, and the precipitation zone where protein aggregates dominate over lattice formation. Understanding where a protein system lies within this landscape is crucial not only for inducing crystal formation, but also for controlling crystal size, morphology and quality. A phase diagram typically varies two or more variables, most commonly protein concentration and precipitant concentration, providing a map of crystallisation space to guide further optimisation.

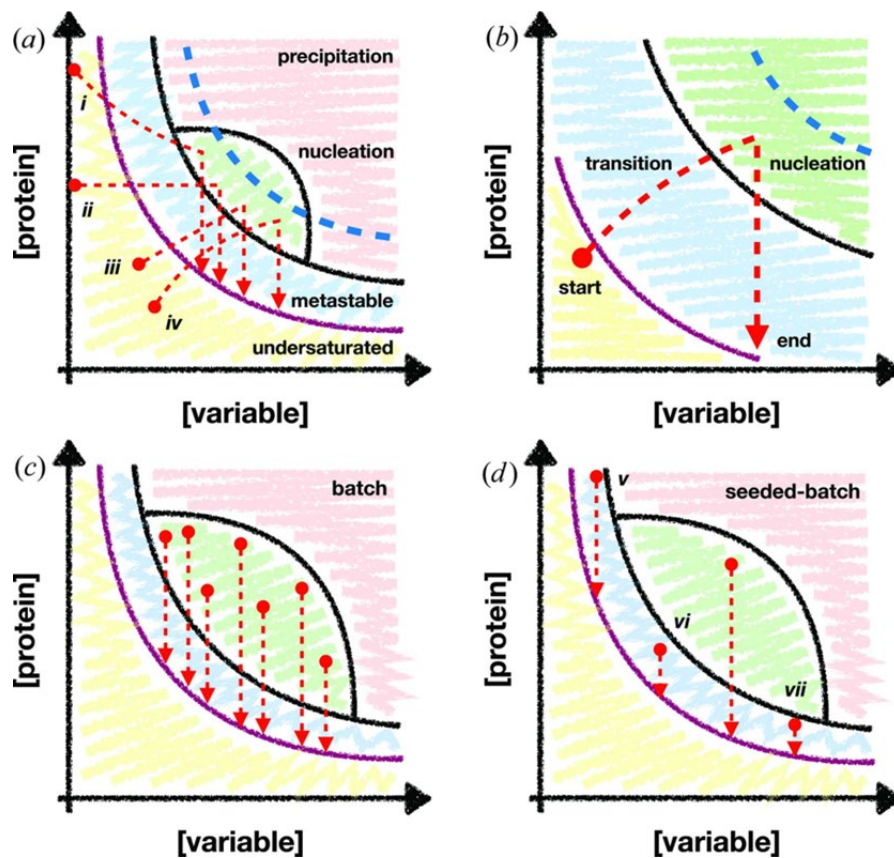


Figure 9. A protein crystallisation phase diagram. (A) The phase diagram is separated into four distinct zones: undersaturated, nucleation, metastable and precipitation. (B) The typical path of a vapour diffusion crystallisation experiment where the system transitions from the undersaturated zone into the nucleation zone where nuclei form, before dropping down into the metastable zone where crystals grow. (C) A batch crystallisation experiment involves a supersaturated solution, following a well-known path originating in the nucleation zone and terminating in the metastable zone. (D) The introduction of seed allows for fine control of where the crystallisation process begins allowing for varying crystallisation trajectories, be that a large single crystal or large amounts of microcrystals. Image taken from Beale *et al.* (58).

In a typical vapour diffusion crystallisation experiment, a droplet containing protein and precipitant is equilibrated against a reservoir with higher precipitant concentration, gradually inducing supersaturation overtime as the system reaches equilibrium via controlled vapour exchange. This leads to the spontaneous development of critical nuclei within the nucleation zone, depleting the free protein concentration as the system enters the metastable zone (Figure 9B). In the metastable zone, nucleation is suppressed, but existing crystals or critical nuclei continue to grow, incorporating additional protein into the lattice. As growth proceeds, protein availability decreases and the system shifts towards the undersaturated zone, at which point crystal growth is ceased (Figure 9B). In contrast to vapour diffusion, batch crystallisation involves rapid mixing of protein and precipitant solutions to generate a supersaturated solution. This bypasses the need for controlled vapour exchange and places the system in a specific region within the phase diagram, usually near to or within the nucleation zone (Figure 9C). By operating at this boundary, rapid formation of crystals is promoted, and excessive precipitation or uncontrolled growth is avoided. The trajectory of batch crystallisation is much more fixed,

and success of crystallisation relies upon prior mapping of crystallisation space through phase diagram mapping. Batch crystallisation is commonly coupled with seeding strategies to overcome the nucleation barrier, by providing artificial nuclei from the fragmentation of previously successful crystals (**Figure 9D**). Seeding enables further trajectories through the phase diagram and allows for finer control of crystal size, number and morphology (**Figure 9D**).

1.2.3.2 Seeding

Seeding is a well-established technique in protein crystallography that involves the deliberate introduction of preformed crystalline nuclei into a crystallisation solution to promote controlled crystal growth within the metastable zone (59). Originally developed in the early 1980s to circumvent the stochastic and often inefficient process of spontaneous nucleation (60). Since then, it has become a critical strategy for improving reproducibility, enhancing crystal quality, and enabling growth under otherwise non-nucleating conditions. Seeding methods are broadly classified into two categories: macroseeding and microseeding. Macroseeding sometimes referred to as seed transfer, involves the transfer of a mature single crystal into a fresh protein solution to promote further crystal growth (61). Microseeding, by contrast entails the mechanical fragmentation of existing crystals into a nanocrystalline suspension, which serves as a scaffold to initiate nucleation in subsequent drops (62,63). Both approaches offer a means to decouple nucleation from growth, allowing finer control over crystal morphology and size, an essential consideration for downstream applications such as serial crystallography or ligand soaking.

Iterative microseeding can be employed at both the initial screening stage and during subsequent optimisation steps. A common approach used is random microseed matrix screening (rMMS), in which concentrated seed stock is introduced into the crystallisation drop containing protein and precipitant (64). This allows for the identification of novel crystallisation conditions, some of which may be unrelated to the original hit (**Figure 10**) (62). Successive rounds of optimisation, involving the selection and reuse of the best seed stocks (65,66) has been demonstrated to improve crystal morphology and enhance X-ray diffraction resolution (**Figure 10**) (67,68).

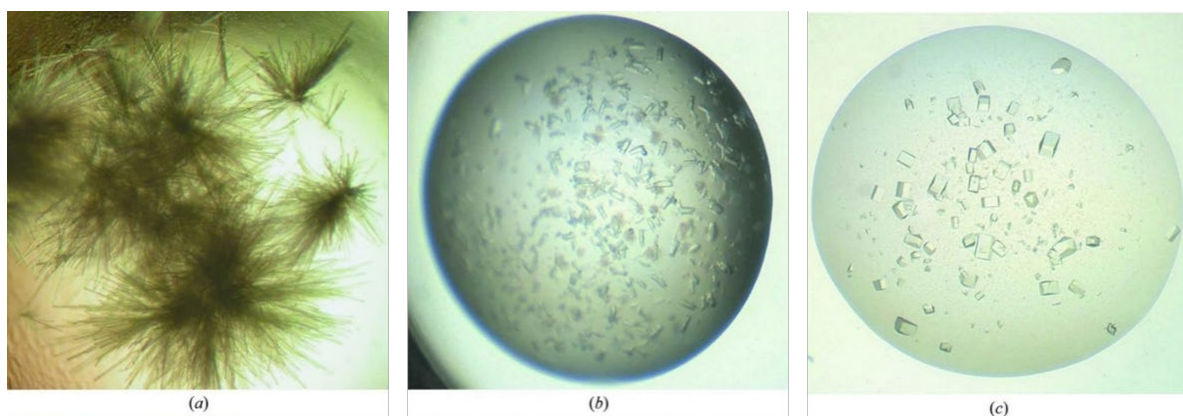


Figure 10. Iterative seeding improves crystal quality of a helicase. A seed stock was prepared from crystals that grew in the polyethylene glycol (PEG) Suite screen, before iterative cycles of rMMS were employed to improve crystal quality and morphology. (A) Crystals grown in 14% (w/v) PEG 8000, 0.1 M Tris-HCl pH 7.5 were used to make an initial seed stock. (B) Crystals grown in 20% (w/v) PEG 3350, 0.2 M magnesium sulfate after the first round of rMMS and used to make the subsequent seed stock. (C) Crystals grown in 40% (v/v) PEG 200, 0.1 M Tris-HCl pH 8.5 after a second round of rMMS. Image taken from D'Arcy *et al.* (69).

Preparation of seed stock usually involves the generation of a dilution series of seed concentration, which can be utilised during phase diagram mapping or optimisation of conditions previously identified through rMMS (69). Importantly, the concentration of seed stock influences nucleation density and final crystal size, with higher seed concentrations resulting in a large number of smaller crystals (Figure 11) (58). By systematically varying the concentration of seed, crystal size can be finely tuned (Figure 11).

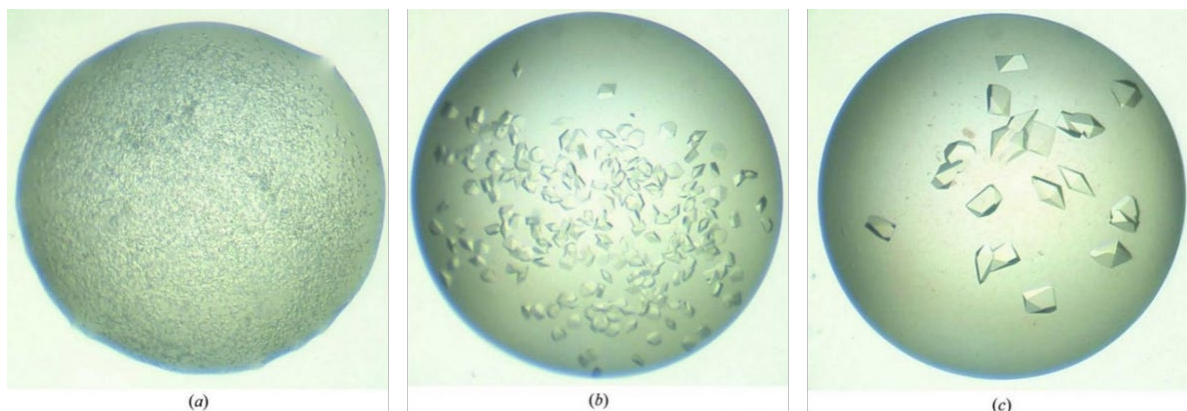


Figure 11. Effect of seed stock concentration on crystal size and number of a tyrosine kinase. Initial seed stock was generated from a crystallisation hit including 0.1 M MES pH 6.5, 25% (w/v) PEG 550 monomethyl ether (MME) from The PEGs Suite. (A) Crystallisation drop supplemented with initial seed stock. (B) Crystallisation drop supplemented with the initial seed stock diluted 1 in 100. (C) Crystallisation drop supplemented with the initial seed stock diluted 1 in 1000. Image taken from D'Arcy *et al.* (69).

It is currently debated as to which preparation method produces the 'best' seeds, although it is most likely protein-dependent (70–73). Seed preparation almost invariably results in heterogenous seeds, which in turn produces non-uniform crystals. Most seed preparation protocols involve the intentional fragmentation of previously successful crystals (66). The most straightforward approach ('seed bead' method) involves the introduction of a physical agitator,

such as a plastic or glass bead into an Eppendorf tube containing previously successful crystals, followed by subjection to vigorous vortexing (63). To prevent heat generation and preserve protein stability, intermittent cooling on ice is employed in between vortexing steps. Alternative strategies include mechanical disruption with a glass probe or capillary (69), or sonication whereby ultrasonic waves generate local shock pulses that fragment crystals through the process of sonofragmentation (74). The effectiveness of seed preparation can be validated via light microscopy, transmission electron microscopy (75,76), dynamic light scattering (77), or second order nonlinear optical imaging of chiral crystals (78).

1.2.3.3 Scaling up from vapour diffusion to batch

Serial crystallography experiments typically require upwards of 100 µL of sample with a crystal density of ideally 10^7 – 10^8 crystals/mL, placing significant demands on crystallisation throughput, reproducibility and scalability. Conventional vapour diffusion setups such as sitting or hanging drop plates are insufficient to meet these requirements without extensive parallelisation, making them impractical for routine serial experiments. To address this, crystallisation protocols are routinely adapted to batch conditions, which enable bulk production of microcrystal slurries and straightforward sample transfer to X-ray facilities in Eppendorf tubes. However, this transition to Eppendorf tubes introduces new variables, notably differing evaporation and equilibration conditions, which may influence crystal size and morphology (58). Scaling up from vapour diffusion to batch crystallisation requires careful optimisation to ensure reproducible production of microcrystal slurries across multiple preparations.

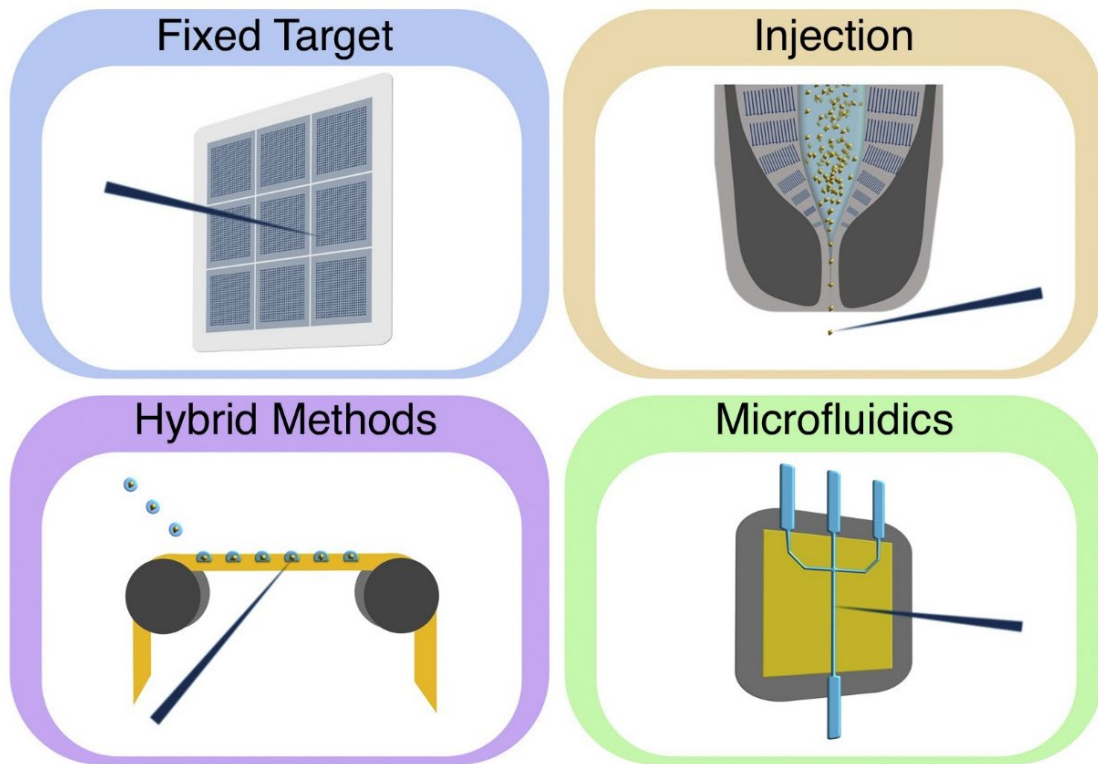
Batch crystallisation offers greater control over nucleation by eliminating the gradual equilibration inherent to vapour diffusion methods (58). Additionally, vapour diffusion suffers from an inherently lower surface area-to-volume ratio, limiting its scalability and throughput. Several key considerations must be addressed when converting to batch conditions, protein and precipitant concentrations are typically higher in vapour diffusion, while equilibration occurs much slower in batch formats, especially in viscous PEG-containing crystallisation conditions (79). Empirical adjustments often involve increasing precipitant concentration by a factor of 1.3 to 2 compared to vapour diffusion trials, with commonly employed protein-to-precipitant ratios ranging from 1:1 to 1:3 (80).

Rapid mixing during batch crystallisation is essential to achieve a supersaturated state. Agitation is commonly used to promote uniform mixing and has been shown, particularly in microbatch mixing (MBM) setups, to induce secondary nucleation through mechanical disturbance (81). However, mixing speeds must be optimised for each crystal system, as excessive agitation can compromise protein stability and reduce overall yield. Additionally,

rapid mixing can be coupled with high-speed centrifugation to generate stratified crystal layers, enabling crystal size separation and subsequent increases in crystal density (82). In principle, batch experiments can be scaled from nanolitre droplets in microbatch-under-oil formats to larger volumes ($>100 \mu\text{L}$) prepared in Eppendorf tubes. Nevertheless, scaling introduces changes in physiochemical dynamics including diffusion rates, mixing efficiency and equilibration kinetics. As such, each increase in volume requires iterative adjustments, and further study is warranted to fully elucidate the influence of scale on crystallisation.

1.2.4 Sample delivery

Following successful preparation of microcrystal slurries, the next critical step in a serial crystallography experiment is efficient sample delivery to the X-ray beam. At both synchrotron and XFEL facilities, this has prompted the development of a wide range of sample delivery platforms tailored to high-throughput data collection, and compatibility with time-resolved modalities. Broadly, current sample delivery methods fall into four categories: fixed-targets, injectors, hybrid methods and microfluidics (**Figure 12**). Fixed-targets (1.2.4.1) use solid supports, such as chips or films, where crystals are immobilised and the beam is rastered across the target. Injectors (1.2.4.2) deliver crystals suspended in a liquid or viscous medium through a nozzle or capillary directly into the path of the X-ray beam. Hybrid methods (1.2.4.3) dispense crystals directly onto a moving tape or substrate that carries the sample across the beam in a continuous fashion. Microfluidics (1.2.4.4) involves sealed devices with engineered channels that present crystals to the beam in a controlled, enclosed environment.



Current Opinion in Structural Biology

Figure 12. Serial crystallography sample delivery methods. Current approaches can be grouped into four primary formats. Fixed-targets use solid supports (e.g. chips or films) onto which crystals are immobilised; the X-ray beam is rastered across the target to collect data. Injectors deliver crystal suspensions in liquid or viscous media through nozzles or capillaries directly into the X-ray beam. Hybrid methods dispense crystal-containing droplets onto a moving tape or substrate that continuously carries the sample through the X-ray beam. Microfluidic devices use enclosed channels within sealed systems to present crystals in a stable, precisely controlled environment. Image taken from Pearson and Mehrabi (83).

It is important to select an appropriate sample delivery system for serial crystallography experiments, carefully considering several factors. These include sample availability, delivery throughput, compatibility with beamline infrastructure, and whether the experiment involves static data collection or more specialised setups. Additional facility-dependent constraints, such as beam characteristics and detector configurations, play an important role in determining a feasible delivery format. A number of comparative studies have systematically evaluated the strengths and weaknesses of established delivery platforms (34,84–86). These insights are summarised in **Table 1**, offering a practical overview of matching experimental aims to delivery capabilities. Nevertheless, ongoing advances in hardware, control systems, and sample handling technology continue to expand the boundaries of what is technically possible.

Table 1. Comparison of sample delivery methods for serial crystallography. *Sample volume requirements are mostly dictated by crystal density. **Sample consumption assumes a dataset of $\geq 10,000$ lattices. Table adapted from Tremlett *et al.* (23).

	Fixed-Targets	Injectors	Hybrid Methods	Microfluidics
Suitable crystal size	$\sim 5 - 50 \mu\text{m}$ but aperture size-dependent (aperture-aligned) $\geq 1 \mu\text{m}$ (directed-raster)	$\leq 20 \mu\text{m}$ (liquid injector) $\leq 50\%$ of the capillary internal diameter (ID) (viscous injector)	$\sim 5 - 50 \mu\text{m}$	$\sim 3 - 25 \mu\text{m}$
Suitable sample volume*	50 – 200 μL (aperture-aligned) 5 – 10 μL (directed-raster)	$\geq 500 \mu\text{L}$	50 – 500 μL	100 – 500 μL
Sample consumption**	Tens of micrograms (directed-raster) Hundreds of micrograms to several milligrams depending upon loading method (aperture-aligned)	Tens of milligrams or more	Hundreds to thousands of micrograms	Tens of micrograms
Sample flow rate	N/A	$\sim 5 - 50 \mu\text{L}/\text{min}$ (liquid injector) $\sim 0.001 - 2 \mu\text{L}/\text{min}$ (viscous injector)	$\sim 1 - 10 \mu\text{L}/\text{min}$	$\sim 1 \mu\text{L}/\text{min}$
Sample velocity (through the interaction region)	Approximately stationary	< 200 m/s (liquid injector) < 10 m/s (viscous injector)	< 10 m/s	< 0.2 m/s
Data acquisition rate	10 – 120 Hz	< 4.5 MHz (liquid injector) < 200 Hz (viscous injector)	< 500 Hz	< 700 Hz
Technical difficulty	Low-moderate	Moderate-high	High	High
Compatibility with complementary data	Electronic absorption spectroscopy	X-ray emission spectroscopy	X-ray emission spectroscopy Electronic absorption spectroscopy	Electronic absorption spectroscopy

1.2.4.1 Fixed-targets

Fixed-target platforms represent a widely adopted method for delivering microcrystals in serial crystallography experiments, particularly at synchrotron beamlines (87). These systems involve immobilising crystals onto a solid support (typically a chip or film), which is rastered through the X-ray beam to collect diffraction data (88–98). Two principal collection strategies are employed: aperture-aligned (predetermined crystal positions within defined wells) and directed-raster (randomly distributed crystals across the support) (99) (**Figure 13**).

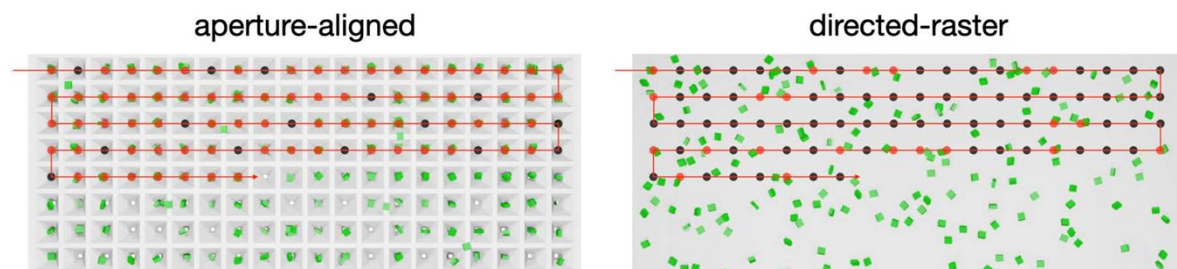


Figure 13. Fixed-target data collection strategies. In aperture-aligned methods, crystals are positioned within predefined wells, enabling precise beam targeting. In directed-raster scanning, the beam traverses the support to locate randomly distributed crystals, accommodating non-uniform sample loading. Image taken from Carrillo *et al.* (99).

For aperture-aligned methods, microcrystal slurry volumes of $\sim 50 - 200 \mu\text{L}$ are pipetted onto regularly spaced arrays with defined apertures (smallest currently available is $5 \mu\text{m}$), with excess liquid removed via vacuum or blotting. For example, the Roadrunner chip uses filter paper to back-blot the sample, analogous to grid preparation in electron cryomicroscopy (95). An alternative chip loading method involves a drop-on-demand strategy, where picolitre volumes of microcrystal slurry are dispensed precisely into each well position, eliminating the need for vacuum-assisted back-blotting (100). To prevent dehydration during data acquisition, hydrated crystals are protected either by covering with mylar film or by maintaining the support within a humidity-controlled environment (101). In some cases, fixed-targets can be sealed and loaded under anaerobic conditions, allowing the study of oxygen-sensitive processes in crystals (102,103). Alignment on the beamline is achieved using fiducial markers etched onto the chip, enabling precise navigation via fast translation stages (104).

Common aperture-aligned fixed-targets include the Oxford (101), Hit-and-return (HARE) (105), Roadrunner (95), and micro-structured polymer (MISP) (99) chips. While the Oxford, HARE, and Roadrunner platforms are fabricated from silicon nitride, the MISP chip employs cyclic olefin copolymer (COC), reflecting a shift towards polymer-based designs due to improved cost-effectiveness and material compatibility (99). Parameters such as fiducial spacing, aperture pitch, and total aperture count vary between designs, and influence both hit rate and imaging efficiency (106). Increasingly, materials like kapton are being explored for fabrication due to their mechanical properties and lower X-ray background along with cost-effectiveness (107).

Matching crystal density to the number of apertures is essential for effective data collection, ideally achieving one or two crystals per aperture. This density may be reduced to one when ligand soaking or substrate addition is intended. Typically, two well-loaded chips provide sufficient data for complete datasets if crystals exhibit random orientation (108). However, elongated crystals often orient non-uniformly within apertures, necessitating additional chips or alternative strategies. One such workaround involves growing crystals directly on the chip by vapour diffusion to reduce preferred orientation artefacts (109,110).

Directed-raster fixed-targets offer a simpler alternative, in which crystals are sandwiched between two mylar films held within a solid frame and directly rastered in the X-ray beam (88,89). These setups require minimal sample volume (as little as 3 μL) and allow rapid data collection in under 10 minutes (88). They also present reduced orientation bias and can yield complete datasets from a single chip if crystal loading is optimised (88). Designs include microgrid-based formats for goniometer mounting (111–114), which commonly utilise the *MeshandCollect* strategy (115), and sheet-on-sheet/sheet-on-sheet-on-spine (SOS/SOSOS) mylar sandwiches (88,89,116). However, the hit rate in these systems is generally lower than that of aperture-aligned fixed-targets due to the random distribution of crystals. Data quality can also be affected by dehydration, radiation damage, or fouling of the support film (88). Careful optimisation of raster spacing and exposure settings is therefore critical (88).

1.2.4.2 Injectors

A central challenge in serial crystallography is the continuous presentation of fresh microcrystals to the X-ray beam at a rate compatible with data collection. Injection methods address this problem by transporting microcrystal slurries into the beam path by precise engineered flow systems, which often operate under high pressures or in vacuum conditions. The three primary classes of injector used in serial crystallography are liquid injectors, viscous injectors, and droplet injectors.

1.2.4.2.1 Liquid injectors

Liquid injectors produce continuous jets of microcrystal suspensions in low viscosity buffers, enabling high-throughput data acquisition. The most prevalent design is the gas dynamic virtual nozzle (GDVN) (**Figure 14A**). This involves a co-axial sheath of pressurised gas which focuses a central liquid stream into a narrow jet, typically 2–5 μm in diameter (117–121). This narrow jet ensures optimal signal-to-noise by reducing background scattering, whilst the accompanying sheath gas flow ensures minimal jet angle deviation. This prevents ice formation and potential clogging of the nozzle (122). GDVNs operate at typical flow rates of ~10–60 $\mu\text{L}/\text{min}$, with a corresponding jet velocity of 10–50 m/s and a back pressure which can often exceed 1000 psi

(123). To address issues with sample consumption and jet stability, the double-flow focusing nozzle (DFFN) introduced an outer gas flow to further focus the liquid jet (**Figure 14B**). This three layer configuration reduces sample flow rates to 5 μ L/min and enables stable jet formation (124). The eight-fold lower sample consumption along with further reductions in background scattering led to improved reliability in comparison to initial GDVN designs (124). Manual fabrication and spatial resolution issues were also resolved by applying 3D printing methods, based on two-photon polymerisation, reducing inherent variability between devices (125–127).

An alternative liquid injector is the microfluidic electrokinetic sample holder (MESH), whereby the microcrystal slurry contains glycerol or PEG and is driven through a capillary eliminating the need for mechanical pressure. The method employs an electric field to generate thin jets by electrospinning at flow rates as low as 0.14 – 3.1 μ L/min (128). The system allows for fine control of flow rate and jet diameter, meaning low sample volumes and fragile crystals are suitable (128). An evolution of this concept is the concentric-flow electrokinetic holder (coMESH) injector. A fine jet is formed by injecting the sample into the meniscus of the sheath liquid followed by acceleration with a gas constriction (129). The addition of a sheath liquid such as 2-methyl-2,4-pentanediol (MPD) along with a flow rate of 1 – 3 μ L/min, results in the process of electro-focusing (129).

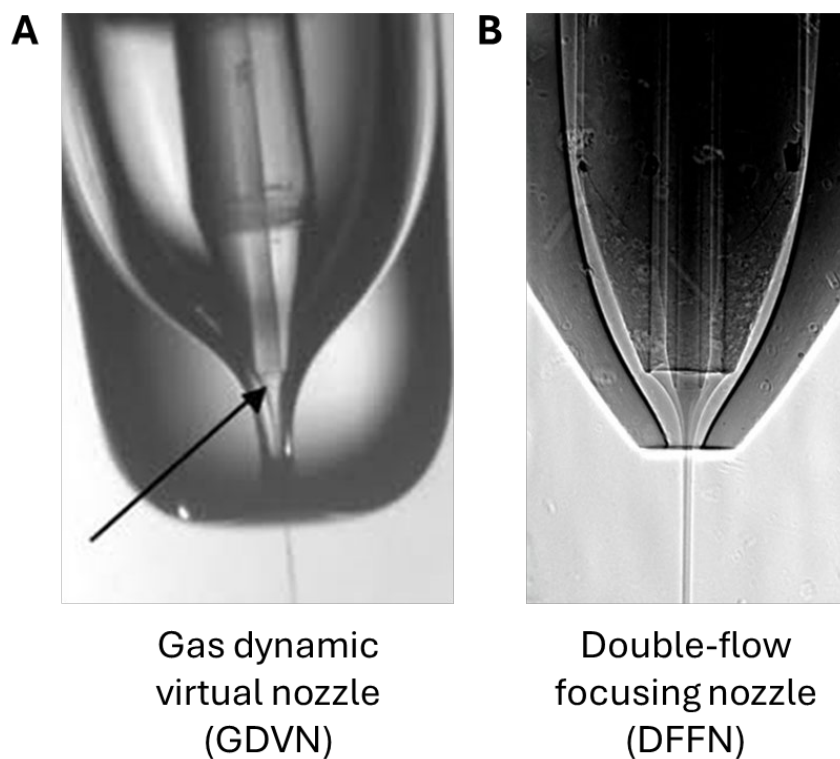


Figure 14. Examples of liquid injectors. (A) A gas dynamic virtual nozzle (GDVN), with an arrow indicating the constriction region from where the jet is generated, image taken from DePonté *et al.* (117). (B) Double flow focusing nozzle (DFFN) with an additional sheath gas glow, image taken from Oberthuer *et al.* (124).

1.2.4.2.2 Viscous injectors

Viscous injectors operate by extruding crystals suspended in high-viscosity carriers such as lipidic cubic phase (LCP), agarose gels, PEG-based greases, or hydrogel blends (120,130–134). Samples are loaded into glass or polymer syringes and dispensed via motorised pistons or pneumatic pressure systems through capillaries ranging from 50 to 200 µm in diameter (120,135). These systems exploit the shear-thinning behaviour of the carrier matrix to maintain uniform flow, even at flow rates below 100 nL/min (131,136). Viscous injectors are well suited to synchrotron experiments due to their slower flow rates, which are amenable to the longer exposure times required for data collection (54,131,137,138). Although high-viscosity carriers are mainly used for structural determination of membrane proteins, the approach can also be applied to soluble proteins. However, several factors must be considered, including shear stress from mechanical mixing with viscous carrier, compatibility between the carrier and crystallisation condition, and crystal density, which directly affects hit rate (139).

1.2.4.2.3 Droplet injectors

Droplet-based injection systems enable the delivery of discrete microvolumes of crystal suspension synchronised precisely with X-ray pulses. These platforms include acoustic droplet ejection, piezoelectric inkjet printing, electrospray dispersion, and pressure-pulsed microfluidics (140). Crystals are suspended in low to medium viscosity buffers to ensure droplet stability, and droplets are deposited into open interaction regions with volume precision down to picolitres. This format reduce sample waste and supports synchronised reaction initiation, which is critical for capturing transient intermediates. A growing subset of droplet injectors utilise droplet-on-demand (DoD) control to generate droplets only when triggered. This approach enables strict temporal gating, ensuring that each droplet aligns with the X-ray pulse and reduces unnecessary sample consumption. For example, Perett *et al.* introduced a pressure-pulsed flow-focusing system that triggers droplets via transient pressure bursts, allowing modular control over volume and frequency (141). This enabled high-throughput data collection and precise alignment with XFEL pulse trains. Similarly, Mafune *et al.* developed a solenoid-actuated T junction injector, where droplet formation is initiated by valve actuation, offering fine control and compatibility with external triggers such as laser excitation (142).

Building on these strategies, Alexandra Ros's lab at Arizona State University (ASU) have introduced several advanced droplet microfluidic platforms for serial crystallography sample delivery. A key innovation is the segmented-flow droplet injector, which produces aqueous crystal-containing droplets segmented by a fluorinated oil phase (**Figure 15**) (143–145). Embedded electrodes utilise electrowetting to trigger droplet generation in alignment with XFEL

pulses. This design allows for low pressure operation and precise timing control. More recently, the lab unveiled the modular droplet injector (MDI), a flexible platform combining microfluidic architecture with programmable control (146,147). Critically, the MDI supports real-time synchronisation with beamline timing electronics allowing droplet formation to be gated by external triggers such as X-ray pulse arrival or laser excitation events. The system's dynamic adjustment of droplet frequency, achieved via programmable pressure pulses and electrowetting control, permits fine tuning of sample throughput and exposure timing, reducing sample waste and enhancing temporal resolution. Collectively, droplet injectors are redefining sample delivery for time-resolved experiments by isolating and synchronising biochemical events within droplets prior to X-ray exposure. Their ability to combine precision, efficiency, and modularity makes them essential tools for capturing molecular dynamics at high temporal resolution.

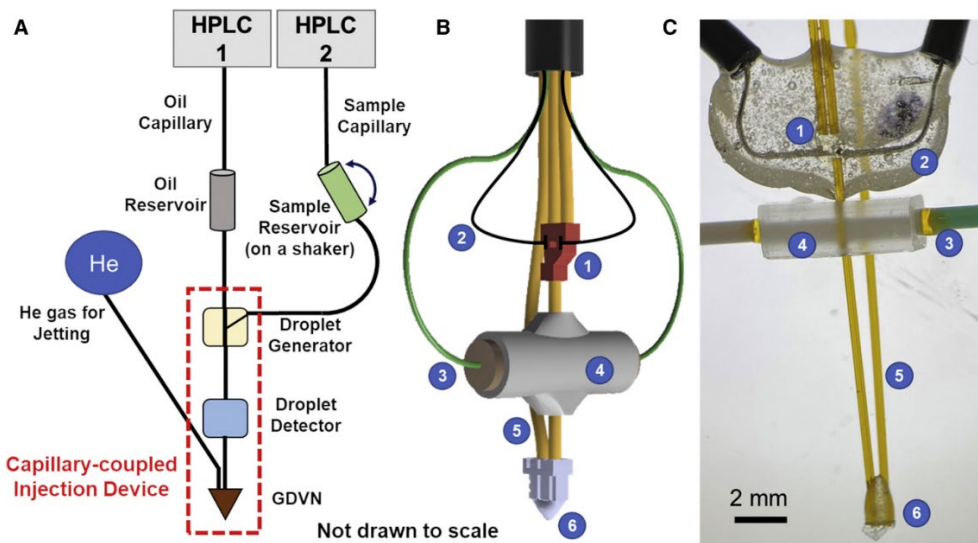


Figure 15. Droplet injector from the Ros lab. (A) All the components that make up the droplet injector system. (B) Schematic of the droplet injector consisting of a droplet generator (1), electrode (2), optical fibre (3), aligner device (4), helium gas supply (5) and GDVN (6). (C) The final assembled droplet injector. Image taken from Sonker *et al.* (145).

1.2.4.3 Hybrid methods

Hybrid sample delivery methods in serial crystallography combine the strengths of fixed-target and continuous injection systems by using X-ray transparent taping drives, typically made of kapton film to transport microcrystals into the beam with high precision and reproducibility. These systems support two main formats: discrete droplet deposition where microcrystals are delivered in synchronised droplets via acoustic droplet ejection (ADE; 2 – 3 nL per droplet) or piezoelectric droplet ejection (PDE; 50 – 200 pL per droplet) (Figure 16A) (140,148,149) or continuous deposition, where crystal suspensions are loaded directly onto the moving tape via capillaries or inkjet nozzles (Figure 16B) (150–153).

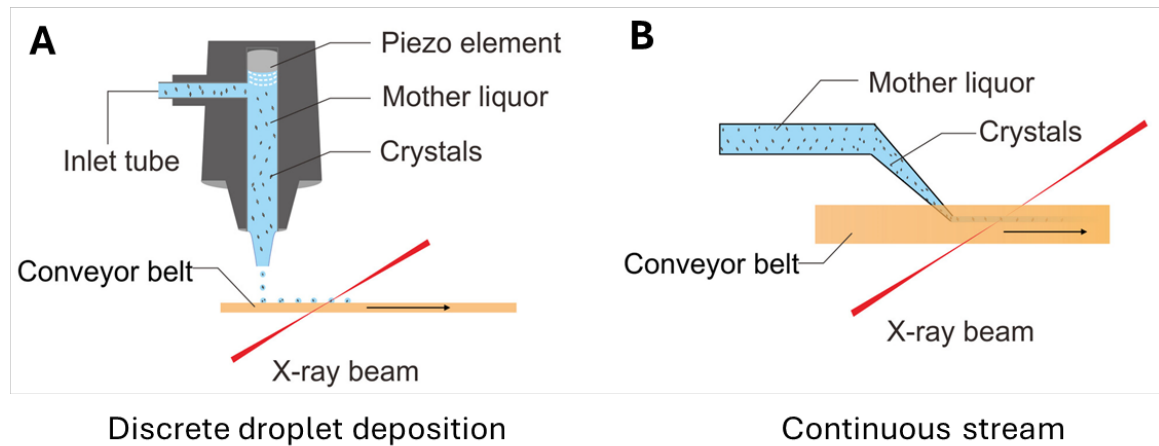


Figure 16. Hybrid methods. (A) Discrete droplet depositions via piezoelectric droplet ejection (PDE) onto a conveyor belt. (B) A continuous stream of microcrystal slurry onto a conveyor belt. Image adapted from Zhao *et al.* (86).

Because ADE/PDE droplet frequencies can be matched to X-ray pulse or detector repetition rates, these systems enable precise synchronisation, minimal sample waste, and high hit rates. (140). Tape-based delivery is compatible with both synchrotron and XFEL sources, and has been tailored to suit specific beamline geometries. A key advantage of tape systems is their one-dimensional coordination; sample-beam interaction is governed solely by tape velocity (154). This contrasts with free-flying droplet methods, which require complex four-dimensional synchronisation (droplet position (x, y, z) and time). Tape platforms also support reaction initiation at defined spatial offsets, allowing time delays from microseconds to tens of seconds to be probed (154). When optimised, tape drive systems offer exceptional sample efficiency and throughput, and have been extended to time-resolved SFX and X-ray emission spectroscopy (XES). This enables simultaneous capture of atomic structure and electronic changes, particularly valuable for studying metalloproteins and enzyme dynamics (154).

1.2.4.4 Microfluidics

Microfluidic platforms are increasingly central to next-generation serial crystallography, offering precise sample control, low consumption and compact geometries ideal for high-throughput experiments (155,156). These systems support two main modes of data collection: either from static crystals housed in sealed microchambers, similar to fixed-target setups, or from crystals flowing continuously through enclosed microchannels (156). Recent advances have focused on microfluidic fixed-target platforms, which are gaining traction due to their scalability, low background scattering, and ease of use (157–159). Most designs incorporate X-ray transparent polymer films such as kapton, mylar or COC, which provide mechanical stability and minimal interference with diffraction data (160–163). These supports often feature microfabricated arrays or patterned wells, enabling precise crystal placement or even *in situ* growth, which simplifies sample preparation and improves reproducibility (163–167).

To extend data collection under ambient conditions, ultra-thin moisture barriers and gas-impermeable polymer films have been developed. These materials help maintain hydration and structural integrity during prolonged X-ray exposure (158,168,169). Compared to conventional fixed-targets (1.2.4.1), microfluidic variants offer better environmental control, reduced manual handling, and compatibility with ligand soaking, making them well suited for dynamic experiments and iterative screening (170). Their modularity and adaptability have led to widespread adoption at both synchrotron and XFEL facilities, particularly at fourth-generation synchrotrons, where high repetition rates and tight beamline constraints demand efficient, reproducible sample delivery formats (161).

In contrast, flow-based microfluidic devices continuously delivery crystal suspensions using flow-focusing geometries that guide sample into the X-ray beam with high precision (**Figure 17**) (171). These systems dramatically reduce sample usage and improve hit rates, but they require careful material selection and robust channel bonding to avoid leakage or device failure under beamline conditions (172). Flow parameters must be finely tuned: too fast, and crystals pass through the beam too quickly for meaningful data; too slow, and clogging becomes a risk in the microchannels (172).



Figure 17. A 3D flow-focusing microfluidic device on the beamline. The microfluidic setup includes a high precision XYZ stage for alignment (1), a 3D-printed holder (2), syringe pumps (3), microcrystal slurry in loaded in a Teflon loop (4) and an outlet waste tube (5). Image taken from Monteiro *et al.* (172).

To prevent clogging and crystal settling, techniques like continuous syringe rotation are used to keep suspensions evenly distributed during long data collection runs (173,174). Importantly, crystals in flow tend to adopt random orientations, which supports statistically robust datasets. While some setups use simple thin-walled capillaries (53,175), others employ fully microfabricated chips with custom three-dimensional flow paths (172), showcasing the versatility and evolving sophistication of microfluidic systems in serial crystallography.

1.2.5 Time-resolved serial crystallography

Building upon innovations in sample delivery, serial crystallography has evolved from static data acquisition towards more dynamic and mechanistically rich experimentation. This progression is exemplified in time-resolved serial crystallography (TR-SX), which captures molecular snapshots at defined intervals following reaction initiation. By observing proteins as they undergo conformational changes, bind ligands, or transition through catalytic cycles, TR-SX unveils structural intermediates that are often invisible to conventional cryocrystallography. These insights not only deepen mechanistic understanding but also complement data from other time-resolved techniques approaches (**Figure 18**).

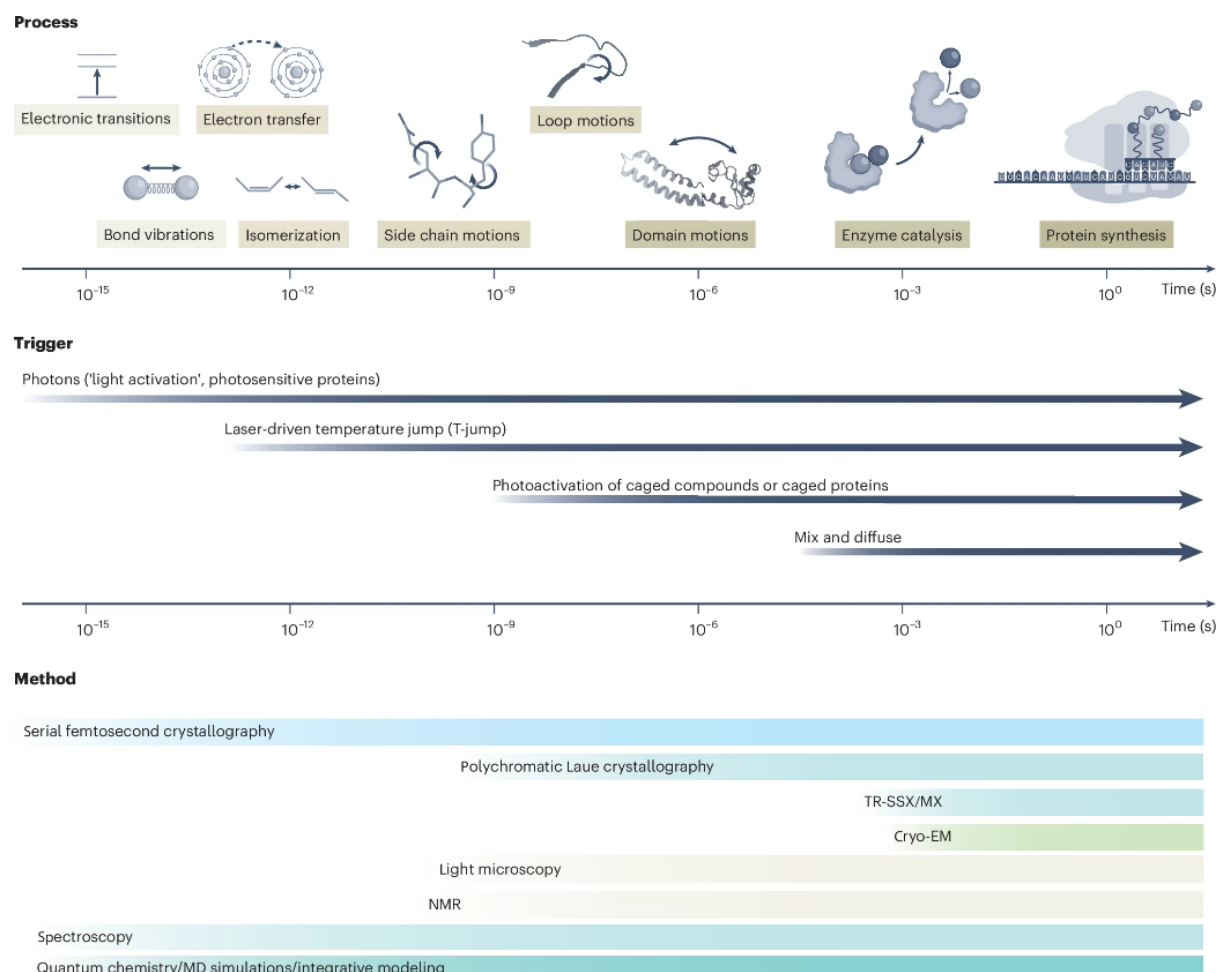


Figure 18. Time-resolved methods and their corresponding timescales. Biology is not static but instead highly dynamic in nature. Time-resolved structural methods capture high temporal and spatial resolution. Time-resolved methods combine the observation of structural and spectroscopic changes to follow dynamics changes following reaction initiation. Image taken from Banari *et al.* (176).

Reactions in TR-SX can be initiated either by photoactivation, where laser light triggers a reaction in a light-sensitive molecule, or through mixing-based mechanisms, in which the rapid introduction of ligands initiates a chemical transformation within the crystals. Photoactivation remains a powerful and widely applicable technique for reaction initiation in TR-SX, spanning

timescales from femtoseconds to seconds (34,177,178). However, its broader utility is constrained by the rarity of naturally photoactivatable systems, which comprise less than 0.5% of known proteins (179). To overcome this limitation, researchers have developed artificial photoremovable groups, such as molecular cages tethered to ligands or proteins residues, that release upon exposure to light (179). While promising, these systems demand meticulous chemical design and rigorous validation to ensure biological relevance and photochemical efficiency.

For the vast majority of proteins, mixing-based reaction initiation offers a more biochemically relevant and versatile alternative. These approaches involve introducing ligands into microcrystal slurries either upstream of the X-ray interaction region or within precisely controlled microfluidic environments. The achievable time resolution depends on both the mixing efficiency and the rate at which ligands diffuse into the crystal lattice. Smaller crystals are preferred, as they reduce diffusion distances and promote synchrony across the sample population. Ultimately, whether reactions are triggered by light or chemical mixing, precise temporal synchronisation is essential. Ensuring that all molecules within the crystal begin their reaction at the same point along the reaction coordinate is critical for capturing accurate structural snapshots of transient intermediates and conformational states.

1.2.5.1 Mix-and-inject serial crystallography (MISC)

Mix-and-inject approaches have become central to capturing millisecond dynamics in TR-SX. These strategies rely upon the rapid diffusion of ligands into microcrystal channels, leveraging short transport distances to enable near synchronous reaction initiation (180,181). The goal is to trigger a reaction within the crystal and capture its progression in real time using X-ray pulses. A range of mixing geometries and delivery formats now exist to accommodate diverse experimental needs and timescales. The most widely adopted setup involves a GDVN or high viscosity extruder (HVE) downstream of a microfluidic mixer using co-flow or double-focusing designs, where mixing is dominated by diffusion (143,182–185). In a co-flow mixer, ligand and crystal slurry are introduced in parallel streams, allowing diffusion to initiate the reaction as they merge. These configurations permit continuous ligand introduction and sample interrogation within a narrow stream, with the reaction delay time defined by the distance between mixing and X-ray probing (186). Tapedrive systems extend this concept by applying crystals to an X-ray compatible tape, either in a continuous stream or as discrete droplets (150,153). The ligand is introduced upstream, and the delay time is governed by travel distance and tape speed.

Emerging methods such as drop-on-demand utilise PDE to deposit picolitre volumes of substrate atop nanolitre crystal droplets dispensed via ADE enabling fast mixing on a moving

tape (148). This technique introduces initial convective mixing via droplet impact, followed by diffusion, and can also be adapted to fixed-target systems like liquid application method for time-resolved analyses (LAMA), where droplets are deposited into wells or apertures (187). Coupling these designs with HARE schemes extends accessible timescales into the range of seconds (188,188). A recent hybrid format, a combination of inject-and-transfer system (BITS), allows crystal-substrate mixtures to be injected directly onto a polyimide raster-scanned target, combining aspects of in flow and fixed-target approaches (189). This design offers flexibility in sample delivery while preserving spatial control over reaction timing. Critically, mixing performance depends on more than geometry alone. Effective time resolution is contingent on liquid homogenisation, ligand diffusion rates into the crystal lattice, and the critical depth, which is the maximum ligand penetration distance that ensures meaningful observation before the biological process progresses (186). Therefore ideal conditions involve small crystals ($\leq 20\text{ }\mu\text{m}$), rapidly diffusing ligands, and low viscosity conditions to maximise mixing efficiency and precisely capture early intermediates (181). Smaller crystals reduce the diffusion path length, allowing ligands to penetrate quickly and uniformly. This is essential for synchronising reaction onset across the crystal population and capturing early intermediates before they evolve.

1.3 Motivation for time-resolved studies: AtPdx1.3

Arabidopsis thaliana Pyridoxal 5'-phosphate synthase subunit 1.3 (AtPdx1.3) is a dodecameric protein complex involved in the biosynthesis of pyridoxal 5'-phosphate (PLP), the biologically active form of vitamin B6. It forms a transient and dynamic complex with its partner protein Pdx2 in a 1:1 stoichiometric ratio, together constituting the PLP synthase machinery (190–195). Structurally, AtPdx1.3 adopts a canonical $(\beta/\alpha)_8$ -barrel fold, a common motif in metabolic enzymes, with its catalytic active site located at the core of the barrel (196). Functionally, AtPdx1.3 catalyses the de novo synthesis of PLP from three precursors: ribose-5-phosphate (R5P), glyceraldehyde 3-phosphate (G3P) and ammonia (197–199). This biosynthetic pathway is absent in humans but conserved across numerous pathogenic microorganisms including *Plasmodium falciparum* and *Mycobacterium tuberculosis* (200). As a result, PLP biosynthesis has emerged as a promising therapeutic target, with Pdx1 inhibition offering a selective strategy for antimicrobial drug development (201).

The enzymatic production of PLP is mechanistically complex, involving approximately 20 distinct steps (202). To dissect the pathway, several structural intermediates of AtPdx1.3 have been captured using conventional X-ray crystallography at cryogenic temperatures. These studies used cryo-trapping techniques, which stabilise transient states by rapidly cryo cooling single crystals, allowing visualisation of intermediates. Extended ligand soaking protocols were

used to improve site occupancy and resolve distinct mechanistic snapshots. These structural insights provide a foundation for understanding PLP biosynthesis at atomic resolution. A complete summary of the resulting *AtPdx1.3* crystal structures is provided in **Table 2**.

Table 2. Crystal structures of *Arabidopsis thaliana* Pyridoxal 5'-phosphate synthase subunit 1.3 (*AtPdx1.3*).

PDB Code	Resolution (Å)	Description	Notes
5K3V	1.90	Apo-Pdx1.3	Apo Pdx1.3 (203)
5K2Z	1.80	Pdx1.3-I320	Pdx1.3 I320 intermediate (203)
5LNS	1.91	Pdx1.3-R5P	R5P covalently bound to Pdx1.3 (202)
5LNU	1.73	Pdx1.3-I320	Pdx1.3 I320 intermediate, collected from a single crystal (202)
5LNV	2.24	Pdx1.3-I320	Pdx1.3 I320 intermediate, collected from multiple crystals (202)
5LNW	1.90	Pdx1.3-I320-G3P	Pdx1.3 intermediate with G3P bound (202)
5LNR	1.61	Pdx1.3-PLP	PLP covalently bound to Pdx1.3 (202)
6HX3	2.00	Pdx1.2-Pdx1.3	Isolated complex of Pdx1.2-Pdx1.3 (204)
6HXG	1.90	Pdx1.2-Pdx1.3-I320	Pdx1.2-Pdx1.3 intermediate (204)
6HYE	2.53	Pdx1.2-Pdx1.3 ^{K97A}	Catalytically inactive complex of Pdx1.2-Pdx1.3 (204)
7NHF	2.53	Pdx1.3 ^{K166R}	P2 phosphate binding site mutant of Pdx1.3 (205)
7NHE	2.23	Pdx1.3 ^{K166R} -I333	Pdx1.3 pre-I320 intermediate complex (205)

AtPdx1.3 offers a uniquely dynamic and structurally rich system for time-resolved serial crystallography, owing to its internal lysine relay mechanism and the formation of spectroscopically detectable intermediates during PLP biosynthesis (202,205). Unlike many enzymes with a single catalytic site, *AtPdx1.3* coordinates chemistry across two spatially distinct active sites designated P1 and P2, separated by approximately 20 Å and bridged by a flexible lysine residue that acts as a swinging arm (206) (**Figure 19**). This internal relay begins when R5P binds covalently to Lys98 in the P1 site, forming a Schiff base that initiates sugar rearrangement (202). A key early event is the delivery of ammonia from the partner protein Pdx2 via a hydrophobic tunnel (191), enabling nucleophilic attack within the R5P-bound Lys98 and formation of a pre-I320 intermediate (202,204). This intermediate then undergoes dehydration and rearrangement to form the I320 chromophore, which is a covalent adduct simultaneously

Chapter 1

tethered to Lys98 and Lys166 (202,203). A conformational shift in strand β 6 allows Lys166 to swing into position, capturing the intermediate and guiding it towards the second active site (P2) (202,203). There, G3P binds and triggers an aldol-like condensation, forming the I320-G3P complex. This sets the stage for phosphate elimination and pyridine ring formation, culminating in PLP synthesis (202). Final steps include Schiff base hydrolysis, PLP release, and active site reset, often accompanied by oligomeric rearrangements modulated by incorporation of Pdx1.2, an alternative allele of Pdx1 (204). Mechanistic features including covalent chromophores, swinging lysines, tunnel-mediated substrate delivery, and oligomeric transitions make AtPdx1.3 an ideal candidate for TR-SX. Each step is structurally distinct and temporally separable, offering multiple anchor points for interrogation. In this context, AtPdx1.3 is not just a biochemical catalyst, it is a molecular machine whose internal choreography could be visualised in real-time. Ideal enzymatic steps to target within the mechanism are summarised in **Table 3.**

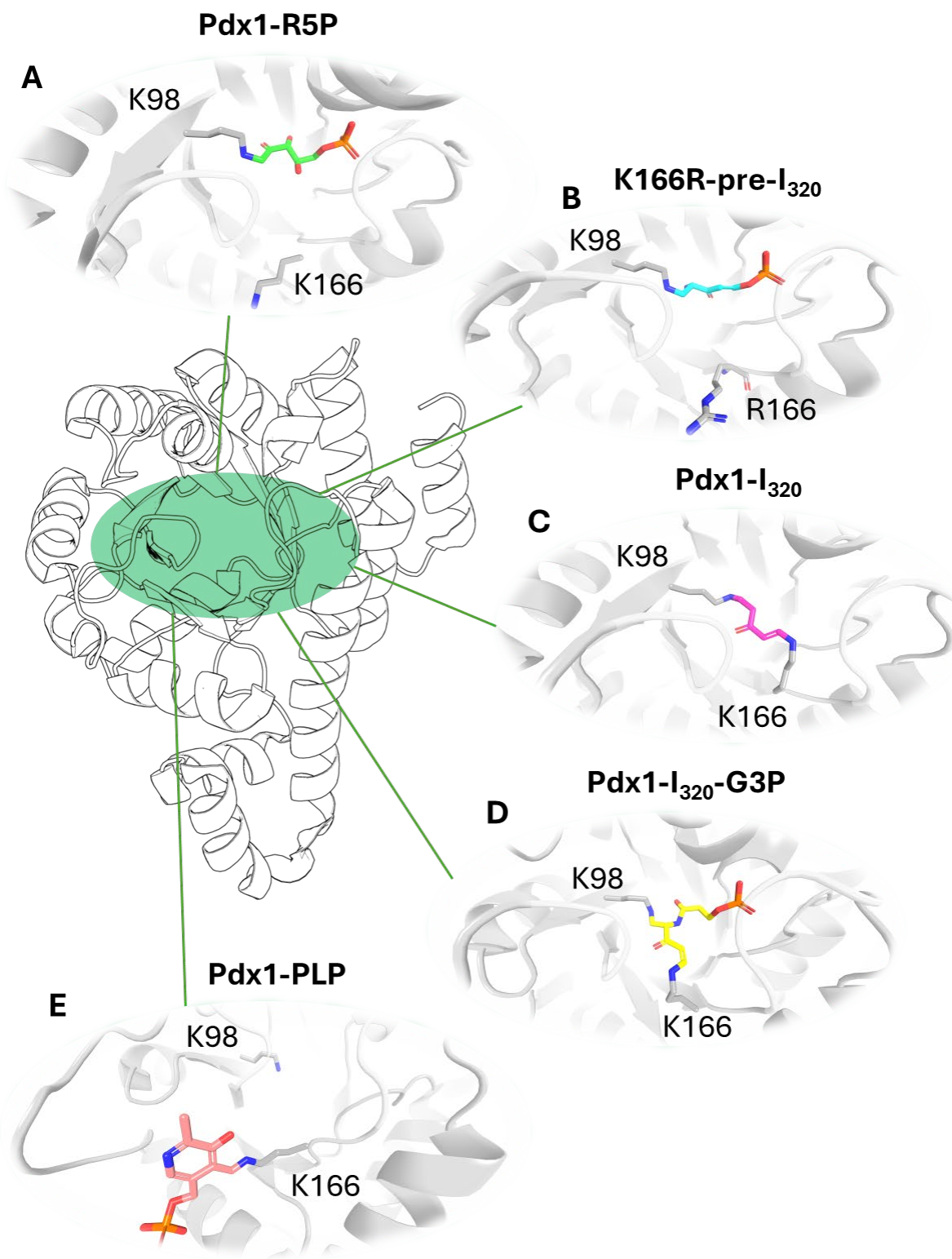


Figure 19. Crystallographic snapshots of the AtPdx1.3 reaction cycle. The active site of AtPdx1.3 is highlighted in green. (A) The binding of R5P in the P1 site leads to Schiff base formation with K98 (PDB: 5LNS). (B) Addition of ammonia leads to a pre-I₃₂₀ intermediate complex when trapping using the K166R mutant (PDB: 5LNT). (C) The formation of the I₃₂₀ chromophore via formation of a second Schiff base with K166 (PDB: 5LNU). (D) Incorporation of G3P leads to a covalent complex with I₃₂₀ (PDB: 5LNW). (E) Covalent complex of PLP bound to the P2 site via a Schiff base with K166 (PDB: 5LNR). Nitrogen atoms in blue, oxygen atoms in red and phosphorous atoms in orange.

Table 3. Targets for time-resolved serial crystallography of AtPdx1.3.

Event	Key residues/structural motifs	TR-SX relevance
R5P binding and ring opening	Lys98 (Schiff base formation)	Structural transition and ring opening
I320 chromophore formation	Lys98/Lys166 (Lysine relay) and β 6 strand hinge	Spectroscopically trackable (~ 315 nm), rapid dehydration and chromophore evolution
Ammonia incorporation	Ammonia tunnel residues and Lys98 receiving ammonia	Substrate channelling from Pdx2 mediated by a tunnel, also a druggable transient
Pyridine ring formation	Lys166 (P2 site)	Final scaffold closure via aromatisation, so far elusive in cryo-trapping studies
PLP release	Active site water and dynamic residues in the Pdx1.2 interface	Structural reset and subsequent oligomeric shifts

1.4 Droplet microfluidics in macromolecular crystallography

Microfluidics refers to the manipulation and transport of small fluid volumes, ranging from microlitres (μ L) down to femtolitres (fL), within microfabricated channels, typically measuring tens to hundreds of micrometres in width (207). These dimensions allow precise control over fluid behaviour at the microscale. A defining feature of microfluidic systems is their characteristic laminar flow, where fluid streams move in parallel without mixing unless externally perturbed. This contrasts with turbulent flow, which is chaotic and unpredictable. The flow regime in microfluidics is described by the Reynolds number (Re), a dimensionless parameter representing the ratio of inertial and viscous forces in a fluid (208). In microfluidic contexts, Re is typically very low ($Re < 2000$) indicating laminar, orderly flow. Higher values ($Re > 4000$) correspond to turbulent regimes, which are rarely encountered in microfluidic devices due to their small scale and low flow rates.

$$Re = \frac{\rho VL}{\mu}$$

Equation 4. Reynolds number. Where ρ is the fluid density, V is the flow velocity, L is the characteristics length and μ is the dynamic viscosity.

Within the broader field of microfluidics, droplet microfluidics has emerged as a powerful technique. It involves the generation and manipulation of discrete droplets, which are small self-contained volumes of aqueous solution, within an immiscible carrier fluid, often a fluorinated oil. These droplets act as miniature reaction chambers, enabling high-throughput experimentation and precise control over chemical environments. Droplet microfluidics has

made a transformative impact across disciplines including cell and molecular biology, chemical synthesis, biotechnology and environmental monitoring (209–212).

In the context of protein crystallography, droplet microfluidics offers unique advantages. It enables controlled crystal growth, rapid mixing of reagents, and efficient use of scarce protein samples. These capabilities are particularly valuable for screening crystallisation conditions and conducting time-resolved studies. The following sections will explore how droplet microfluidics has been adapted for crystallisation workflows and integrated with structural biology techniques.

1.4.1 Principles of droplet microfluidics

In microfluidic systems, fluid flow is typically laminar, meaning that streamlines move in parallel without turbulent mixing. However, even in laminar regimes, dispersion can occur due to differences in flow velocity across the channel cross-section. This phenomenon, known as Taylor dispersion, arises from the parabolic velocity profile in single-phase continuous flow systems, where fluid near the channel walls moves more slowly than fluid at the centre due to shear forces. As solutes travel through the channel, these velocity gradients cause them to spread longitudinally, blurring concentration fronts and compromising both temporal and spatial resolution in microfluidic experiments (**Figure 20A**) (213). Droplet microfluidics overcomes this limitation by introducing two immiscible phases: a continuous carrier phase (typically fluorinated oil) and a dispersed aqueous phase that forms discrete droplets (214). Each droplet behaves as an isolated reaction chamber, encapsulating reagents and maintaining a consistent incubation time as it travels through the channel. This compartmentalisation effectively eliminates the dispersion effects seen in continuous flow, preserving sharp concentration boundaries and enabling precise timing of chemical reactions (**Figure 20B**) (215). In addition to spatial isolation, droplets exhibit internal recirculation, a flow pattern driven by chaotic advection that enhances mixing within the droplet. This rapid mixing often occurs on the millisecond timescale and ensures homogeneity of reagents and supports fast reaction kinetics, making droplet microfluidics particularly well-suited for time-sensitive biochemical assays and crystallisation workflows (216–219).

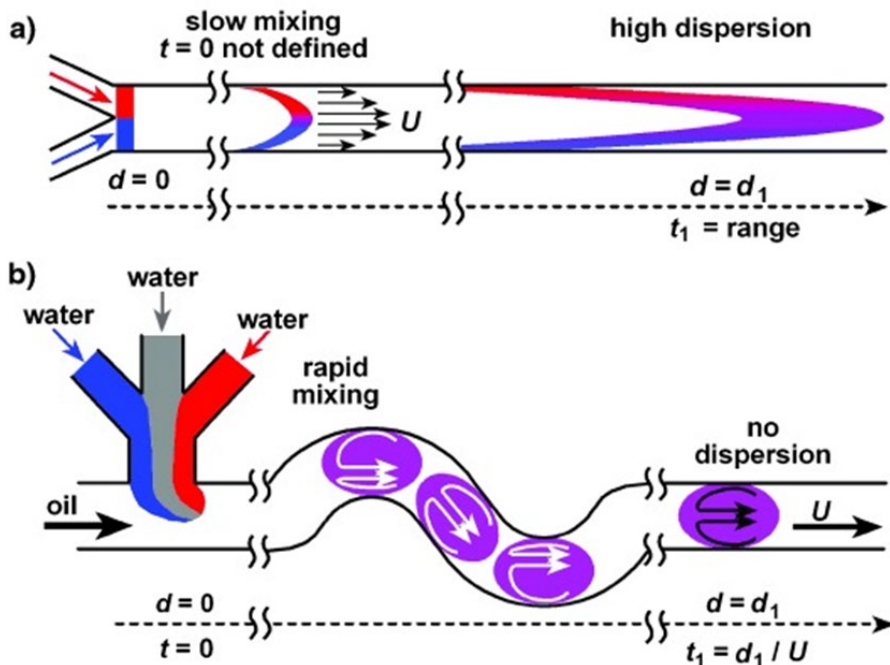


Figure 20. Effect of Taylor dispersion in microfluidic channels. (A) In single-phase continuous-flow microfluidics, laminar flow produces a parabolic velocity profile, resulting in slow, diffusion-limited mixing of reactants and a broad dispersion of reaction times. (B) In contrast, droplet-based microfluidics generates discrete, compartmentalised aqueous plugs within an immiscible oil phase. Each droplet functions as an independent reaction chamber, with internal recirculations (chaotic advection) promoting rapid and uniform mixing of reagents upon formation. Image taken from Song *et al.* (213).

Microfluidic droplet systems are widely used in chemical and biological experiments due to their ability to compartmentalise reactions with high precision. Droplets are typically classified into four main types based on their internal structure: water-in-oil (W/O), oil-in-water (O/W), water-in-oil-in-water (W/O/W) and oil-in-water-in-oil (O/W/O) (211). These configurations allow researchers to tailor droplet environments for specific applications, such as encapsulating cells, reagents, or crystals. The formation of droplets within microfluidic channels occurs via either active or passive mechanisms. Active droplet generation requires external forces such as acoustic waves to induce droplet breakup. In contrast, passive droplet generation, which is more commonly used, relies solely on the geometry of the microfluidic device (220). Among passive methods, flow-focusing is especially popular due to its ability to generate monodisperse droplets at kilohertz frequencies, making it ideal for high-throughput applications. Droplet-based microfluidics offers several advantages over traditional bulk-phase methods. These include reduced sample consumption, precise control over reaction conditions, high reproducibility, and a large surface-area-to-volume ratio, which enhances mixing efficiency and accelerates mass transport. While this does not alter the intrinsic chemical kinetics, it facilitates faster reaction onset in diffusion-limited systems by rapidly homogenizing reactants within droplets (214). However, the size and uniformity of droplets are influenced by multiple parameters including the flow rate of the continuous and dispersed

phases, the ratio between these flow rates, channel geometry, surface tension forces, viscoelastic properties of the fluid, and the presence and type of surfactants (215,221–224).

The formation of droplets occurs under distinct regimes: squeezing, dripping, and jetting, each governed by the interplay of viscous, inertial, and interfacial forces. In the squeezing regime, the dispersed phase obstructs the channel and is pinched off by the continuous phase, producing uniform droplets primarily determined by the relative flow rates. The dripping regime is characterised by droplet detachment at the orifice, where interfacial tension overcomes shear forces, resulting in highly monodisperse droplets with precise temporal control. At higher flow rates, the system transitions into the jetting regime, where the dispersed phase forms a continuous jet that breaks into droplets downstream due to flow instabilities, often yielding polydisperse droplets. The transition between these regimes depends on channel geometry, fluid properties such as viscosity, density, and interfacial tension, and flow parameters. Understanding and controlling these regimes is essential for tailoring droplet size, frequency, and uniformity in microfluidic experiments.

The accessibility of droplet microfluidics has been greatly enhanced by advances in soft lithography, a fabrication technique that allows researchers to rapidly prototype microfluidic devices at low cost (**Figure 21**) (225,226). Although the initial step of creating an SU-8 master still requires photolithography, where ultraviolet light patterns a photoresist on a silicon wafer, the introduction of polydimethylsiloxane (PDMS) has revolutionised device fabrication (227,228). PDMS can be cast against the SU-8 master to produce flexible, transparent microchannels, enabling fast iteration and widespread adoption (229). To ensure proper droplet formation, the surface wettability of PDMS channels must be carefully tuned (230–232). Plasma treatment temporarily oxidises the PDMS surface, converting hydrophobic methyl groups into hydrophilic silanol groups. This not only facilitates irreversible bonding to glass or other PDMS layers, but also allows for controlled droplet generation by modifying the channel's affinity for aqueous or oil phases (233,234). Beyond fabrication, PDMS remains the material of choice due to its optical transparency, biocompatibility, and gas permeability, making it suitable for a wide range of biological and chemical assays, from enzyme kinetics to crystallisation workflows.

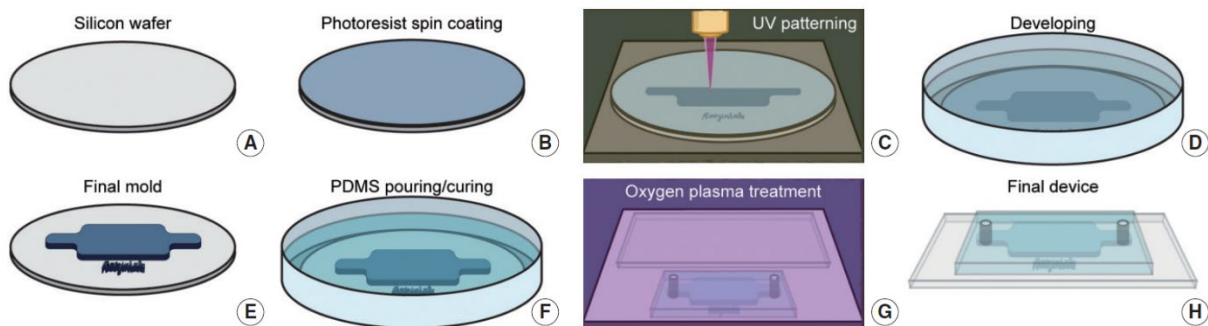


Figure 21. Microfluidic device fabrication by photolithography and soft lithography. (A) A silicon wafer is (B) spin coated with a photoresist before (C) UV exposure leads to patterning of the microfluidic device design. (D) During developing, the unexposed photoresist is removed to generate (E) the final SU-8 master. (F) A PDMS mixture is poured onto the SU-8 master before baking at overnight, enabling curing. (G) The peeled off PDMS device and glass are treated with oxygen plasma, before (H) bonding the two components together to generate the final microfluidic device. Image taken from Hwang et al. (235).

1.4.2 Droplet microfluidics in sample preparation

Protein crystallisation was one of the earliest and most transformative applications of droplet microfluidics, driven by the need to miniaturise screening, reduce sample consumption, and exert finer control over nucleation and growth (214,236–238). This marked a transition away from conventional crystallisation formats such as sitting-drop vapour diffusion, where there is limited control over supersaturation and the timing of nucleation. Microfluidic platforms enabled real-time modulation of chemical gradients and droplet environments. Initial microfluidic efforts focused on large-scale screening of chemical space by high-throughput screening of multiple precipitant solutions (239–242). A key method was free interface diffusion (FID) in glass/PDMS devices, where protein and precipitant solutions meet at a controlled interface. This interaction leads to supersaturation through gradual mixing, promoting crystallisation (239). The geometry of the interface and rate of diffusion can tune the nucleation landscape, offering finer control than was previously attainable.

Building on this foundation, Ismagilov and colleagues introduced a droplet-based system using nanolitre volumes to perform high-throughput screening by varying the flow rates of protein and precipitant, prior to droplet generation (243–245). This approach enabled fine-tuning of local supersaturation profiles within individual droplets, controlling crystal morphology and nucleation probability. By leveraging water-impermeable and water-permeable oils, both batch and vapour diffusion conditions could be emulated within droplets. These droplets were either incubated on-chip or transferred into glass capillaries (244) for external incubation and *in situ* X-ray data collection, circumventing the precarious step of manual crystal harvesting (246). The integration of crystallisation and structural analysis workflows reduced mechanical stress on crystals and streamlined the transition from screening to diffraction.

While on-chip X-ray analysis also proved feasible (164,241,247,248), further innovations tackled the challenge of droplet stability. Gas plugs were introduced to prevent coalescence, and allow reintegration of droplets into PDMS T-junction devices for crystallisation screening (243,249). These plugs acted as physical barriers, preventing unwanted merging during reinjection. Further enhancement of surfactant formulations ensured droplet integrity. This format was particularly effective when combined with optimisation workflows for membrane protein crystallisation (250).

Beyond screening, microfluidic architecture itself shaped crystallisation dynamics. Fraden and colleagues developed the phase chip (206), a droplet-based microsystem where preformed droplets reside in wells beneath a thin layer of oil, contacting an osmotic bath. The setup enabled independent control over nucleation and growth via osmotic regulation (206,251,252). Supersaturation was also tuned using seeding strategies, enhancing reproducibility and crystal quality (253). Spatial confinement within droplets resulted in local depletion of soluble protein during crystal growth, generating a self-limiting feedback loop that prevented overgrowth and promoted monodispersity. Droplet environments offer further advantages by enabling protein depletion during crystal growth, a negative feedback mechanism that limits crystal size based on droplet volume (248,254–256). Spatial confinement enhances nucleation control and crystal uniformity (248,257). Recently, fluorinated oil emulsions have enabled the preservation of diffraction quality crystals during transport, with emulsions applied directly to silicon fixed-target chips for room temperature SSX (258).

Significant advances have been made in adapting droplet microfluidics for protein crystallisation. Early innovations focused on enabling high-throughput crystallisation screening with nanolitre volumes, reducing sample use and improving control over nucleation. Advances such as water-permeable oils, gas plugs, and surfactants enhanced droplet stability and emulated batch and vapour diffusion conditions. These systems supported *in situ* X-ray analysis and facilitated crystallisation of challenging targets such as membrane proteins. More recent developments including osmotic regulation, seeding strategies, and fluorinated oil emulsions have improved crystal quality and reproducibility. Despite this progress, critical gaps remain. Miniaturisation must be pushed further to reliably produce crystals only a few microns in size. More importantly, time-resolved experiments demand crystal size uniformity at scale to synchronise reaction kinetics and enable consistent diffraction behaviour. These challenges frame the need for next-generation droplet systems that balance throughput, precision, and structural insights, motivating the approaches explored in this thesis.

1.4.3 Droplet microfluidics in sample delivery

Droplet-based sample delivery has become an essential technique in serial crystallography, offering precise handling of microcrystals, efficient use of limited sample volumes and compatibility with time-resolved setups (146). This shift reflects a broader evolution in sample delivery, moving away from continuous jets and towards discrete, synchronised presentation formats that better accommodate the demands of time-resolved studies. By encapsulating crystals within picolitre to nanolitre-sized droplets, this approach provides chemically stable and spatially isolated microenvironments that mitigate Taylor dispersion, while supporting synchronous delivery to the X-ray interaction region (213,214). Compared to viscous jets or fixed-targets, droplet systems offer superior temporal resolution along with reduced background scattering and significantly lower sample consumption, which is particularly relevant for difficult to crystallise targets.

Droplets have been implemented in both injector-based and hybrid tapedrive configurations. In droplet injector systems, crystal-containing droplets are produced on demand via piezoelectric actuation, surface acoustic waves, or pressure modulation, and delivered in sync with X-ray pulses to reduce sample waste and maximise hit rates (140–142,145–147). The confined geometry of droplets also facilitates rapid and uniform mixing of reagents, enabling precise control over reaction initiation, an essential feature for capturing short-lived intermediates. Hybrid tapedrive platforms complement this by depositing crystal-laden droplets onto a continuously moving tape, which presents them to the X-ray beam in a programmable and repeatable manner (148,149). These systems also enable tuneable delay times for pump-probe experiments by controlling the interval between droplet deposition and exposure. Successful implementation of these platforms requires tight integration with beamline infrastructure. Additionally several engineering challenges remain, including droplet evaporation, alignment and stability during transit. Taken together, droplet-based delivery systems exemplify the kind of methodological innovation that enables precise temporal control, efficient mixing and synchronised reaction initiation. These capabilities are increasingly central to the evolving landscape of time-resolved structural biology.

1.5 Aims

This thesis aims to develop and integrate droplet-based microfluidic and microcrystallisation strategies to enable time-resolved serial crystallography of enzymatic systems at synchrotron and XFEL sources. By combining innovations in sample preparation, crystal delivery, and reaction initiation, this project aims to overcome current limitations in capturing transient biochemical events with high spatial and temporal resolution.

Chapter 3 aims to establish *Arabidopsis thaliana* Pdx1.3 (*AtPdx1.3*) as a biologically relevant model for time-resolved mechanistic investigation. This PLP-dependent enzyme, central to vitamin B6 biosynthesis, provides a tractable system for probing catalytic progression within the crystal lattice. The transition from single-crystal growth to reproducible microcrystal slurry generation is explored, tailored for high-flux environments. Diffraction experiments at XFELs aim to validate crystal quality and assess ligand soaking protocols, while complementary techniques, including kinetic cryo-trapping and *in crystallo* UV-Vis spectroscopy, aim to define preliminary timescales for future time-resolved studies.

Chapter 4 aims to address the challenge of scalable and reproducible crystal production by developing high-throughput droplet crystallisation workflows. These workflows are optimised for precise control over crystal size and uniformity, enabling consistent sample delivery and mitigating issues such as clogging. Crystallisation conditions are refined to meet the demands of serial experiments and improve reproducibility across time-resolved datasets.

Chapter 5 aims to design and implement a droplet microfluidic platform for rapid substrate mixing and controlled reaction initiation within an X-ray transparent device. This system aims to enable on-chip catalysis under physiologically relevant conditions and support time-resolved interrogation of enzymatic intermediates. By integrating micromixing with serial crystallography, the platform aims to capture structural snapshots of catalytic events in real time, bridging microfluidic innovation with structural enzymology to illuminate dynamic reaction landscapes with unprecedented clarity.

Together these chapters converge towards a unified goal: to establish a versatile, reproducible, and biologically grounded framework for time-resolved serial crystallography, with each component explicitly designed toward revealing enzymatic mechanisms as they unfold within the crystal lattice. Conclusions and future work are outlined in Chapter 6.

Chapter 2 Materials and Methods

2.1 Transformation of AtPdx1.3 for protein expression

The sequence encoding wild type *Arabidopsis thaliana* Pdx1.3 (UniProt ID: Q8L940; EC: 4.3.3.6) was previously cloned into the pET-21a-d(+) vector at the NdeI and Xhol restriction sites (259). The primary protein sequence of AtPdx1.3 including C-terminal His₆-tag (317 amino acids, MW = 34.2 kDa, $\epsilon = 5960 \text{ M}^{-1} \text{ cm}^{-1}$ as calculated using ProtParam from the ExPASY server) is shown below:

MEGTGVAVYGNGAITEAKKSPFSVKVGLAQMLRGVIMDVNAEQARIAEEAGACAVMALERVPADIR
 AQGGVARMSDPQMIKEIKQAVTIPVMAKARIGHFVEAQILEAIGIDYIDESEVLTADEDHHINKHNFRIPF
 VCGCRNLGEALRRIREGAAMIRTGEAGTGNIIAEVRHVRSGNDIRVLRNMDDDEVFTFAKKLAAPYDL
 VMQTQQLGRLPVVQFAAGGVATPADAALMMQLGCDGVFGSGIFKSGDPARRARAIVQAVTHYSDPE
 MLVEVSCGLGEAMVGINLNDEKVERFANRSELEHHHHHH

Materials

- pET-21a-d(+) - *pdx1.3* (90 – 100 µg/nL)
- Competent BL21 (DE3) *E.coli* cells (New England Biolabs)
- LB Broth (yeast extract 5 g/L, sodium chloride 5 g/L, casein digest peptone 10 g/L) (Melford)
- LB Agar (agar 12 g/L, sodium chloride 10 g/L, yeast extract 5 g/L, casein digest peptone 10 g/L) (Melford)
- Ampicillin 100 mg/mL (Melford)

Protocol

2 µL of plasmid was mixed with 20 µL of competent BL21 (DE3) *E.coli* cells, incubated on ice for 30 minutes, and then heat shocked at 42 °C for 45 seconds. Cell recovery involved addition of 200 µL of LB broth before incubating in a shaking incubator at 37 °C, 200 RPM for 1 hour. The cell culture was then spread onto an LB agar plate containing 100 µg/mL ampicillin and incubated overnight at 37 °C.

2.2 Transformation of AtPdx1.3 for plasmid amplification

Materials

- pET-21a-d(+)–*pdx1.3* (90 – 100 µg/nL)
- Competent DH5 α *E.coli* cells (New England Biolabs)
- LB Broth (yeast extract 5 g/L, sodium chloride 5 g/L, casein digest peptone 10 g/L) (Melford)
- LB Agar (agar 12 g/L, sodium chloride 10 g/L, yeast extract 5 g/L, casein digest peptone 10 g/L) (Melford)
- Ampicillin 100 mg/mL (Melford)

5 µL of plasmid was mixed with 50 µL of competent DH5 α *E.coli* cells, incubated on ice for 30 minutes, and then heat shocked at 42 °C for 45 seconds. Cell recovery involved addition of 500 µL of LB broth before incubating in a shaking incubator at 37 °C, 200 RPM for 1 hour. The cell culture was then spread onto an LB agar plate containing 100 µg/mL ampicillin and incubated overnight at 37 °C. 10 mL of LB broth containing 100 µg/mL ampicillin was inoculated with a single colony of transformed DH5 α *E.coli* and incubated in a shaking incubator at 37 °C, 200 RPM overnight. AtPdx1.3 plasmid was extracted from the cells using the QIAprep Spin Miniprep Kit (Qiagen) following manufacturer's instructions, eluted in milliQ water and stored at -20 °C. Glycerol stocks for long-term storage were prepared by mixing 500 µL of overnight culture with 500 µL 50% (v/v) glycerol and flash frozen in liquid nitrogen before storing at -80 °C.

2.3 AtPdx1.3 protein expression

Materials

- LB Broth (yeast extract 5 g/L, sodium chloride 5 g/L, casein digest peptone 10 g/L) (Melford)
- 100 mg/mL Ampicillin (Melford)
- 25% (w/v) D-Lactose monohydrate (Sigma-Aldrich)
- 50% (v/v) Glycerol (Melford)

Protocol

100 mL of LB broth containing 100 µg/mL ampicillin was inoculated with a single colony of transformed BL21 (DE3) *E.coli*. The cells were incubated in a shaking incubator at 37 °C, 200 RPM for 16 – 20 hours. 1L of LB broth (prewarmed overnight at 37 °C) containing 100 µg/mL ampicillin in a 2L baffled flask was inoculated with 1 mL of overnight culture and incubated in a

shaking incubator at 37 °C, 150 RPM, until the optical density at 600 nm (OD₆₀₀) reached 0.6 – 0.8. The temperature was then reduced to 30 °C, and protein expression induced by addition of 60 mL of 25% (w/v) D-Lactose monohydrate. Cells were incubated in a shaking incubator at 30 °C, 150 RPM for 16 – 20 hours, before pelleting by centrifugation at 4 °C, 6240 x g for 30 minutes (Avanti JXN-26 centrifuge, JLA 8.1000 rotor). Cell pellets were subsequently weighed and stored at -20 °C. Glycerol stocks for long-term storage were prepared by mixing 500 µL of overnight culture with 500 µL 50% (v/v) glycerol and flash frozen in liquid nitrogen before storing at -80 °C.

2.4 AtPdx1.3 protein purification

Materials

- Lysozyme from Chicken Egg White (Melford)
- Lysis Buffer (50 mM Tris, 500 mM NaCl, 10 mM Imidazole, 2% Glycerol, pH 7.5)
- Elution Buffer (50 mM Tris, 500 mM NaCl, 500 mM Imidazole, 5% Glycerol, pH 7.5)
- Gel Filtration Buffer (200 mM KCl, 50 mM Tris, pH 8.0)
- 1 mL HisTrap HP Column (Cytiva)
- PD-10 Desalting Column (Cytiva)
- Vivaspin 20 Centrifugal Concentrator, PES Membrane MWCO 30,000 Da (Sartorius)

Protocol

6 – 8 g of thawed cell pellet were resuspended in 20 mL lysis buffer and lysed via sonication on ice for a total probe time of 3 minutes (10 second probe duration with a 30 second pause between probes) at 50% amplitude (Q700 Sonicator, QSonica). Lysates were clarified by centrifugation at 311 400 x g for 1 hour at 4 °C (Optima XPN-80 Ultracentrifuge with a Type 70 Ti Fixed-Angle Titanium Rotor, Beckman Coulter). The supernatant was filtered with a 0.45 µm membrane (Ministart syringe filter, Sartorius) and applied to a 1 mL HisTrap HP column (Cytiva) for immobilised metal ion affinity chromatography (IMAC). Throughout the IMAC protocol, the peristaltic pump (MINIPULS 3, Gilson) was run at a flow rate of 1 mL/min. AtPdx1.3 was washed (to remove non-specific proteins) and eluted with lysis buffer, containing 50 mM and 500 mM imidazole, respectively, as well as 5% (v/v) glycerol.

Eluted protein was desalted and buffer-exchanged into gel filtration buffer (20 mM Tris pH 8.0, 200 mM KCl) using a PD-10 desalting column (Cytiva). Fractions containing AtPdx1.3 were verified by absorbance at 280 nm using a NanoDrop 2000 spectrophotometer (ThermoFisher) and SDS-PAGE (see section 2.5), before pooling and concentrating to 30 mg/mL using a 30 kDa MWCO Vivaspin 20 centrifugal concentrator (Sartorius).

2.5 SDS-PAGE

Materials

- 0.75 mm 12% (w/v) SDS-PAGE Gel
- Sample Buffer (100 mM Tris, 1.2 M β -mercaptoethanol, 0.004% (w/v) Bromophenol Blue, 20% (v/v) glycerol, pH 6.8)
- Cathode Buffer (100 mM Tris, 0.1% (w/v) SDS, 100 mM Tricine, pH 8.2)
- Anode Buffer (200 mM Tris pH 8.9)
- InstantBlue® Coomassie Protein Stain (ISB1L) (Abcam)

Protocol

Sodium dodecyl sulphate-polyacrylamide gel electrophoresis (SDS-PAGE) was carried out using 12% (w/v) handmade SDS-PAGE gels. 5 μ L of sample buffer was added to 5 μ L of sample before incubating at 90 °C for 5 minutes. The Mini-PROTEAN Tetra Cell (BioRad) was setup with the inside containing cathode buffer and the outside containing anode buffer. 8 μ L of PageRuler™ Plus Prestained Protein Ladder (ThermoFisher) (molecular weight standards) and 10 μ L of sample was loaded into the wells before running the gel at 180 V for 1 hour. The gel was then transferred into InstantBlue® Coomassie Protein Stain (ISB1L) (Abcam) for 15 minutes, before being imaged with an Invitrogen™ iBright FL1500 imaging system (ThermoFisher).

2.6 Protein crystallisation

2.6.1 Lysozyme

The following protocol was used for all lysozyme microcrystallisation experiments presented in Section 4.1, 4.3.1 and 5.1, based on previously published protocols (138).

Lysozyme (L38100, Melford) was dissolved in 20 mM sodium acetate, pH 4.5 to a final concentration of 20 mg/mL. Microcrystals were grown in batch by mixing lysozyme solution in a 1:4 ratio with a precipitant solution containing 6% (w/v) PEG 6000, 3.4 M NaCl, 1 M sodium acetate, pH 3.0 before vortexing for 5 seconds. Rectangular-shaped microcrystals appeared within 1 hour at 21 °C, with a typical crystal size of ~10 μ m x 5 μ m x 5 μ m.

In order to improve reproducibility, an optimised protocol for lysozyme microcrystallisation was used for GlcNac binding experiments presented in Section 5.3, based on previously published protocols (163).

Chapter 2

Lysozyme (L4919, Sigma-Aldrich) was dissolved in 500 mM sodium acetate, pH 3.5 to a final concentration of 40 mg/mL. Microcrystals were grown in batch by mixing lysozyme solution in a 1:5 ratio with a precipitant solution containing 20% (w/v) NaCl, 6% (w/v) PEG 6000 before vortexing for 30 seconds. Rectangular-shaped microcrystals appeared within 10 minutes at 21 °C, with a typical crystal size of ~ 15 µm x 15 µm x 10 µm.

For lysozyme single-crystal GlcNac soaking experiments, the following protocol was used:

Lysozyme (L4919, Sigma-Aldrich) was dissolved in milliQ water to a final concentration of 100 mg/mL. Large single crystals were grown by vapour diffusion in a 24-well hanging drop XRL crystallisation plate (Molecular Dimensions) by mixing lysozyme solution in a 1:1 ratio with a precipitant solution containing 20% (w/v) PEG 5000 MME, 500 mM NaCl onto a 22 mm² Siliconised Cover Slip (Molecular Dimensions) over a 500 µL reservoir of the same solution, before sealing with Molykote High Vacuum Grease (Sigma-Aldrich). Large cube-shaped crystals appeared overnight at 21 °C, with a typical crystal size of ~ 300 µm x 200 µm x 200 µm. Before cryo-cooling, the crystals were transferred into a cryoprotectant containing the precipitant solution with an additional 20% (v/v) glycerol.

2.6.2 AtPdx1.3

Crystals were grown by vapour diffusion in a 24-well hanging drop XRL crystallisation plate (Molecular Dimensions). 10 – 25 mg/mL AtPdx1.3 in 200 mM KCl, 50 mM Tris, pH 8.0 was mixed in a 1:1 ratio with precipitant solution containing 350 – 600 mM sodium citrate, 100 mM HEPES pH 7.0 onto a 22 mm² Siliconised Cover Slip (Molecular Dimensions) over a 500 µL reservoir of the same solution, before sealing each well with Molykote High Vacuum Grease (Sigma-Aldrich). Large diamond-shaped crystals appeared overnight at 21 °C, with typical crystal sizes ranging from ~ 20 µm x 15 µm x 15 µm to ~ 150 µm x 100 µm x 50 µm. For cryo-trapping experiments, the crystals were transferred into a cryoprotectant containing the precipitant solution with an additional 20% (v/v) glycerol.

Seed stocks were generated based on the ‘seed bead’ method (63). Crystals were pipetted into an Eppendorf tube containing a PTFE MicroSeed Bead (Molecular Dimensions) along with the precipitant solution (usually between 20 – 50 µL per drop). Crystals were then crushed for a total of 180 seconds by alternating between 30 seconds of vortexing and 30 seconds on ice, before immediately storing at -20 °C. If a larger volume of seed stock was required, multiple vapour diffusion drops were pooled together and depending on the number, additional volumes of precipitant solution were added.

Microcrystals were grown in seeded-batch conditions by mixing in a 1:1:1 ratio, 10 – 25 mg/mL AtPdx1.3 in 200 mM KCl, 50 mM Tris, pH 8.0, seed stock diluted 1 in 100 and precipitant solution containing 600 mM sodium citrate, 100 mM HEPES (pH 7.0) before vortexing for 30 seconds. Diamond-shaped microcrystals appeared overnight at 21 °C with a typical crystal size of ~ 20 µm x 20 µm x 15 µm and a crystal density of 10⁶ – 10⁷ crystals/mL.

2.6.3 Trypsin

Preparation of trypsin microcrystals was based on previously published protocols (248). Trypsin from *Bovine pancreas* type I (T8003, Sigma-Aldrich) was dissolved in 3 mM CaCl₂, 10 mg/mL benzamidine to a final concentration of 65 mg/mL. Seed stocks were prepared (see Section 2.6.2) by pooling crystals from many vapour diffusion drops growing in a precipitant solution containing 11– 14% (w/v) PEG 4000, 15% (v/v) ethylene glycol, 200 mM SiSO₄, 100 mM MES pH 6.5. Trypsin solution was mixed in a 1:1:1 ratio with precipitant solution and neat seed stock before vortexing for 10 seconds. Needle-shaped microcrystals appeared overnight at 21 °C, with a typical crystal size of ~ 50 µm x 5 µm x 5 µm.

2.6.4 Chlorite dismutase

Purified chlorite dismutase and associated seed stock were kindly provided by Dr Jos Kamps, formerly at Diamond XFEL-Hub and now ESRF structural biology group. 30 µL of 22 mg/mL chlorite dismutase solution in 10 mM HEPES pH 7.0 was mixed with 60 µL of precipitant solution containing 15% (w/v) PEG 3350, 40 mM MgSO₄, 50 mM Tris pH 6.5 and 10 – 15 µL of seed stock (depending on density) before vortexing for 10 seconds. Plate-like microcrystals appeared overnight at 21 °C, with a typical crystal size of ~ 15 µm x 5 µm x 2 µm .

2.6.5 Thaumatin

Preparation of thaumatin microcrystals was based on previously published protocols (260). Thaumatin from *Thaumatococcus danielii* (T7639, Sigma-Aldrich) was dissolved in milliQ water to a final concentration of 50 mg/mL. Thaumatin solution was mixed in a 1:1 ratio with a precipitant solution containing 40% (w/v) sodium potassium tartrate, 0.1 M bis-Tris propane pH 6.5 in a 1.5 mL Eppendorf tube at 21 °C before vortexing for 10 seconds. Bipyramidal-shaped microcrystals appeared overnight at 21 °C, with a typical crystal size of ~ 15 µm x 15 µm x 10 µm.

2.7 Phase diagrams

2.7.1 Vapour diffusion phase diagram

Vapour diffusion phase diagram trials were undertaken at the Macromolecular Crystallisation Facility at the University of Southampton. The method was based on a previously published protocol (261). A 96-well grid screen varying the concentration of sodium citrate from 300 – 850 mM whilst keeping the 100 mM HEPES pH 7.0 buffer constant was pipetted into an Intelli-Plate 96-3 LVR plate (Art Robbins Instruments) using the Gryphon system (Art Robbins Instruments). AtPdx1.3 was sequentially diluted from 20 to 6 mg/mL using gel filtration buffer. 150 nL of AtPdx1.3 was dispensed into drop 1 and 2 using an Oryx8 liquid handling robot (Douglas Instruments) before 150 nL of well solution was added to drop 1, and 100 nL of well solution and 50 nL of neat seed stock was added to drop 2. The plate was then sealed with a ClearVue Sealing sheet (Molecular Dimensions) and incubated at 21 °C. Drops were imaged after 24 hours using a UV Minstrel Crystal Imager (Rigaku).

2.7.2 Microbatch-under-oil phase diagram

The method for generating phase diagrams in microbatch-under-oil was developed in collaboration with the CASE Partner, Douglas Instruments during the industrial PIPS placement. An Oryx8 liquid handling robot (Douglas Instruments) with a 4-channel dispensing tip was used to dispense 2 µL drops (final volume) into an untreated hydrophobic silver vapor batch plate (VB-SILVER-1/1-10, Douglas Instruments), covered with 100% paraffin oil (HR3-411, Hampton Research). Each drop contained AtPdx1.3 (30 mg/mL stock), crystallisation cocktail (1M Sodium Citrate, 167 mM HEPES pH 7.0) and in some cases additional neat seed stock. The amount of protein stock, precipitant stock and diluent for each drop was determined using a custom-made automated script available on Oryx8 systems within the WaspRun menu. The following parameters can be varied; concentration at the four corners of the plate, the number of wells to be dispensed and drop volume. Successful drops were scaled up in 100 µL PCR tubes contained within a MUHWA PCR tube rack, allowing direct production of microcrystal slurries appropriate for initial SSX screening (see section 2.8.1 and section 4.3). The robot paused after dispensing solutions into PCR tubes, allowing for 30 seconds of vortexing, ensuring rapid mixing of solutions. Drops were imaged after 24 hours using a 3D digital microscope (HRX-01, Hirox).

2.8 Serial synchrotron crystallography

2.8.1 Sample delivery and data collection

SSX data were collected at beamline ID29 (262) at the European Synchrotron Radiation Facility (ESRF, France) over multiple beamtime visits (under proposals MX2438, MX2548 and MX2636). Measurements were performed with a 4 μm (horizontal) by 2 μm (vertical) X-ray beam, at an energy of 11.56 keV (1.072 \AA), 1% bandwidth and a flux of $\sim 3 \times 10^{15}$ ph/s. An integrated heat load chopper system generated 90 μs pulses at a repetition rate of 231.25 Hz. Diffraction data were collected on a JUNGFRAU 4M detector with a sample-to-detector distance of 175 mm (SOSOS), 103 mm (SOSOS) or 150 mm (Tape4SSX, TH Lübeck).

Data were collected using a sheet-on-sheet on SPINE chip (SOSOS chip) (88), or with the tapedrive (Tape4SSX) developed by external TH Lübeck colleagues. For the SOSOS chip, 5 μL of microcrystal slurry was sandwiched between two 6 μm mylar films (Fisher Scientific) and sealed within a metal mount, allowing direct mounting to the MD3upSSX diffractometer. Diffraction data were collected in a rapid raster scan mode with a serpentine trajectory, and a vertical and horizontal spacing of 20 μm between images.

For the tapedrive, microcrystal slurries and ligand solutions were loaded into 500 μL SETonic syringes, running on CETONI Nemix 50 and CETONI NEMESYS syringe pumps respectively, the flow rate of both was 1 $\mu\text{L}/\text{min}$. An internal bead within the syringes (NEMIX 50 syringe stirrer) ensured the crystals did not sediment during data collection. Samples are transported from the syringe to the nozzle via 250 μm ID/ 360 μm OD fused silica capillaries (Polymicro Technologies LLC). Co-flow mixing of crystal and ligand, means they only meet at the 3D-printed nozzle (proprietary ESRF in-house project), where they are subsequently ejected onto a moving 10 μm thick polycarbonate hydrophilic ipPORE™ Track Etched membrane tape. The distance between the X-ray interaction region and the nozzle along with the tape speed of 30 mm/min allows for timepoint calculation (a Thorlab kinetic mount allows for precise distance measurement). At 0.25 mm, the fastest possible mixing time is 500 milliseconds, whilst 1.00 mm gives a 2 second timepoint and 2.5 mm gives a 5 second timepoint. The mixing occurs on the tapedrive, and therefore the flow rate of the sample and ligand is not involved in calculation of the timepoint.

2.8.2 Data processing

Images from the detector (in .h5 file format) were prefiltered for diffraction hits using the on-line data analysis plugin LImA2 and subsequently indexed and integrated with *indexamijig* in *CrystFEL* (version 0.11.1) (263). Detector geometry refinement was performed with

align_detector using calibration data written from *indexamijig*. An example of the command used for *indexamijig* can be found below:

```
$ indexamijig -i files.lst --peaks=peakfinder8 --indexing=xgandalf --
--multi --int-radius=4,6,10 --peak-radius=4,6,10 --min-peaks=30 --
min-snr=4.0 --threshold=1500 --local-bg-radius=5 --min-res=80 --max-
res=1200 --min-pix-count=3 --max-pix-count=200 -g *.geom -p *.cell -
o *.stream -j 60 --mille --mille-dir ./optimise

$ align_detector -g *.geom -o *_optimised.geom -l 2 --camera-length
optimise/*.bin
```

Indexing ambiguities present in the *AtPdx1.3* data (arising from the *H*3 space group) were resolved using *ambig*, an example of the command used can be found below:

```
$ ambig -i *.stream -y 3_H --operator=k,h,-l --iterations=20 --
highres=3.0 --fg-graph=ambi.dat -o *_reindexed.stream -j 60
```

Data were merged using *partialator* with partialities, post-refinement and scaling. Figures of merit and mtz files for structure determination were generated using the *import_serial* task (https://github.com/MartinMalyMM/import_serial) currently available in the latest version of CCP4 (264), an example of the command used can be found below:

```
$ partialator -i *.stream -o *.hkl -y 3_H --model=xsphere --
iterations=1

$ import_serial --wavelength --hklin *.hkl --half-dataset *.hk11
*.hk12 --spacegroup --cell --nbins 20 --dmin --project
```

2.8.3 Structure solution and refinement

Molecular replacement with MOLREP (265) used 6H79 (171), 7NHF (205), 7AC3 (260) and 5MAU (266) as initial search models for lysozyme, *AtPdx1.3*, thaumatin and chlorite dismutase respectively. Iterative rounds of model building and refinement used Coot (267) and REFMAC5 (268) within CCP4i2 (269). Optimised refinement parameters were set using the PDB-REDO server (270). Model validation was performed using the wwPDB validation service (271) and MolProbity (272). Structure factor files and atomic coordinates have been deposited in the PDB with accession codes 8S2U (Lysozyme Control), 8S2V (Lysozyme Droplet), 8S2W (*AtPdx1.3* Control), 8S2X (*AtPdx1.3* Droplet), 9QXW (Thaumatin Control), 9QXY (Thaumatin Droplet).

2.9 Serial femtosecond crystallography

2.9.1 Sample delivery and data collection

All SFX structures were generated from *AtPdx1.3* microcrystal slurries with a crystal size of $\sim 20\text{ }\mu\text{m} \times 20\text{ }\mu\text{m} \times 15\text{ }\mu\text{m}$ and an average crystal density of 10^7 crystals/mL. SFX data were collected at beamline BL2 EH3 at the SPring-8 angstrom compact free electron laser (SACLA, Japan) over two beamtime visits, May 2022 (as part of proposal 2022A8002) and November 2022 (as part of proposal 2022B8041). A silicon fixed-target setup was used at a repetition rate of 30 Hz, with data collected on a Rayonix MX 300 detector with a 10 fs pulse length. In May, the X-ray energy was 10.9971 keV with a beam size of $1.65\text{ }\mu\text{m}$ (horizontal) $\times 1.29\text{ }\mu\text{m}$ (vertical) at the sample, whilst in November the X-ray energy was 11.003 keV with a beam size of $1.41\text{ }\mu\text{m}$ (horizontal) $\times 1.37\text{ }\mu\text{m}$ (vertical) at the sample.

The full sample loading protocol is described elsewhere (101). Briefly, a silicon nitride chip with $20 \times 20\text{ }\mu\text{m}$ apertures in size was glow discharged to ensure hydrophilicity and therefore even dispersal of crystalline sample across the chip. A $200\text{ }\mu\text{L}$ sample of microcrystal slurry was pipetted on the surface of the chip within a humidity-controlled enclosure, before a weak vacuum was applied to bottom of the chip to remove excess liquid and draw crystals into the apertures. The fully loaded chip was placed between two $6\text{ }\mu\text{m}$ thick sheets of mylar before sealing inside a metal sample holder. The sample holder was magnetically mounted onto the sample stage and chip alignment was performed with inbuilt fiducial markers and the use of an on-axis viewing system (OAV). Each image corresponded to a single X-ray exposure at each individual aperture.

2.9.2 Data processing

Images from the detector (in .h5 file format) were prefiltered for diffraction hits using *Cheetah* (273) to generate the input files for *CrystFEL* (version 0.11.1) (263). Detector geometry refinement was performed using the inbuilt *CrystFEL* script, *detector-shift*. The following input parameters were used in *indexamajig* to index and integrate the diffraction patterns:

```
$ indexamajig -i files.lst -g rayonix_refine_10175.geom --
peaks=peakfinder8 --threshold=300 --min-snr=5 --indexing=xgandalf --
int-radius=3,4,5 --tolerance=5,5,5,1.5,1.5,1.5 --min-pix-count=2 --
multi --local-bg-radius=3 --xgandalf-fast-execution -o WT.stream -p
pdx1.pdb
```

Indexing ambiguities present in the data (arising from the *H*3 space group) were resolved using *ambigator* with the following command:

```
$ ambigator WT_nomask.stream -o WT_nomask_ambi.stream -y 3_H --
operator=k,h,-l -j 60 --highres=3
```

Data were merged using *partialator* without partialities and post-refinement but with scaling.

The point group -3_H was chosen, allowing merging of Friedel pairs ensuring high data quality with improved signal-to-noise but at the cost of anomalous information and redundancy.

Figures of merit and mtz files for structure determination were generated using the *import_serial* task (https://github.com/MartinMalyMM/import_serial) currently available in the latest version of CCP4 (264), an example of the command used can be found below:

```
$ partialator -i WT_ambi.stream -o WT_unity5.hkl -y -3_H --
model=unity --iterations=5 --no-logs

$ import_serial -w 1.1274 --hklin WT_nomask_ambi.hkl --half-dataset
WT_nomask_ambi.hkl1 WT_nomask_ambi.hkl2 --spacegroup H3 --cellfile
WT.cell --project ambi_highres3 --dmin 1.93 --nbins 20
```

2.9.3 Structure solution and refinement

Molecular replacement with MOLREP (265) used 8S2X (274) as an initial search model. Iterative rounds of model building and refinement used Coot (267) and REFMAC5 (268) within CCP4i2 (269). Optimised refinement parameters were set using the PDB-REDO server (270). Model validation was performed using the wwPDB validation service (271) and MolProbity (272).

2.10 Droplet Microfluidics

2.10.1 Device fabrication

Soft lithography was used to fabricate microfluidic devices using SU-8 on silicon wafers (225). Each device was designed with a fluorinated oil inlet and 3 aqueous inlets allowing the generation of droplets, ranging from 5 μm (82 fL) to 112 μm (754 pL). The design of choice (in CAD format) was sent to MicroFIT, Korea for the generation of an SU-8 wafer, containing the microstructures patterned onto the SU-8 photoresist by photolithography with UV exposure at 365 nm. The SU-8 wafer service from MicroFIT was used primarily for the fabrication of custom microfluidic devices, essential for time-resolved experiments at the beamline (see section 5.2), otherwise devices for droplet generation were repurposed from previous projects originating from the West Lab at the University of Southampton.

A 10:1 (w/w) mixture of polydimethylsiloxane (PDMS, Sylgard 184) pre-polymer and curing agent was mixed and degassed in a vacuum desiccator. PDMS was cured onto the SU-8 microstructures for a minimum of 2 hours at 60 °C, generating thick PDMS devices for counter moulding polyurethane (Smooth-ON, Oomoo 30TM). Components A and B were thoroughly shaken for 5 minutes, then a 1:1 mixture of component A and B was shaken thoroughly for 2 minutes before pouring over thick PDMS devices (microstructures facing upwards) secured to a silicon mould using double sided tape (3M). The mixture was degassed for 7 minutes using a vacuum desiccator, followed by overnight curing at room temperature and subsequent baking at 60 °C for 4 hours. Once cooled, the PDMS negative was removed from the polyurethane mould, allowing subsequent replica moulding of PDMS microstructures as above.

Tubing ports (hourglass-shaped) were introduced using a 1 mm-diameter Miltex biopsy punch (Williams Medical Supplies Ltd) for plug and play interconnection, followed by particulate and fibre removal with scotch tape (3M). Microstructures were bonded onto a glass microscope slide (VWR), also cleaned with scotch tape (3M). PDMS devices were bonded to glass microscope slides (VWR) by oxygen plasma treatment for 30 seconds (Femto, Diener Electronic), before channel surface functionalisation via the addition of 1% (v/v) tri-chloro-(1H,1H,2H,2H-perfluoro-octyl) silane (Sigma Aldrich) in HFE-7500 (3M). Subsequent baking overnight at 60 °C resulted in conformal contact and a pressure-tolerant bond.

2.10.2 Microfluidic experimental setup and flow conditions

The microfluidic experimental setup for droplet generation is shown in (Figure 22). Syringes are prepared containing protein, precipitant solution (with or without seed stock) and fluorinated oil (QX200, BioRad) that acts as a carrier phase. Plastic (2.5 mL, Terumo) or glass (0.5/2.5/10 mL, SGE) syringes are interfaced with inlet and outlet ports via polythene tubing (ID = 0.38 mm, OD = 1.09 mm, Smiths Medical). Solutions necessary for droplet generation are delivered by displacement syringe pumps (Fusion 100, Chemyx), allowing direct control of flow rates throughout the experiment. The flow rates were varied depending on the desired droplet size, see Tables 4 – 8. During droplet stabilisation, tubing was fed into a waste container, after which tubing was inserted into a 1.5 mL Eppendorf tube containing a layer of mineral oil, to reduce air-mediated droplet coalescence. Droplet emulsions formed between the upper mineral oil layer and the lower fluoro-oil carrier oil layer and were stored at room temperature for a maximum of 2 – 3 days. Droplet generation was monitored during the experiment using a Phantom Miro310 (Ametek Vision Research) high-speed camera mounted to an inverted microscope (CKX41, Olympus). Droplet emulsions were analysed by applying 10 μ L of emulsion to a counting chamber (Fast Read® 102, VWR) and subsequently imaging using brightfield microscopy via an inverted microscope (CKX41, Olympus) or 3D digital microscope (HRX-01, Hirox).

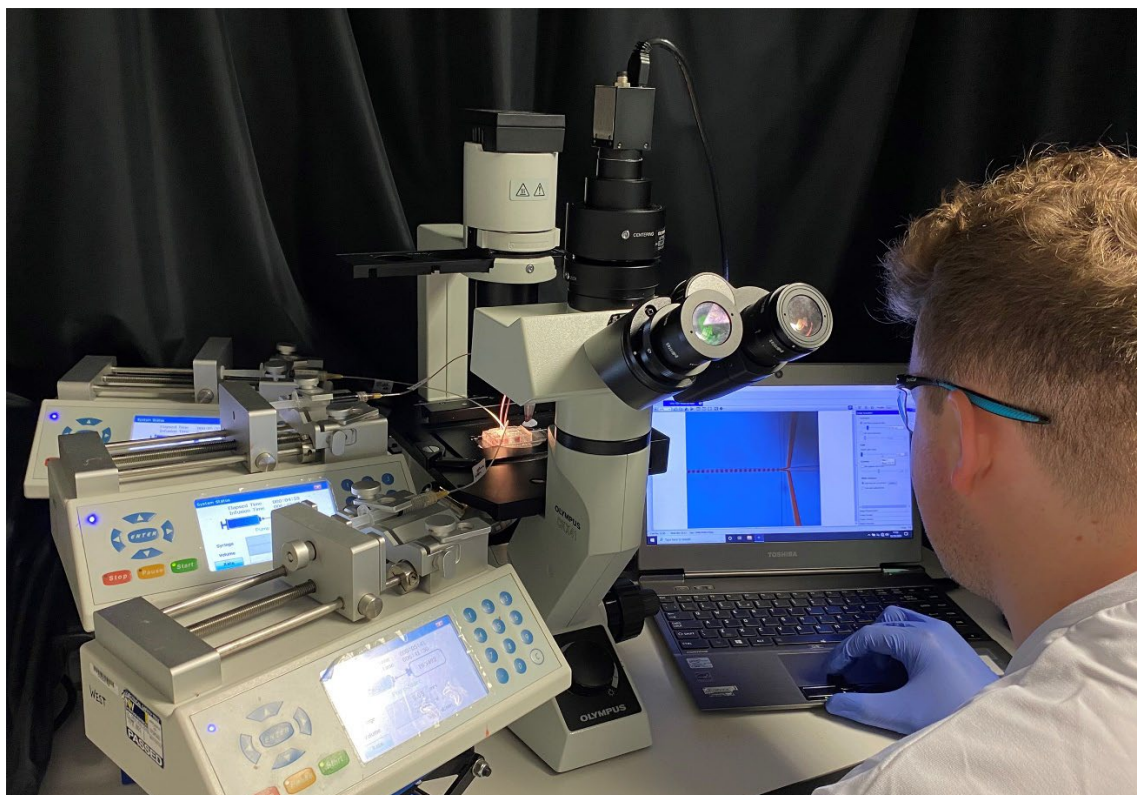


Figure 22. Microfluidic experimental setup for droplet generation. Oil and aqueous solutions are introduced by syringe pumps (LHS), allowing precise control of flow rates throughout the experiment. Tubing from syringes allows plug and play interconnection to the PDMS device (middle), which is visualised using a standard inverted microscope connected to a laptop (RHS).

Table 4. Flow conditions for preparing Lysozyme crystals in droplets.

Junction Dimensions (w, h)	QX200 oil	Precipitant	Lysozyme	Droplet Diameter	Droplet Volume
125 x 100 μm	60 $\mu\text{L}/\text{min}$	16 $\mu\text{L}/\text{min}$	4 $\mu\text{L}/\text{min}$	112.9 μm	754 pL
70 x 75 μm	37.5 $\mu\text{L}/\text{min}$	10 $\mu\text{L}/\text{min}$	2.5 $\mu\text{L}/\text{min}$	71.8 μm	194 pL
50 x 50 μm	22.5 $\mu\text{L}/\text{min}$	6 $\mu\text{L}/\text{min}$	1.5 $\mu\text{L}/\text{min}$	54.4 μm	84.3 pL
35 x 35 μm	15 $\mu\text{L}/\text{min}$	3 $\mu\text{L}/\text{min}$	0.75 $\mu\text{L}/\text{min}$	33.5 μm	19.7 pL
22 x 20 μm	8 $\mu\text{L}/\text{min}$	2 $\mu\text{L}/\text{min}$	0.5 $\mu\text{L}/\text{min}$	23.2 μm	6.54 pL
20 x 12 μm	8 $\mu\text{L}/\text{min}$	1.6 $\mu\text{L}/\text{min}$	0.4 $\mu\text{L}/\text{min}$	17.6 μm	2.85 pL
10 x 12 μm	5 $\mu\text{L}/\text{min}$	1 $\mu\text{L}/\text{min}$	0.25 $\mu\text{L}/\text{min}$	11.9 μm	0.89 pL

Table 5. Flow conditions for preparing AtPdx1.3 crystals in droplets.

Junction Dimensions (w, h)	QX200 oil	Precipitant + Seed	AtPdx1.3	Droplet Diameter	Droplet Volume
70 x 75 μm	90 $\mu\text{L}/\text{min}$	26.67 $\mu\text{L}/\text{min}$	13.33 $\mu\text{L}/\text{min}$	74.8 μm	219 pL
50 x 50 μm	60 $\mu\text{L}/\text{min}$	13.33 $\mu\text{L}/\text{min}$	6.67 $\mu\text{L}/\text{min}$	48.6 μm	60.1 pL
35 x 35 μm	40 $\mu\text{L}/\text{min}$	6.67 $\mu\text{L}/\text{min}$	3.33 $\mu\text{L}/\text{min}$	32.5 μm	18.0 pL
20 x 12 μm	16 $\mu\text{L}/\text{min}$	2.67 $\mu\text{L}/\text{min}$	1.33 $\mu\text{L}/\text{min}$	19.6 μm	3.94 pL
10 x 12 μm	8 $\mu\text{L}/\text{min}$	1.33 $\mu\text{L}/\text{min}$	0.67 $\mu\text{L}/\text{min}$	12.7 μm	1.07 pL
10 x 5 μm	2x1 $\mu\text{L}/\text{min}$	0.2 $\mu\text{L}/\text{min}$	0.1 $\mu\text{L}/\text{min}$	5.38 μm	82 fL

Table 6. Flow conditions for preparing Trypsin crystals in droplets.

Junction Dimensions (w, h)	QX200 oil	Precipitant + Seed	Trypsin	Droplet Diameter	Droplet Volume
70 x 75 μm	54 $\mu\text{L}/\text{min}$	12 $\mu\text{L}/\text{min}$	6 $\mu\text{L}/\text{min}$	75 μm	221 pL
50 x 50 μm	27 $\mu\text{L}/\text{min}$	6 $\mu\text{L}/\text{min}$	3 $\mu\text{L}/\text{min}$	50 μm	65 pL
35 x 35 μm	9 $\mu\text{L}/\text{min}$	2 $\mu\text{L}/\text{min}$	1 $\mu\text{L}/\text{min}$	35 μm	22 pL

Table 7. Flow conditions for preparing Chlorite Dismutase crystals in droplet.

Junction Dimensions (w, h)	QX200 oil	Precipitant + Seed	Chlorite Dismutase	Droplet Diameter	Droplet Volume
50 x 40 μm	22.5 $\mu\text{L}/\text{min}$	6 $\mu\text{L}/\text{min}$	1.5 $\mu\text{L}/\text{min}$	51.43 μm	71.22 pL

Table 8. Flow conditions for preparing Thaumatin crystals in droplets.

Junction Dimensions (w, h)	QX200 oil	Precipitant	Thaumatin	Droplet Diameter	Droplet Volume
50 x 40 μm	22.5 $\mu\text{L}/\text{min}$	6 $\mu\text{L}/\text{min}$	1.5 $\mu\text{L}/\text{min}$	55.13 μm	87.71 pL

2.10.3 Crystal retrieval and analysis

Crystal retrieval was performed using a procedure called ‘breaking the emulsion’, as shown in **Figure 23**. First, the sample was allowed to settle and form three layers (**Figure 23A**), the top layer contains mineral oil, the middle contains the droplet emulsion and the bottom layer contains the QX200 fluorinated carrier oil. The QX200 fluorinated oil is first removed (**Figure 23B**), followed by a 10-fold dilution (relative to emulsion volume) with precipitant solution (**Figure 23C**). A volume of 1H,1H,2H,2H-perfluoro-1-octanol (PFO, Sigma Aldrich) is added to the droplet emulsion and gently pipetted up and down to break open the emulsion (**Figure 23D**). The aqueous component of the droplets contact each other and coalesce, due to the exchange of PFO with commercial surfactant. Finally, the single layer of aqueous volume (containing crystals) can be retrieved (**Figure 23E**). The crystals are then analysed by either mounting on a coverslip for oil immersion imaging with a 60 \times /1.4NA objective (Olympus) or pipetting 10 μL into a counting chamber (Fast Read® 102, VWR) for brightfield microscopy with a 3D digital microscope (HRX-01, Hirox). Crystal dimensions were measured both manually using the 2D measurements and statistics functionality within the interface of the HRX-01 Hirox microscope, or semi-automated with a custom MATLAB script (<https://github.com/luiblaes/Crystallography>).

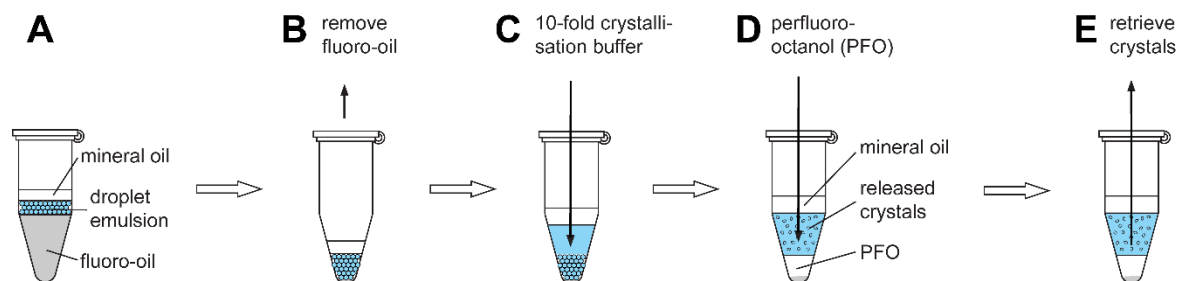


Figure 23. Breaking the emulsion. The collected sample settles to form three distinct layers, the upper mineral oil, the middle droplet emulsion and lower fluorinated oil. (B) Fluorinated oil is removed from the sample before (C) diluting 10-fold with precipitant solution (relative to emulsion volume). (D) The addition of PFO exchanges with surfactant in the QX200 fluoro-oil preparation, producing pin holes for droplet coalescence. (E) All droplets coalesce as a single, large volume for crystal retrieval with a pipette.

2.10.4 Mixing in droplets and image analysis

For studying mixing by droplet generation and transport, lysozyme crystals grown in batch (see section 2.6.1) were mixed with 25 mM sulfanilic acid azochromotrop (SAA, Sigma-Aldrich) at an oil:aqueous flow ratio of 2:1. A device with a droplet generation junction measuring 30 x 40 μm ($w \times h$) was used, with the total flow rate of lysozyme:SAA varying from 7.5 – 45 $\mu\text{L}/\text{min}$. Syringe rotation was used during the experiment, to ensure a continuous delivery of crystals and avoid sedimentation (173).

In both cases, diffusive-convective mixing of SAA dye with lysozyme crystals was captured by high-speed imaging. Droplets with and without crystals were analysed to understand the effect of the presence of a crystal on mixing and the crystal to dye (ligand) volume ratio. Mixing was measured by defining a coefficient of variation (CV) for pixel intensity within each individual droplet. A 5% CV for pixel intensity was defined as a fully mixed state. A semi-automated MATLAB script developed by Niall Hanrahan at the University of Southampton was used for mixing analysis. Mixing time statistics were calculated from 15 single droplet kymographs.

Chapter 3 Towards time-resolved studies of AtPdx1.3

We are entering an era of dynamic structural biology in which elucidating protein dynamics is as critical as determining static structures. In the case of AtPdx1.3, gaining insight into the dynamic changes that occur during catalysis is now essential for a more complete mechanistic understanding; key steps include sugar ring opening, ammonia transfer and the migration of intermediates. Achieving this goal requires a fundamental shift in the crystallographic experiment. Data collection is now performed at room temperature rather than cryogenic conditions, and single-crystal rotation methods are increasingly replaced by serial approaches using large volumes of microcrystal slurry.

To enable time-resolved crystallography experiments, several preparatory steps must be completed. Initial screening is essential to assess crystal quality and diffraction properties under room-temperature conditions. The experimenter must identify the most appropriate experimental modality to answer the biological question and be able to prepare the corresponding microcrystalline sample at scale. This often requires transitioning from vapour diffusion to batch crystallisation, demanding large volumes of highly pure protein. Small-volume room-temperature diffraction tests from microcrystal slurries are necessary to validate unit cell parameters, resolution limits, and lattice stability, especially when compared to previous single crystal data collected under cryogenic conditions.

If successful, compatibility with the chosen sample delivery method must be confirmed, for example, assessing whether crystals remain monodisperse and stable within viscous carriers suitable for high-viscosity extrusion. For time-resolved serial data collection, additional constraints arise. Crystals must be sufficiently small to permit uniform light penetration or rapid ligand diffusion into the lattice. Moreover, uniformity of crystal size is critical to ensure synchronised reaction initiation and to enable accurate interpretation of electron density and difference maps generated from time-resolved data.

In this chapter, I describe the optimisation of AtPdx1.3 microcrystals, highlighting the transition from vapour diffusion to seeded-batch crystallisation. Emphasis is placed on the use of microbatch-under-oil phase diagrams to guide the generation of high-density microcrystal slurries suitable for serial experiments. I present the first damage-free room-temperature structures of native and ligand-soaked AtPdx1.3, collected at an XFEL, and introduce complementary *in crystallo* UV–Vis spectroscopy and cryo-trapping studies that provide the foundation for future time-resolved experiments aimed at capturing mechanistically relevant intermediates of AtPdx1.3.

3.1 From single crystals to microcrystals of AtPdx1.3

To facilitate crystallographic studies of AtPdx1.3, a robust and reproducible purification protocol was established. The protein was expressed with a C-terminal His₆-tag, which remained intact throughout purification and did not impede subsequent crystallisation. AtPdx1.3 was purified to homogeneity using a 1 mL HisTrap HP nickel affinity column, with successful elution achieved by applying 3 mL of elution buffer containing 500 mM imidazole. Purity was confirmed by SDS-PAGE, which showed a single band at ~35 kDa in the final lane (**Figure 24**). The eluted protein was subsequently buffer-exchanged into gel filtration buffer using a PD-10 desalting column, allowing for both sample concentration and the removal of imidazole, which can interfere with accurate protein quantification due to its absorbance around 280 nm. This streamlined single-step purification consistently yielded large volumes (>500 µL) of highly pure AtPdx1.3 at concentrations exceeding >10 mg/mL, suitable for crystallisation optimisation and scale-up to batch crystallisation conditions.

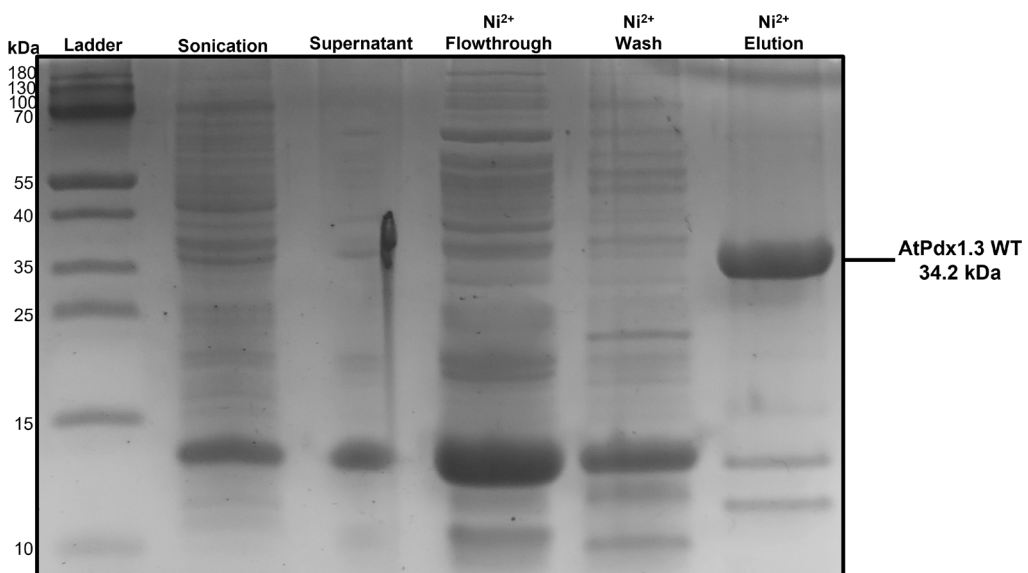


Figure 24. Nickel His-Tag purification of AtPdx1.3. Representative SDS-PAGE gel showing successful purification of AtPdx1.3. A prominent band is observed in the final lane at ~35 kDa, corresponding to AtPdx1.3, following elution with 3 mL of elution buffer containing 500 mM imidazole.

With a reliable purification protocol established, efforts shifted towards identifying crystallisation conditions suitable for structural studies of AtPdx1.3. To enable the transition from pure protein to large volumes of microcrystals suitable for serial crystallography, a structured crystallisation workflow was employed (**Figure 25**), drawing inspiration from previous sample preparation strategies (58,275). This workflow comprises several key stages: initial condition screening, optimisation, phase diagram construction, and scale-up via batch crystallisation. The process begins with sparse matrix screening to identify favourable conditions for crystal growth. These initial hits are refined through targeted optimisation,

typically using hanging-drop vapour diffusion, to ensure reproducibility and robustness. Once reliable crystallisation conditions are established, a phase diagram was constructed to systematically map the effects of varying protein and precipitant concentrations. Although these variables are sampled during earlier stages, the phase diagram offers a more comprehensive understanding of the crystallisation landscape and guides subsequent scale-up efforts.

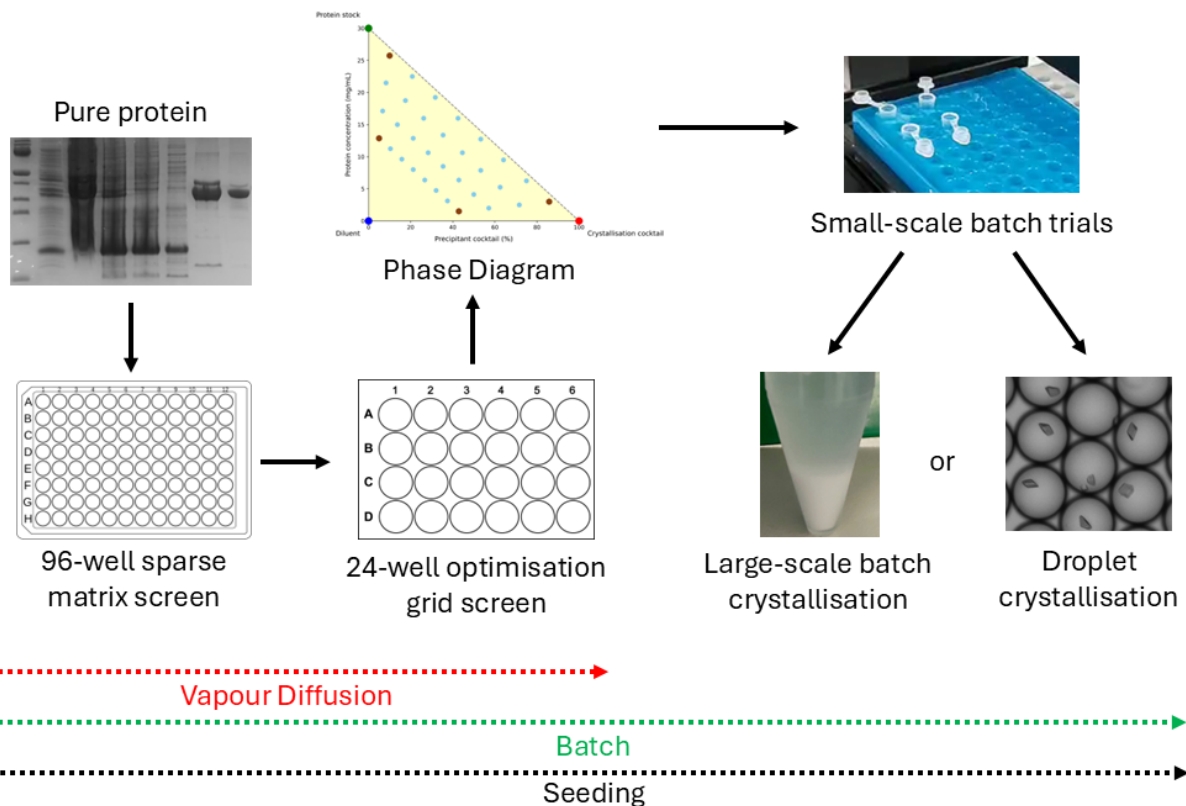


Figure 25. Crystallisation workflow for transitioning from single crystals to large volumes of microcrystals. Purified protein is initially screened using sparse-matrix vapour diffusion screens to identify favourable crystallisation conditions. These conditions are then refined in smaller format grid screens. Once reliable crystallisation conditions are established, a phase diagram is constructed, preferably under batch conditions, allowing for the effect of protein and precipitant concentration to be systematically explored. Promising conditions identified from the batch phase diagram are tested in small-scale trials to assess the impact of increasing drop volumes on crystal growth. Successful trials are subsequently scaled up to larger volumes or adapted for use in droplet microfluidic crystallisation systems. Throughout the workflow, seeding should be utilised enabling fine control of nucleation, with the aim of generating well-ordered crystals with high diffraction power.

To generate the larger crystal volumes required for serial experiments, the workflow transitions from vapour diffusion to batch crystallisation. While this shift is ideally made early in the process, it often coincides with the construction of the phase diagram. Vapour diffusion, which relies on gradual equilibration, is well suited for initial screening but becomes impractical for scaling up due to its limited volume and variability in nucleation. Batch crystallisation, by contrast, involves direct mixing of protein and precipitant at defined concentrations, offering greater control and reproducibility at scale. However, this transition is not always

straightforward, many crystallisation conditions that perform well in vapour diffusion may not translate to batch formats. Constructing the phase diagram under batch conditions therefore serves a dual purpose; it maps the crystallisation landscape while simultaneously assessing the feasibility of scaling up under conditions compatible with batch crystallisation.

Promising conditions within the nucleation and metastable zones of the phase diagram are advanced to small-scale batch trials to evaluate crystal growth at increased volumes. These trials serve to confirm whether the crystallisation behaviour observed in vapour diffusion is retained under batch conditions. Successful batch formulations are subsequently scaled up or adapted for use in droplet-based microfluidic platforms (discussed in the next chapter) allowing fine control over crystal size and uniformity.

Freshly concentrated *AtPdx1.3* protein (25 mg/mL), eluted from the PD-10 desalting column, was used immediately for crystallisation trials. Previous sparse-matrix vapour diffusion screens identified several favourable conditions for *AtPdx1.3* crystallisation, including 500 mM sodium citrate and 100 mM HEPES (pH 7.0) (202). Building on these conditions, a 24-well hanging drop optimisation grid screen was designed by varying the sodium citrate concentration from 300 to 850 mM, whilst maintaining HEPES at 100 mM (pH 7.0). Diamond-shaped crystals ranging from 30 to 200 μ m in size typically appeared overnight within the 400 – 700 mM sodium citrate range, and in some cases within just a few hours (Figure 26). The increase in sodium citrate concentration led to a greater number of smaller crystals, indicating elevated nucleation at higher precipitant concentrations (Figure 26).

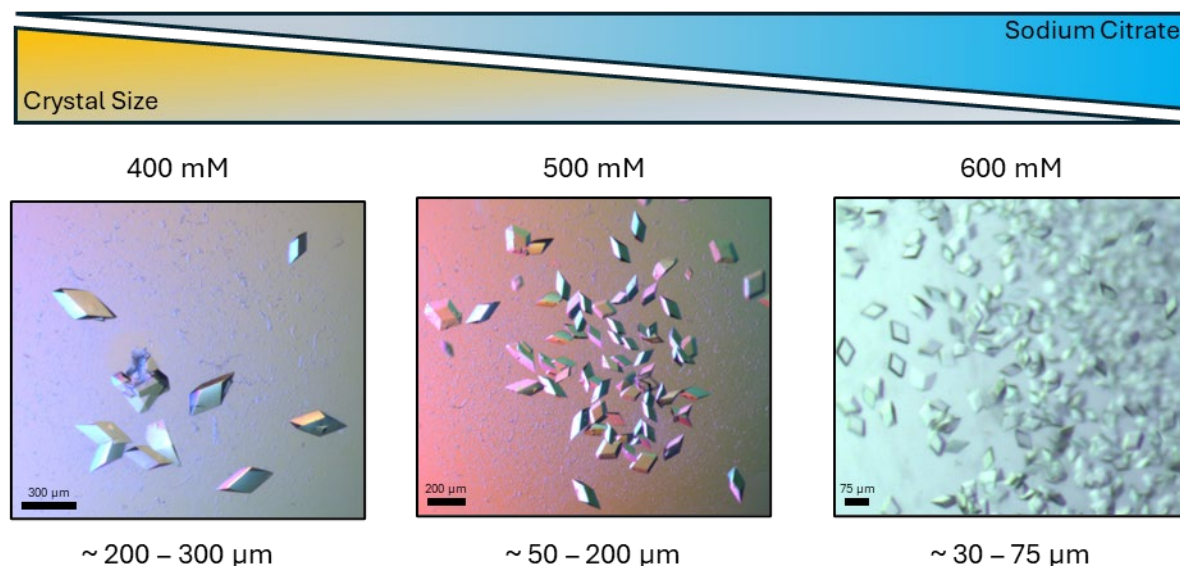


Figure 26. Effect of sodium citrate concentration on *AtPdx1.3* crystal size under vapour diffusion conditions. Representative images showing *AtPdx1.3* crystals formed using hanging-drop vapour diffusion. Crystals typically appeared overnight. Increasing concentrations of sodium citrate resulted in a higher number of crystals per drop, accompanied by a reduction in average crystal size.

Chapter 3

The rapid appearance of *AtPdx1.3* crystals under vapour diffusion, often within a few hours, suggested that the sodium citrate crystallisation condition was inherently ‘batch-like’. This behaviour indicates a high nucleation rate and minimal reliance on slow equilibration, both of which are favourable traits for batch crystallisation. To better understand the interplay between protein and precipitant concentration, an initial phase diagram was constructed under vapour diffusion conditions. The phase diagram explored a range of sodium citrate concentrations (300 – 850 mM) on the x-axis, with HEPES held constant at 100 mM (pH 7.0), and *AtPdx1.3* protein concentration ranging from 6 to 20 mg/mL on the y-axis. Since crystallisation was reliably observed at 25 mg/mL in previous vapour diffusion trials, the protein concentration range was deliberately shifted lower to identify the minimum concentration at which crystal formation could still take place, reducing sample consumption.

To further refine the crystallisation landscape, seeding was introduced as a second variable. Seed stock was prepared by mechanically fragmenting crystals previously grown under hanging-drop vapour diffusion conditions. These seed crystals were suspended in precipitant solution and crushed to form a suspension of nanocrystallites. For each condition in the phase diagram, two drops were prepared, one unseeded and one supplemented with seed stock. This allowed for identification of conditions within the metastable zone, where spontaneous nucleation does not occur, but crystal growth can be initiated by seeding. Crystallisation outcomes were assessed after 24 hours, and the results were used to generate a seeded versus unseeded phase diagram (**Figure 27**).

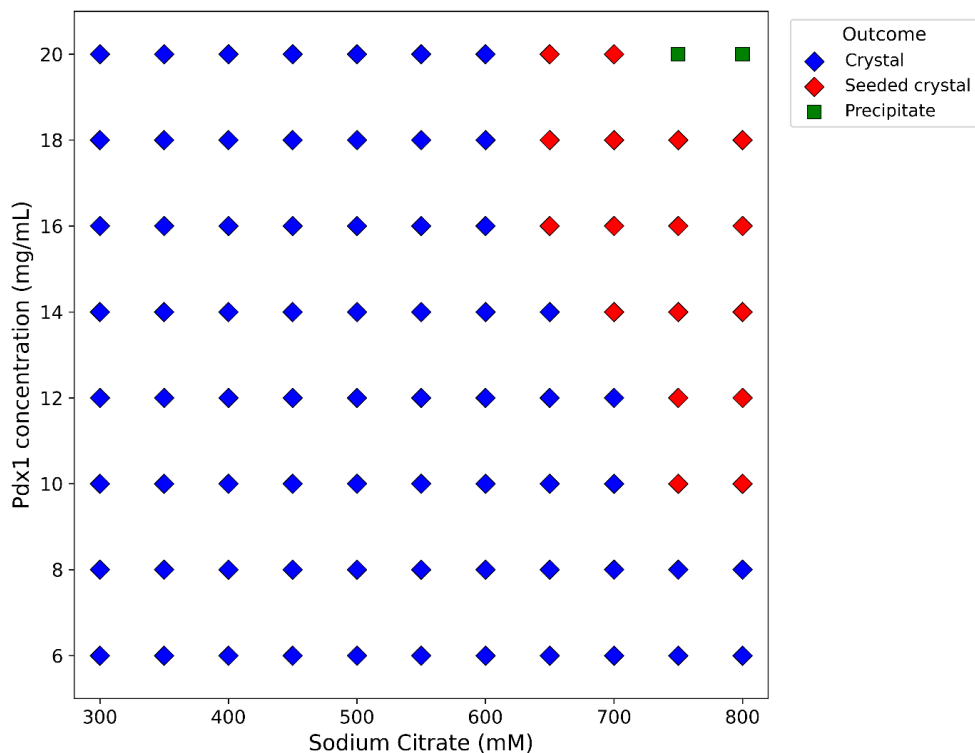


Figure 27. Vapour diffusion phase diagram of AtPdx1.3. The phase diagram was constructed by varying both protein concentration and sodium citrate concentration, while maintaining HEPES at 100 mM (pH 7.0). Blue diamonds indicate conditions where crystals formed spontaneously; red diamonds represent conditions where crystals formed only upon the addition of seed stock, green boxes indicate conditions that resulted in precipitation.

The majority of conditions in the vapour diffusion phase diagram resulted in crystal formation, even at the lowest protein and precipitant concentrations tested (Figure 27). This suggests that AtPdx1.3 exhibits a high intrinsic nucleation rate, when using the sodium citrate crystallisation condition. Conditions in which crystals formed only upon the addition of seed stock are highlighted in red on the phase diagram, clearly distinguishing them from those where spontaneous nucleation occurred. These seeded-only conditions defined the metastable zone.

Interestingly, the metastable zone for AtPdx1.3 appears at higher protein and precipitant concentrations, contrasting with the typical layout of a crystallisation phase diagram, where the metastable zone typically lies below the nucleation zone. In this case, the addition of seed stock enabled drops that were previously precipitated to yield well-formed crystals. This inversion suggests that under vapour diffusion conditions, the kinetics of supersaturation and equilibration may shift the crystallisation landscape. Importantly, the metastable zone is often preferred during optimisation, as it tends to produce fewer but better-ordered crystals, which are more likely to yield high-quality diffraction data.

During the process of vapour diffusion (sitting drop and hanging drop setups), the concentration of components within the drop changes, with the final concentration usually ending up higher than expected. When aiming to scale up crystallisation to the required volumes for serial

crystallography, this can cause problems. Protein can be lost at the surface of the drop meaning the drop surface area-to-volume ratio will change with increasing drop volumes. In contrast, microbatch-under-oil involving drops covered in paraffin oil (**Figure 28A**), results in true batch conditions where the concentration of components with the drop remains constant. Therefore, successful crystallisation conditions in microbatch-under-oil can be easily scaled up without adjusting concentrations, avoiding equilibration and simplifying interpretation. In addition, microseeding can be applied in microbatch-under-oil setups allowing for fine tuning of the number of nucleation events and consequently crystal size and number.

With this in mind, during an industrial PIPS placement at Douglas Instruments, in collaboration with Patrick Shaw Stewart and Stefan Kolek, I developed an automated microbatch-under-oil setup on the Oryx8 crystallisation robot for generating phase diagrams in true batch conditions. The simple but rapid method enables the generation of a phase diagram from just 15 – 60 μL of pure protein. By mixing a protein stock, crystallisation cocktail and diluent, any point within the yellow triangle can be reached, allowing greater coverage of crystallisation space, whilst also sampling high concentrations of protein and precipitant (**Figure 28B**). The experiment samples a diagonal path across the phase diagram that is parallel to the expected solubility curve, which is achieved by varying the ratio of protein stock to crystallisation cocktail. Within an 8 x 4 array, the experimenter selects the concentrations of components to be dispensed at the four corner wells of the batch plate (brown circles), after which the software automatically defines the remaining wells (light blue circles) (**Figure 28B**). The experimenter also selects the droplet volume and number of wells to be dispensed during the experiment (**Figure 28C**). A three-channel dispensing tip is typically used in the microbatch-under-oil setup, however alternatively a four-channel dispensing tip can be used, allowing for the addition of seed stock and subsequent identification of the metastable zone.

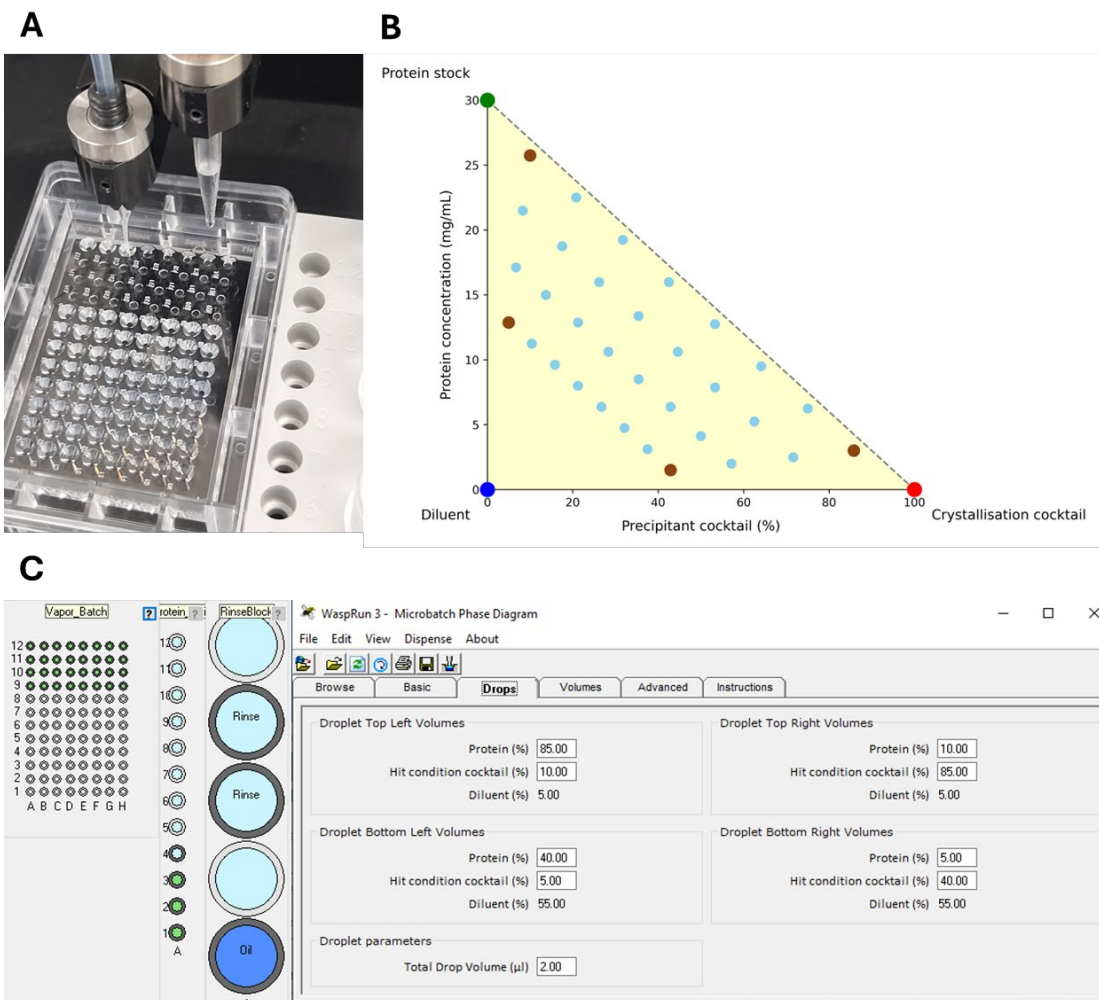


Figure 28. A simple and rapid microbatch-under-oil setup for generating phase diagrams. (A) The protein stock, crystallisation cocktail and diluent are simultaneously dispensed by the three/four channel microtip into the microbatch plate to form an aqueous drop, which is immediately covered with paraffin oil by the V tip. (B) Mixing protein stock (green circle), crystallisation cocktail (red circle) and diluent (blue circle) allows any point within the yellow triangle to be achieved. The four corner wells of the phase diagram (brown circles) are selected by the experimenter (C) and the software automatically fills in the remaining wells to generate an 8 x 4 array. The droplet volume, ratio of protein stock to crystallisation cocktail, and number of wells to be dispensed can be varied within the software menu, prior to starting the experiment.

For generating a phase diagram of *AtPdx1.3* in batch conditions, a four-channel dispensing microtip was used to enable the addition of seed stock, allowing for identification of the crucial metastable zone. The phase diagram was dispensed into a hydrophobic silver vapor batch plate with a final drop volume of 2 μ L, followed by covering with 100% paraffin oil to ensure no evaporation and therefore true batch conditions. A 30 mg/mL protein stock of *AtPdx1.3* and crystallisation cocktail containing 1M sodium citrate and 167 mM HEPES (pH 7.0) along with water as a diluent was supplied to generate the phase diagram. The phase diagram experiment was performed twice, firstly unseeded and secondly supplemented with neat seed stock. Crystallisation outcomes were assessed after 24 hours, and the results were used to generate a seeded versus unseeded phase diagram (Figure 29).

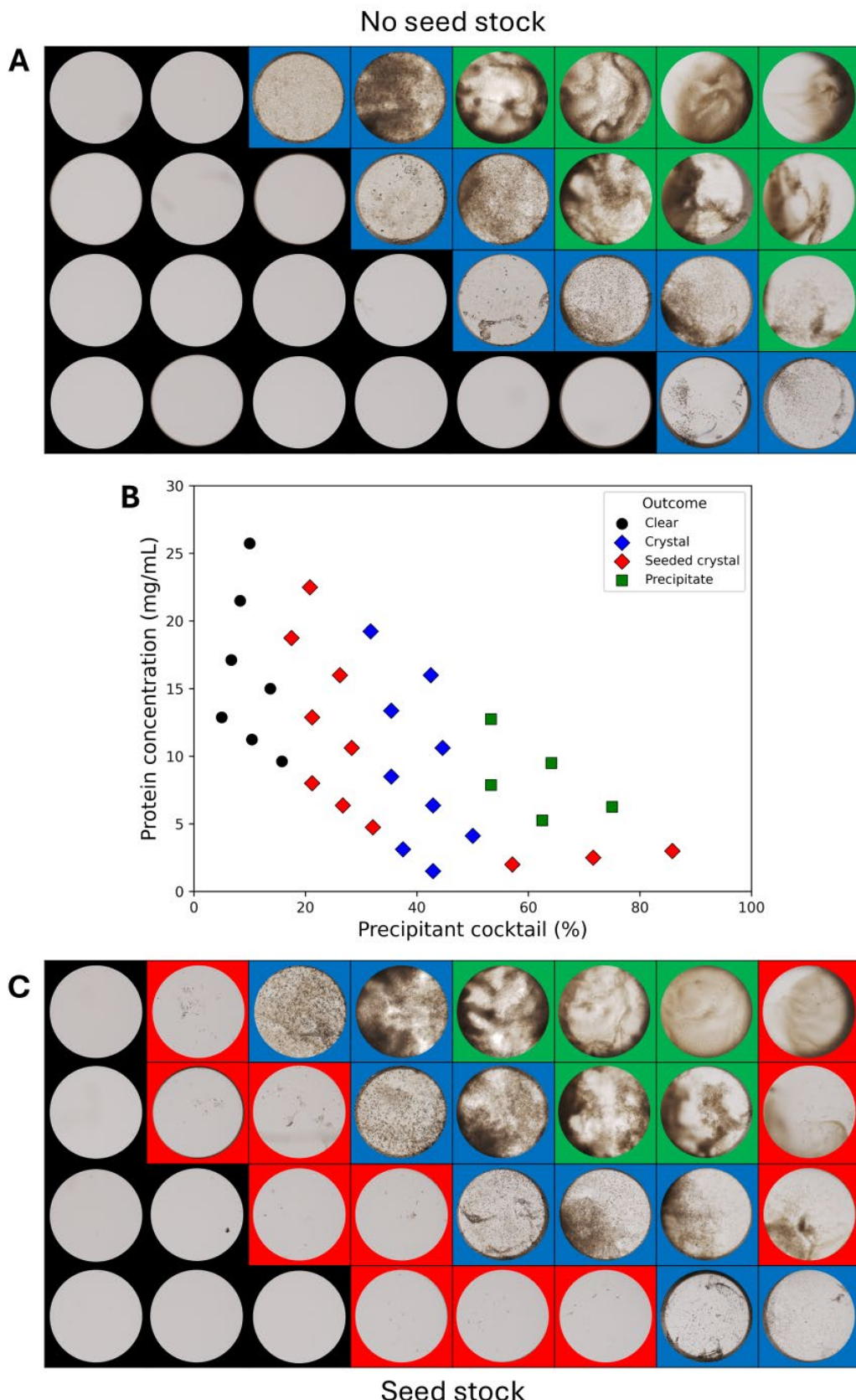


Figure 29. A microbatch-under-oil phase diagram of AtPdx1.3. (A) Representative images of crystallisation drops without seed stock. (B) Crystallisation outcomes from experiments with and without seed stock plotted on a phase diagram. Black circles represent a clear drop, blue diamonds represent crystal formation, red diamonds represent seeded-only crystal growth (metastable zone), and green squares denote precipitation. (C) Representative images of crystallisation drops supplemented with seed stock are highlighted in red.

The microbatch-under-oil phase diagram of AtPdx1.3 follows a more notional crystallisation phase diagram, with clear drops observed at low protein and precipitant concentrations as expected (**Figure 29A**). The central region denotes the nucleation zone where crystals are observed and the precipitant concentrations are similar to those observed in vapour diffusion trials, with the higher protein and precipitant concentrations inevitably resulting in precipitation throughout the drop (**Figure 29B**). The addition of seed stock in the second phase diagram, clearly highlights the metastable zone where crystal growth is initiated by seeding, despite only a smaller number of crystals being observed (**Figure 29C**). Interestingly, a second metastable zone is observed at higher protein and precipitant concentrations, akin to the previous vapour diffusion phase diagram but once again, the number of observed crystals is small. The observation of two distinct metastable zones in the microbatch-under-oil phase diagram may be driven by salting-in and salting-out effects. At low salt concentrations, salting-in likely increases protein solubility, suppressing nucleation despite supersaturation. At higher salt concentrations, salting-out reduces solubility, but nucleation remains kinetically hindered under oil, resulting in sparse crystal formation in both regions.

Successful conditions identified in both the metastable and nucleation zones of the microbatch-under-oil phase diagram of AtPdx1.3 (**Figure 29B**) were selected for further validation in small-scale batch crystallisation trials. Since the phase diagram was constructed under batch conditions, conversion into batch crystallisation within Eppendorf tubes was straightforward. The only procedural modification was the omission of the paraffin oil overlay typically used in microbatch-under-oil setups. The microbatch plate format was replaced with a 96-well PCR tube rack, where each PCR tube contained a 10 μ L crystallisation mixture, an increase in drop volume from the previous 2 μ L used for microbatch-under-oil experiments (**Figure 30A**). The automated setup on the Oryx8 crystallisation robot enabled precise dispensing of successful conditions identified from microbatch-under-oil phase diagrams directly into individual PCR tubes (**Figure 30A**). Following dispensing, the protocol included a programmed pause, allowing for the removal of each tube and a brief vortexing step, ensuring thorough mixing of protein and precipitant components prior to incubation (**Figure 30B**). No crystals were observed after 24 hours in conditions within the metastable zone, despite the addition of seed stock. This follows the same trend as microbatch-under-oil phase diagrams, where sparse crystal formation was observed even in the presence of additional seed stock.

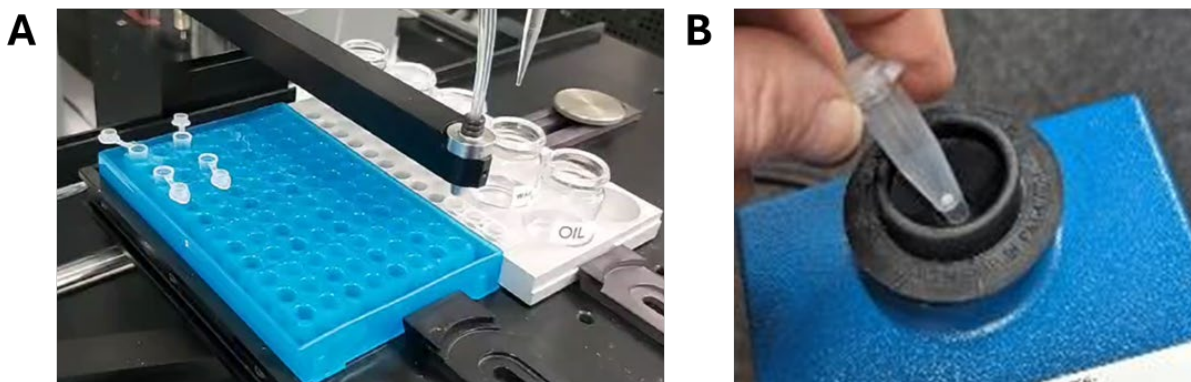


Figure 30. Experimental setup for scaling up of batch conditions on the Oryx8 crystallisation robot. (A) The microbatch plate is replaced with a 96-well PCR tube rack, enabling precise dispensing of previously successful crystallisation conditions, with the possibility of increasing volumes. (B) A programmed pause in the experiment allows for the vortexing of the PCR tube, ensuring thorough mixing of the crystallisation mixture, prior to incubation.

As a result, seeded conditions corresponding to the nucleation zone were trialled instead, to promote crystal growth under conditions where spontaneous nucleation had previously been observed resulting in large numbers of crystals. Two successful crystallisation conditions in the larger 10 μ L format consisted of 13.3 mg/mL AtPdx1.3 with 350 mM sodium citrate, 60 mM HEPES (pH 7.0) and neat seed stock (Mixture 1), and 6.735 mg/mL AtPdx1.3 with 430 mM sodium citrate, 71 mM HEPES (pH 7.0) and neat seed stock (Mixture 2) respectively. Mixture 1 produced crystals with a size of \sim 10 – 15 μ m and a crystal density of 10^6 crystals/mL, whilst mixture 2 produced crystals with a size of \sim 15 – 18 μ m and a crystal density of 10^5 crystals/mL (Figure 31). The reaction volume was then increased from 10 to 50 μ L to understand the effect of volume on resulting crystal size and density. The increasing volume resulted in a crystal size reduction in mixture 1, along with a slight increase in crystal density, while mixture 2 resulted in a microcrystal slurry with a similar crystal size and density (Figure 31). Therefore, caution must be taken when scaling up from smaller plate formats to large volume preparations in PCR or Eppendorf tubes if a particular crystal size or density is required.

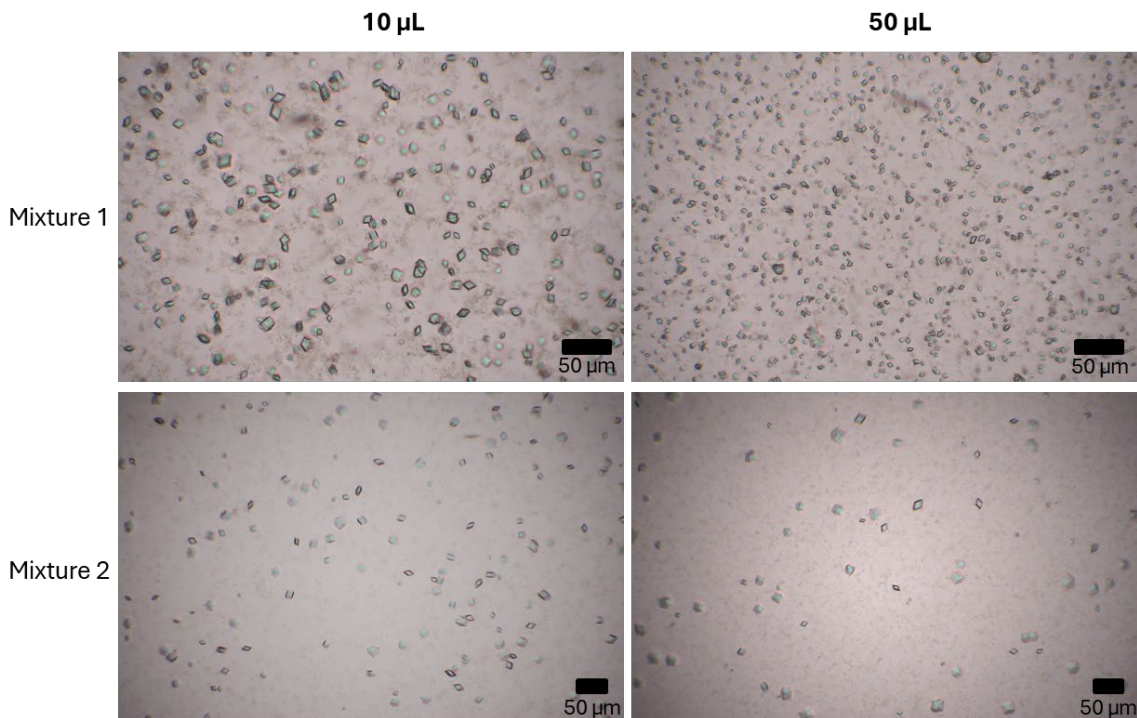


Figure 31. Effect of volume scaling on crystal size and density in microcrystal slurries. Mixture 1 consists of 13.3 mg/mL AtPdx1.3 with 350 mM sodium citrate, 60 mM HEPES (pH 7.0) and neat seed stock, producing crystals with an average size of ~10 – 15 µm and a crystal density of 10^6 crystals/mL in a total volume of 10 µL. Increasing the reaction volume of Mixture 1 to 50 µL resulted in a reduction in crystal size and a corresponding slight increase in crystal density. Mixture 2 consists of 6.735 mg/mL AtPdx1.3 with 430 mM sodium citrate, 71 mM HEPES (pH 7.0) and neat seed stock, producing crystals with an average size of ~15 – 18 µm and a crystal density of 10^5 crystals/mL in a total volume of 10 µL. Increasing the reaction volume of Mixture 2 to 50 µL resulted in a similar crystal size and density.

During microbatch trials, the concentration of both sodium citrate and HEPES (pH 7.0) was varied, resulting in several new crystallisation combinations. However, the sharpest crystal morphology was consistently achieved with the 100 mM concentration of HEPES (pH 7.0) and varying only the concentration of sodium citrate. With this knowledge and results from all of the previous steps in the crystallisation workflow, successful conditions from previous 50 µL trials were optimised further. This led to a successful larger volume (150 µL) seeded-batch preparation in a 1.5 mL Eppendorf tube consisting of a 1:1:1 ratio of 12 mg/mL AtPdx1.3, 600 mM sodium citrate, 100 mM HEPES (pH 7.0) and a 1 in 100 diluted seed stock. The crystallisation mixture was vortexed for 30 seconds resulting in a distinctive cloudy appearance, which subsequently formed a white pellet at the bottom of the Eppendorf tube following settling of the microcrystals. Within 10 minutes of vortexing, sharp diamond-shaped crystals were observed under a microscope with an average size of ~20 µm and a corresponding crystal density of 10^7 crystals/mL (Figure 32). These successful conditions were replicated several times in order to produce the required sample volumes for a serial crystallography experiment, with a consistent crystal size and density achieved across batches.

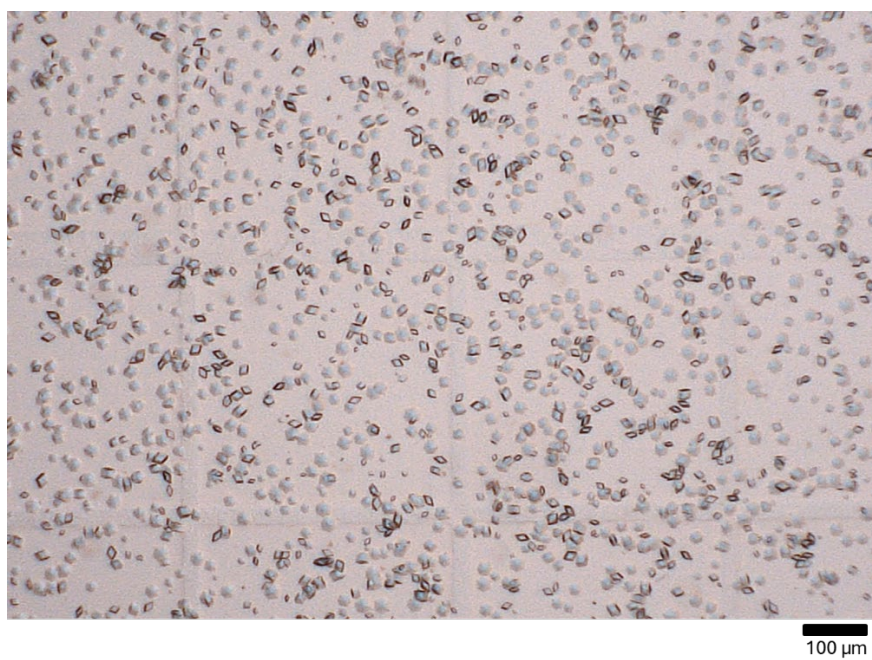


Figure 32. Optimised AtPdx1.3 microcrystal slurry produced via seeded-batch conditions. Microcrystals were grown using a 1:1:1 volumetric ratio of 12 mg/mL AtPdx1.3, precipitant (600 mM sodium citrate and 100 mM HEPES (pH 7.0)) and 1 in 100 dilution of seed stock. The resulting slurry contained well-formed crystals averaging ~20 μ m, with a crystal density of 10^7 crystals/mL.

3.2 Serial femtosecond crystallography (SFX) of AtPdx1.3

Previous crystallographic studies of AtPdx1.3 at cryogenic temperature revealed a dodecameric assembly with a notably large unit cell in the *H*3 space group, which produces closely spaced Bragg reflections, increasing the potential for spot overlap and complicating the indexing process. To overcome these limitations and to evaluate the suitability of AtPdx1.3 microcrystals for future time-resolved experiments, initial room-temperature SFX experiments were conducted at the SPring-8 angstrom compact free electron laser (SACLA). SFX data were collected from the previously optimised microcrystal slurries of AtPdx1.3 grown under seeded-batch conditions with an average crystal size of 20 μ m and a crystal density of 10^7 crystals/mL (Figure 32). The Oxford fixed-target chip, previously employed for serial crystallography at synchrotrons was chosen for sample delivery into the X-ray interaction region at SACLA. Microcrystals were loaded onto Oxford fixed-target chips, consisting of patterned silicon nitride membranes with 25,600 funnel-shaped apertures of a defined size sandwiched between two 6 μ m thick mylar films (Figure 33A). Prior to sample loading, chips were glow-discharged to ensure crystal adherence and suitable wettability. Microcrystals were pipetted onto the surface of the chip within a humidified environment to prevent dehydration, which would otherwise affect resulting diffraction quality (Figure 33B). A weak vacuum was then applied to draw the crystals into the apertures and remove excess liquid, ensuring a uniform distribution of crystals (Figure 33C).

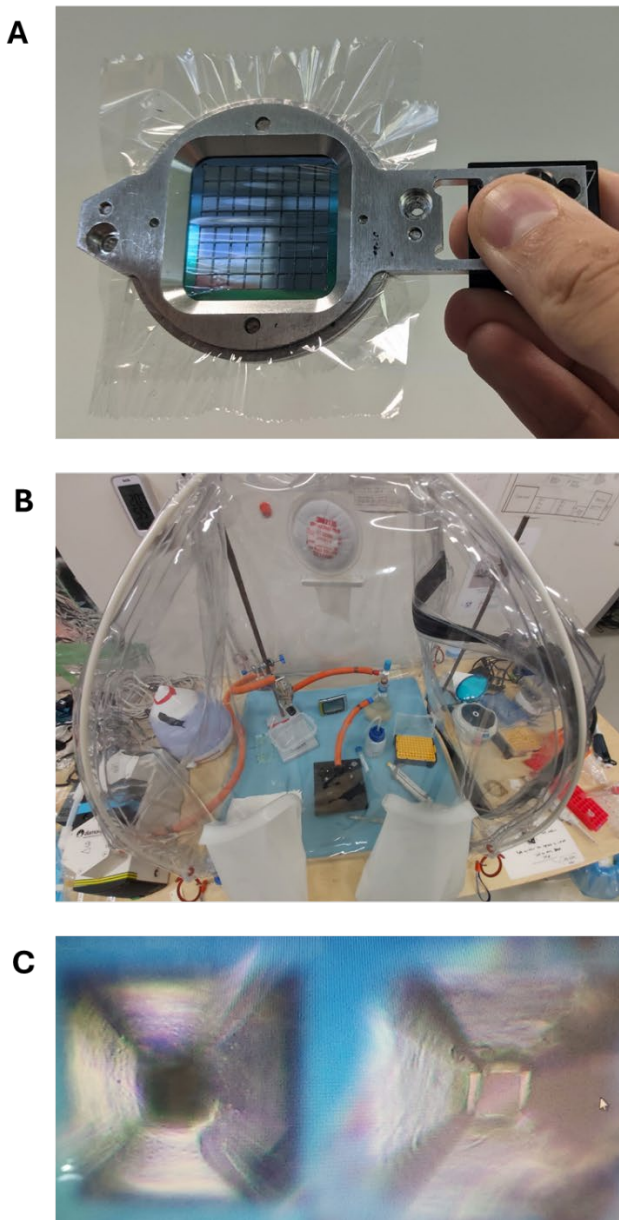


Figure 33. Oxford fixed-target chip for SFX sample delivery. (A) The Oxford fixed-target chip consists of a patterned silicon nitride membrane sandwiched between mylar films and held within a metal mount containing a Thor lab kinetic mount allowing easy transfer to the sample environment. (B) Sample loading is performed inside a humidity controlled environment ensuring the crystals are not dehydrated. (C) After application of a weak vacuum, crystals are randomly pulled into apertures. A AtPdx1.3 microcrystal can be seen trapped in the right-hand aperture.

Oxford fixed-target chips loaded with AtPdx1.3 microcrystals were mounted onto a high-precision XYZ raster stage within the SACLÀ sample environment (**Figure 34A**). Chip alignment was performed with embedded fiducial markers in the four corners of the Oxford fixed-target chip, enabling micrometre spatial calibration (**Figure 34B**). Data collection proceeded in a serpentine raster scanning mode, sequentially exposing each defined aperture to the XFEL beam. Synchronisation between the movement of the chip stage and XFEL pulses was maintained by the SACLÀ master timing system, operating at a repetition rate of 30 Hz. Each aperture was aligned and exposed to a ten femtosecond X-ray pulse, allowing for high-throughput data collection whilst minimising radiation damage effects.

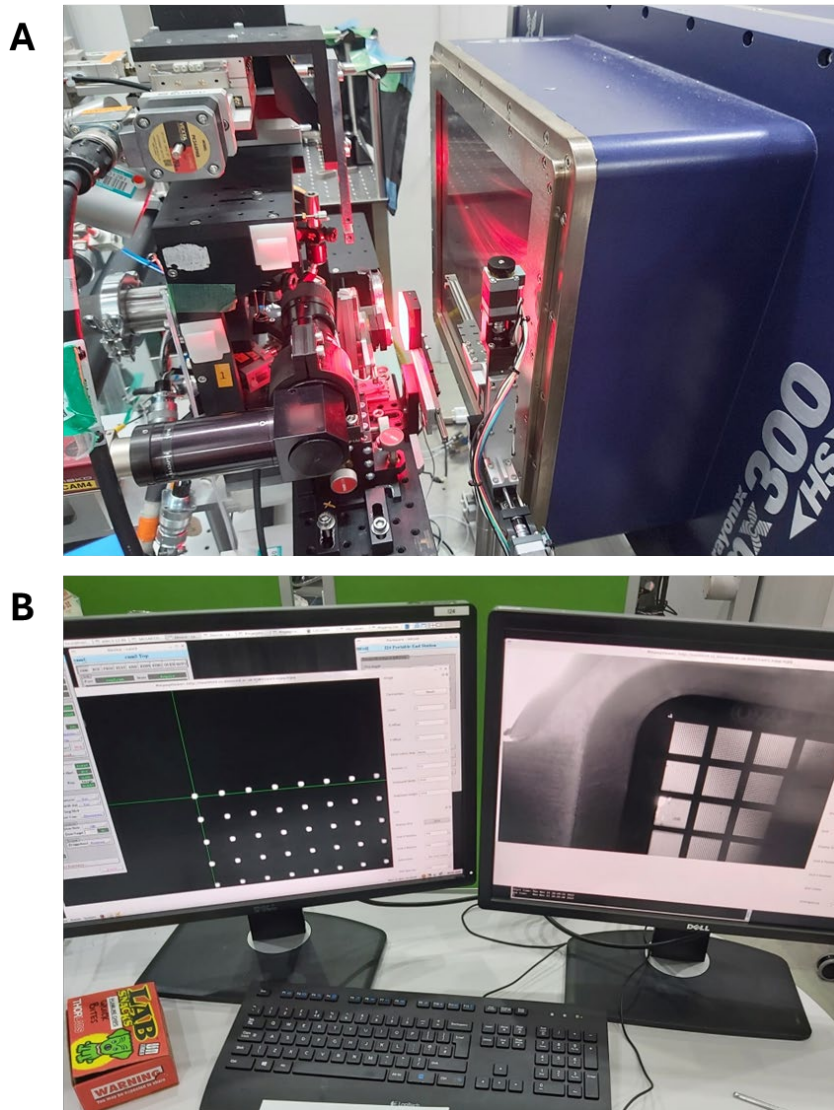


Figure 34. Oxford fixed-target chip sample delivery system at the SACLAC XFEL. (A) The Oxford fixed-target chip mounted on the fast translation stage within the SACLAC sample environment. (B) Sample alignment and calibration is performed outside the hutch taking advantage of embedded fiducial markers within the Oxford fixed-target chip.

Initial datasets collected from Oxford fixed-target chips containing apo AtPdx1.3 microcrystals served as the benchmark to evaluate diffraction quality and structural consistency under XFEL conditions. Data collection from two chips of apo AtPdx1.3 microcrystals yielded 16,836 hits, corresponding to a hit rate of 32.8% (Table 9). Of these hits, 16,604 diffraction patterns were successfully indexed, resulting in an indexing rate of 98.6% (Table 9). Notably, multiple lattices were observed within individual apertures, contributing to a total of 24,885 integrated lattices (Table 9). The final merged and scaled apo AtPdx1.3 dataset incorporated 23,456 lattices and achieved a high-resolution cutoff of 1.83 Å (Table 9). Structural refinement of the apo AtPdx1.3 dataset revealed well-defined electron density for the active site residues, Lysine 98 (K98) and Lysine 166 (K166) (Figure 35).

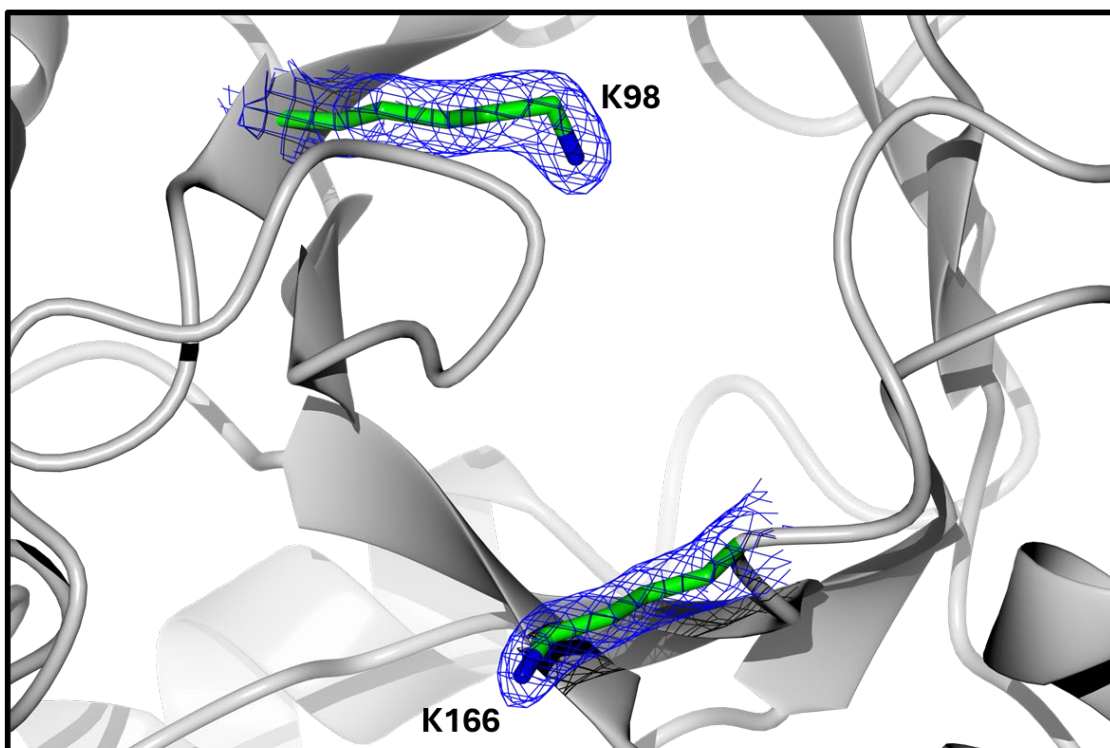
2F_o-F_c Electron Density Map

Figure 35. SFX crystal structure of wildtype AtPdx1.3 at a resolution of 1.83 Å. The sidechains of the active site lysines K98 and K166 are shown (carbon atoms are green and nitrogen atoms blue). 2F_o-F_c electron density map contoured around K98 and K166 at 1.5 σ .

To explore the suitability of microcrystals for ligand binding under static conditions and to ensure reaction intermediates were structurally distinguishable, apo AtPdx1.3 microcrystal slurries were soaked with ribose-5-phosphate (R5P), pyridoxal-5-phosphate (PLP) or a combination of R5P and ammonium sulfate to generate the key I320 reaction intermediate. To rigorously validate ligand incorporation and eliminate model bias in the resulting SFX structures, both omit and polder maps were generated. Omit maps exclude the ligand during refinement to test whether unbiased electron density supports its presence. Polder maps go a step further by excluding bulk solvent around the ligand region, enhancing the visibility of weakly occupied ligands. This dual-map strategy provided complementary validation, ensuring confident identification of bound ligands and intermediates.

Table 9. Data collection and refinement statistics for AtPdx1.3. Values in parentheses are for highest-resolution shell.

	WT	R5P	PLP	I320
Data Collection				
No. of collected images	51,200	51,200	51,200	25,600
No. of hits	16,836	10,687	6644	3556
Hit rate (%)	32.8	20.8	12.9	13.8
No. of indexed images	16,604	10,357	6320	3483
Indexing rate (%)	98.6	96.9	95.1	97.9
No. of integrated lattices	24,885	13,948	8482	4442
No. of merged lattices	23,546	12,886	8427	4328
Space group	H3	H3	H3	H3
<i>a, b, c</i> (Å)	178.88, 178.88, 118.35	178.84, 178.84, 118.27	178.75, 178.75, 118.50	178.80, 178.80, 117.98
α, β, γ (°)	90.0, 90.0, 120.0	90.0, 90.0, 120.0	90.0, 90.0, 120.0	90.0, 90.0, 120.0
Resolution (Å)	24.90 – 1.83 (1.86 – 1.83)	25.17 – 1.83 (1.86 – 1.83)	25.17 – 1.94 (1.97 – 1.94)	24.88 – 1.98 (2.01 – 1.98)
No. of unique reflections	124,499 (6228)	124,308 (6150)	104,416 (5209)	97,883 (4906)
Completeness (%)	100.00 (100.00)	100.00 (100.00)	100.00 (100.00)	100.00 (100.00)
Multiplicity	135.15 (128.18)	68.20 (64.91)	45.07 (42.14)	25.64 (24.29)
SNR	4.7 (0.9)	3.8 (1.0)	3.2 (0.9)	2.7 (0.9)
CC _{1/2}	0.966 (0.320)	0.913 (0.323)	0.868 (0.278)	0.838 (0.322)
CC [*]	0.991 (0.697)	0.977 (0.699)	0.964 (0.660)	0.955 (0.698)
<i>R</i> _{split}	15.8 (124.5)	22.9 (119.1)	27.5 (129.8)	34.4 (128.2)
Wilson <i>B</i> -factor (Å ²)	31.91	28.60	29.32	27.51
Refinement				
Resolution (Å)	23.80 – 1.83	24.37 – 1.83	23.80 – 1.94	24.90 – 1.98
No. of reflections	124,446	124,268	104,376	97,852
Reflections used for <i>R</i> _{free}	6224	6217	5366	4848
<i>R</i> _{work}	0.168	0.155	0.180	0.207
<i>R</i> _{free}	0.187	0.190	0.207	0.235

	WT	R5P	PLP	I320
Ramachandran favoured	1057 (99%)	1090 (99%)	1044 (98%)	1082 (98%)
Ramachandran allowed	15 (1%)	12 (1%)	17 (2%)	16 (2%)
Ramachandran outliers	0 (0%)	0 (0%)	0 (0%)	0 (0%)
Bond lengths (Å)	0.0068	0.0052	0.0075	0.0025
Bond angles (°)	1.473	1.213	1.545	1.060

The first soaking experiment focused on the binding of the initial substrate, R5P to the active site residue Lysine 98. An apo *AtPdx1.3* microcrystal slurry was allowed to settle, after which most of the precipitant solution was carefully removed, leaving behind a concentrated white crystal pellet. This pellet was resuspended in fresh precipitant solution supplemented with 100 mM R5P and soaked for 15 minutes prior to chip loading. The extended soaking time was selected to promote full substrate binding and achieve high ligand occupancy, approximating an equilibrium-bound state. R5P is clearly resolved in the $2F_o - F_c$ electron density map contoured at 1.5σ , forming a covalent bond with Lysine 98 (**Figure 36A**). Ligand presence was further validated using both polder and omit maps, with the polder map exhibiting slightly enhanced density at 3σ compared to the omit map, consistent with its improved sensitivity to weakly occupied regions (**Figure 36B**).

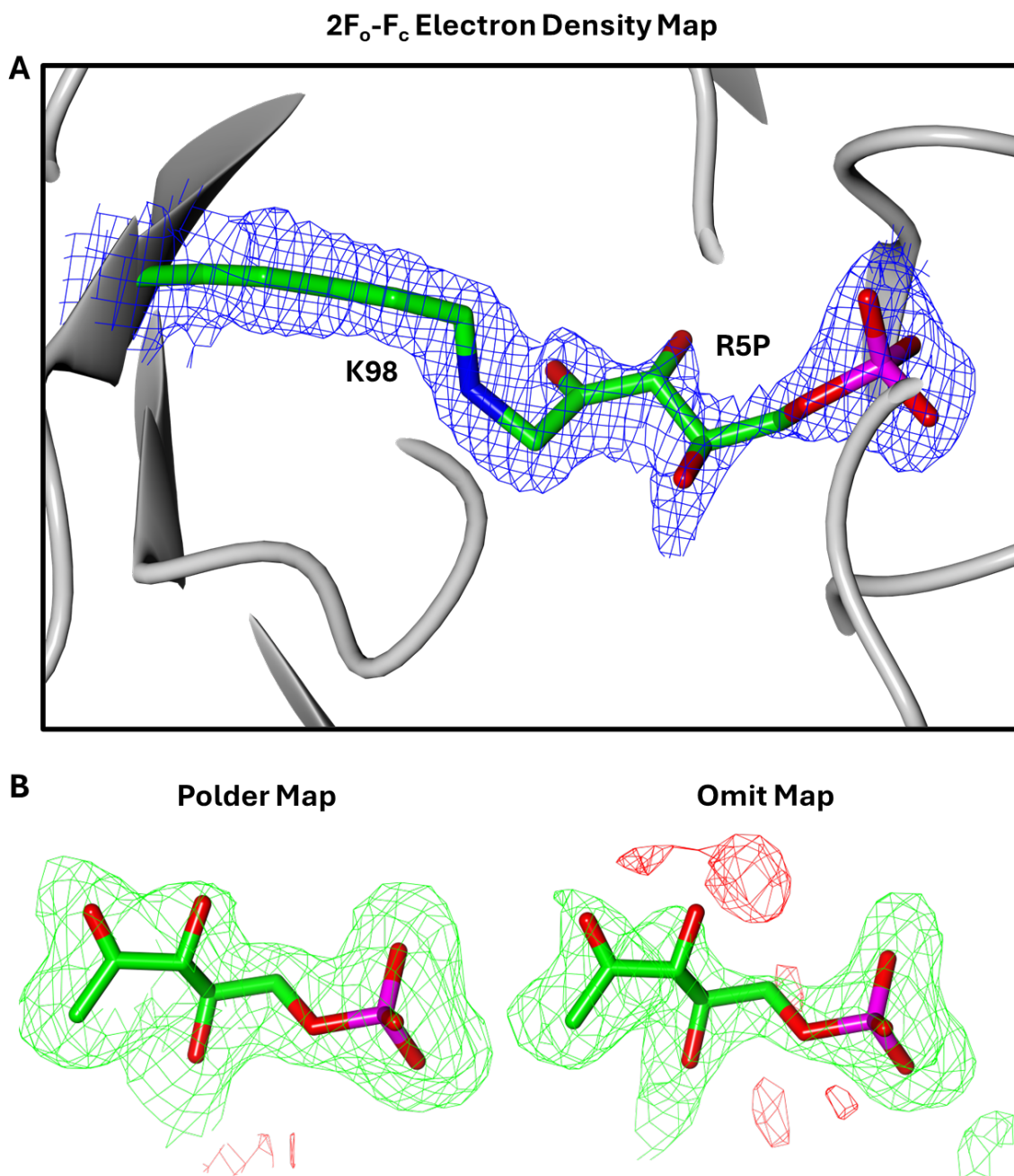


Figure 36. SFX crystal structure of AtPdx1.3 with R5P bound at a resolution of 1.83 Å. (A) 2F_o-F_c electron density map contoured around Lysine 98 and R5P at 1.5 σ . The sidechain of Lysine 98 is shown (carbon atoms green and nitrogen atoms green). R5P forms a covalent bond between C1 and Lys98 (R5P carbon atoms green, oxygen atoms red and phosphorous atoms pink). (B) Polder and omit maps contoured at 3 σ confirm the presence of the R5P ligand.

To investigate the binding of PLP, a direct soaking approach was employed. Previous cryo-trapping attempts involving incubation of the I320 intermediate with glyceraldehyde-3-phosphate (G3P) failed to yield PLP, resulting in poor diffraction of crystal degradation (202). To circumvent these limitations, microcrystal slurries were soaked directly with PLP to assess its binding potential under static conditions. Following removal of the original precipitant, the crystal pellet was resuspended in fresh solution containing 50 mM PLP and incubated for 15 minutes to promote full ligand occupancy. PLP was clearly resolved in the 2F_o-F_c electron density map contoured at 1.5 σ , forming the expected covalent bond with Lysine 166 (Figure

37A). Validation through omit and polder maps confirmed PLP binding, with the omit map showing minor negative difference density near the ligand, while the polder map provided more robust signal at 3 σ (Figure 37B).

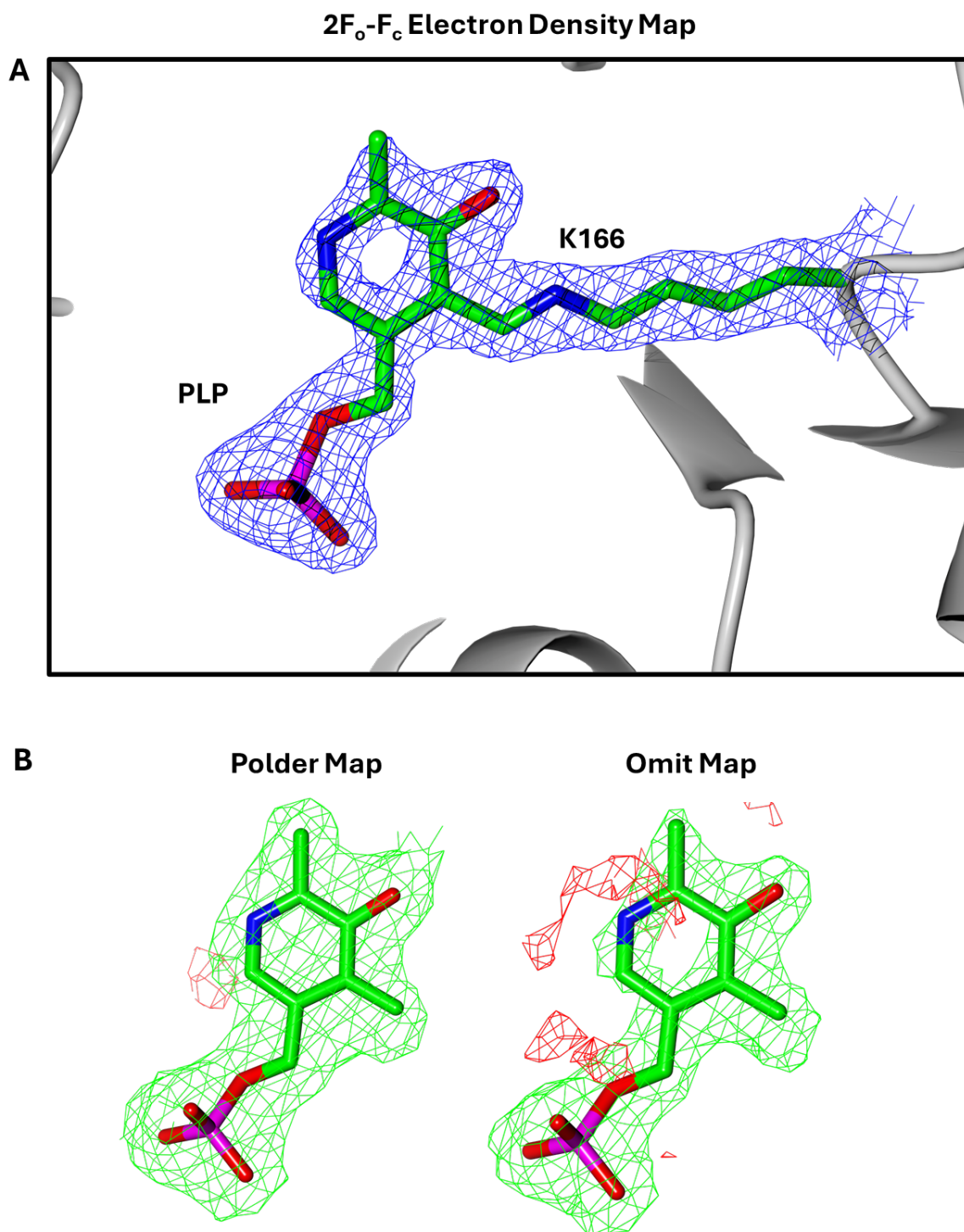


Figure 37. SFX crystal structure of AtPdx1.3 with PLP bound at a resolution of 1.94 Å. (A) 2F_o-F_c electron density map contoured around K166 at 1.5 σ . The sidechain of K166 is shown (carbon atoms green and nitrogen atoms green). PLP forms a covalent bond at K166 (carbon atoms green, nitrogen atoms blue, oxygen atoms red, phosphorus atoms pink). (B) Polder and omit maps contoured at 3 sigma confirm the presence of the PLP ligand.

Building on the successful R5P soaking strategy, the final soaking experiment aimed to capture the I320 intermediate, a key species in the *AtPdx1.3* reaction pathway. Apo microcrystal slurries were first incubated with 100 mM R5P for 15 minutes to ensure substrate binding.

Subsequently, 1 M ammonium sulfate was added to introduce the ammonia source required for intermediate formation, before further incubation for 30 minutes. The resulting structure revealed the I320 intermediate in the $2F_o-F_c$ electron density map contoured at 1σ , spanning both Lysine 98 and Lysine 166, indicating that the lysine flip had occurred (**Figure 38A**). This intermediate was further corroborated by omit and polder maps contoured at 3σ , both showing strong positive density with minimal negative difference, confirming its presence with high confidence (**Figure 38B**).

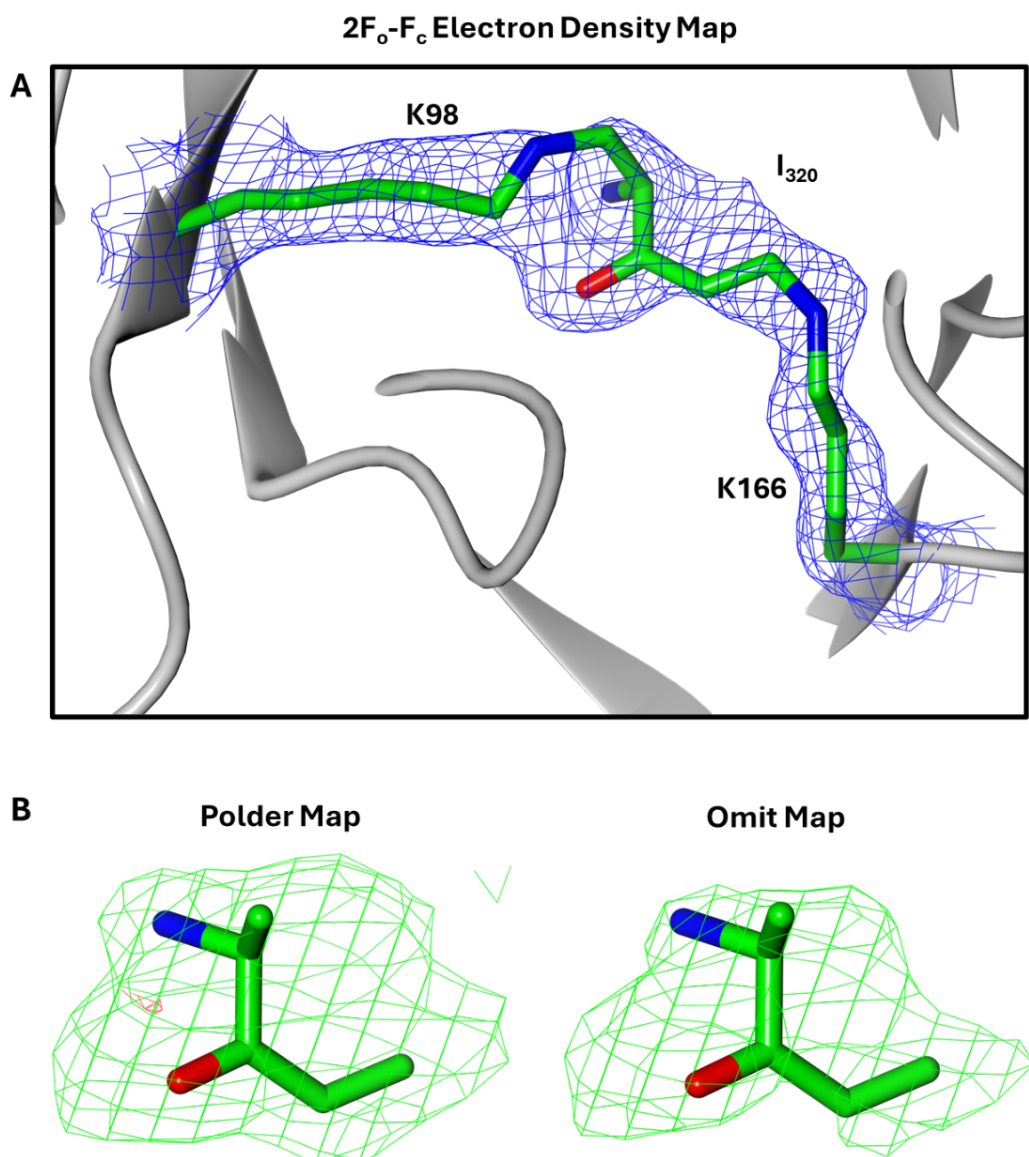


Figure 38. SFX crystal structure of *AtPdx1.3* with the I320 intermediate formed at a resolution of 1.98 \AA . (A) $2F_o-F_c$ electron density map contoured at 1.0σ around Lysine 98, Lysine 166 and the I320 intermediate. The sidechains of Lysine 98 and Lysine 166 are shown (carbon atoms green and nitrogen atoms green). The I320 intermediate bridges across Lysine 98 and Lysine 166 (carbon atoms green, nitrogen atoms blue, oxygen atoms red). (B) Polder and omit maps contoured at 3σ confirm the presence of the I320 intermediate.

3.3 Kinetic crystallography of AtPdx1.3

SFX data collection at SACLÀ demonstrated that AtPdx1.3 microcrystal slurries are well suited for room-temperature serial crystallography, and can withstand soaking with all relevant ligands in the reaction mechanism. The successful acquisition of ground state protein-ligand complexes confirmed the structural integrity of microcrystals post-soaking. Long incubation times were employed to ensure full ligand occupancy and facilitate high-resolution data collection.

Building on these results, initial kinetic cryocrystallography experiments were conducted to probe the timescales of key reaction steps. This approach was selected for its efficiency: only a small number of large single crystals were required, and multiple timepoints could be rapidly screened using automated data processing workflows to assess ligand incorporation. To complement this strategy, *in crystallo* UV-Vis spectroscopy was performed prior to diffraction measurements. This allowed for the detection of ligand binding and intermediate formation via characteristic chromophores, following by rapid cryocooling to trap the crystal at defined time points. Subsequent diffraction experiments validated the structural presence of the ligand or intermediate. Although reaction kinetics are expected to accelerate in microcrystals under room-temperature conditions, cryo-trapping experiments provide a valuable estimate of relevant timescales. These benchmarks inform the design of future time-resolved serial experiments. In particular, the use of UV-Vis spectroscopy to detect chromophoric intermediates offers a powerful orthogonal method for confirming the identify of trapped states and validating structural data.

In crystallo UV-Vis spectroscopy data were collected both online and offline, depending on the experiment. For the I320 intermediate, measurements were performed online at beamline BM07 at ESRF, allowing synchronised acquisition of UV-Vis spectra and subsequent X-ray diffraction at consistent timepoints. In contrast, the PLP experiment was conducted offline at the icOS lab, where UV-Vis spectra were first acquired and used to define new timepoints for diffraction experiments. Despite the difference in data collection environments, both setups employed an identical optical configuration: a white light source connected to an upper objective, which focused illumination onto the crystalline sample mounted in a standard loop, while a lower objective directed transmitted light to a spectrophotometer equipped with a CCD detector for spectral acquisition (**Figure 39**).

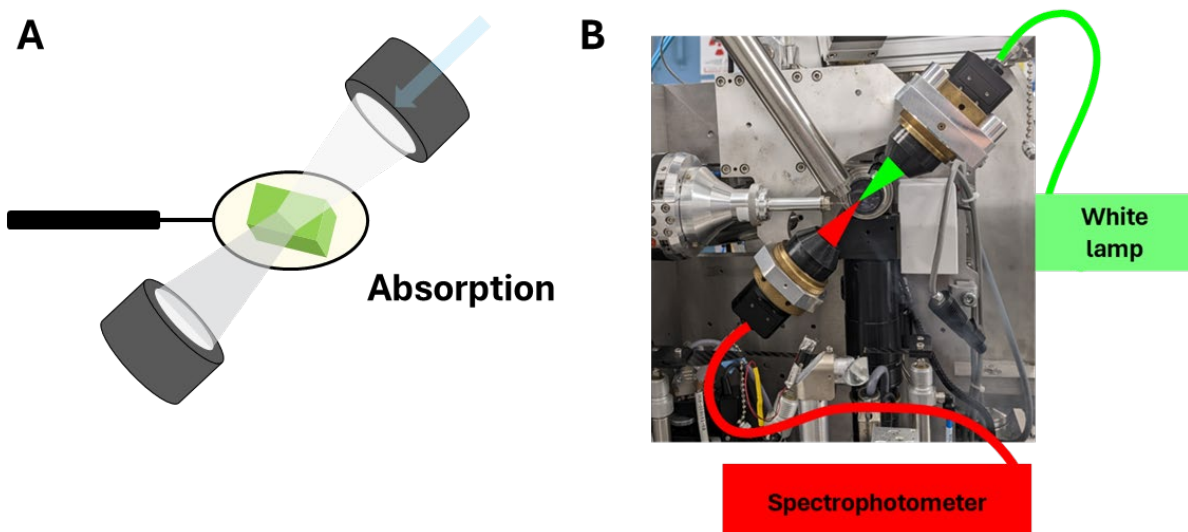


Figure 39. The experimental setup for *in crystallo* UV-Vis spectroscopy. (A) A protein crystal mounted in a sample loop is positioned on the goniometer and maintained at 100 K using a liquid nitrogen stream (Cryostream Series 700, Oxford Cryosystems). Prior to spectral acquisition, loop centering and adjustment of the omega angle are performed to optimise light transmission through the crystal. (B) The optical system consists of two objectives aligned 180° apart. The upper objective is connected via an optical fiber to a deuterium-halogen white light source (Mikropack DH2000-BAL, Ocean Optics), while the lower objective is coupled to a spectrophotometer equipped with a CCD detector (HR2000+/QE65Pro, Ocean Optics), enabling real-time spectral acquisition. Figure generated from images kindly provided by Nicolas Caramello, ESRF.

In crystallo UV-Vis spectroscopy was employed to monitor the formation of the I320 intermediate using Apo AtPdx1.3 single crystals ranging from 100 – 200 μm in size. Crystals were initially pre-soaked in a 100 mM R5P solution to ensure binding of R5P to the active site lysine residue (K98). As R5P lacks a chromophore, its binding cannot be monitored via spectroscopic methods such as UV-visible absorption. Therefore, extended soaking was employed to ensure sufficient ligand occupancy within the crystal lattice, enabling structural confirmation via electron density maps. This strategy was essential for generating a fully populated R5P-bound complex, which serves as a critical ground state reference for observing the formation of the I320 intermediate. Following R5P incubation, crystals were transferred to a 1 M ammonium sulfate solution and subsequently cryocooled manually in liquid nitrogen. The interval between crystal transfer and cryocooling defined the final soaking timepoints, which varied from 30 seconds to 13 minutes (**Figure 40**).

Spectral analysis of the 30-second timepoint revealed a prominent peak at 280 nm, consistent with the absorbance of aromatic amino acids in proteins. By 2 minutes, a weak signal emerged near 315 nm, indicative of initial I320 formation. At the 5-minute mark, the spectrum displayed a peak maximum at 320 nm, deviating from the expected I320 profile and resembling something similar to the pre-I320 complex, which typically exhibits a signal closer to 330 nm. Extended soaking durations of 7 and 13 minutes yielded spectra with a more defined peak at 315 nm, characteristic of the fully formed I320 intermediate (**Figure 40**).

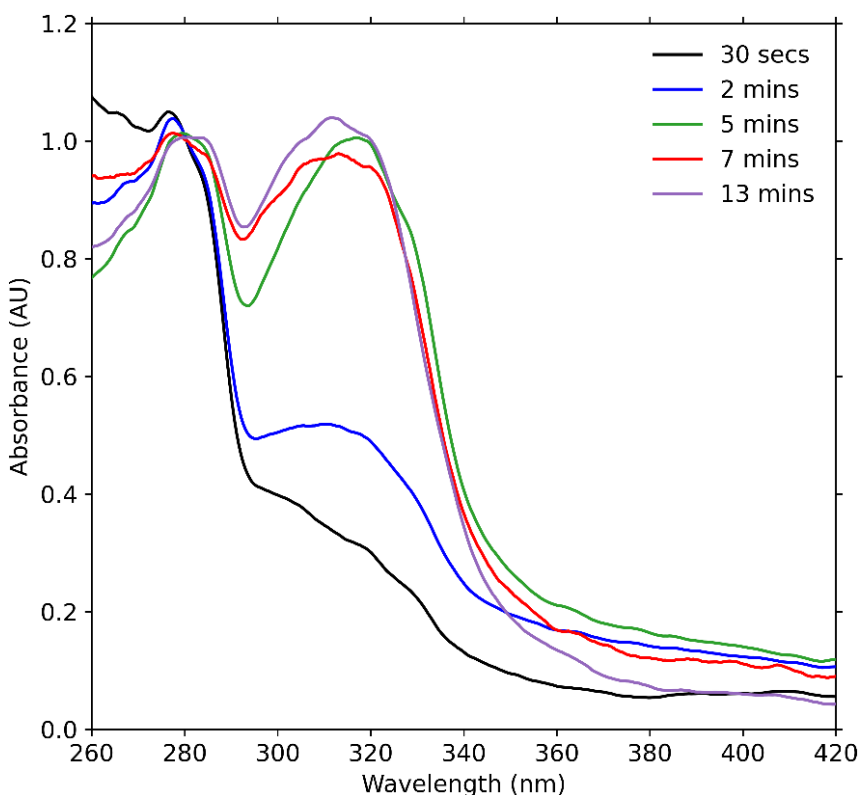


Figure 40. *In crystallo* UV-Vis absorption spectra tracking I320 intermediate formation in AtPdx1.3. Crystals were initially pre-soaked with R5P, before incubating in 1 M ammonium sulfate for defined time intervals from 30 seconds to 13 minutes, prior to manual cryocooling. Spectra were acquired post-cryocooling and processed using constant-baseline correction and smoothing. The emergence and evolution of absorbance features near 315 nm reflect the progressive formation of the I320 intermediate.

Diffraction data were collected for all samples using an online setup, enabling cross-validation between UV-Vis spectra and structural features. At the 30-second timepoints, the $2F_o - F_c$ electron density map contoured at 1.5σ revealed clear density for the R5P-bound state, with well-defined ligand presence in both the polder and omit maps (Figure 41). After 2 minutes, the structural data became less definitive; the electron density failed to fully encompass the R5P ligand, and the omit map showed minimal signal for ligand presence (Figure 41). Notably, strong density around Lys166 suggested that the lysine flip had not yet occurred, indicating a low probability of pre-I320 formation at this timepoint. At the 5-minute timepoints initial signs of I320 formation emerged (Figure 41). Electron density appeared for the central I320 molecule, although density for Lys98 remained weak. This may be attributed to the lower resolution of the dataset and the absence of I320 signal in the omit map. By 7 and 13 minutes, the I320 intermediate was clearly resolved in the $2F_o - F_c$ electron density map, with consistent ligand density in both polder and omit maps (Figure 41). Despite the presence of some negative difference density adjacent to the intermediate, the overall structural data strongly support the formation and stabilisation of I320 at these later timepoints.

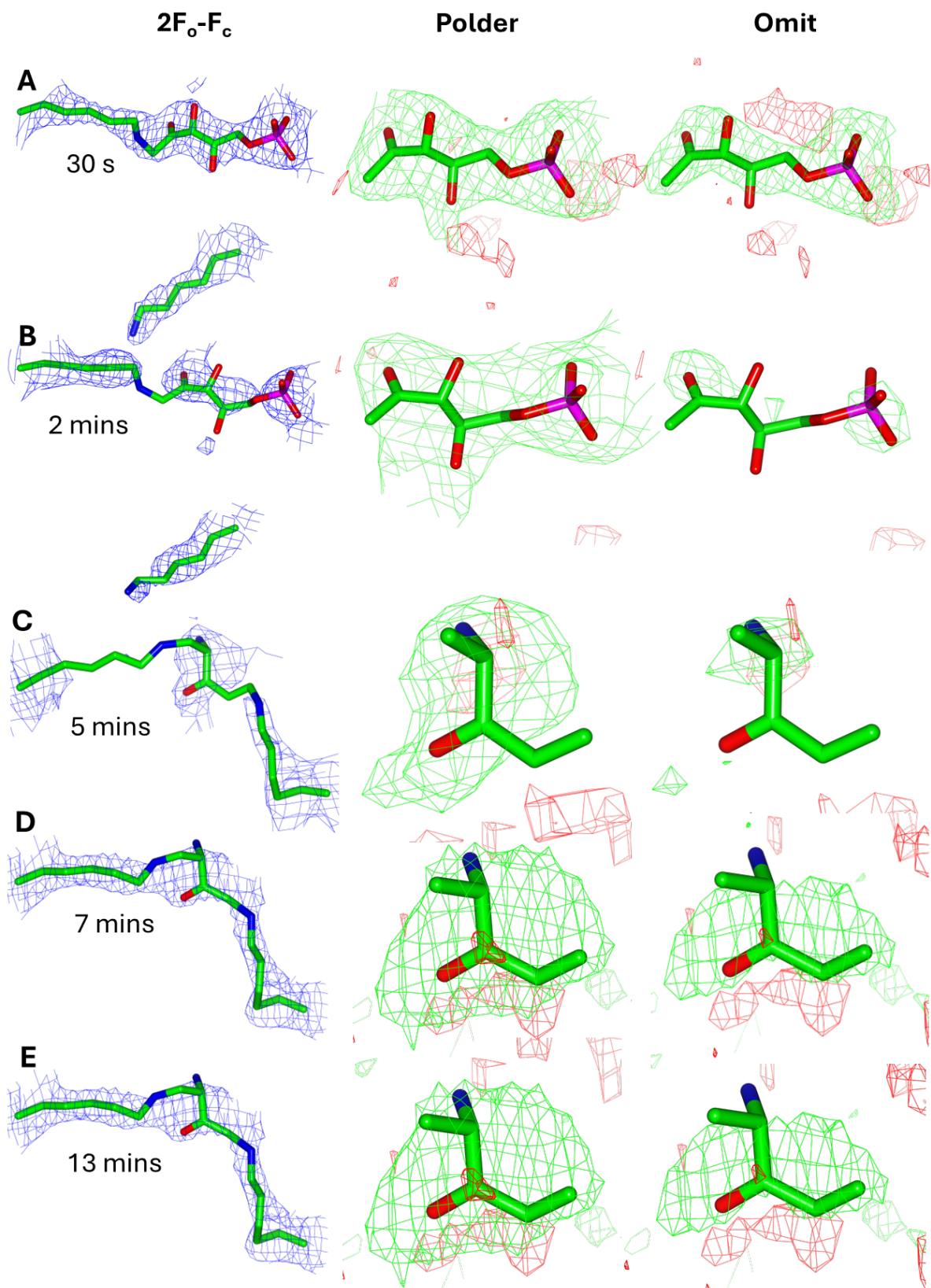


Figure 41. Time-resolved structural snapshots of I320 formation in AtPdx1.3 crystals. (A-E) corresponding to soaking timepoints of 30 seconds, 2 minutes, 5 minutes, 7 minutes, and 13 minutes, respectively. For each timepoint, the $2F_o-F_c$ electron density map (contoured at 1.5σ), polder map (contoured at 3σ) and omit map (contoured at 3σ) are shown. Progressive changes include R5P occupancy, lysine conformational shifts, and the emergence of I320-specific density. Stick representation depicts carbon atoms as green, nitrogen atoms as blue, oxygen atoms as red and phosphate atoms as pink.

To investigate the early binding dynamics of PLP to AtPdx1.3, *in crystallo* UV-Vis absorption spectra were collected at 0, 3, 6, 9, 12, 22, and 83 seconds post-incubation using the offline *in crystallo* optical spectroscopy (icOS) setup at ESRF. Despite baseline correction and smoothing, the resulting spectra did not reveal distinct features attributable to PLP binding within the crystal lattice (Figure 42). In solution, PLP typically exhibits a broad absorbance peak around 380 nm, while PLP covalently bound within a protein crystal often shifts to approximately 414 nm due to change in its electronic environment. However, in this experiment, the expected spectral signature at 414 nm was not clearly resolved. Instead the spectra appeared notably bumpy and irregular, complicating interpretation and obscuring any subtle shifts that might indicate PLP binding.

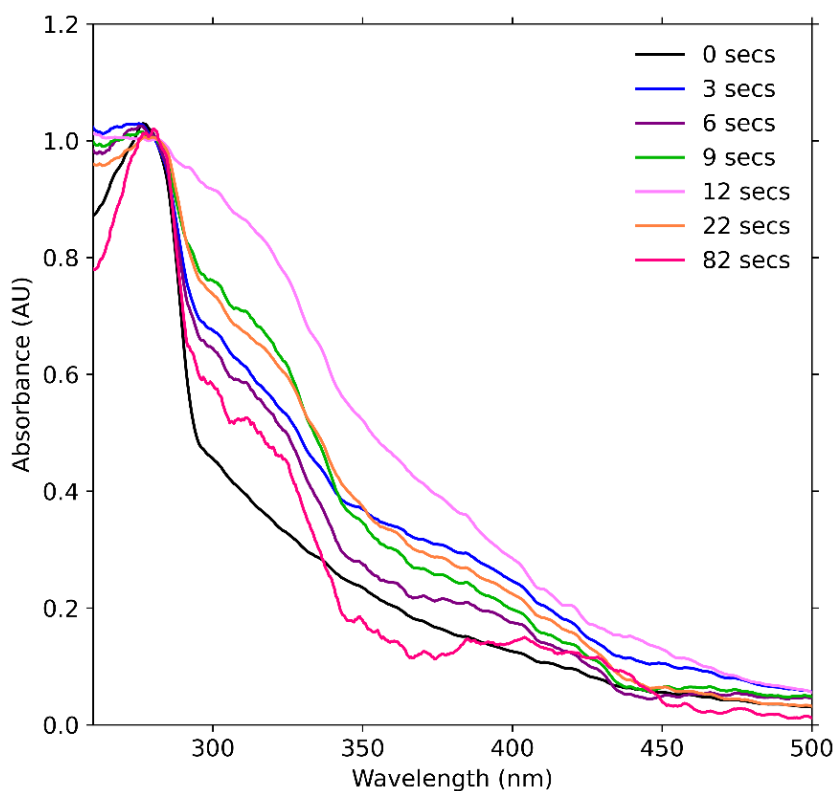


Figure 42. *In crystallo* UV-Vis absorption spectra of AtPdx1.3 following incubation with PLP. Crystals were soaked in PLP for varying time intervals prior to manual cryocooling and spectral acquisition. Spectra shown have been processed using constant-baseline correction and smoothing. No distinct PLP-associated spectral features were observed across timepoints.

This spectral roughness likely stems from a combination of experimental and physical constraints. Light scattering from crystal imperfections and mounting geometry introduces baseline instability while the crystal size and short optical path length may limit absorbance intensity, resulting in a low signal-to-noise ratio. Excess PLP in the surrounding buffer may contribute to strong absorbance at \sim 380 nm, overwhelming any expected crystal-specific features. In addition, rapid binding kinetics of PLP may mean that even early timepoints captured reflect a mixture of bound and unbound states, obscuring transient intermediates.

Given the limited spectral resolution and interpretability of the *in crystallo* UV-Vis data, I proceeded to investigate PLP binding using diffraction data. A cryo-trapping approach was employed again, where crystals were incubated with PLP for defined durations, then rapidly cryocooled to halt the reaction at specific timepoints. Clear $2F_o - F_c$ electron density maps corresponding to the PLP ligand were observed at all timepoints examined: 23, 68, 90 and 150 seconds, using both polder and omit maps (**Figure 43**). The ligand was consistently positioned within the active site and covalently bound to Lysine 166, confirming successful incorporation. The omit maps became marginally better at the later timepoints of 90 and 150 seconds, suggesting progressive stabilisation of the PLP-Lys166 adduct (**Figure 43**). However, this improvement in positive density was accompanied by increasing negative difference density, particularly in the later datasets. This may reflect partial occupancy, conformational heterogeneity or merely differences in dataset resolution. Additionally, crystal sizes varied between soaks and could not be precisely controlled, potentially contributing to inconsistencies in map quality. These factors underscore the difficult in interpreting dynamic ligand incorporation within the framework of cryo-trapping, which is often assumed to yield simpler, static structural snapshots.

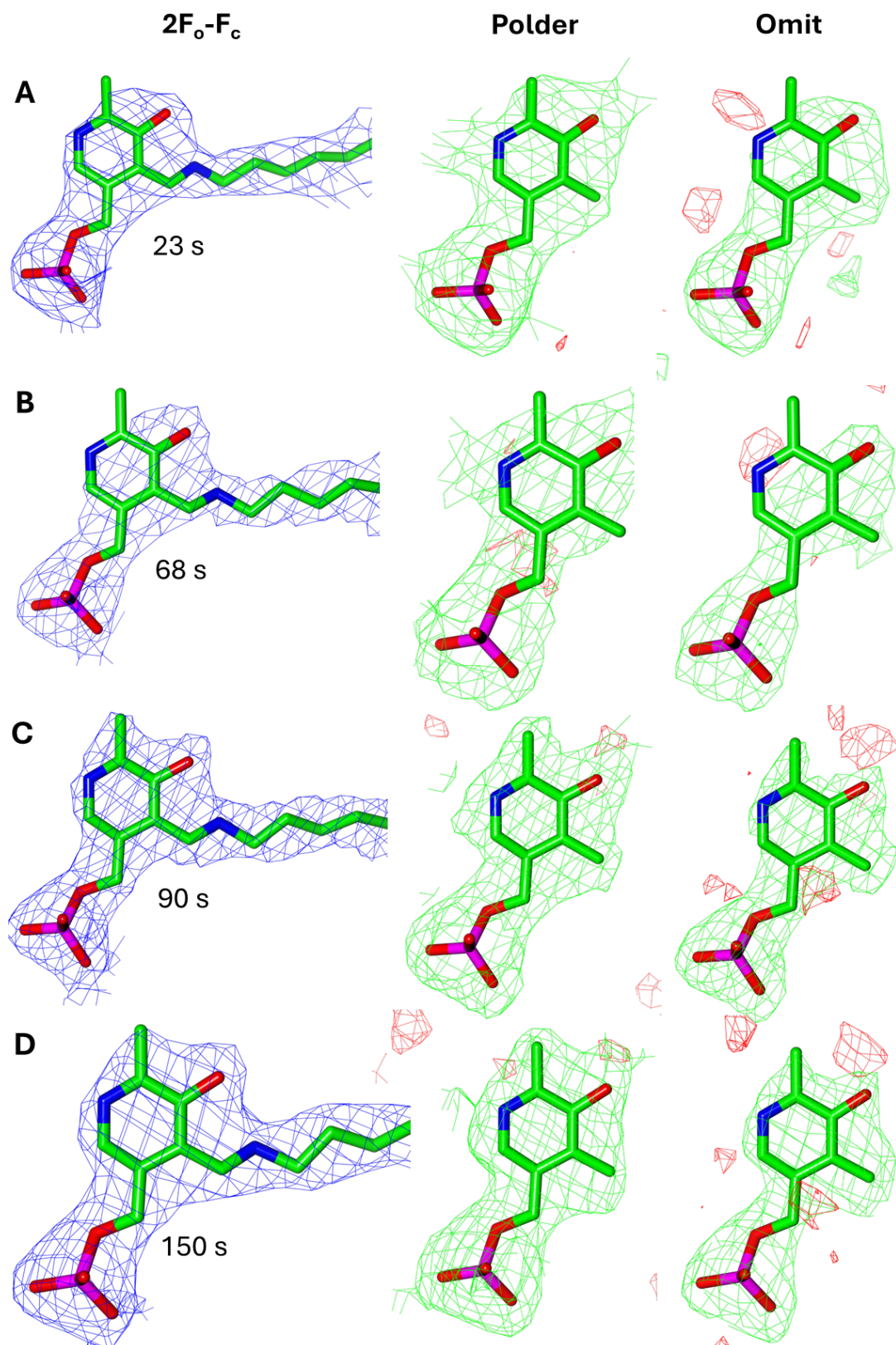


Figure 43. Time-resolved structural snapshots of PLP binding to AtPdx1.3 crystals. Electron density maps for PLP covalently bound to Lys166 are shown at four timepoints post incubation: (A) 23 seconds, (B) 68 seconds, (C) 90 seconds, (D) 150 seconds. For each timepoint the $2F_o - F_c$ maps are contoured at 1σ , omit maps and polder maps at 3σ . PLP density is consistently observed across all timepoints. Stick representation depicts carbon atoms as green, nitrogen atoms as blue, oxygen atoms as red and phosphate atoms as pink.

3.4 Discussion

The work presented in this chapter establishes a reproducible and scalable pipeline for time-resolved serial crystallography of AtPdx1.3, a PLP-dependent enzyme of considerable mechanistic interest. The primary objective was to develop a workflow capable of generating high-quality microcrystal slurries in sufficient volumes for SFX experiments, while also enabling preliminary kinetic characterisation of ligand binding events. The successful integration of protein purification, crystallisation optimisation, and spectroscopic validation lays the foundation for future time-resolved experiments at XFEL sources.

Purification workflows routinely yielded large volumes of high pure AtPdx1.3 at concentrations exceeding 10 mg/mL. This level of purity and yield was essential not only for crystallisation trials but also for downstream ligand soaking and spectroscopic assays. Notably the combination of high purity, large sample volume, and consistent crystallisation behaviour represents a transferable framework applicable to other protein systems targeted for serial crystallography. The protein's stability across multiple preparations enabled reproducible crystallisation behaviour, which proved critical for batch workflows. These findings align with previous studies identifying *Arabidopsis thaliana* Pdx1.3 as a robust and reproducible crystal system, particularly amenable to soaking experiments and capable of delivering high-resolution structures that resolve intermediate states (202,205). A key methodological differences lies in the purification strategy. While earlier protocols employed a two-step process including size-exclusion chromatography, the current workflow relied solely on nickel affinity chromatography. Despite this simplification, comparable purity was achieved with reduced processing time, allowing crystallisation trials to commence immediately post-purification, a factor shown to enhance reproducibility and critically diffraction resolution.

A key methodological advance in this work was the early transition from vapour diffusion screening to batch crystallisation, guided by the generation of a phase diagram. While phase diagram construction is not a novel concept in crystallisation optimisation, existing protocols remain heavily reliant on vapour diffusion conditions. This reliance introduces additional, often tedious, optimisation steps when transitioning to batch formats (58,261). These steps are essential for producing the large volumes of microcrystals required for serial crystallography. To address this bottleneck, a rapid, automated microbatch-under-oil protocol was developed, enabling phase diagram generation under true batch conditions using minimal sample volumes. Incorporating a microseeding strategy within this framework allowed for precise identification of the metastable zone, a critical region for reproducible nucleation. Microseeding is a broadly applicable technique across microcrystal workflows and has demonstrated success across a diverse range of protein systems (67,276). This approach yielded a detailed crystallisation

landscape and enabled direct scalability into seeded-batch conditions. Notably, the same scripting framework used for phase diagram generation was repurposed for scale-up, producing dense microcrystal slurries with size distributions suitable for SFX data collection. This modularity is particularly valuable for future workflows, where initial small-volume screening combined with SSX data collection can be followed by efficient scale-up for more complex, multidimensional experiments. By streamlining the transition from screening to production, this workflow significantly reduced the time and material costs typically associated with batch optimisation. Importantly, it offers a broadly applicable strategy for high-throughput microcrystal production. Given that large-scale microcrystal production remains a major barrier for new users to serial crystallography, this protocol lowers that threshold and supports the wider adoption of time-resolved methods.

Using the optimised workflow discussed above, the first room-temperature SFX datasets were successfully collected for apo AtPdx1.3 and three ligand-bound complexes with R5P, the I320 intermediate and PLP. These structures provide static snapshots of key catalytic states and confirm the suitability of microcrystals for high-resolution diffraction. Importantly, the ligand-bound datasets demonstrate that soaking protocols developed here are effective across a range of ligand chemistries and binding modes, despite the inherent challenges of diffusion into microcrystalline slurries. Compared to previous cryo-trapping datasets obtained from single crystals soaked for extended incubation times, the resolution cutoffs achieved in the current SFX datasets were broadly similar. The R5P-bound structure, in particular reached a higher resolution of 1.83 Å, compared to 1.91 Å reported previously (202). Resolution cutoffs appeared to correlate with the number of merged lattices, with a tipping point around 10,000 lattices, suggesting that further improvements could be achieved through increased dataset multiplicity. A key distinction from prior cryo-trapping studies lies in the ligand incubation strategy. To overcome the lower signal-to-noise ratio inherent to microcrystal soaking, ligand concentrations were substantially increased, up to fivefold in some cases. This adjustment proved critical for achieving sufficient occupancy and enabling structural resolution of bound states. Given the large unit cell and persistent indexing ambiguity in the *H3* space group of AtPdx1.3, future studies should be conducted at XFEL sources. Emphasis should be placed on collecting high-multiplicity datasets to maximise resolution, which will be essential for time-resolved experiments where subtle changes in electron density and difference maps must be confidently interpreted. Unlike static soaked structures, time-resolved datasets often reveal transient or low-occupancy states, requiring both high data quality and rigorous statistical validation (277,278).

To establish preliminary timescales for future time-resolved experiments, an integrated *in crystallo* UV-Vis spectroscopy and cryo-trapping strategy was employed. This dual approach

enabled real-time monitoring of ligand binding and subsequent structural validation via X-ray diffraction. Such integration builds on foundational work in kinetic crystallography, where catalytically active protein crystals allow turnover to be induced and intermediate states captured through cryo-trapping methods (279,280). In this work UV-Vis spectra indicated formation of the I320 intermediate within 5 minutes, while diffraction data confirmed complete occupancy after 7 minutes. This discrepancy likely reflects a lag between initial chromophore formation and full incorporation across the crystal lattice, possibly due to heterogeneity in soaking efficiency or crystal packing constraints. Notably, previous cryo-trapping studies required incubation times of up to four days to stabilise the I320 intermediate (202). In contrast, the current workflow demonstrates that high-occupancy datasets can be achieved within minutes, validated by both omit and polder maps. This represents a significant acceleration in intermediate capture and highlights the utility of combining spectroscopic and crystallographic modalities to define actionable timescales for future XFEL-based time-resolved experiments.

In contrast to the I320 intermediate, PLP binding was not detected via *in crystallo* UV-Vis spectroscopy, despite its presence being confirmed by diffraction data at all timepoints between 23 to 150 seconds. This absence of spectroscopic signal was unexpected, as previous studies captured the covalent bound PLP state, characterised by an absorption maxima at 414 nm (202). Free PLP in solution typically exhibits a distinct absorption maxima at 388 nm. In this study, it was hypothesised that the dominant signal from unbound PLP in the surrounding solution to the crystal may have masked the covalent PLP signature. However, the expected 388 nm peak was not directly observed, making it difficult to confirm this explanation. These findings underscore the utility and limitations of *in crystallo* UV-Vis spectroscopy for monitoring ligand binding. While effective for chromophoric intermediates like I320, its sensitivity to PLP was insufficient under conditions tested. This highlights the importance of complementary structural validation, particularly when dealing with ligands that exhibit subtle or overlapping spectral features.

Nonetheless, the cryo-trapping strategy proved robust for capturing discrete timepoints, and this combined approach offers a valuable framework for refining time-resolved protocols. While this method enables preliminary mapping of reaction timescales, the ideal experiment would involve simultaneous collection of UV-Vis spectra and diffraction data at room temperature. Such conditions would likely reveal even faster timepoints, given the known kinetic discrepancies between cryogenic and room temperature environments. A further source of variability in the current work was crystal size, which many have influenced incubation times due to differential diffusion rates. For optimal reproducibility, each timepoint should ideally be collected from crystals of similar size, preferably matched in all three dimensions. Achieving this introduces engineering challenges, including uniform reaction initiation and precise ligand

delivery. However, these are increasingly tractable with existing droplet ejection technologies already integrated in the serial crystallography toolkit. Notable examples include the SPITROBOT platform, which enables rapid cryo-trapping with delay times as short as 23 ms (281,282) and the millisecond mix-and-quench crystallography (MMQX) instrumentation, capable of sub-10 ms time delays (283,284). Both systems are compatible with microcrystals mounted in standard mesh loops, offering scalable solutions for dynamic structural studies. However, while smaller crystals are advantageous for future serial applications, they pose limitations for *in crystallo* UV-Vis spectroscopy. Adequate signal-to-noise ratios require larger crystals along with optimised experimental setups in order to mitigate optical artifacts such as Rayleigh scattering, reflection and refraction (285). Crystal size must therefore be carefully optimised to balance absorbance peak resolution with saturation avoidance, ensuring reliable spectral interpretation.

To guide future time-resolved experiments, a preliminary set of ligand-specific timepoints is proposed based on observed structural occupancy and known binding kinetics. Although R5P was not directly monitored spectroscopically, its consistent persistence in datasets after 15 minutes, alongside prior reports of rapid sugar binding, suggests a binding window spanning seconds to a few minutes. In contrast, the I320 intermediate emerged spectroscopically around 5 minutes and was structurally confirmed at 30 minutes via XFEL data collection, supporting a capture window of approximately 5 – 10 minutes. PLP binding was structurally evident at all timepoints from 23 to 150 seconds, indicating a binding event likely faster than 30 seconds. Accordingly, sub-minute sampling should be prioritised for PLP and R5P, while a broader 5 – 10 minute window is appropriate for capturing I320 formation. This tiered strategy offers a rational framework for capturing transient states with maximal temporal resolution and directly supports the long-term goal of establishing reproducible workflows capable of resolving short-lived biochemical events *in crystallo*.

Chapter 4 Droplet microfluidics for crystal size engineering

When performing serial crystallography experiments and in particular time-resolved experiments, control of crystal size and uniformity is critical. Crystal dimensions must be carefully matched to the X-ray beam size at the synchrotron or XFEL source, in order to minimise background scattering and maximise the volume of diffracting material, thereby improving the signal-to-noise ratio (286). In time-resolved studies, small crystals are especially advantageous: they enable rapid ligand diffusion into the lattice for efficient reaction triggering via mixing (181), and ensure full penetration of excitation light for photochemical initiation. Uniformity in crystal size not only facilitates synchronised reaction initiation but also prevents clogging in sample delivery systems caused by the presence of larger crystals. Thus the ability to engineer the size and uniformity of microcrystal slurries is critical for robust sample delivery and uniform reaction initiation.

A persistent challenge in the field is scaling up from initial hits, often obtained via sparse-matrix vapour diffusion screens, into batch crystallisation methods capable of producing the large volumes required for serial and time-resolved experiments (58,275). In this context, microfluidics has emerged as a powerful tool for controlling crystallisation environments with high precision. Droplet-based microfluidics in particular offers exceptional control over reagent mixing and protein concentration, enabling the generation of highly monodisperse droplets that promote crystal uniformity.

The following chapter explores the use of droplet microfluidics, specifically droplet miniaturisation as a strategy to regulate crystal size and uniformity across a range of standard and non-standard protein systems. For systems with inherently low nucleation rates, a microseeding strategy was employed to enhance nucleation density at small scales. Crystals grown in droplets were benchmarked against conventional batch-grown crystals and evaluated for diffraction power using serial synchrotron crystallography (SSX). Finally, key factors influencing crystallisation in microfluidic droplets are discussed, with a view towards extending this approach to diverse protein targets in future studies.

Some of the results presented in this chapter have been published in the following article: Stubbs, J., Hornsey, T., Hanrahan, N., Esteban, L.B., Bolton, R., Malý, M., Basu, S., Orlans, J., De Sanctis, D., Shim, J., Shaw Stewart, P.D., Orville, A.M., Tews, I., West, J., 2024. Droplet microfluidics for time-resolved serial crystallography. *IUCrJ* 11, 237–248. The publication is included within the Appendix for reference.

4.1 Crystal size control by droplet miniaturisation

4.1.1 Lysozyme

To investigate the influence of droplet confinement on crystallisation dynamics, PDMS microfluidic devices were fabricated with integrated flow-focusing junctions designed for high-throughput droplet generation. Each device incorporated three inlets for protein, precipitant and fluorinated oil, facilitating controlled encapsulation within discrete droplets (**Figure 44A**).

By systematically varying the droplet junction dimensions (width and height) and adjusting the flow rates of the input streams (see **Table 4** in Chapter 2), droplet formation in the dripping regime at kilohertz frequencies was achieved (**Figure 44A**). Monodisperse droplets ranging from 194 to 0.89 pL (\varnothing 71.8 – 11.9 μ m) were produced, exhibiting a coefficient of variation (CV) \leq 4% (**Figure 44B**). The flow rate ratio of continuous phase (fluorinated oil) to dispersed phase (protein/precipitant) was maintained at either 3:1 or 4:1 across all devices, ensuring sufficient shear force for consistent droplet breakup and subsequent encapsulation. As expected, higher flow rate ratios yielded smaller droplets due to the increased shear stress at the flow-focusing junction. This experimental setup enabled precise control of droplet volume and uniformity, providing a tuneable platform for probing crystallisation conditions from a variety of protein systems.

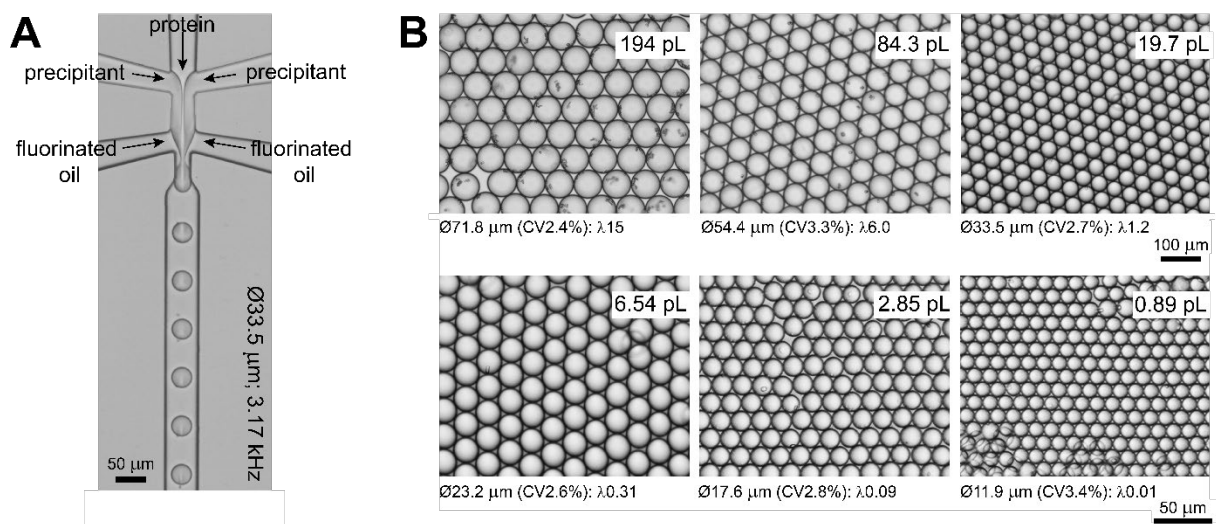


Figure 44. Droplet miniaturisation for lysozyme crystallisation. (A) Picolitre-sized droplets for protein crystallisation generated at kilohertz frequencies using a flow-focusing microfluidic device operating in the dripping regime. Three input streams, protein solution, precipitant solution, and fluorinated oil were combined to produce confined crystallisation environments. (B) Monodisperse droplets (CV \leq 4%) were achieved by tuning the droplet junction dimensions (width and height) and adjusting the flow rates of the input streams.

To evaluate droplet confinement under crystallisation conditions, lysozyme was selected as a model protein due to its well characterised and exceptionally fast nucleation behaviour (287). Under batch conditions, mixing 1 part of 20 mg/mL lysozyme in 20 mM sodium acetate (pH 4.5) with 4 parts precipitant solution containing 6% (w/v) PEG 6000, 3.4 M NaCl, 1 M sodium acetate (pH 3.0) resulted in rapid nucleation. The nucleation rate exceeded the temporal resolution of the setup, occurring within the dead time of mixing. Crystal growth ceased after 15 minutes post mixing (**Figure 45**), yielding a resulting crystal density of 8×10^7 crystals/mL (80 crystals/nL). This rapid crystallisation introduced negative feedback, likely due to the local depletion of supersaturation or spatial crowding, which suppressed further nucleation events from taking place. Interestingly this self-limiting behaviour promoted crystal uniformity, producing crystals with an average size of 8 μm and a CV of 18.9% (**Figure 46A**, blue).

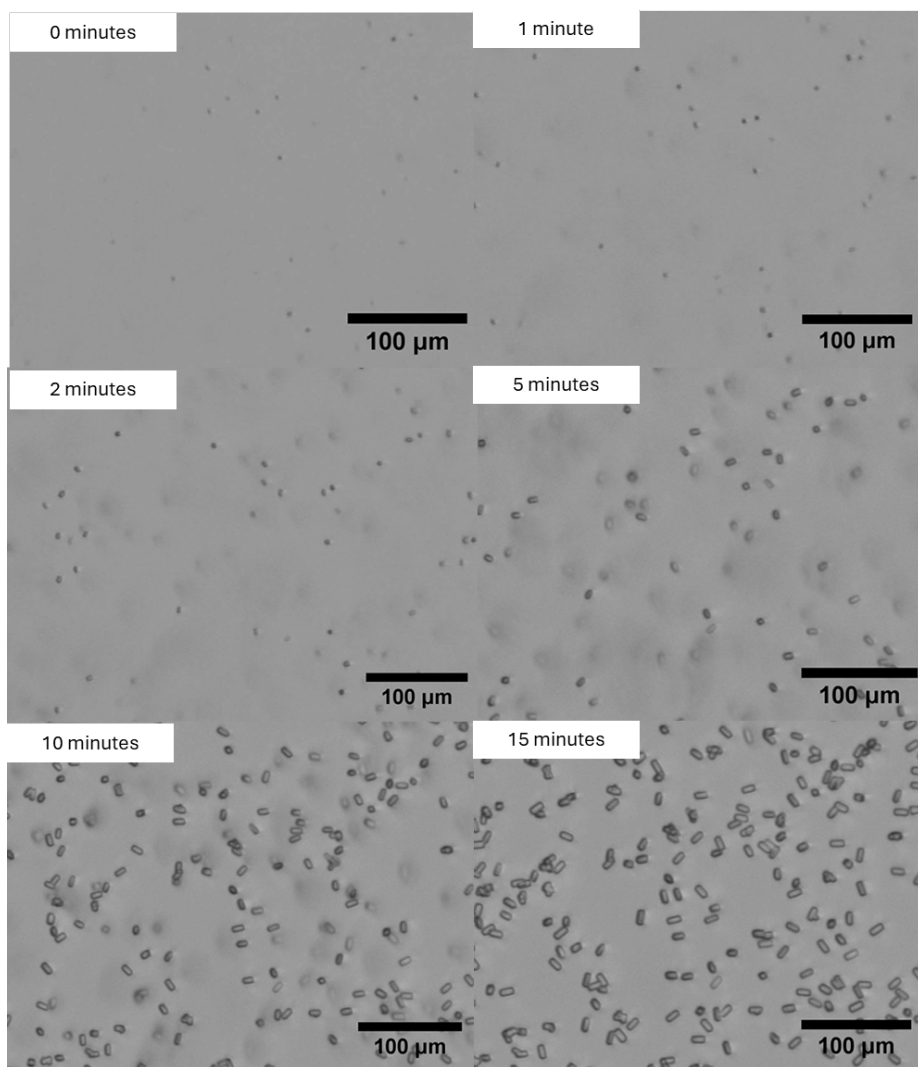


Figure 45. Rapid growth of lysozyme microcrystals under batch conditions. Time-lapse images show lysozyme microcrystal formation at intervals from 0 to 15 minutes. The 0-minute timepoint corresponds to the rapid mixing of 20 mg/mL lysozyme in 20 mM sodium acetate (pH 4.5) with precipitant solution containing 6% (w/v) PEG 6000, 3.4 M NaCl, and 1 M sodium acetate (pH 3.0). Crystal growth ceases by 15 minutes, due to negative feedback mechanisms triggered by rapid nucleation and growth.

Using batch-grown crystals as a benchmark, the effects of volume scaling by droplet confinement were investigated. Monodisperse crystallisation droplets ($CV \leq 4\%$) ranging from 194 to 0.89 pL produced lysozyme crystals ranging from 20 to 2 μm in size (**Figure 46A**, salmon and **Figure 44B**). As droplet volume decreased, crystal size was progressively reduced, and the mean occupancy (λ) dropped below 0.01, with occupied droplets containing only a single crystal. This single occupancy promoted crystal uniformity, yielding a crystal size CV of 14.8% in the smallest droplets (0.89 pL). In contrast, multiple nucleation events in larger droplets increased the mean occupancy (λ) and led to broader size distributions. Specifically, droplets of 194 pL contained an average of 15 crystals ($\lambda15$), whereas the smallest droplets (0.89 pL) were stochastically loaded with just 0.01 crystals per droplet ($\lambda0.01$). The combination of single occupancy and precise volume control enabled crystal miniaturisation, with $\sim 3 \mu\text{m}$ lysozyme crystals growing in the smallest droplets (0.89 pL) (**Figure 46B**, bottom).

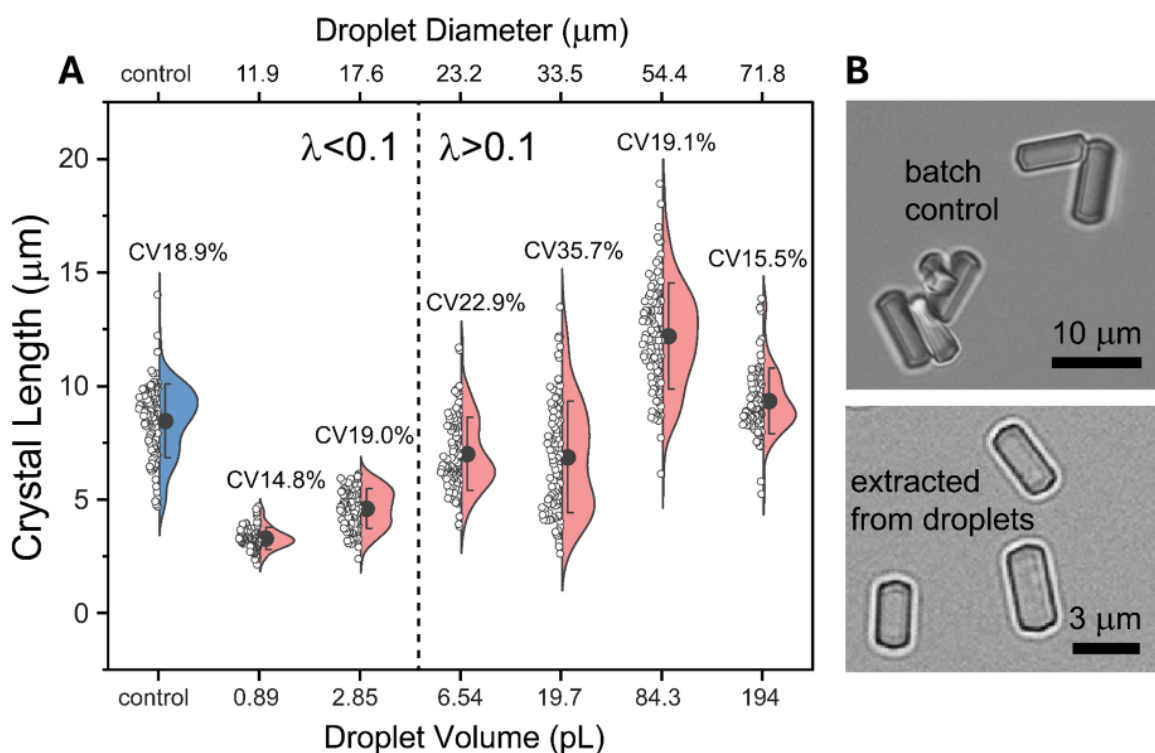


Figure 46. Control of lysozyme crystal size through droplet volume scaling. (A) Lysozyme crystals grown under batch conditions (control, blue) exhibit an average size of 8 μm . In contrast, crystal size correlates with droplet volume in microfluidic environments (droplet, salmon), with the smallest crystals ($\sim 3 \mu\text{m}$) observed in 0.89 pL droplets. Central black dots represent average crystal size, whilst error bars denote ± 1 standard deviation. (B) Representative microscope images comparing lysozyme crystals formed under batch conditions (control) and those extracted from droplets following emulsion disruption (“breaking the emulsion”; see **Figure 23**).

By limiting droplet volume, crystal size can be reduced and single-crystal occupancy achieved, resulting in high uniformity. However, this approach comes at the cost of nucleation density. Compared to batch conditions and larger droplets (194 pL), droplet miniaturisation leads to substantial losses in crystal yield, with crystal density falling from ~80 to ~7 crystals/nL in the smallest droplets (0.89 pL) (**Figure 47A**, grey line). This reduction is likely driven by the increased surface area-to-volume ratio, where the droplet-surfactant interface may inhibit nucleation and subsequent crystal growth (**Figure 47A**, green line). Despite this inefficiency, throughput can be recovered by increasing droplet generation frequency. A 20-fold increase was observed, rising from 1 kHz for 194 pL droplets to 23.5 kHz for 0.89 pL droplets (**Figure 47B**). Thus, a balance must be struck between desired crystal size and uniformity versus overall crystal yield. Importantly, droplets can be incubated off-chip, enabling mass production of microcrystals that would be impractical to generate through on-chip crystallisation alone.

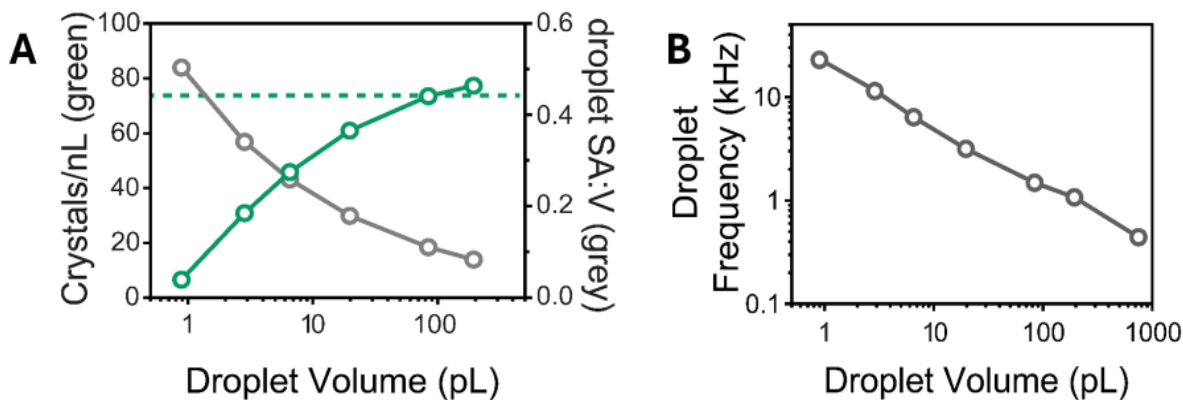


Figure 47. Trade-offs associated with droplet volume miniaturisation. (A) Droplet miniaturisation leads to a reduction in crystal density (green), which correlates with an increase in the droplet surface area-to-volume (SA:V) ratio (grey) in the droplet. The crystal density achieved under batch conditions is indicated by the green dashed line, allowing for direct comparison. (B) Decreasing droplet volume results in a substantial gain in droplet generation frequency, with a 20-fold increase observed between 194 pL and 0.89 pL droplets.

4.1.2 Thaumatin

To investigate the impact of droplet confinement across distinct crystallisation regimes, an alternative protein system was selected. Lysozyme, previously crystallised in a PEG-based system, exhibited rapid nucleation, readily forming crystals under batch and droplet conditions. In contrast, thaumatin, a disulfide-rich protein with a markedly lower nucleation rate was chosen to assess confinement effects in a salt-based system, where nucleation is more challenging and crystal uniformity more difficult to achieve.

A 1:1 mixture of 50 mg/mL thaumatin and 40% (w/v) sodium potassium tartrate, 0.1 M bis-Tris propane pH 6.5 produced bipyramidal crystals overnight under batch conditions, with an

average size of 14 μm (**Figure 48A**). When confined to monodisperse 87 pL droplets ($\varnothing 55 \mu\text{m}$, CV 3.6%), thaumatin crystals grew larger, averaging 24.8 μm in size (**Figure 48B**). Further confinement into reduced volumes may indicate the potential to achieve crystal sizes comparable to those obtained under batch conditions. More strikingly, the crystal size distribution narrowed substantially, with the crystal size CV reduced from 39.3% to 12.0%, indicating enhanced uniformity (**Figure 48C**). Despite this improvement, a bimodal size distribution persisted in the droplet-grown sample, potentially reflecting secondary nucleation events within the confined environment (**Figure 48C**). While this may be linked to variation in droplet diameters, droplet size was not directly measured or correlated with crystal dimensions in this study. Thaumatin crystallisation appears to be sensitive to droplet size, but this interpretation remains speculative and is based on qualitative observations. Minor fluctuations in droplet volume could plausibly promote bimodal distributions, whereas tighter control over droplet size might suppress such effects. Further experiments would be required to confirm this relationship.

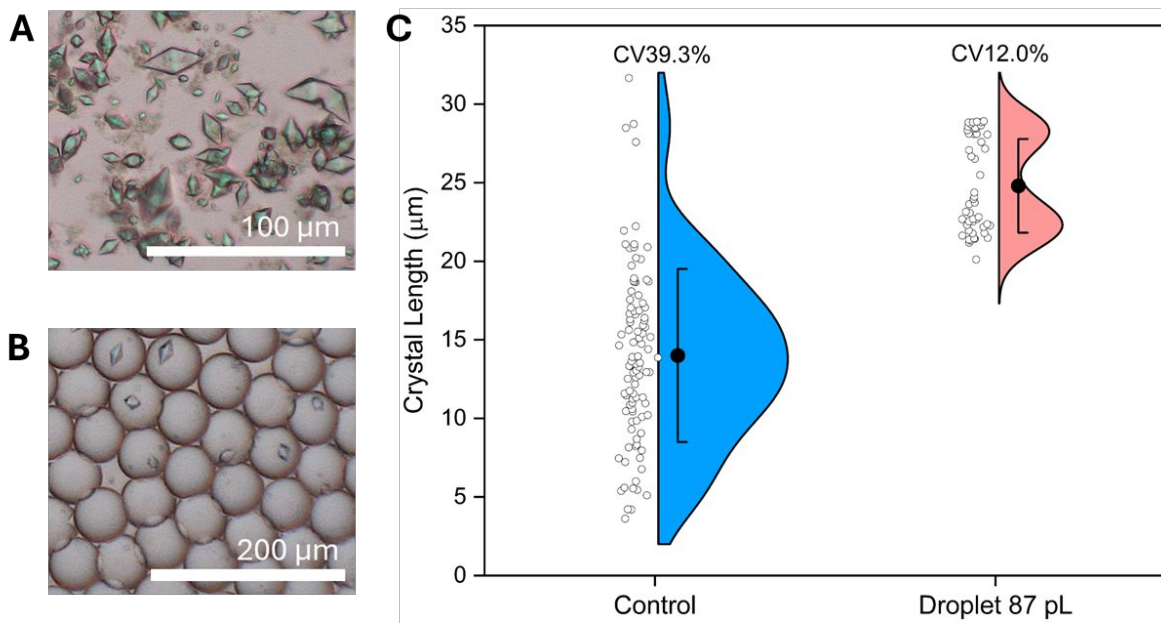


Figure 48. Droplet confinement enhances crystal size uniformity in thaumatin. (A) Bipyramidal thaumatin crystals formed under batch conditions by mixing 50 mg/mL thaumatin in a 1:1 ratio with precipitant solution containing 40% (w/v) sodium potassium tartrate, 0.1 M bis-Tris propane (pH 6.5). (B) Bipyramidal thaumatin crystals grown in monodisperse 87 pL droplets ($\varnothing 55 \mu\text{m}$, CV 3.6%) following off-chip incubation. (C) Comparison of crystal size distributions, batch-grown crystals (blue) exhibit an average crystal size of 14 μm , while droplet-grown crystals (salmon) average 24.8 μm . Central black dots represent average crystal size, whilst error bars denote ± 1 standard deviation.

4.2 Microseeding strategies to overcome low nucleation rates at small scales

4.2.1 AtPdx1.3

Having established droplet crystallisation protocols using well-behaved model proteins such as lysozyme and thaumatin, attention was next directed towards proteins exhibiting more typical and challenging crystallisation behaviour. AtPdx1.3, a representative example, demonstrated significantly lower nucleation rates under droplet conditions, with initial trials yielding negligible crystal formation. This underscored the difficulty of achieving spontaneous nucleation in confined volumes and highlighted the need for strategies to overcome this barrier. To address this, a microseeding approach was employed, using previously grown crystals which were mechanically fragmented to generate seeds that act as nucleation sites, facilitating crystal growth. The goal of introducing seeds was to enhance crystal density while promoting synchronised nucleation to improve size uniformity.

Under seeded-batch conditions, AtPdx1.3 crystals formed with an average size of $\sim 11 \mu\text{m}$ and a crystal density of 10^7 crystals/mL (**Figure 49**). A ten-fold dilution of the seed stock with precipitant solution produced larger crystals ($\sim 18 \mu\text{m}$), attributed to increased protein availability per crystals, and was accompanied by the expected reduction in crystal density (**Figure 49**). Further dilution by a hundred-fold yielded even larger $\sim 30 \mu\text{m}$ crystals (**Figure 49**). In theory, microseeding should promote crystal uniformity by synchronising nucleation and ensuring consistent protein supply during growth. However, AtPdx1.3 crystals under seeded-batch conditions exhibited notable size variability, with a consistent CV of $\sim 25\%$ across the dilution series.

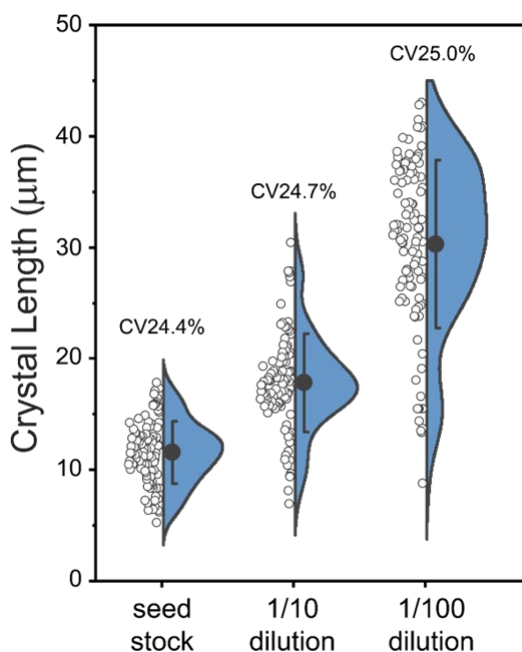


Figure 49. Effect of seed stock dilution on seeded-batch crystallisation of AtPdx1.3. Seeded-batch crystallisation of AtPdx1.3 was performed using a 1:1:1 mixture of protein (~12 mg/mL), precipitant (600 mM sodium citrate, 100 mM HEPES (pH 7.0)) and seed stock (10^5 – 10^7 crystals/mL). Successive dilution of the seed stock resulted in increased crystal size, attributed to greater protein availability per crystal. Despite changes in size, the CV remained consistent across the dilution series. Central black dots represent average crystal size, whilst error bars denote ± 1 standard deviation.

Building on the successful seeded-batch conditions established for AtPdx1.3, microseeding was next applied to droplet-based crystallisation to enhance control over crystal size and uniformity. Using a seed stock at a concentration of 10^7 crystals/mL, single-crystal occupancy was achieved across a 200-fold range of droplet volumes (1.1 – 219 pL), with consistent crystal size uniformity (Figure 50A). As droplet volume decreased, crystal size scaled accordingly from ~20 μm in the largest 219 pL droplets to ~2 μm in the smallest 1.1 pL droplets. Compared to batch conditions (Figure 50A, blue), droplet-based crystallisation markedly improved size uniformity, reducing the coefficient of variation (CV) from 24.4% to as low as 7.4% at a droplet volume of 3.9 pL. Notably, crystal size scaled linearly with droplet diameter (Figure 50A, inset), indicating precise volumetric control over crystal growth.

These results demonstrate that droplet volume not only dictates final crystal size but also plays a critical role in maintaining uniformity (Figure 50B). However, consistent with observations from lysozyme crystallisation, crystal occupancy and thus crystal density declined with decreasing droplet volume, likely due to reduced nucleation probability (Figure 50B). At the lowest tested droplet volume of 1.1 pL, crystal size CV increased again, reflecting a loss of uniformity driven by stochastic nucleation events and reduced crystallisation likelihood.

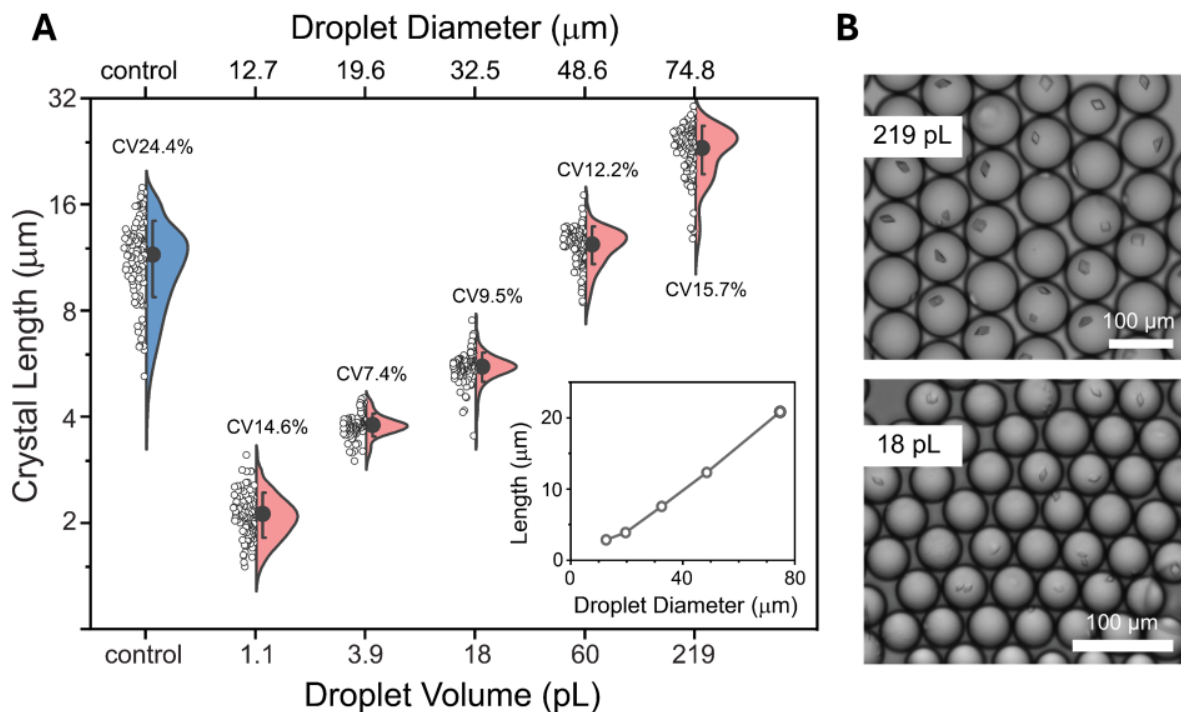


Figure 50. Droplet volume scaling enables crystal size uniformity in AtPdx1.3 crystallisation. (A) Across a 200-fold range of droplet volumes, AtPdx1.3 crystal size is precisely controlled from ~20 to ~2 μm (salmon). Crystal size scales proportionally with droplet diameter, as shown in the inset. Central black dots represent average crystal size, whilst error bars denote ± 1 standard deviation. (B) Droplet-based crystallisation was performed using a 2:1 volume ratio of seed suspension (10^7 crystals mL $^{-1}$) in precipitant solution. Single-crystal occupancy was consistently achieved at droplet volumes of 219 pL ($\varnothing 74.8$ μm) and 18 pL ($\varnothing 32.5$ μm), demonstrating robust control over nucleation and growth.

4.2.2 Chlorite dismutase

Having demonstrated that microseeding combined with droplet volume scaling enables precise control over crystal size and uniformity in AtPdx1.3, the workflow was next applied to chlorite dismutase, a second non-standard protein system. Chlorite dismutase is a haem-containing oxidoreductase that efficiently converts chlorite into chloride and molecular oxygen (266,288). Although the molecular mechanism responsible for covalent oxygen-oxygen bond formation remains under debate, the enzyme is known to be essential in microbial systems for the detoxification of chlorite, a harmful reactive intermediate that can induce oxidative damage within cells (266,288).

Purified chlorite dismutase and corresponding seed stock were kindly provided by Dr. Jos Kamps, whose prior work had established reliable seeded-batch conditions for production of microcrystal slurries. However, the preparations consistently yielded heterogeneous slurries, with distinct larger crystals appearing alongside smaller ones. This heterogeneity posed a significant challenge for time-resolved experiments, where consistent crystal size is essential to ensure homogeneous mixing with ligand and compatibility with sample delivery systems. To

address this, droplet-based crystallisation was employed with the specific aim of eliminating oversized crystals and generating more uniform microcrystal slurries, thereby enhancing reproducibility and experimental control.

Seeded-batch crystallisation of chlorite dismutase was performed using a 2:3:1 mixture of 22 mg/mL purified chlorite dismutase in 10 mM HEPES (pH 7.0), precipitant solution containing 15% (w/v) PEG 3350, 40 mM MgSO₄, 50 mM Tris (pH 6.5), and neat seed stock at a density of 10⁷ crystals/mL. This mixture reproducibly yielded two-dimensional plate-like microcrystals overnight, with an average size of ~14 µm and a characteristic red colouration arising from the haem prosthetic group integral to the enzyme's catalytic function (**Figure 51A**). Crystal size was modulated by diluting the seed stock with precipitant solution, demonstrating the expected inverse relationship between seed concentration and crystal growth. However, even across the dilution series, a non-uniform distribution of crystal sizes persisted. A 10-fold dilution produced crystals averaging ~70 µm (**Figure 51B**), while a 20-fold dilution resulted in slightly larger ~85 µm crystals (**Figure 51C**). Further dilution to 50-fold resulted in the formation of crystals up to ~150 µm in size (**Figure 51D**), accompanied by a noticeable reduction in crystal density. These observations underscore the limitations of seeded-batch conditions in achieving consistently uniform microcrystal populations, particularly when precise control over size and density is required for downstream applications.

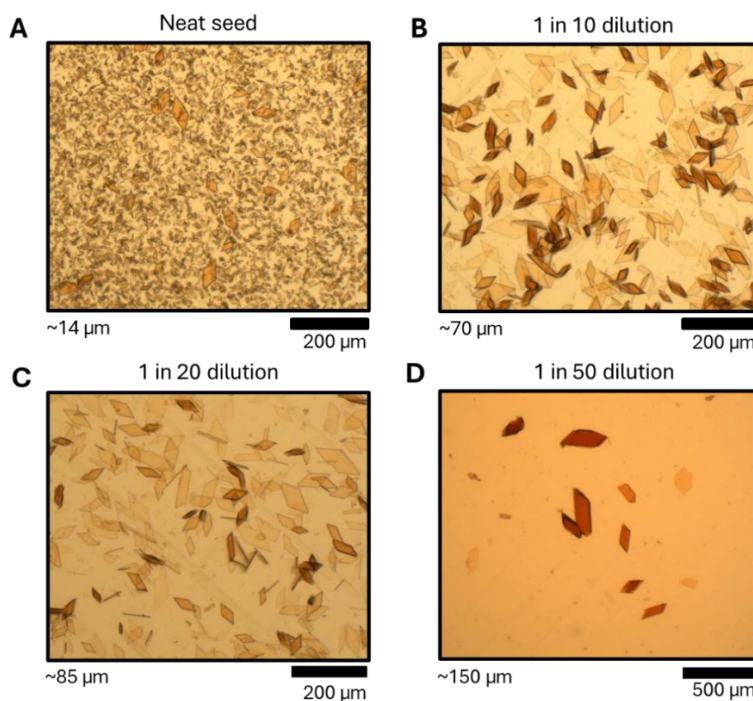


Figure 51. Effect of seed stock dilution on seeded-batch crystallisation of chlorite dismutase. Progressive dilution of the seed stock from neat (A), through 1 in 10 (B), 1 in 20 (C), and up to 1 in 50 (D), led to a marked increase in crystal size from approximately 14 µm to 150 µm, accompanied by a noticeable decline in crystal density. The characteristic red/brown colouration of the crystals originates from the haem prosthetic group, an essential cofactor in the enzyme's catalytic function.

Following initial optimisation under seeded-batch conditions and variations in seed stock dilutions, attention shifted towards implementing these refined seeding protocols in droplet-based crystallisation of chlorite dismutase. Early experiments revealed a recurring technical challenge: clogging of the internal filters within the microfluidic device due to the presence of dense or aggregated seed stock. This obstruction disrupted flow stability and impeded droplet formation, leading to poor reproducibility and compromised droplet uniformity (**Figure 52A**). Upon removing the seed stock from the same experimental setup, droplet flows stabilised, resulting in the generation of monodisperse 65 μm droplets (**Figure 52B**), although at the expense of observable crystal growth.

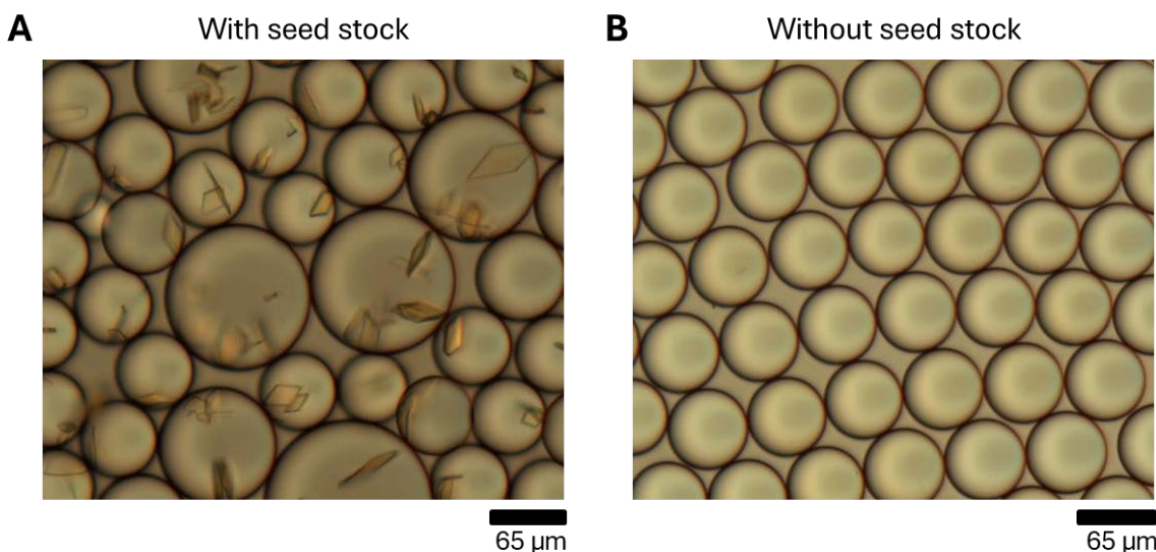


Figure 52. Influence of chlorite dismutase seed stock on droplet flow stability. (A) The presence of dense or aggregated seed stock leads to clogging of filters within the microfluidic device, resulting in disrupted flow dynamics and the production of non-uniform droplet sizes. (B) Removal of the seed stock restores flow stability, enabling the formation of consistently monodisperse droplets ($\varnothing 65 \mu\text{m}$) but at the expense of crystal growth.

To address the issue of clogging internal filters within the microfluidic device due to the presence of larger crystals (**Figure 53A**), the seed stock was prefiltered through CellTrics mesh filters (10 μm) prior to introduction into the microfluidic device. Under seeded-batch conditions, this approach proved effective in eliminating larger, undesirable crystals, thereby refining the seeding population (**Figure 53B**). Importantly, this filtration step not only preserved the reproducibility of crystallisation outcomes but also removed outliers that may disrupt crystal size distributions.

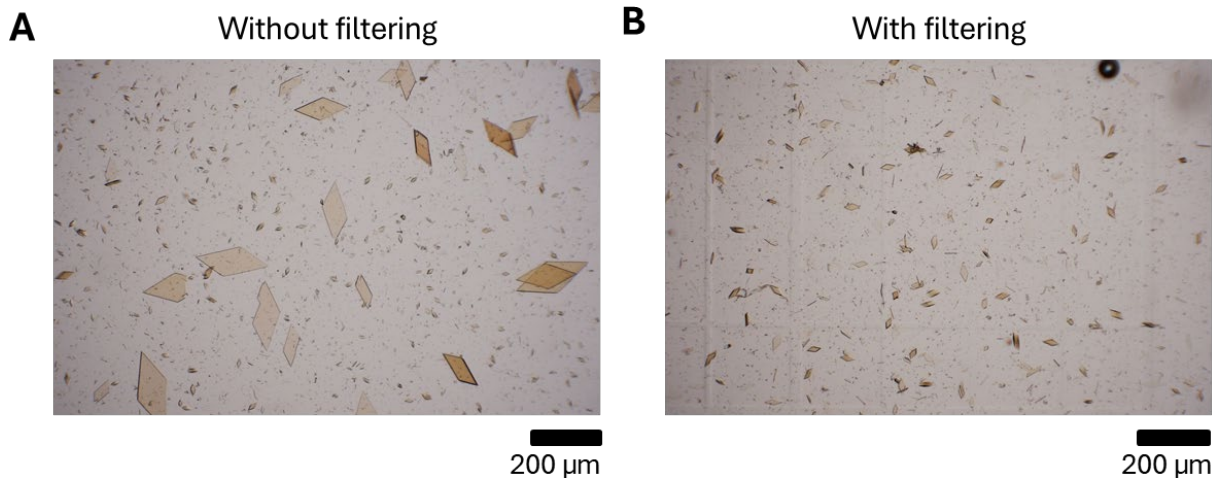


Figure 53. Effect of seed stock filtering on crystal size distribution in chlorite dismutase crystallisation under seeded-batch conditions. (A) Representative image of crystals generated from unfiltered seed stock, showing a heterogeneous population within numerous oversized crystals. (B) Representative image following CellTrics mesh filtration of seed stock, demonstrating effective removal of larger, undesirable crystal while preserving the smaller ones essential for consistent seeding.

Despite the success in filtration in seeded-batch conditions, where the removal of oversized crystals from the microcrystal slurry enhanced population uniformity, droplet experiments were further employed to investigate whether crystal size could be actively engineered in confined environments. Building on the insights gained, the same CellTrics mesh filtration strategy was applied to precondition the seed stocks prior to droplet encapsulation. The aim was to assess whether enriching for smaller seed crystals would improve crystal uniformity within droplets and yield sizes consistent with those obtained in seeded-batch conditions. Larger seed crystals are not necessarily incapable of nucleation, but they may be less effective at initiating new nucleation events in confined droplet environments, where spatial constraints and surface area considerations favour smaller seeds.

Droplet-based crystallisation of chlorite dismutase was performed using a consistent droplet volume across all conditions, enabling direct comparison with seeded-batch crystallisation using both unfiltered and filtered seed stock. Under seeded-batch conditions, the unfiltered seed stock produced crystals with an average size of 60 μm and a high CV of 94.95% reflecting substantial heterogeneity and the presence of disproportionately large crystals (Figure 54, blue). In contrast, filtration of the seed stock prior to seeded-batch crystallisation markedly improved uniformity, reducing the average crystal size to 38 μm and the CV to 20.71% (Figure 54, blue).

In droplet-based crystallisation, supplementation with neat filtered seeded stock resulted in smaller crystals, averaging 28 μm , although with a slightly elevated CV of 34.90% compared to the filtered seeded-batch conditions (Figure 54, salmon). A 1 in 5 dilution of seed stock within droplets led to increased variability, with a CV of 60.12% and sporadic formation of large

crystals (**Figure 54**, salmon). Unexpectedly, a further 1 in 20 dilution reduced the average crystal size to 51 μm and improved uniformity, with a CV of 49.10% (**Figure 54**, salmon).

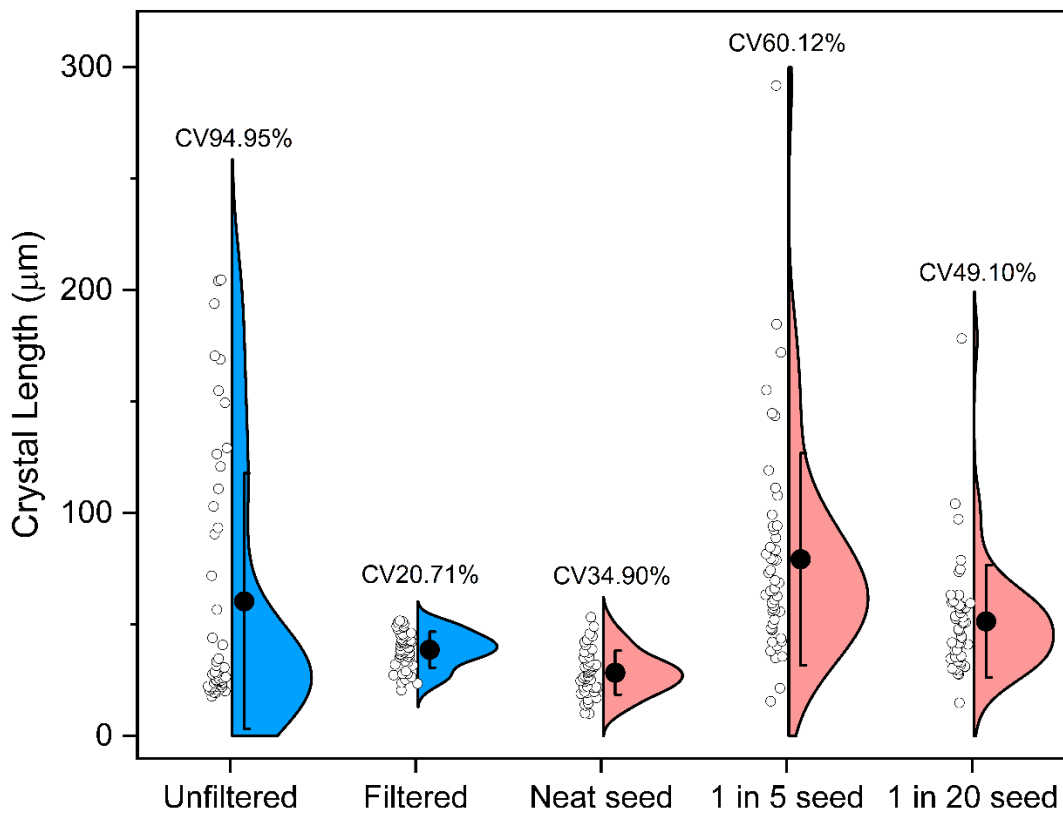


Figure 54. Droplet confinement of chlorite dismutase with filtered seed stock. The unfiltered and filtered seed stock result in vastly different microcrystal populations under seeded-batch conditions with a marked reduction in crystal size and CV, as well as the removal of large outlier crystals (blue). In droplets with a consistent droplet volume, the dilution of seed stock results in an increase in crystal size accompanied by an increased in CV; however the smaller crystal size in the 1 in 20 seed versus 1 in 5 seed is unexpected. Central black dots represent average crystal size, whilst error bars denote ± 1 standard deviation.

In summary, the chlorite dismutase system exhibits a strong dependence on seed stock parameters, with flow stability, filtration, and seed concentration each playing a critical role in shaping crystal size and uniformity. Filtration effectively removes larger outlier crystals and improves reproducibility, while droplet confinement reveals non-linear effects of seed dilution on growth dynamics. These observations suggest that increasing the number of seeds per droplet enhances crystal uniformity by distributing the available protein across multiple nucleation sites, thereby limiting excessive growth. In contrast, lower seed densities may permit a small number of crystals to utilise the protein supply, resulting in larger and more variable populations. Together, these findings underscore the importance of precise seed stock control in modulating crystal behaviour within microfluidic environments and in achieving uniform microcrystal populations suitable for time-resolved studies.

4.3 Serial synchrotron crystallography (SSX) for testing diffraction quality of microcrystals grown in batch and droplet conditions

Although microcrystals grown in batch and droplet conditions appeared visually similar, a comparison of diffraction quality was essential, allowing subsequent structure determination. In previous studies, droplet-grown crystals were directly dispensed onto silicon fixed-targets (258). In contrast, following off-chip incubation, fluorinated oil and surfactant were removed from droplet samples by the procedure of ‘breaking the emulsion’ (Figure 23). This ensured optimal signal-to-noise and generated final samples in an equivalent environment to batch conditions, specifically microcrystals contained within precipitant solution. All SSX experiments were performed on the serial beamline ID29 at the European Synchrotron Radiation Facility (ESRF) (262). A fixed-target device, in the form of a sheet-on-sheet on spine (SOSOS) chip (88) was chosen for data collection (Figure 55A). A serpentine directed-raster scan across the SOSOS chip was performed in ten minutes and required as little as 3–5 µL of microcrystal slurry (Figure 55B). The data presented in this section represents data collected over multiple beamtime visits to ID29 at ESRF (under proposals MX2438, MX2548 and MX2636).

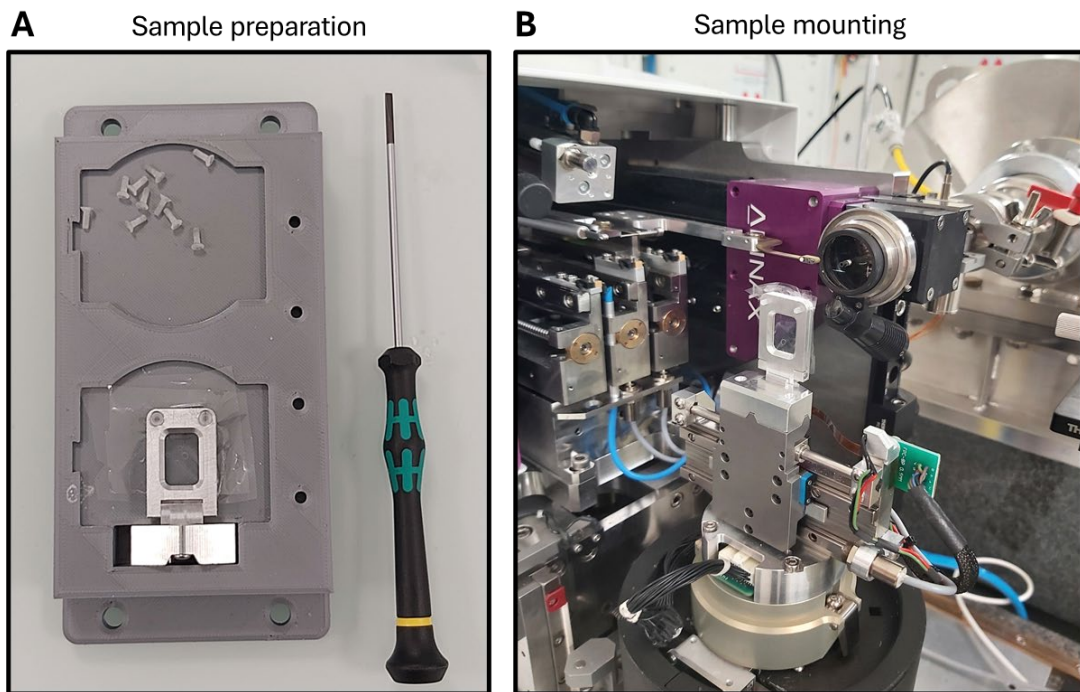


Figure 55. The sheet-on-sheet on spine (SOSOS) chip for SSX experiments at ESRF ID29. (A) A small volume of microcrystal slurry (3–5 µL) is dispensed between two 6 µm-thick mylar films, housed within an aluminium chip holder, sealed shut with two plastic screws. (B) The base contains a unique magnetic mount, providing quick and easy sample transfer of the SOSOS chip onto the MD3upSSX head at ID29, allowing routine directed-raster scan data collection at 231.25 Hz.

4.3.1 Lysozyme

To establish a baseline for SSX performance and refine the detector geometry ahead of more complex systems, lysozyme crystals were analysed using both batch-grown and droplet-grown preparations. Crystal sizes were matched at $\sim 15\text{ }\mu\text{m}$ to eliminate size-dependent effects, and complete datasets were obtained from a single chip for each preparation. Although the batch-grown sample exhibited a higher crystal density (10^8 crystals/mL compared to 10^7 crystals/mL), resulting in a greater hit rate of 41.6%, the droplet-grown crystals demonstrated superior indexing efficiency (**Table 10**). This suggests enhanced lattice order and reduced mosaicity in the microfluidic-grown crystals, likely due to more controlled nucleation and growth environments.

Table 10. Data collection and refinement statistics for Lysozyme crystals growth under batch and droplet conditions. Values in parentheses are for highest-resolution shell.

	Lysozyme Batch	Lysozyme Droplet
Data Collection		
No. of collected images	81,800	81,800
No. of hits	34,032	22,815
Hit rate (%)	41.6	27.9
No. of indexed images	29,954	22,304
Indexing rate (%)	88.0	97.7
No. of integrated lattices	58,984	51,812
Space group	$P4_{3}2_{1}2$	$P4_{3}2_{1}2$
$a, b, c\text{ }(\text{\AA})$	79.0, 79.0, 37.9	78.9, 79.0, 37.9
$\alpha, \beta, \gamma\text{ }(^{\circ})$	90, 90, 90	90, 90, 90
Resolution (\AA)	79.00 – 1.80 (1.83 – 1.80)	78.90 – 1.80 (1.83 – 1.80)
No. of unique reflections	11,636 (669)	11,607 (663)
Completeness (%)	100.0 (100.0)	100.0 (100.0)
Multiplicity	438.0 (47.67)	464.0 (51.94)
SNR	13.5 (0.2)	17.2 (0.9)
$CC_{1/2}$	0.99 (0.49)	0.99 (0.44)
CC^*	0.99 (0.81)	0.99 (0.78)
R_{split}	5.2 (343.7)	4.9 (100.8)
Wilson B -factor (\AA^2)	30.5	24.1
Refinement		
Resolution (\AA)	55.92 – 1.80	55.85 – 1.80
No. of reflections	11,597	11,567

	Lysozyme Batch	Lysozyme Droplet
Reflections used for R_{free}	581	581
R_{work}	0.171	0.146
R_{free}	0.231	0.190
Ramachandran favoured	127 (98%)	130 (98%)
Ramachandran allowed	2 (2%)	3 (2%)
Ramachandran outliers	0 (0%)	0 (0%)
Bond lengths (Å)	0.0066	0.0080
Bond angles (°)	1.551	1.767

Both preparations showed a high incidence of multiple lattice hits due to the directed-raster strategy, with nearly double the number of integrated lattices relative to indexed ones (**Table 10**). Unit cell parameters remained consistent across the conditions in the $P4_{3}2_{1}2$ space group, with only a minor contraction in the *a*-axis observed for the droplet-grown sample (**Table 10**).

A similar number of integrated lattices and a consistent high resolution cut-off of 1.8 Å enabled a direct assessment of data quality between the two preparations. While $\text{CC}_{1/2}$ and CC^* values remained similar, the droplet-grown crystals exhibited a clear enhancement in signal-to-noise ratio and a marked reduction in R_{split} (**Table 10**). These improvements were further supported by a lower reduced Wilson *B*-factor, indicating reduced overall disorder. Refinement statistics also favoured the droplet-grown sample, with lower R_{free} and a narrower gap between R_{work} and R_{free} , reflecting improved model accuracy and data consistency (**Table 10**). Superposition of the protein models from batch-grown and droplet-grown crystals results in a Ca root mean square deviation (RMSD) of 0.0063 Å and an all-atom RMSD of 0.760 Å, indicating high structural similarity between the preparations (**Figure 56A**). Such high similarity is also observed in the $2F_{\text{o}}-F_{\text{c}}$ electron density maps of selected residues, W63, I98 and W108 contoured at 1 σ (**Figure 56B**).

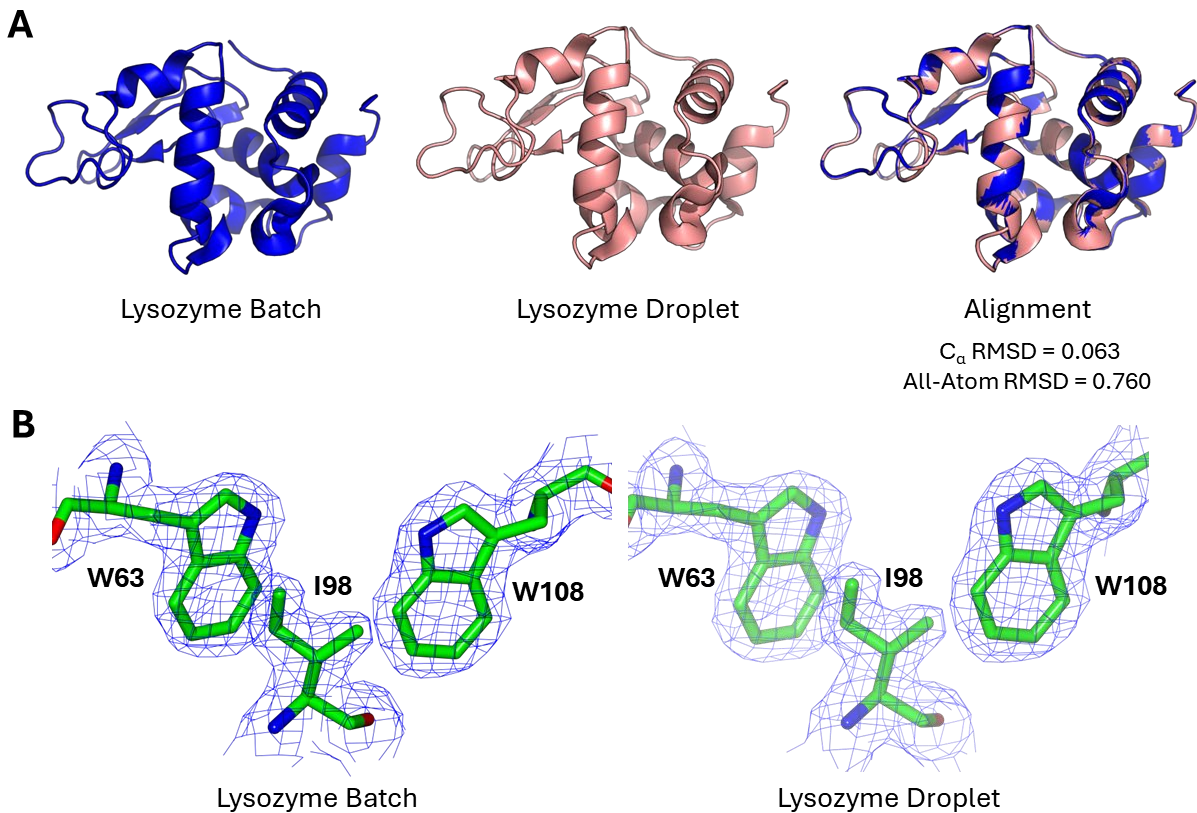


Figure 56. Structural comparison of Lysozyme from batch-grown and droplet-grown crystals. (A) Ribbon representation of the overall Lysozyme fold from batch-grown (left) and droplet-grown (middle) crystals. Superposition of the two models (right) yields a C_α RMSD of 0.0063 Å and an all-atom RMSD of 0.760 Å. (B) Representative $2F_o - F_c$ electron density maps for batch-grown (left) and droplet-grown (right) crystals, contoured at 1.0σ highlighting the residues W63, I98 and W108. Stick representation depicts carbon atoms as green, nitrogen atoms as blue and oxygen atoms as red.

4.3.2 Thaumatin

Thaumatin, a moderately challenging sample with known orientation bias in SSX, was analysed to evaluate the impact of crystal uniformity on data quality and structural resolution. A larger format SOSOS chip was employed for this dataset, enabling the acquisition of up to 240,000 images per chip, in comparison to the previous 81,800 images collected with lysozyme. Hit rates were notably lower for thaumatin overall, with a slight advantage for the batch-grown sample, consistent with its higher crystal density, 10^7 crystals/mL instead of 10^6 crystals/mL (**Table 11**). Crystal sizes differed between conditions, with batch-grown crystals averaging 14 µm and droplet-grown crystals reaching 24 µm. As with lysozyme, the droplet-grown sample exhibited a marginally higher indexing rate, suggesting improved lattice order and reduced mosaicity (**Table 11**). The batch-grown sample yielded more integrated lattices, likely due to increased multiple lattice hits arising from crystal clustering observed previously (**Figure 48A**).

Table 11. Data collection and refinement statistics for thaumatin crystals grown under batch and droplet conditions. Values in parentheses are for highest-resolution shell.

	Thaumatin Batch	Thaumatin Droplet
Data Collection		
No. of collected images	240,000	240,000
No. of hits	28,964	17,659
Hit rate (%)	12.0	7.3
No. of indexed images	26,357	17,129
Indexing rate (%)	91.0	97.0
No. of integrated lattices	35,295	19,053
Space group	$P4_{1}2_{1}2$	$P4_{1}2_{1}2$
a, b, c (Å)	58.9, 58.9, 152.5	58.9, 58.9, 152.7
α, β, γ (°)	90, 90, 90	90, 90, 90
Resolution (Å)	58.97 – 1.68 (1.71 – 1.68)	58.97 – 1.60 (1.63 – 1.60)
No. of unique reflections	31,714 (1541)	36,626 (1791)
Completeness (%)	100.0 (100.0)	100.0 (100.0)
Multiplicity	412.9 (265.02)	224.1 (94.2)
SNR	6.4 (0.5)	7.1 (0.5)
$CC_{1/2}$	0.98 (0.42)	0.99 (0.31)
CC^*	0.99 (0.77)	0.99 (0.69)
R_{split}	11.5 (170.1)	9.5 (202.4)
Wilson B -factor (Å ²)	17.9	18.3
Refinement		
Resolution (Å)	55.08 – 1.68 (1.71 – 1.68)	55.07 – 1.60 (1.63 – 1.60)
No. of reflections	31,628	36,538
Reflections used for R_{free}	1554	1860
R_{work}	0.168	0.146
R_{free}	0.192	0.175
Ramachandran favoured	212 (99%)	212 (99%)
Ramachandran allowed	3 (1%)	3 (1%)
Ramachandran outliers	0 (0%)	0 (0%)
Bond lengths (Å)	0.0043	0.0098
Bond angles (°)	1.218	1.677

Both datasets refined in the $P4_12_12$ space group, with only a minor elongation of the c-axis observed in the droplet-grown sample (**Table 11**). Despite having fewer integrated lattices, the droplet-grown crystals diffracted to a high-resolution cutoff of 1.60 Å compared to 1.68 Å for the batch-grown sample. This improvement may be partially attributed to the larger crystal size, but real-time hit finder analysis performed during the beamtime indicated greater sample uniformity, evidenced by consistent spot counts per diffraction pattern. Data quality metrics again favoured the droplet-grown preparation, with a higher signal-to-noise ratio, improved $CC_{1/2}$ and CC^* , and lower R_{split} values (**Table 11**). Interestingly, the Wilson B -factor was slightly elevated for the droplet-grown sample, deviating from the trend observed in lysozyme (**Table 11**). Nonetheless, refinement statistics aligned with expectations for higher resolution data, showing reduced R_{work} and R_{free} values in the droplet-grown dataset (**Table 11**).

Superposition of the protein models from batch-grown and droplet-grown crystals results in a Ca RMSD of 0.048 Å and an all-atom RMSD of 0.408 Å, indicating high structural similarity between the preparations (**Figure 57A**). Such high similarity is also observed in the $2F_o - F_c$ electron density maps (contoured at 1.5 σ) of the crystallisation agent tartrate present in the structure. A clearly identifiable disulfide bond between Cysteine 134 and 145 is also visible, which is one of eight intramolecular disulfide bonds present in thaumatin (**Figure 57B**).

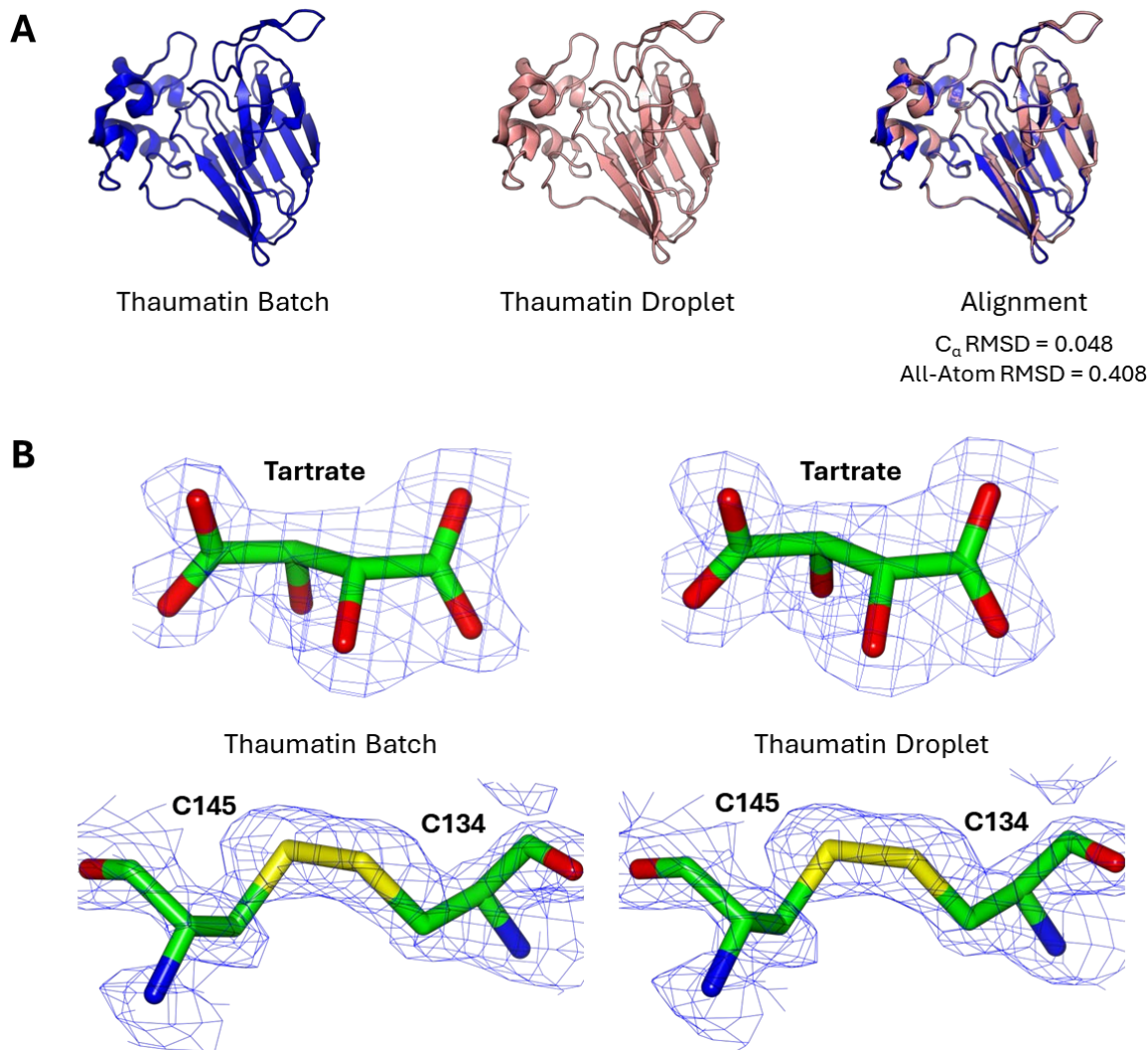


Figure 57. Structural comparison of thaumatin from batch-grown and droplet-grown crystals. (A) Ribbon representation of the overall thaumatin fold from batch-grown (left) and droplet-grown (middle) crystals. Superposition of the two models (right) yields a C_α RMSD of 0.048 Å and an all-atom RMSD of 0.408 Å. (B) Representative $2F_o - F_c$ electron density maps for batch-grown (left) and droplet-grown (right) crystals, contoured at 1.5σ highlighting the tartrate crystallisation agent, and the C145/C134 residue pair that constitute one of the eight intramolecular disulfide bonds present in thaumatin. Stick representation depicts carbon atoms as green, nitrogen atoms as blue, oxygen atoms as red and sulfur atoms as yellow.

4.3.3 AtPdx1.3

Due to the lower symmetry of the *H*3 space group and the associated indexing ambiguity, data collection for AtPdx1.3 required three smaller format SOSOS chips to achieve a complete dataset. An increased number of integrated lattices was required to resolve the indexing ambiguities and ensure robust coverage across reciprocal space. Crystal densities were matched at 10⁷ crystals/mL for both batch and droplet-grown preparations, with crystal sizes held constant at 15 µm.

Hit rates and indexing efficiencies were similar across both conditions, with a slight improvement in indexing observed for the droplet-grown sample (**Table 12**). As seen in previous systems, the batch-grown preparation yielded a higher number of integrated lattices, likely due to increased crystal clustering under seeded-batch conditions (**Table 12**). Both datasets refined in the *H*3 space group, although unit cell parameters differed across all axes, with consistently larger dimensions observed in the droplet-grown crystals (**Table 12**). The origin of this expansion remains uncertain, but factors such as slower supersaturation kinetics, reduced mechanical stress, and controlled evaporation in the microfluidic environment may influence lattice packing and contribute to the observed changes.

Table 12. Data collection and refinement statistics for AtPdx1.3 crystals grown under batch and droplet conditions. Values in parentheses are for highest-resolution shell.

	AtPdx1.3 Batch	AtPdx1.3 Droplet
Data Collection		
No. of collected images	245,400	245,400
No. of hits	20,268	20,827
Hit rate (%)	8.2	8.5
No. of indexed images	19,325	20,635
Indexing rate (%)	95.3	99.0
No. of integrated lattices	27,581	25,464
Space group	<i>H</i> 3	<i>H</i> 3
<i>a</i> , <i>b</i> , <i>c</i> (Å)	177.9, 177.9, 117.3	180.3, 180.3, 119.2
α , β , γ (°)	90, 90, 120	90, 90, 120
Resolution (Å)	93.33 – 2.50 (2.54 – 2.50)	94.75 – 2.50 (2.54 – 2.50)
No. of unique reflections	47,878 (4703)	50,011 (4635)
Completeness (%)	100.0 (100.0)	100.0 (100.0)
Multiplicity	47.4 (45.18)	44.2 (41.83)
SNR	4.4 (0.5)	5.0 (0.8)
CC _{1/2}	0.96 (0.17)	0.96 (0.27)

	AtPdx1.3 Batch	AtPdx1.3 Droplet
CC*	0.99 (0.54)	0.99 (0.65)
R_{split}	19.6 (212.2)	17.1 (147.3)
Wilson <i>B</i> -factor (Å ²)	49.4	45.3
Refinement		
Resolution (Å)	64.47 – 2.50	65.40 – 2.50
No. of reflections	47,873	50,003
Reflections used for R_{free}	2316	2510
R_{work}	0.168	0.158
R_{free}	0.193	0.188
Ramachandran favoured	1042 (98%)	1057 (99%)
Ramachandran allowed	25 (2%)	15 (1%)
Ramachandran outliers	0 (0%)	0 (0%)
Bond lengths (Å)	0.0054	0.0062
Bond angles (°)	1.407	1.511

Both datasets reached a high-resolution cutoff of 2.50 Å and contained a comparable number of integrated lattices, enabling a direct comparison of data quality (**Table 12**). While CC_{1/2} and CC* values were similar, the droplet-grown crystals exhibited a higher signal-to-noise ratio, reduced R_{split} , and a lower Wilson *B*-factor, indicating improved diffraction quality (**Table 12**). Refinement statistics further supported this trend, with a lower R_{free} value and a greater proportion of favoured Ramachandran angles in the droplet-grown model, suggesting enhanced backbone geometry and overall structural integrity (**Table 12**).

Superposition of the protein models from batch-grown and droplet-grown crystals results in a Ca RMSD of 0.494 Å and an all-atom RMSD of 3.307 Å, indicating highly similar overall folds with a stable backbone (**Figure 58A**). However, an all-atom RMSD greater than 1 Å indicates side chains are adopting different conformations between the preparations. This difference in side-chain conformation can be clearly observed in the 2F_o-F_c electron density maps (contoured at 1.5 σ) of K98, a key residue in the active site of AtPdx1.3 (**Figure 58B**).

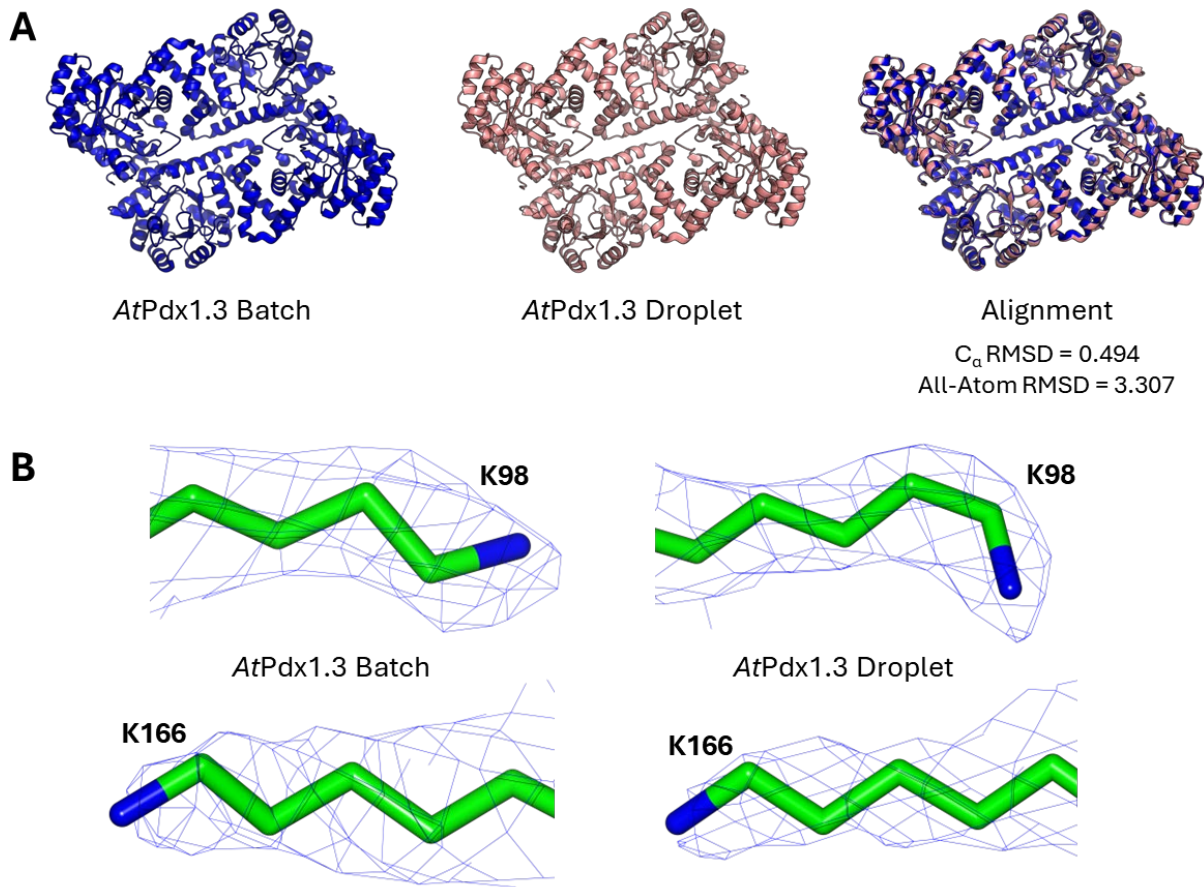


Figure 58. Structural comparison of AtPdx1.3 from batch-grown and droplet-grown crystals. (A) Ribbon representation of the overall AtPdx1.3 fold from batch-grown (left) and droplet-grown (middle) crystals, with four copies in the asymmetric unit (ASU). Superposition of the two models (right) yields a C_α RMSD of 0.494 Å and an all-atom RMSD of 3.307 Å. (B) Representative $2F_o - F_c$ electron density maps for batch-grown (left) and droplet-grown (right) crystals, contoured at 1.5 σ highlighting the key active site lysine residues, K98 and K166. Stick representation depicts carbon atoms as green and nitrogen atoms as blue.

4.3.4 Chlorite dismutase

Chlorite dismutase contains a haem prosthetic group. Due to initial crystallisation challenges, it was selected to test whether droplet-based crystallisation could improve crystal uniformity, data quality and structural resolution in SSX. Due to the low symmetry $P1$ space group, extensive data collection was required to achieve complete datasets. The batch-grown dataset comprised pooled crystals from experiments performed under multiple seeding conditions (neat seed, 1 in 10 seed, 1 in 20 seed and 1 in 50 seed; see **Figure 51**), with sizes ranging from 14 to 150 μm . In contrast, the droplet-grown sample exhibited consistent crystal dimensions, averaging 28 μm .

Crystal densities differed markedly between preparations, with the batch-grown sample at 10^8 crystals/mL and the droplet-grown sample at 10^6 crystals/mL. Using the larger format SOSOS chip (240,000 images per chip), four chips were collected for the batch-grown sample and three for the droplet-grown sample, due to limited sample availability. As expected, the batch-grown

crystals yielded a hit rate approximately three times higher than that of the droplet-grown sample (**Table 13**). However, the droplet-grown crystals also exhibited a roughly two-fold reduction in indexing rate, likely due to their smaller size and weaker diffraction, which diminished both hit identification and indexing success (**Table 13**). Indexing rates across both conditions were substantially lower than observed in the previous systems tested, reflecting the inherent challenges of the *P1* space group, namely the absence of symmetry constraints and internal redundancy, which complicate orientation determination and indexing reliability.

Table 13. Data collection and refinement statistics for chlorite dismutase crystals grown under batch and droplet conditions. Values in parentheses are for highest-resolution shell.

	Chlorite Dismutase Batch	Chlorite Dismutase Droplet
Data Collection		
No. of collected images	960,000	720,000
No. of hits	293,978	77,725
Hit rate (%)	30.6	10.8
No. of indexed images	162,746	19,376
Indexing rate (%)	55.3	24.9
No. of integrated lattices	221,767	20,075
Space group	<i>P1</i>	<i>P1</i>
<i>a</i> , <i>b</i> , <i>c</i> (Å)	53.0, 53.6, 55.7	53.0, 53.6, 55.7
α , β , γ (°)	107.3, 98.4, 110.0	107.3, 98.4, 110.0
Resolution (Å)	51.13 – 1.80 (1.84 – 1.80)	51.11 – 2.36 (2.40 – 2.36)
No. of unique reflections	49,072 (2435)	21,770 (1094)
Completeness (%)	100.0 (100.0)	100.0 (100.0)
Multiplicity	739.4 (747.8)	39.6 (41.6)
SNR	8.1 (0.6)	3.6 (0.9)
CC _{1/2}	0.99 (0.27)	0.94 (0.26)
CC [*]	0.99 (0.65)	0.98 (0.64)
<i>R</i> _{split}	7.9 (210.5)	24.8 (140.9)
Wilson <i>B</i> -factor (Å ²)	31.62	37.37
Refinement		
Resolution (Å)	51.13 – 1.80	51.11 – 2.36
No. of reflections	49,060	21,768
Reflections used for <i>R</i> _{free}	2516	1055
<i>R</i> _{work}	0.167	0.171
<i>R</i> _{free}	0.205	0.221

	Chlorite Dismutase Batch	Chlorite Dismutase Droplet
Ramachandran favoured	346 (97%)	343 (95%)
Ramachandran allowed	12 (3%)	14 (4%)
Ramachandran outliers	0 (0%)	1 (1%)
Bond lengths (Å)	0.0086	0.0072
Bond angles (°)	1.733	1.643

The batch-grown dataset contained a high number of multiple lattice hits, attributed to the presence of large outlier crystals that were repeatedly sampled during directed-raster data collection (**Table 13**). This contributed to a greater number of integrated lattices and enabled a high-resolution cutoff of 1.80 Å, compared to 2.36 Å for the droplet-grown sample (**Table 13**). The lower resolution in the droplet-grown dataset was accompanied by a reduced signal to noise ratio, elevated R_{split} and a substantially higher Wilson- B factor, indicating increased disorder and diminished diffraction quality (**Table 13**).

Superposition of the protein models from batch-grown and droplet-grown crystals results in a Ca RMSD of 0.092 Å and an all-atom RMSD of 2.837 Å, once again highlighting a stable overall fold but varying side-chain conformations (**Figure 59A**). The $2F_o - F_c$ electron density maps for batch-grown crystals contoured at 2.0σ reveals holes in the haem prosthetic group consistent with a delocalised π -electron system, that is not visible in the droplet-grown crystals (**Figure 59B**). Additionally, the active site water is clearly defined above the plane of the haem in the batch-grown crystals whilst the density appears continuous in the droplet-grown crystals (**Figure 59B**). The loss of such features is a direct effect of lower resolution data for the droplet-grown crystals.

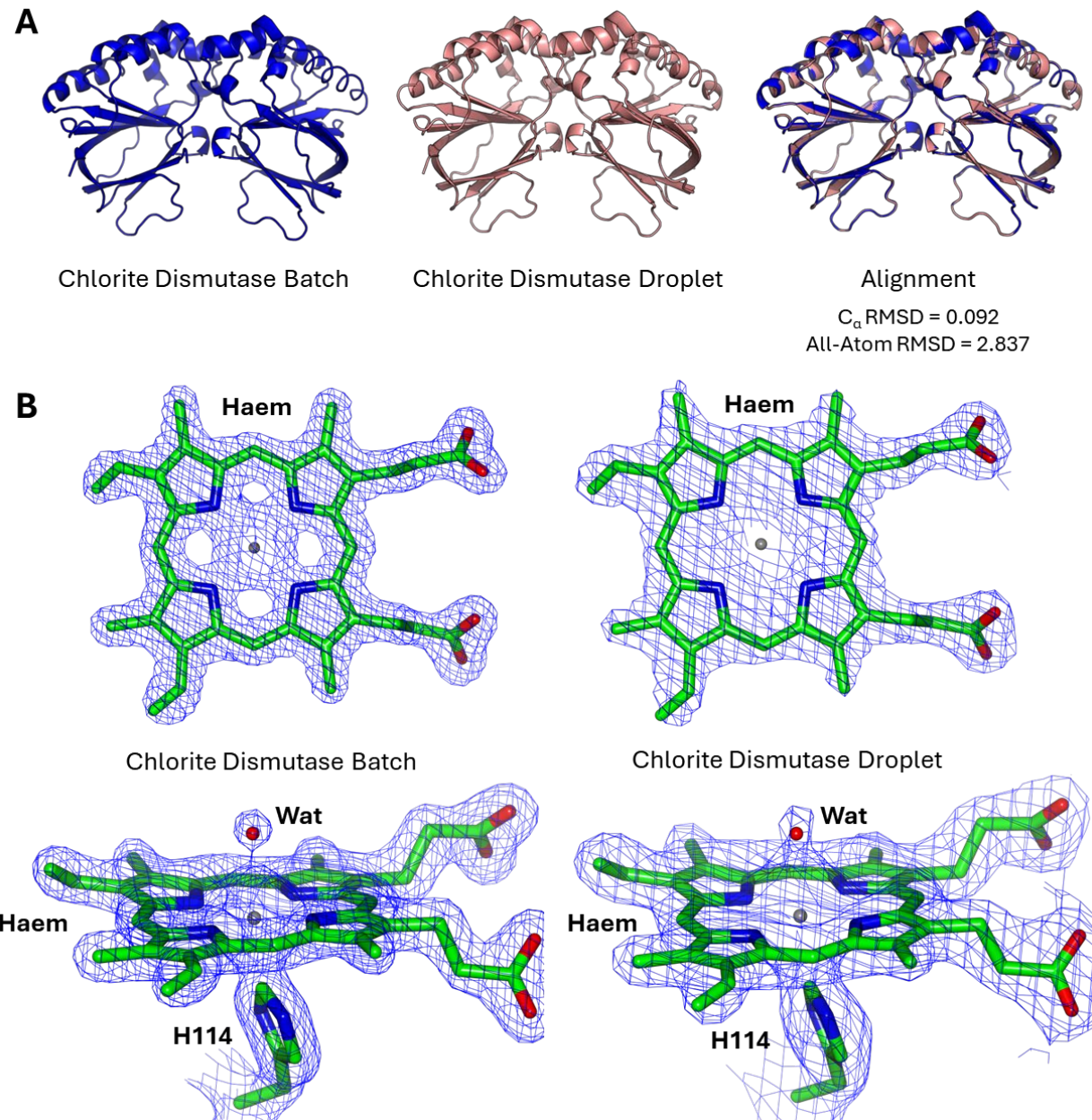


Figure 59. Structural comparison of chlorite dismutase from batch-grown and droplet-grown crystals. (A) Ribbon representation of the overall chlorite dismutase fold from batch-grown (left) and droplet-grown (middle) crystals, with two copies in the asymmetric unit (ASU). Superposition of the two models (right) yields a C_α RMSD of 0.092 Å and an all-atom RMSD of 2.837 Å. (B) Representative $2F_o - F_c$ electron density maps for batch-grown (left) and droplet-grown (right) crystals, contoured at 2.0σ and 1.5σ respectively, highlighting the active site Haem, water (Wat) and H114. Stick representation depicts carbon atoms as green, nitrogen atoms as blue and oxygen atoms as red. The grey sphere in the centre of the haem porphyrin ring depicts an iron atom.

4.4 Considerations for crystallisation in microfluidic droplets

Beyond miniaturisation and microseeding strategies, expanding the applicability of crystallisation in microfluidic droplets calls for consideration of physical parameters including crystal axial ratio, solution viscosity and the minimum crystal size for structural analysis.

4.4.1 Axial ratio

The preparation of crystals in droplet environments has been applied to a range of systems in previous work (248,258). To extend applicability, an alternative crystal morphology was chosen, and we tested the effect of droplet confinement on the growth of needle shaped crystals. The model needle system selected was trypsin type I. Under batch conditions, trypsin needles grew to a variety of sizes, with a corresponding axial ratio of ~ 10 (Figure 60A). In contrast, trypsin needles grown in droplets environments were unable to elongate fully, with a corresponding axial ratio of ~ 5 (Figure 60B). This is caused by an insufficient droplet volume, leading to the fragmentation of crystals into smaller needles, lowering the crystal axial ratio (l/w). A similar effect is observed with parallelepiped-shaped Lysozyme crystals, as the droplet volume decreases, the crystal size reduces as shown earlier, but the axial ratio also decreases with the crystal length and width becoming equal (Figure 60C).

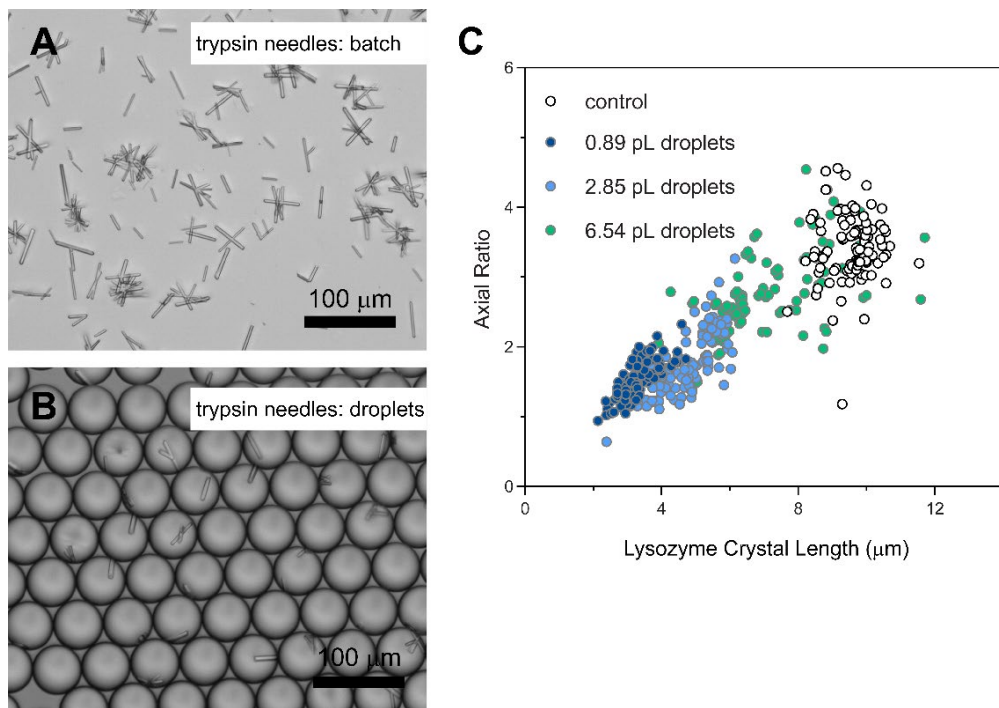


Figure 60. The effect of droplet confinement on crystal axial ratio. (A) Trypsin type I needles grown under batch conditions lead to non-uniform crystal sizes with an axial ratio of ~ 10 . (B) Trypsin type I needles grown in droplet environments result in smaller needles with an axial ratio of ~ 5 . (C) In the case of parallelepiped-shaped Lysozyme crystals, the axial ratio is reduced to near unity when reducing the droplet volume and corresponds to much smaller crystals in comparison to the control sample grown in batch conditions.

4.4.2 Viscosity

For droplet crystallisation to be applicable to a wider range of crystals systems, it must be able to withstand a variety of different crystallisation mixtures. Many crystallisation conditions contain precipitating agents such as PEG with a naturally high viscosity. The higher viscosity component may impact the generation of stable droplet flows at high enough throughput for crystallisation trials in droplets. To test the effect of viscosity, a concentration series of PEG 6000 was prepared ranging from 0 to 25 % (w/v) corresponding to viscosities from 1 to 21 mPa·s. In droplets with a diameter of 50 µm, only a three-fold reduction in throughput was observed in the concentration series from ~ 1.3 kHz to 0.4 kHz (Figure 61), implying that droplet microfluidics is compatible with high viscosity and difficult to handle crystallisation conditions. If high droplet throughput is required, a lower viscosity crystallisation condition would be recommended to ensure stable droplet flows throughout the experiment.

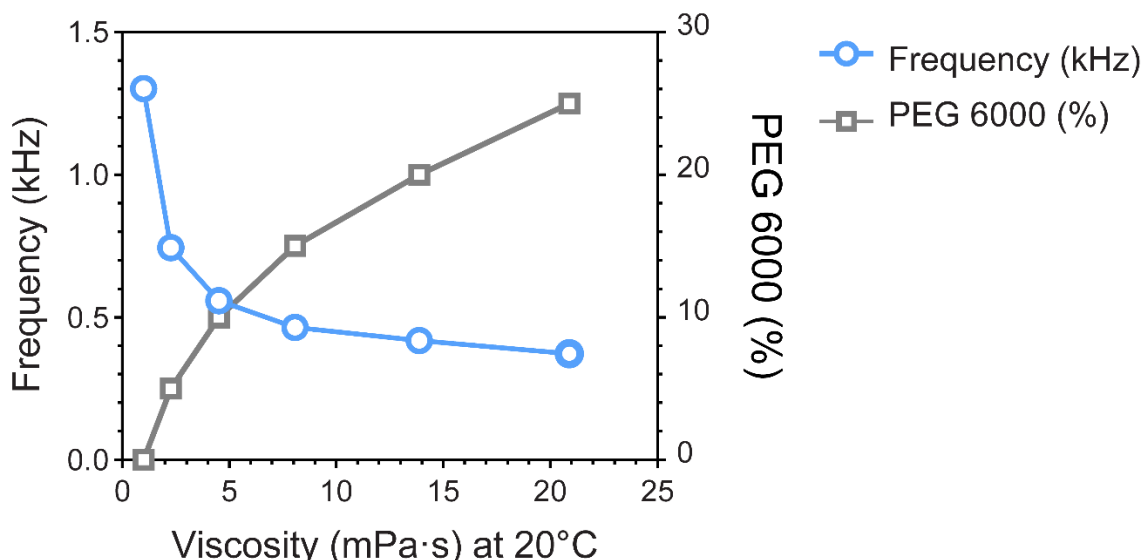


Figure 61. The effect of viscosity on droplet throughput. Droplet crystallisation can withstand high viscosity crystallisation conditions, for example 0 to 25% (w/v) PEG 6000, but reductions in droplet throughput are observed and the production of stable droplet flows will be anticipated to take longer.

4.4.3 Minimum crystal size

Brighter and more-focused X-ray sources now allow useable diffraction data to be collected from submicron crystals. As shown earlier (Figure 50), AtPdx1.3 crystals as small as 1 micron can be prepared in 1 pL droplets but it would be feasible to reduce this droplet volume even further with the hope to generate submicron crystals in droplets. Monodisperse droplets as small as 5.4 µm in diameter and 82 fL in volume can be prepared with AtPdx1.3 and precipitant solution containing seed stock at a droplet generation frequency of 61 kHz (Figure 62). However, reduced likelihood of crystal growth at smaller scales and reduced occupancy of droplets with seed leads to prevention of crystal growth in femtolitre droplets.

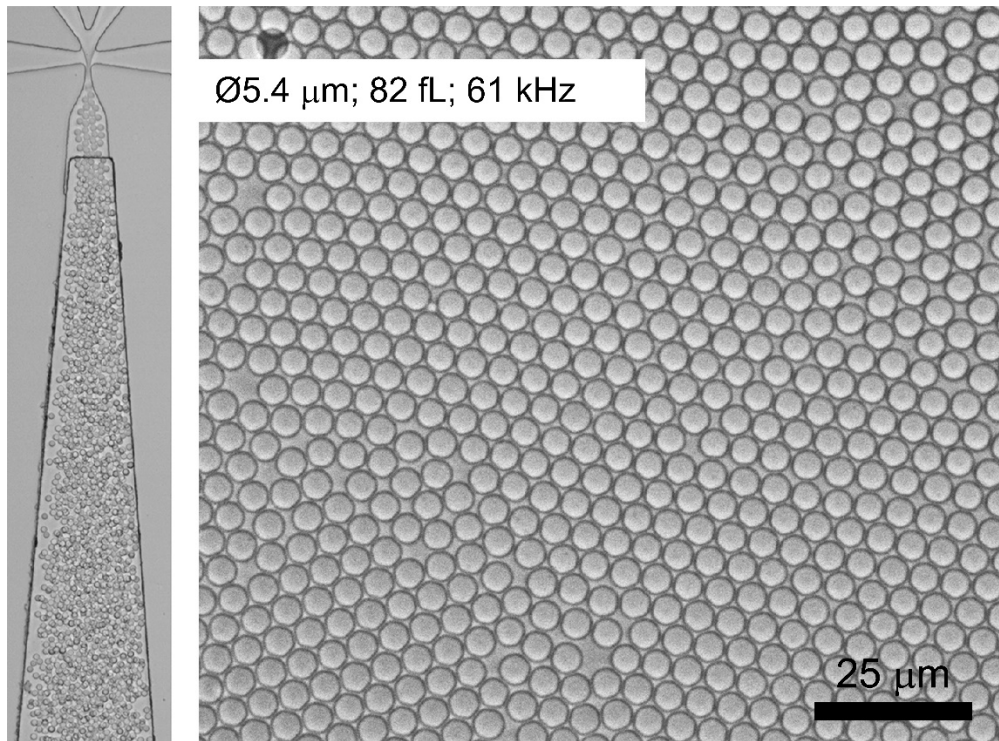


Figure 62. The production of femtolitre-sized droplets for AtPdx1.3 crystallisation. Droplet miniaturisation allows for the high-throughput generation of $\varnothing 5.4\text{ }\mu\text{m}$ droplets with a volume of 82 fL (left). Even in the presence of seed stock, no AtPdx1.3 crystals were observed in 82 fL droplets when using a 60x/1.4NA oil immersion objective (right).

4.5 Discussion

This chapter demonstrates the utility of droplet microfluidics as a versatile platform for engineering crystal size and uniformity across a range of protein systems. By systematically varying droplet volume and crystallisation conditions, clear relationships between droplet scale, crystal morphology, and sample quality were established, providing a reproducible framework for generating microcrystals tailored to serial crystallography workflows.

Using a PEG-based system with lysozyme, monodisperse crystallisation droplets were generated across a volume range from 194 to 0.89 pL, producing crystals between 20 and 2 µm in size. These crystal dimensions are substantially smaller than those reported in earlier droplet microfluidic studies, where lysozyme crystals typically exceeded 50 µm (244,245,255,257,289). As droplet volume decreased, both crystal size and size distribution narrowed, with the lowest CV observed in the smallest droplets tested. Below 6.54 pL, droplets were stochastically loaded with single crystals, yielding highly uniform populations ideally suited for serial crystallography. This miniaturisation, however introduced a trade-off: crystal yield declined from 80 crystals/nL to just 7 crystals/nL in the smallest droplets. Notably, this loss was offset by a 20-fold increase in droplet generation frequency, indicating that throughput and sample quality can be balanced through careful optimisation of droplet parameters.

The inverse relationship between droplet volume and crystal yield is consistent with previous microfluidic lysozyme crystallisation studies, where reported lower nucleation percentages were seen in smaller droplets despite identical supersaturation conditions (255). For instance, 4 nL droplets (\varnothing 200 µm) exhibited reduced nucleation efficiency compared to 24 nL droplets (360 µm), even though the calculated nucleation rate remained constant across volumes (255). Protein concentration has also been shown to influence crystal yield in droplet systems, although this variable was not investigated during this work. A previous study demonstrated that increasing the concentration of lysozyme from 20 to 30 mg mL⁻¹ raised nucleation percentages from 12% to 69% in 60 nL droplets, confirming that crystallisation remains concentration-dependent even under confinement (256). Importantly, droplet-based methods consistently yield single crystals per droplet, in contrast to batch approaches which generate multiple crystals per well (256). This isolation effect enables precise tracking of individual crystal growth trajectories and facilitates face-specific growth analysis, capabilities not readily achievable in bulk crystallisation formats (256). Alternative strategies have also emerged, where polydisperse emulsions are first generated by batch methods to identify optimal droplet diameters, which are then subsequently used to generate monodisperse emulsions tailored for downstream crystallographic applications (248).

Thaumatin crystallised in a salt-based system, showing comparable improvements in crystal uniformity relative to batch conditions, despite slightly larger crystal sizes. The crystals obtained in this work are consistent with previous reports using tartrate-based precipitants, ranging from 25 to 50 μm (245,246,255,256). Although only one droplet size was tested in this work, the results suggest that further miniaturisation could reduce crystal dimensions whilst preserving sample homogeneity. Importantly, the sensitivity of droplet volume coefficient of variation (CV) emerged as a potential contributing factor, as minor instabilities in droplet formation may have influenced the emergence of bimodal crystal distributions. While this relationship was not directly measured, the observation underscores the importance of maintaining precise control over droplet generation to minimise variability and improve reproducibility in crystallisation outcomes. Studies have further demonstrated the influence of droplet volume on thaumatin crystallisation outcomes. When comparing 200 μm (4 nL) and 500 μm (50-65 nL) droplets, single crystal formation was consistently observed in the smaller droplets, where larger droplets yielded multiple crystals per droplet (255,256). At a constant protein concentration of 10 mg/mL, the nucleation percentage increased sixfold in the 500 μm droplets, highlighting the strong dependence of nucleation behaviour on droplet volume (255). Together, these insights support the broader conclusion that droplet miniaturisation not only improves crystal homogeneity but also enables single crystal isolation, facilitating downstream analysis and integration with serial crystallography platforms. However, achieving reproducibility at these scales requires stringent control over droplet formation and protein concentration, particularly when operating near the critical volume threshold for nucleation suppression.

For AtPdx1.3, a more typical protein, initial droplet crystallisation attempts yielded negligible crystal formation. To overcome this, a seeding strategy was employed, introducing fragmented crystals into the precipitant solution prior to droplet generation. This approach aligns with principles demonstrated by Gerdts *et al.*, who used time-controlled microfluidic seeding to decouple nucleation and growth stages within nanolitre-sized droplets, enabling the formation of diffraction quality crystals even for proteins defiant against traditional crystallisation methods (253). Moreover, the integration of seeding within a microfluidic framework aligns with the findings of Heymann *et al.*, who developed a kinetically optimised device for room-temperature serial crystallography (248). The emulsion-based platform exploited the negative feedback mechanism inherent to small droplet volumes, where initial nucleation locally reduced supersaturation to promote single crystal formation per droplet (248). Combining kinetic control, spatial confinement and seeding precision offers a robust framework for crystallising proteins with low intrinsic nucleation propensity.

In batch conditions, seed dilution predictably increased AtPdx1.3 crystal size while maintaining a consistent CV. This observation matches previous findings in batch crystallisation systems

where higher seed concentrations typically yield a larger number of smaller crystals, and lower seed concentrations favour fewer, larger crystals (58,80). Interestingly, while increased crystal size is expected to coincide with greater heterogeneity, AtPdx1.3 maintained a relatively uniform size distribution across the seed dilution series. This deviation from the anticipated behaviour may reflect protein-specific crystallisation kinetics or intrinsic growth constraints unique to AtPdx1.3. In droplets, decreasing volume again reduced crystal size and improved uniformity, with AtPdx1.3 crystal dimensions scaling proportionally with droplet diameter. However, the smallest droplets tested showed an increased CV, likely due to stochastic effects and reduced nucleation probability. Overall yield remained lower than lysozyme and thaumatin, reflecting protein-specific limitations in crystallisation efficiency.

Chlorite dismutase presented a distinct challenge, with previous seeded-batch crystallisation protocols producing heterogeneous slurries with large outlier crystals. Initial droplet experiments were hindered by seed stocks clogging internal filters within the microfluidic device, compromising droplet integrity and throughput. To mitigate this, seed stocks were filtered prior to crystallisation, effectively removing oversized crystals and aggregates. This approach not only restored reproducible droplet formation but also aligned with strategies reported by Shoeman *et al.*, who demonstrated that seed stock filtering enhances crystal monodispersity and reduced variability in nucleation outcomes (275). When applied to both batch and droplet workflows, the filtering seed strategy yielded comparable crystal sizes across formats, although batch samples exhibited a slightly lower CV, likely reflecting reduced sensitivity to flow perturbations and device constraints. These findings underscore the utility of seed stock filtration as a scalable, cross-platform strategy for improving crystal uniformity and workflow robustness in serial crystallography applications.

Visual inspections confirmed morphological similarity between batch and droplet grown crystals, but diffraction validation was essential to assess sample quality. To this end, a directed-raster fixed-target SSX setup was employed at the ID29 beamline at ESRF, enabling efficient data acquisition from minimal sample volumes. High-resolution datasets were successfully obtained from lysozyme, thaumatin, AtPdx1.3, and chlorite dismutase, confirming the compatibility of batch and critically droplet-grown samples with serial crystallography workflows. These findings reinforce the reliability of droplet microfluidics for generating serial compatible crystals across diverse protein systems. They further support recent work demonstrating that microcrystals grown in droplet emulsions can be stored for extended periods and transported remotely without compromising diffraction quality (258). This convergence of morphological consistency, diffraction robustness, and logistical flexibility positions droplet-based crystallisation as a scalable and beamline-ready strategy for high-throughput structural biology.

Additional considerations emerged during optimisation. In needle-forming systems such as trypsin and parallelepiped lysozyme crystals, droplet miniaturisation was associated with crystal fragmentation and reduced axial ratios. While this observation suggests a possible link, it remains a qualitative interpretation rather than a quantitatively confirmed outcome. Notably, existing studies involving trypsin crystallisation in droplet environments have largely focused on throughput and diffraction compatibility, without explicitly addressing the impact of droplet confinement on crystal morphology or axial ratio (248). Viscosity also influenced throughput, PEG 6000 concentrations from 0 to 25% (w/v) increased solution viscosity from 1 to 21 mPa·s, resulting in a three-fold reduction in droplet generation for 50 µm droplets. While the system tolerated high viscosity, lower concentrations are recommended to maintain throughput. These observations are consistent with prior work by Tice *et al.*, who demonstrated that droplet formation in segmented flow microfluidics remains reliable across a range of viscosities, provided that the Capillary number and flow rate ratios are appropriately tuned (290). Viscosity measurements can be inferred from the behaviour of microfluidic droplets, enabling precise calculation of fluid viscosity under operational conditions (291). These measurements are essential for characterising flow dynamics and optimising droplet-based systems, particularly in protein crystallisation and serial sample delivery platforms. In such applications, mixing efficiency is strongly influenced by viscosity, and the stability and performance of droplet generation are critical for sustaining long-duration data collection.

Finally, attempts to generate submicron crystals of *AtPdx1.3* using 1 pL and 82 fL droplets revealed a lower limit to crystal formation. No crystal growth was observed at 82 fL, likely due to stochastic limitations in nucleation at extreme miniaturisation. To the best of my knowledge, this represents the first attempt to crystallise a protein within sub-picrolitre droplets, marking an initial step towards ultra-miniaturised crystallisation platforms. Further optimisation such as enhanced seeding strategies, nucleant additives, or modified droplet geometries will be necessary to overcome nucleation barriers and enable crystal growth at these scales. In particular, altering droplet geometry may influence internal flow patterns, surface-to-volume ratios, and confinement effects, all of which can impact nucleation kinetics and crystal morphology.

Taken together, this work establishes droplet microfluidics as a powerful tool for crystal size engineering, offering precise control over morphology, uniformity, and throughput. By integrating seeding strategies, filtration protocols, and device optimisation, a modular workflow was developed, which is adaptable to a range of protein targets. These findings directly support the broader goal of reproducible, size-controlled microcrystal production for time-resolved serial crystallography, where crystal uniformity and volume efficiency are critical.

Chapter 5 Droplet microfluidics for rapid micromixing

To enable time-resolved crystallography experiments triggered by the addition of substrate or ligand, rapid and synchronised mixing of crystal and substrate volumes must be achieved.

Given that the median enzyme turnover rate (k_{cat}) is 13.7 s^{-1} (292), corresponding to a reaction cycle of 70 ms, effective resolution of catalytic intermediates requires efficient mixing, substrate diffusion and binding with a few milliseconds. Conventional microfluidic mixing, limited by slow laminar diffusion, presents a major bottleneck under these constraints.

To overcome this, droplet-based microfluidic strategies can be used, which offer convective-diffusive mixing via internal circulations within individual droplets (**Figure 63**). This results in mixing times orders of magnitude faster than in single-phase systems. Crucially, droplets provide consistent incubation times due to their uniform flow velocities, mitigating dispersion effects caused by parabolic velocity profiles in traditional microchannels. Furthermore, the use of periodic droplet generation opens up the possibility of synchronisation with high-repetition-rate XFEL pulses to increase hit rates. However, challenges persist in maintaining droplet periodicity during sample ejection into the beam path, limiting current implementation efficiency.

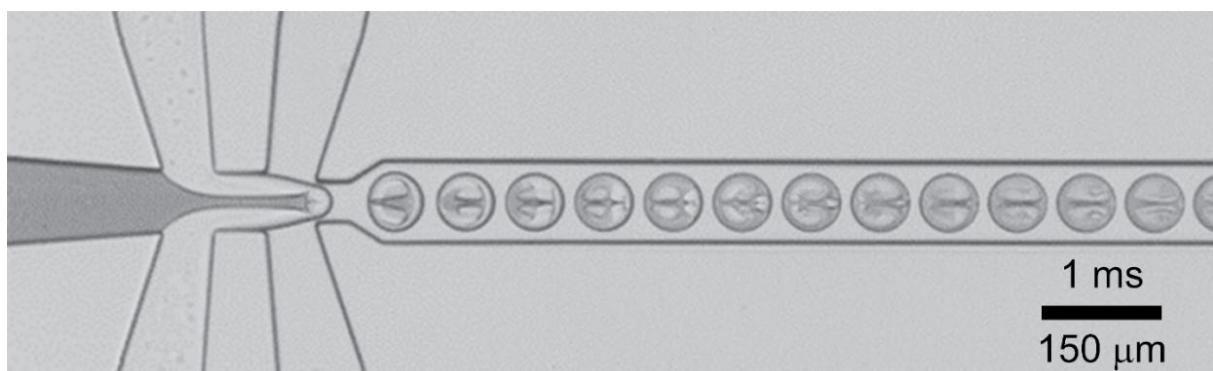


Figure 63. Rapid connective-diffusive mixing in droplets. During droplet generation and transport of the subsequent droplet within a microchannel, circulations take place which can be easily observed when applying a coloured dye to the system. The internal circulations drive rapid connective-diffusive mixing within the droplet.

An alternative to sample ejection directly into the beam is data collection from within the microfluidic device itself, commonly referred to as *in situ* X-ray crystallography. Additional material introduced into the X-ray path by the microfluidic device itself, ultimately leads to signal attenuation which adversely affects data collection. Traditionally droplet microfluidic devices are composed of millimetre thick layers of PDMS and glass, which would not allow for effective transmission of X-rays. Therefore, fabricating an X-ray compatible microfluidic device necessitates that any material interacting with the X-ray path must be reduced in thickness enough to achieve high signal-to-noise. However, this introduces challenges in terms of

fabricating such thin-film materials for minimal attenuation whilst ensuring high stability and reproducibility, key attributes for performing an in-flow experiment.

In this chapter, I present droplet microfluidic strategies for rapid and uniform mixing of crystals and ligand. By applying image analysis alongside high-speed microscopy imaging, fast mixing times on the order of milliseconds are observed. Material feasibility tests for PDMS are performed at low and high energy modes at a microfocus beamline to elucidate the potential of thin-film devices for the collection of diffraction data. Fabrication strategies are then introduced to produce thin-film PDMS droplet microfluidic devices. A proof-of-principle experiment is employed by studying the binding of N-Acetylglucosamine (GlcNAc) to Lysozyme, a previously well-known model system for verifying time-resolved mixing approaches. Finally, the effect of ligand concentration on time-resolved mixing data and ligand occupancy is studied.

Some of the results presented in this chapter have been published in the following article:
Stubbs, J., Hornsey, T., Hanrahan, N., Esteban, L.B., Bolton, R., Malý, M., Basu, S., Orlans, J., De Sanctis, D., Shim, J., Shaw Stewart, P.D., Orville, A.M., Tews, I., West, J., 2024. Droplet microfluidics for time-resolved serial crystallography. *IUCrJ* 11, 237–248. The publication is included within the Appendix for reference.

5.1 Mixing in droplets

To study mixing during droplet generation and transport, $\sim 7 \times 2 \mu\text{m}$ Lysozyme crystals were encapsulated into droplets along with a stream of highly absorbing red dye (25 mM sulfanilic acid azochromotrop, SAA), providing contrast for subsequent image analysis performed by Dr Niall Hanrahan. Initially, the crystal and dye streams converge with diffusion initiating slow mixing before the process of droplet generation, resulting in stream thinning allowing rapid mixing with short diffusion paths. Subsequently, droplets containing crystal and dye are transported down the microchannel with further internal circulations within the droplet driving mixing to completion. During image analysis, mixing calculations began once the crystal and dye streams converged. A fully mixed state is achieved when the droplet pixel intensity coefficient of variation (CV) reaches 5%. When applying a 1:1 volume ratio of crystal and dye at a velocity of 60 mm/s, the presence of crystals did not affect the mixing time, resulting in a consistent mixing time of ~ 6 milliseconds, with and without crystals (**Figure 64**).

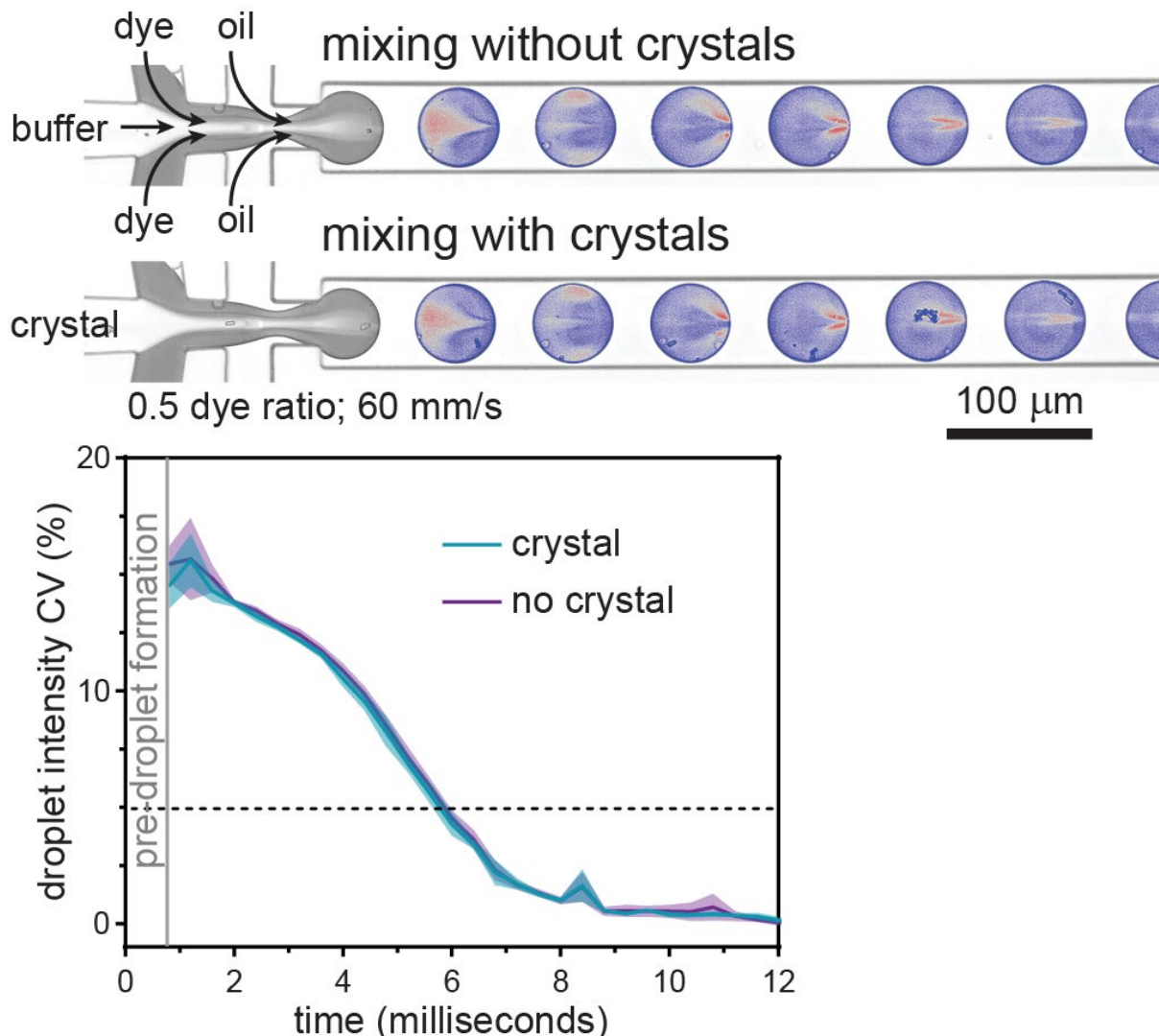


Figure 64. The presence of crystals does not affect mixing times in droplets. High speed microscopy allows the observation of mixing during droplet generation and transport within a microchannel. Droplets have been colour-enhanced to allow easier observation of the mixing process. Image analysis involved 12 droplets with crystals and 10 droplets without crystals. The droplet pixel intensity CV is plotted as the mean \pm SD, with and without crystals.

With the knowledge that the presence of crystals did not affect mixing time, the next test was to understand the effect of crystal to dye ratio. At a set velocity of 300 mm/s, the volume fraction of dye was increased from 0.1 to 0.5, leading to a reduction in mixing time (Figure 65A). The optimal dye ratio was achieved at 0.5 or more simply a 1:1 ratio by volume of crystal suspension to dye, equating to a mixing time of 1.73 milliseconds (Figure 65A). This observation supports the 'entropy of mixing' theory (293), which suggests that mixing is most efficient when the initial volumes of the component liquids are equal. Gibbs free energy is lowest and entropy is highest resulting in fast mixing. However, once you deviate from the optimal 1:1 Gibbs-free energy driven mixing you begin to observe the evolution of mixing along the channel length. This effect is also observed when simply varying the flow ratios between a precipitant solution and red dye, without the need for crystals (Figure 65B).

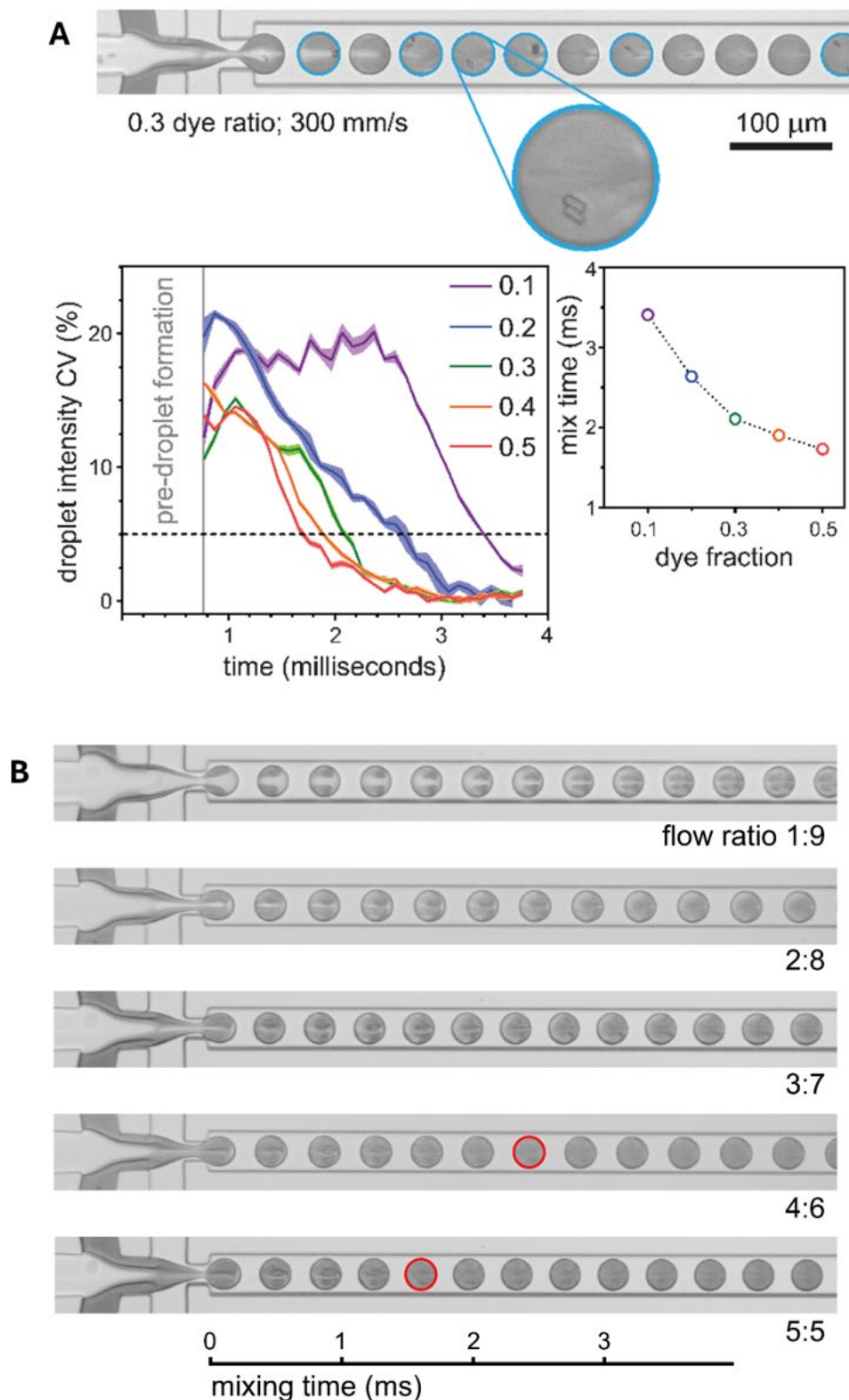


Figure 65. The ratio of components being mixed effects mixing times in droplets. (A) A high speed microscope frame of crystal and dye mixing at a dye ratio of 0.3 and a droplet velocity of 300 mm/s. Droplets containing crystals are highlighted with blue circles. The droplet pixel intensity CV is plotted as the mean \pm SD for 15 droplets for each ratio of crystal suspension to dye solution by volume. At a droplet velocity of 300 mm/s the mixing time decreases as the volume fraction of dye increases, with the optimal ratio of 0.5 resulting in mixing times sub 2 milliseconds. (B) Varying the ratio of precipitant solution (removing crystals) to red dye at a droplet velocity of 300 mm/s leads to rapid mixing within less than 2 milliseconds at a 5:5 flow ratio (1:1).

Taking this further, the effect of droplet velocity on mixing time was tested. Applying the optimal 1:1 ratio of crystal to dye, the velocity was increased from 60 to 300 mm/s leading to increased circulations within the droplets. In addition, the higher velocity led to higher shear forces imparted during droplet generation, leading to a reduction in droplet volume from 126 to 39 pL (**Figure 66**). The smaller droplets provide a shorter diffusion path, resulting in mixing times as fast as 1.85 milliseconds at 300 mm/s and 6.0 ms at 60 mm/s (**Figure 66**). The current limit of droplet generation velocity is 300 mm/s, but smaller and higher velocity droplets would be anticipated to give faster mixing times. The mixing times observed with droplets is on par with the current state of the art in terms of GDVN co-flow mixers (2 ms) and exceeds mixing by other delivery systems such as drop-on-demand or drop-on-chip.

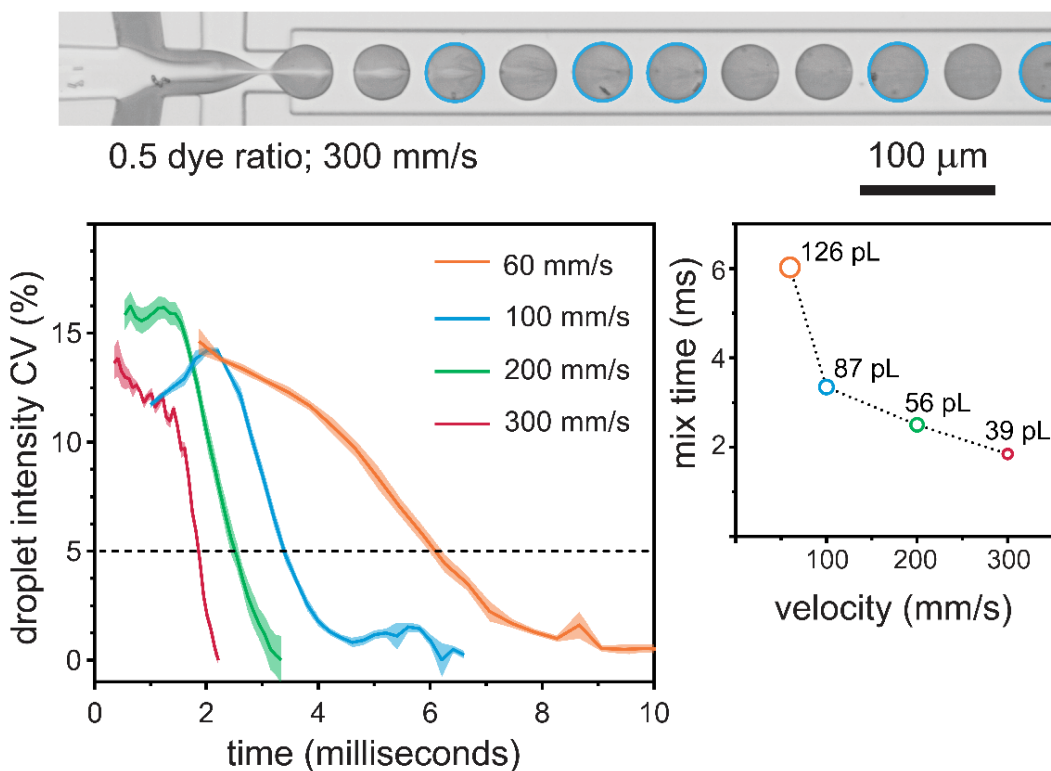


Figure 66. Increasing droplet velocity leads to faster mixing times. A high speed microscope frame of crystal and dye mixing at a dye ratio of 0.5 and a droplet velocity of 300 mm/s. Droplets containing crystals are highlighted with blue circles. The droplet pixel intensity CV is plotted as the mean \pm SD for 15 droplets. Increasing droplet velocity leads to increased circulations with droplets (convection) and reduces the droplet volume and diffusion paths allowing for fast mixing.

5.2 Fabrication of an X-ray transmissible droplet microfluidic device

When designing an X-ray transmissible microfluidic device for in-flow experiments at the beamline, it is crucial to consider how the device material interacts with X-rays. The primary factors include the diffraction strength from the protein crystals, the extent of scattering through the material, and most critically the attenuation caused by photon absorption, which reduces the intensity of the incident X-ray beam and compromises signal quality (294). At the same time, in-flow experiments demand robust device bonding and mechanical stability, often requiring thicker materials to prevent leakage and maintain consistent flow. This creates a design trade-off, with increased thickness improving structural integrity, but exacerbating radiative interference. Achieving optimal performance therefore requires a careful balance between minimising scattering and attenuation and ensuring mechanical reliability under beamline conditions.

5.2.1 Material feasibility testing of PDMS

PDMS was chosen as the material of choice due to its reliable device bonding and stable flow characteristics, which support consistent and uniform droplet generation. Building on the droplet crystallisation workflows outlined in the previous chapter, substantial insight was gained into optimal flow parameters for effective droplet formation. However, previous studies have noted that PDMS exhibits a high attenuation coefficient and poor X-ray transmission at increased material thicknesses. To evaluate the impact of PDMS thickness on background scattering, and critically, the signal-to-noise ratio, a series of experimental tests were conducted. Commercially available PDMS thin films with characterised thicknesses ranging from 20 to 200 μm were positioned in front of the X-ray interaction region at I24 beamline at Diamond Light Source, utilising a $7 \times 7 \mu\text{m}$ X-ray beam, operating at 100% transmission. Given literature reports that higher X-ray energies reduce attenuation (294), measurements were performed at both 12.4 and 20 keV. Consistent with theoretical predictions, PDMS produced an evident scattering ring at approximately 7.5 \AA , which intensified with increasing film thickness (**Figure 67**). Raising the X-ray energy to 20 keV attenuated this scattering feature, with the 20 μm film displaying only a weak ring (**Figure 67**). Notably the 50 μm film at 20 keV exhibited multiple scattering rings, likely originating from residual contaminants associated with the plastic backing used during shipping of the commercial PDMS films.

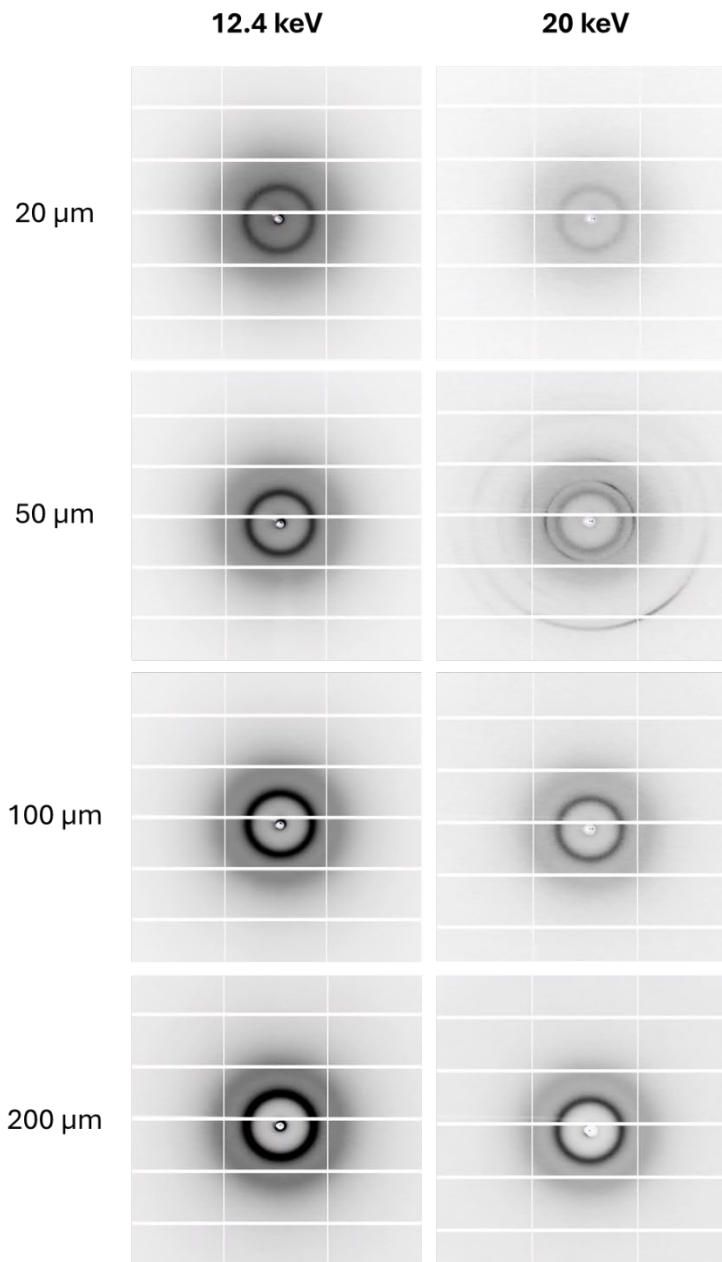


Figure 67. Effect of PDMS film thickness and X-ray energy on background scattering. A characteristic PDMS scattering ring at $\sim 7.5\text{\AA}$, increasing in intensity with film thickness at both 12.4 and 20 keV. The higher X-ray energy of 20 keV reduced ring prominence, with 20 μm films showing minimal background scattering.

Given that an X-ray energy of 20 keV was identified as optimal for minimising PDMS-induced background scattering, control experiments were performed to assess the severity of background scattering. The first condition involved no material in the X-ray path, capturing scattering solely from air. The second used a 6 μm thick mylar film, commonly used to seal aperture-aligned fixed target setups and prevent crystal dehydration. As anticipated, both conditions produced negligible background scattering, with no detectable scattering rings observed in the collected diffraction patterns (Figure 68).

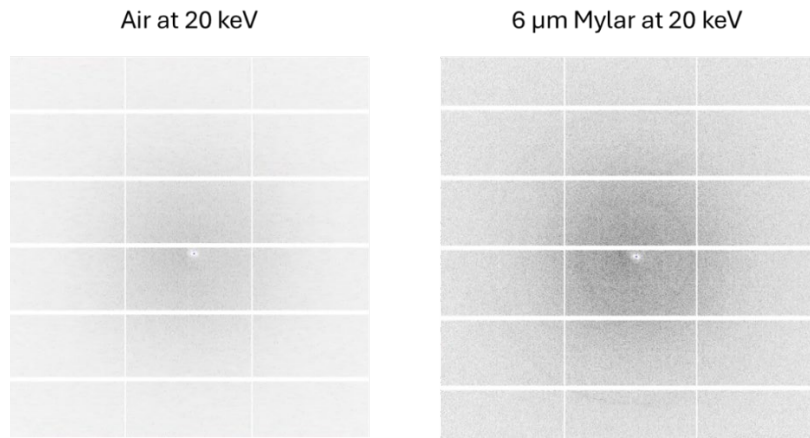


Figure 68. Control measurements of background scattering for air and 6 μm thick mylar. Diffraction patterns of air and 6 μm thick Mylar showing negligible background scattering, following X-ray interaction.

To quantify PDMS-induced background scattering further, diffraction patterns were analysed using the program *dials.background* to extract absolute scattering values. As expected, increasing PDMS thickness led to elevated background scattering, with values exceeding 100 arbitrary units for the 200 μm film at 12.4 keV (Figure 69). Notably, raising the X-ray energy to 20 keV resulted in an approximate 10-fold reduction in background scattering for the same thickness, confirming the energy-dependent behaviour of PDMS (Figure 69). Interestingly, the peak background scattering at 12.4 keV was observed at $\sim 6.5 \text{ \AA}$, deviating from the commonly reported $\sim 7.5 \text{ \AA}$ scattering ring. At 20 keV, this peak shifted towards the expected 7.5 \AA position, suggesting an energy-dependent modulation of the dominant scattering feature.

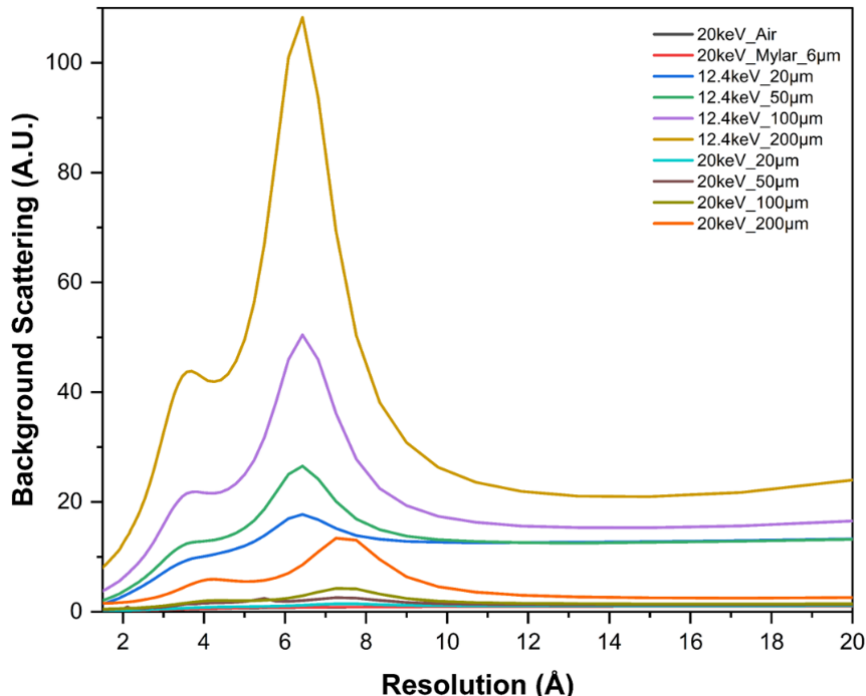


Figure 69. PDMS-induced background scattering as a function of film thickness and X-ray energy. Background scattering profiles extracted using *dials.background* are plotted against resolution (\AA). Thicker PDMS films and lower X-ray energies yield higher background levels, with dominant scattering peaks observed at $\sim 6.5 \text{ \AA}$ for 12.4 keV and $\sim 7.5 \text{ \AA}$ for 20 keV.

Subsequently, peak background scattering values were extracted from the diffraction patterns, further confirming that increased PDMS thickness substantially amplified background scattering, by nearly sixfold at an X-ray energy of 12.4 keV (**Figure 70**). This effect is markedly attenuated at 20 keV, where peak background values reach only ~10 arbitrary units even at the maximum thickness of 200 μm (**Figure 70**).

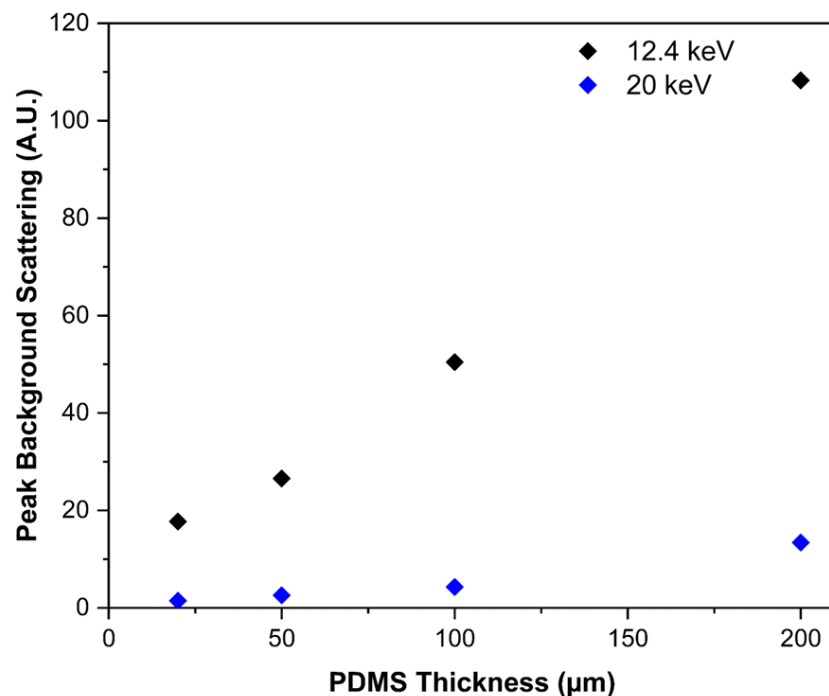


Figure 70. Peak background scattering from PDMS across varying film thicknesses and varying X-ray energies. Peak scattering values were extracted from diffraction patterns using *dials.background*. Peak background scattering values across PDMS thickness (20 to 200 μm) at 12.4 keV and 20 keV, highlighting the attenuation effect at higher energy.

With PDMS attenuation and scattering properties characterised, the final feasibility test assessed its suitability for diffraction data collection from protein crystals, ensuring acceptable signal-to-noise ratios could be achieved. A thin-film, chipless chip sample delivery method (116) was employed, whereby a 3 μL volume of 20 – 25 μm lysozyme microcrystals (**Figure 71A**) was sandwiched between a 6 μm mylar film and a 100 or 200 μm PDMS thin film. This assembly was mounted onto the beamline goniometer using a magnetic tweezer pin (**Figure 71B**). Data collection involved selecting a crystal-rich region and generating a raster grid for scanning, following a directed-raster approach, analogous to fixed-target setups (**Figure 71C**).

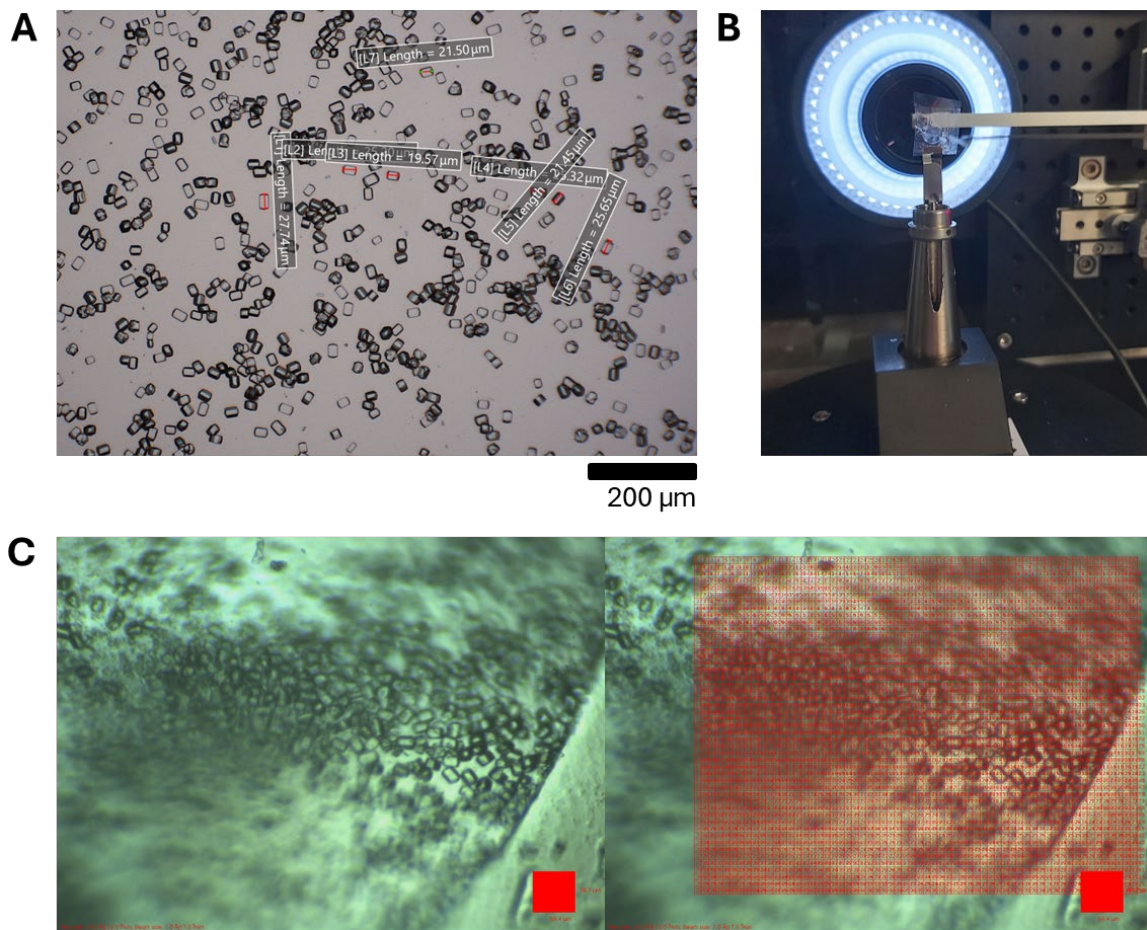


Figure 71. X-ray diffraction testing of lysozyme microcrystals embedded in PDMS thin-film assemblies. (A) Lysozyme microcrystal slurries (20 – 25 µm) prepared for diffraction testing. (B) Experimental setup showing a 6 µm mylar film containing the microcrystal slurry adhered to either a 100 or 200 µm PDMS thin film, mounted onto the beamline goniometer using a magnetic tweezer pin. (C) Microcrystals visible within the circular region of the sample assembly, with an overlaid raster grid used for X-ray diffraction data collection.

A total of four grid scans were performed for each PDMS thickness (100 and 200 µm) at X-ray energies of 12.4 keV and 20 keV. To assess diffraction data quality across these conditions, datasets were processed by merging 1888 crystals using *dials.combine_experiments* and *dials.split_experiments*, whilst applying a high-resolution cutoff of 1.60 Å. Two key data quality metrics, CC_{1/2} and SNR were extracted and plotted against resolution for all four datasets. Increasing PDMS thickness and X-ray energy led to a reduction in CC_{1/2} values (**Figure 72A**), indicating diminished data correlation at higher resolution shells. A similar trend was observed for SNR (**Figure 72B**), attributed to increased X-ray attenuation from thicker PDMS and reduced photon flux at higher energies. Based on a CC_{1/2} cutoff of 0.3 and a SNR cutoff of 1.0, the 100 µm datasets support a realistic resolution cutoff of ~1.70 Å, while the 200 µm datasets are limited to ~1.80 Å.

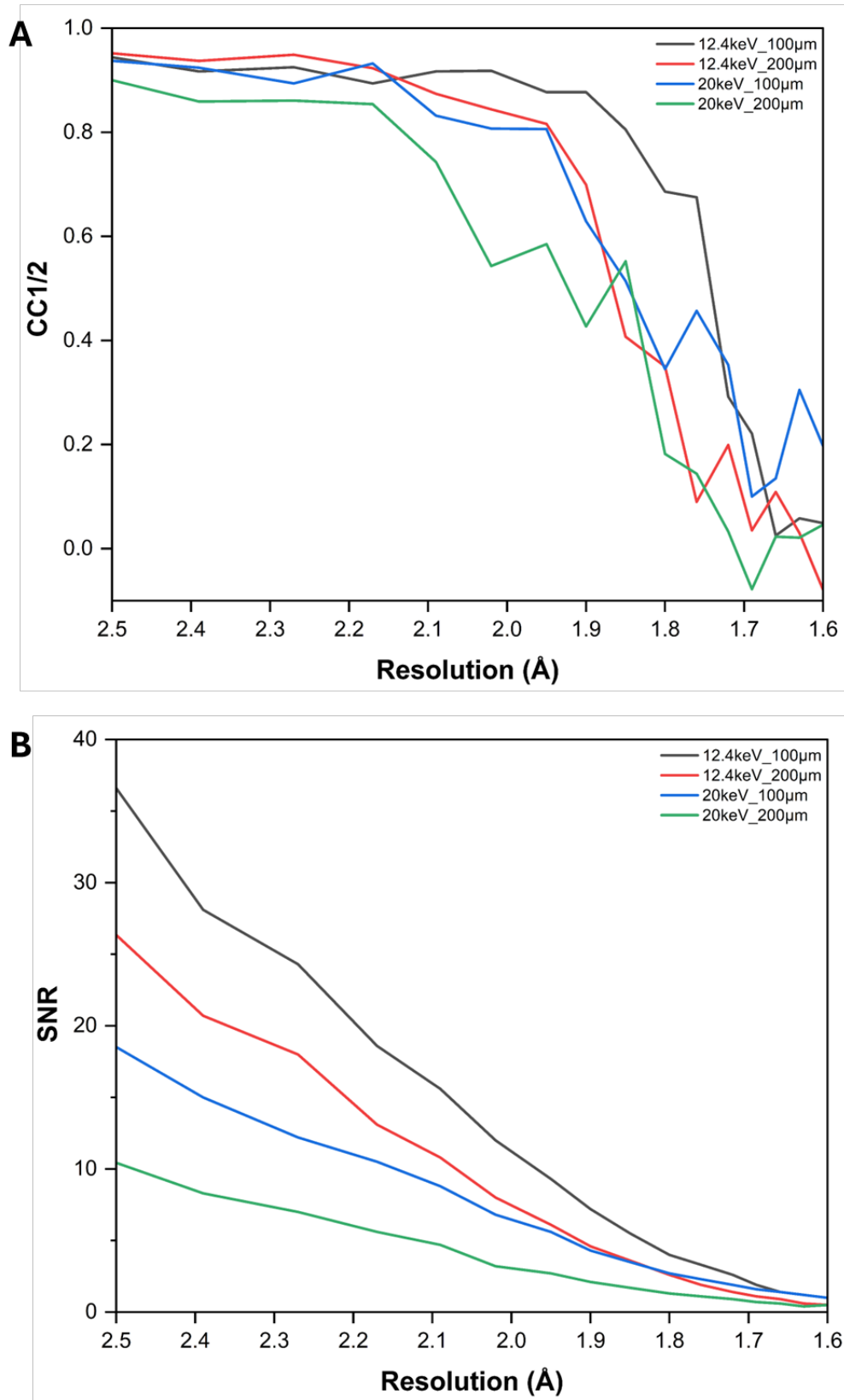


Figure 72. Effect of PDMS thickness and X-ray energy on diffraction data quality. (A) $CC_{1/2}$ values plotted against resolution for datasets collected using 100 μm and 200 μm PDMS films at 12.4 keV and 20 keV. (B) Signal-to-noise ratio (SNR) profiles for the same four conditions, highlighting attenuation effects from increased material thickness and X-ray energy.

5.2.2 Fabrication of a thin-film PDMS droplet microfluidic device for in-flow experiments at a beamline

Following the successful validation of PDMS as a viable material for thin-film sample delivery, the next phase focused on the design and fabrication of a microfluidic circuit compatible with time-resolved serial crystallography workflows. The aim was to develop a PDMS-based microfluidic device capable of mixing protein crystals with ligands in droplets under controlled flow conditions. Key design criteria included the ability to achieve millisecond mixing for capturing rapid biochemical reactions, while accommodating a broad dynamic range from milliseconds to seconds, to support diverse protein systems. Additionally, sample velocity at the X-ray interaction region needed to be optimised to ensure sufficient diffraction signal from crystals in flow.

To meet these requirements, a computer-aided design (CAD) of the microfluidic device was generated in preparation for SU-8 master fabrication (**Figure 73A**). The circuit incorporated three inlets for fluorinated oil, protein crystals, and ligand or crystallisation solution, with extended channel lengths to facilitate straightforward bonding during fabrication. As in the previous droplet crystallisation platform, integrated filters were positioned immediately downstream of the inlets to prevent foreign material from disrupting flow conditions. The crystal inlet featured slightly larger filter gaps to minimise clogging near the droplet generation junction. The droplet generation junction employed a flow-focusing geometry with a width of 60 µm and a height of 40 µm. Downstream, channel widenings were introduced to reduce sample velocity and create a localised region for X-ray interaction and alignment (position 1, **Figure 73A**). Serpentine channels followed, enabling droplet incubation within a compact footprint (position 2, **Figure 73A**). To accommodate longer timepoints, a series of eleven widened incubation cells were incorporated, interspersed with narrow constrictions to sequentially decelerate and accelerate droplets (position 3 and 4, **Figure 73A**).

The CAD design was sent to MicroFIT (South Korea) for SU-8 master fabrication. This process involved spin-coating SU-8 onto a silicon wafer, followed by heat curing ensuring a uniform thickness. The CAD pattern was then transferred via UV exposure, and the desired microstructures developed with a solvent (**Figure 73B**). Prior to shipment, the SU-8 master was measured using a digital length gauge, confirming a final height of 40.9 µm (**Figure 73C**). Upon receipt, a large PDMS replica was cast for polyurethane counter moulding. A PDMS device was plasma bonded to a glass slide for quality control, which confirmed the high-fidelity reproduction of microstructures as specified in the CAD design (**Figure 73D**).

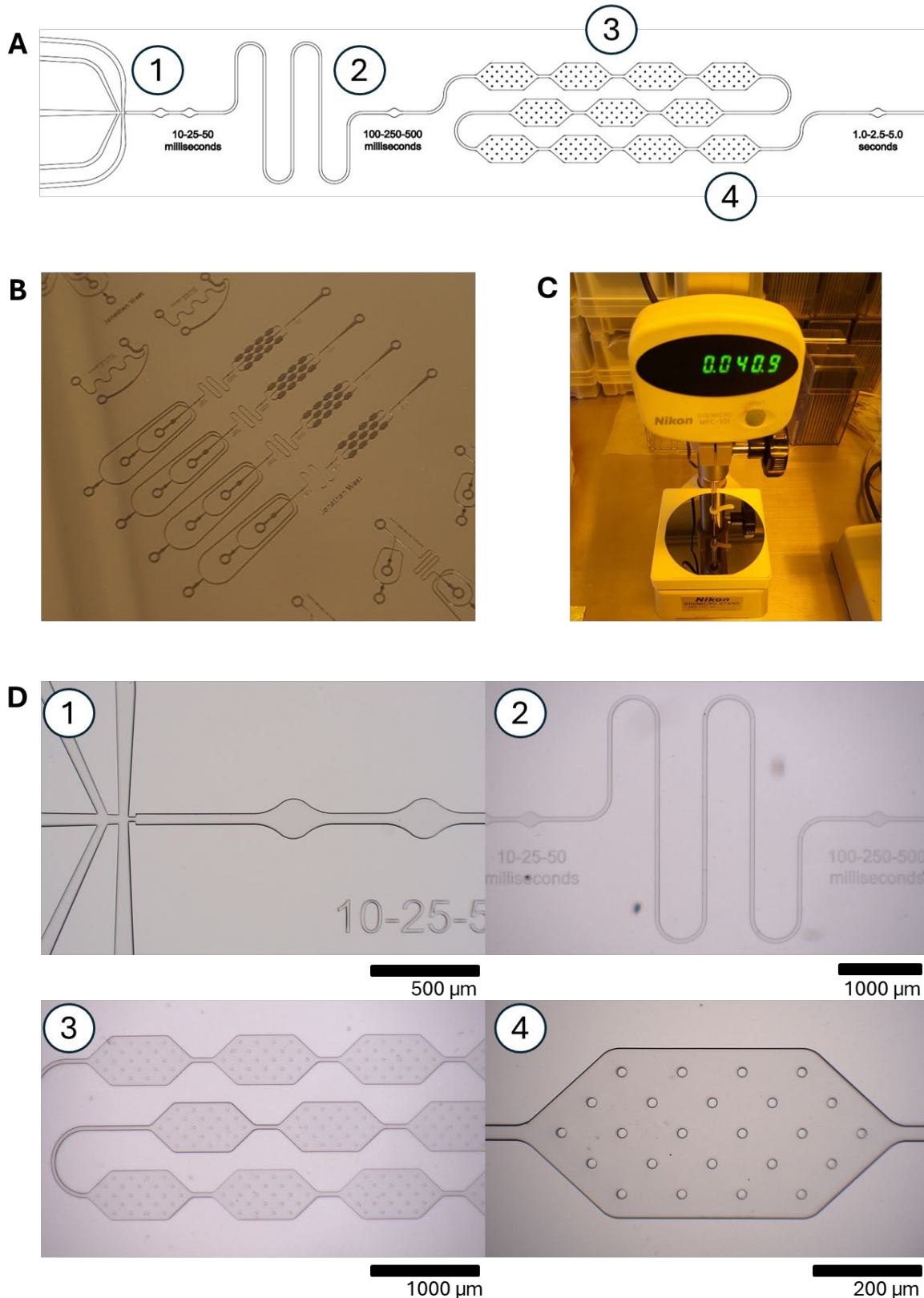


Figure 73. Droplet microfluidic device design for time-resolved serial crystallography. (A) CAD rendering of the microfluidic circuit, highlighting key design features: (1) channel widenings to reduce droplet velocity and defined a localised X-ray interaction region, (2) serpentine channels for droplet incubation, (3) a series of eleven widened incubation cells with narrow constrictions to modulate droplet velocity for longer timepoints, (4) a final widened cell leading to the terminal X-ray interaction region and device outlet. (B) Fabricated SU-8 master exhibiting the intended microstructures. (C) SU-8 master height measured at 40.9 μm using a digital length gauge. (D) Light microscopy images acquired with a Hirox microscope confirming high-fidelity reproduction of desired microfluidic features from the CAD design.

To translate the geometric design into experimentally useable timepoints, flow rate and velocity calculations were performed based on the channel dimensions (60 μm width x 40 μm height) and desired temporal resolution range of 5 milliseconds to 5 seconds. These calculations enabled estimation of droplet residence times at key regions of the device, particularly the X-ray interaction regions and incubation segments. By correlating flow velocity with channel length, it was possible to map specific timepoints to physical locations within the circuit, thereby guiding experimental setup and data collection strategies.

A channel cross-sectional area of $2.4 \times 10^{-3} \text{ mm}^2$ was used to derive flow velocities from volumetric flow rates. Three flow rates, 5 $\mu\text{L}/\text{min}$, 10 $\mu\text{L}/\text{min}$ and 25 $\mu\text{L}/\text{min}$ were selected based on prior success in droplet crystallisation workflows and their compatibility with stable droplet formation and transport with an oil-to-aqueous flow rate ratio of 4:1. These correspond to linear velocities of 34.7, 69.4 and 173.6 mm/s , respectively. X-ray interaction regions were positioned downstream of the droplet generation junction according to these calculated velocities, ensuring accurate temporal targeting during serial data collection. The spatial offsets and corresponding timepoints for each flow condition are summarised in **Table 14**.

Table 14. Calculated X-ray interaction distances and corresponding timepoints for selected flow rates in the droplet microfluidic device.

Q_{Total} ($\mu\text{L}/\text{min}$)	Velocity (mm/s)	Distance from droplet generation junction	Timepoint	Distance from droplet generation junction	Timepoint	Distance from droplet generation junction	Timepoint
5	6.94	350 μm	50 ms	3.47 mm	500 ms	34.72 mm	5 s
10	13.88	350 μm	25 ms	3.47 mm	250 ms	34.72 mm	2.5 s
25	34.72	350 μm	10 ms	3.47 mm	100 ms	34.72 mm	1 s

To confirm that the selected flow rates yielded droplets of consistent size and predictable behaviour, droplet diameters were experimentally validated across all conditions using the 60 μm wide x 40 μm high channel. All three flow rates (5 $\mu\text{L}/\text{min}$, 10 $\mu\text{L}/\text{min}$ and 25 $\mu\text{L}/\text{min}$) produced monodisperse droplets, with stable flow profiles established within minutes of initiating syringe pump infusion. Increasing the flow rate from 5 to 25 $\mu\text{L}/\text{min}$ resulted in a reduction in droplet diameter CV from 3.01 to 1.37 %, indicating improved uniformity at higher flow rates. The mean droplet diameter reduced from 40.78 μm at 5 $\mu\text{L}/\text{min}$ to 38.49 μm at 25 $\mu\text{L}/\text{min}$, although a slight increase was observed at 10 $\mu\text{L}/\text{min}$, suggesting that flow stabilisation may not have been fully achieved. Full droplet diameter statistics are shown in **Table 15**. The intended channel widening from 40 μm to 200 μm at the X-ray interaction regions led to a marked reduction in flow velocity, resulting in visible bunching within the expanded

region (**Figure 74**). Upon re-narrowing of the channel, droplets reaccelerated. This geometry-induced modulation supports extended residence times for time-resolved data collection.

Table 15. Droplet diameter measurements from the droplet microfluidic devices.

Q_{Total} ($\mu\text{L}/\text{min}$)	Minimum droplet diameter (μm)	Maximum droplet diameter (μm)	Mean droplet diameter (μm)	Standard deviation	Droplet diameter CV (%)
5	38.13	43.71	40.78	1.23	3.01
10	38.02	44.17	41.13	1.01	2.45
25	37.15	39.97	38.49	0.53	1.37

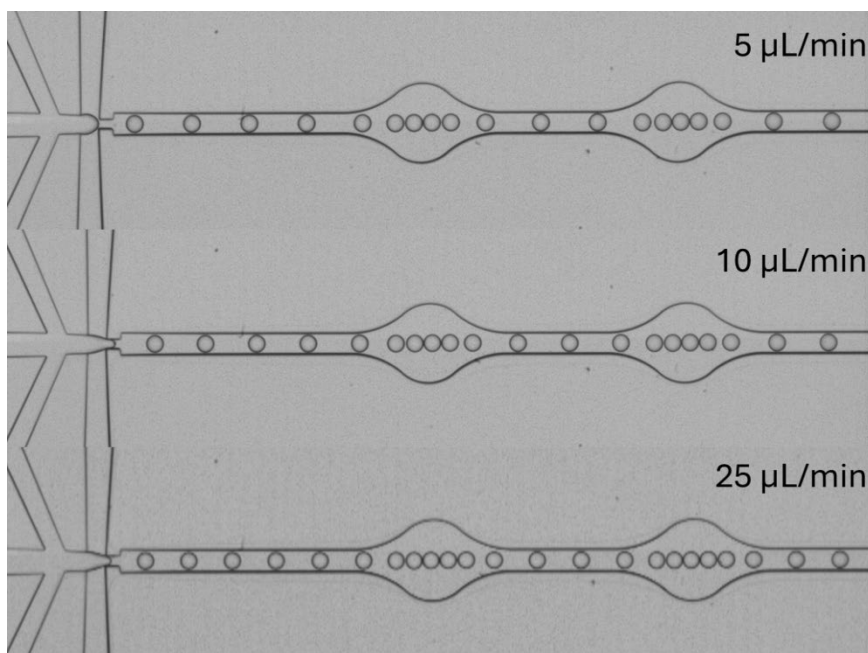


Figure 74. Effect of channel widening on droplet velocity and spacing. Light microscope images showing droplet behaviour at the X-ray interaction region. Channel expansion from 40 to 200 μm resulted in reduced flow velocity and droplet bunching, followed by reacceleration upon channel narrowing.

To assess the uniformity of incubation times across the eleven widened incubation cells (**Figure 75A**), experiments were conducted at three flow rates: 5 $\mu\text{L}/\text{min}$, 10 $\mu\text{L}/\text{min}$ and 25 $\mu\text{L}/\text{min}$. Protein crystals within droplets served as visual markers, enabling manual tracking of droplet movement using ImageJ (**Figure 75B**). For each flow condition, the number of video frames required for a droplet to traverse each individual cell, from the first to the eleventh was recorded. These frame counts were converted to residence times based on the acquired frame rate, and the CV was calculated for each cell to quantify temporal consistency. This analysis provided insight into how effectively the widened geometry maintained uniform incubation across droplets, and whether flow modulation introduced variability in residence time distribution. Across all three flow conditions, increasing the number of expansion cells helped compensate for variability in the residence time of droplets within individual cells, leading to more consistent overall residence times, with final CV values dropping below 4% (**Figure 75C**).

This low CV indicates that droplets arriving at the furthest X-ray interaction region do so with highly consistent incubation times, regardless of the flow rate. Despite this geometric complexity introduced by the eleven expansion cells, the system maintains temporal uniformity, ensuring that structural snapshots collected at the final X-ray interaction region correspond to well-defined and reproducible timepoints. This minimises temporal blurring and enhances confidence in assigning mechanistic interpretations in time-resolved diffraction data.

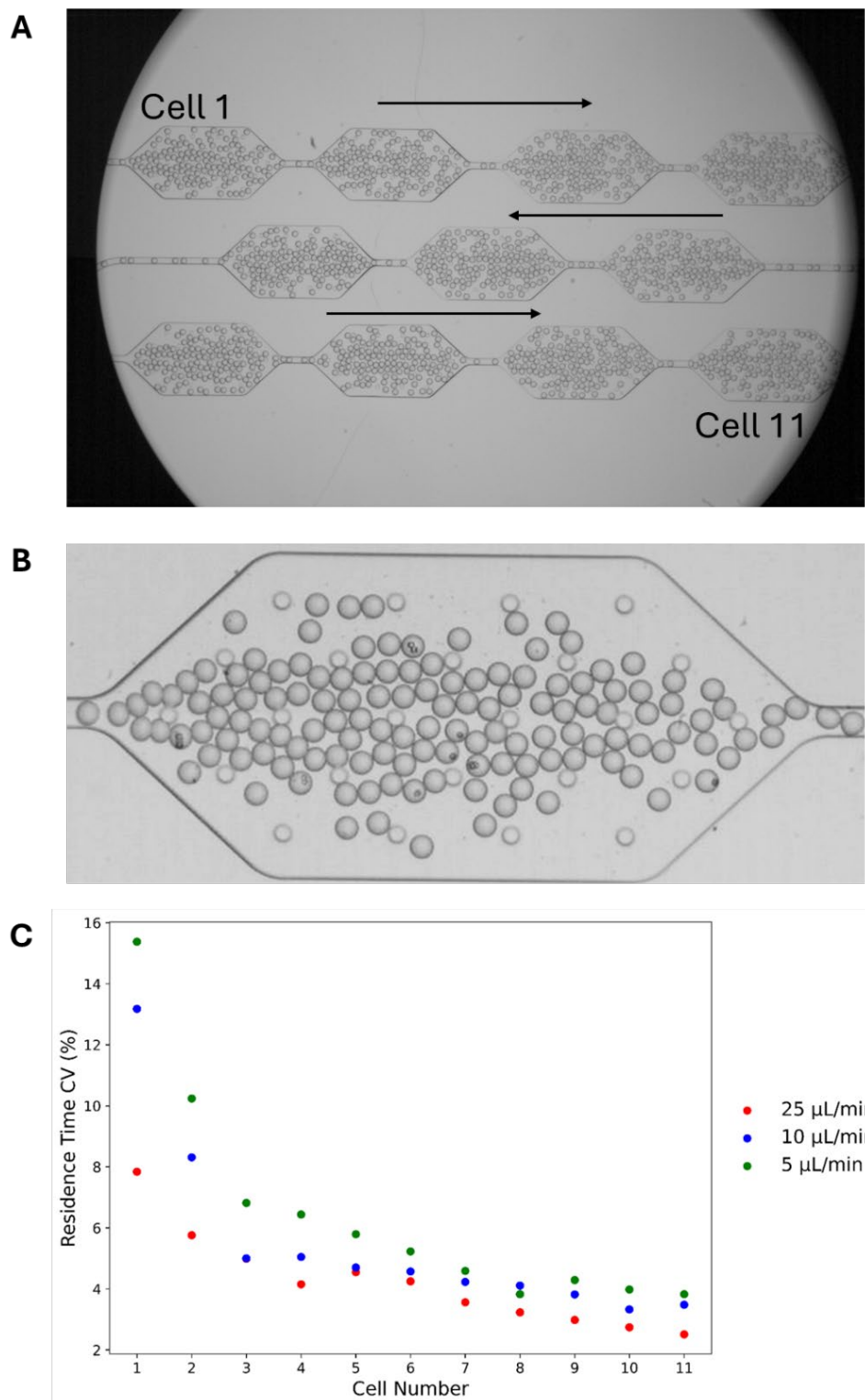


Figure 75. Assessment of droplet residence time uniformity across eleven widened incubation cells. (A) Schematic of the widened incubation region comprising eleven expansion

cells. (B) Representative image of crystal-containing droplets with the expansion cell allowing manual tracking of droplets for determining residence time. (C) Residence time CV plotted across cells for flow rates of 5, 10 and 25 $\mu\text{L}/\text{min}$. CV values converge below 4% by the final cell indicating uniform incubation times.

Following validation of droplet uniformity and temporal precision within the microfluidic circuit, fabrication efforts shifted towards developing a thin-film PDMS assembly compatible with synchrotron beamline conditions. Material feasibility testing indicated that minimising PDMS thickness was ideal to reduce background scattering. However, as previously stated, this is not always possible, and there must be a compromise to ensure robust device bonding and mechanical stability under flow conditions. Additional design constraints stemmed from the need to introduce sample via tubing, which required tight, undisturbed fittings to prevent leakage and flow disruption.

To address these challenges, a three-layer PDMS assembly was devised. The bottom layer consisted of a commercially available PDMS thin film with a characterised thickness of 100 μm , selected for its low X-ray scatter and uniformity. The middle layer housed the microfluidic structures and posed fabrication difficulties due to the need for reduced thickness. Initial attempts involved mixing PDMS with chloroform to lower viscosity, allowing controlled dispensing onto a polyurethane mould. However, the most effective strategy proved to be direct pouring of small PDMS volumes (1 – 2 g) into the mould placed on a 90 °C hot plate, which resulted in progressive spreading of the material and subsequent curing. This method yield middle layer thicknesses between 500 to 750 μm , although with some non-uniformity across the film. The top layer was fabricated by casting a large volume of PDMS into a square petri dish containing a laser-cut block. This introduced a hole in the thick top layer, defining the X-ray interaction region such that only the bottom and middle layers were exposed during data collection. Bonding was performed in two stages. First, plasma bonding of the top layer to the middle layer followed by overnight curing, then bonding of the combined top-middle assembly to the bottom thin-film. After final curing, the channel surfaces were functionalised with 1% (v/v) tri-chloro-(1H,1H,2H,2H-perfluoro-octyl) silane to ensure droplet compatibility and prevent wetting. A representative image of the final thin-film PDMS device assembly is shown in **Figure 76**.

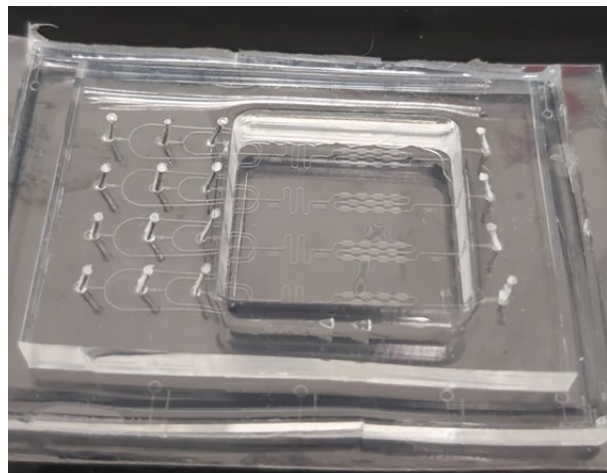


Figure 76. Thin-film PDMS microfluidic assembly for synchrotron experiments. Image showing the completed three-layer PDMS device designed for time-resolved serial crystallography experiments. The assembly consists of a bottom 100 μm commercial PDMS thin film layer, a microstructured middle layer, and a thick top layer with a laser-cut aperture defining the X-ray interaction region.

To further support beamline compatibility and mitigate common sample handling challenges, two auxiliary components were developed. These included a 3D-printed holder for device stabilisation and a perpetual sedimentation system designed to counteract crystal settling during data collection. The 3D-printed holder, kindly fabricated by Jacob Kleboe (University of Southampton), ensures secure positioning of the PDMS device within the beamline environment (Figure 77A). Its modular design accommodates varying device geometries, while the integration of a Thorlabs kinematic mount enables rapid integration with existing Thorlabs translation stages, currently employed in many beamline fixed-target setups. This compatibility streamlines experimental transitions and reinforces the platform's adaptability across beamline infrastructures.

Complementing this, a perpetual sedimentation system originally developed by Simon Lane and Jonathan West (University of Southampton) was repurposed with minor modifications to suit the demands of serial crystallography (Figure 77B). The system maintains crystal suspensions through gentle, continuous agitation, effectively preventing gravitational settling and preserving sample homogeneity (173). Crucially, the design incorporates a coaxial rotating interface that decouples the syringe from the stationary outlet tubing, allowing uninterrupted rotation without entangling the fluidic connections. This open instrumentation approach enables consistent delivery of particulate samples to microfluidic processors and is particularly well suited for maintaining fragile crystal suspensions. This is particularly critical for dilute or polydisperse microcrystal slurries, where sedimentation can lead to inconsistent delivery and reduced hit rates. Experimental validation was performed using lysozyme microcrystal slurries, demonstrating that the system sustained continuous crystal delivery during droplet generation in a glass/PDMS microfluidic device (Figure 77C). It successfully prevented clogging and crystal

accumulation, even at densities up to 2 million crystals/ mL, well within the operational range for beamline experiments. A key advantage of the system is its remote operability via a graphical user interface, allowing real-time control of agitation and flow rates without requiring physical access to the experimental hutch.

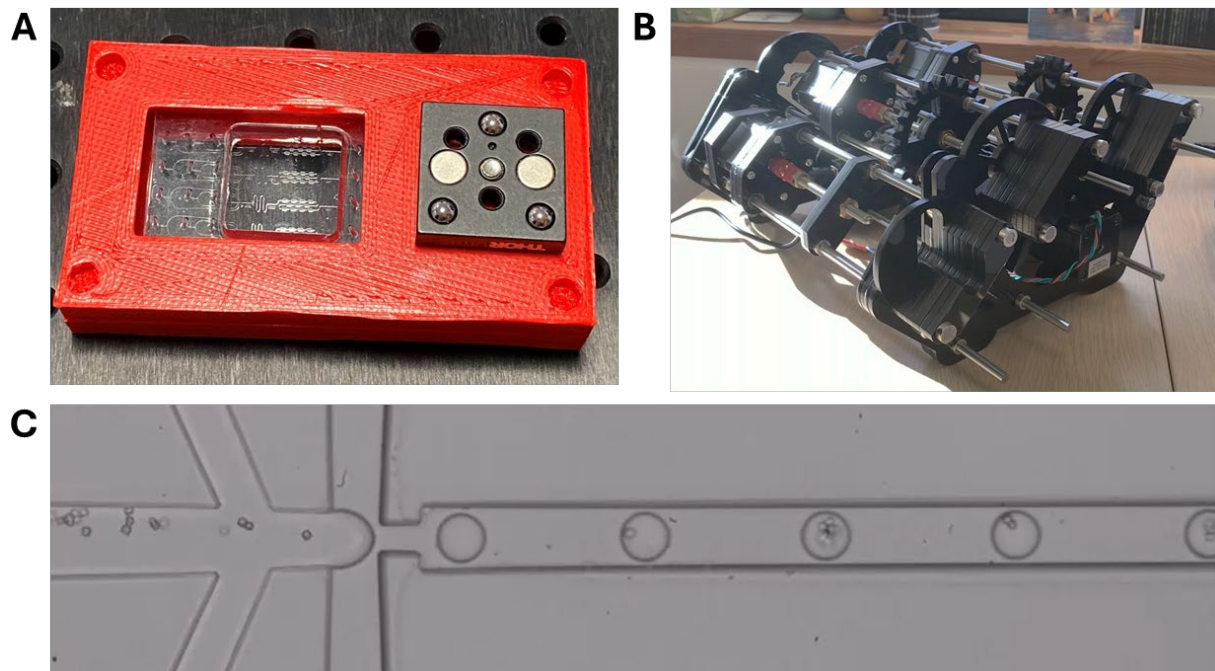


Figure 77. Supplementary equipment for enhanced beamline functionality. (A) Custom 3D-printed sample holder designed for direct mounting on Thorlabs fixed-target translation stages, enabling stable sample positioning. (B) Perpetual sedimentation system engineered to counteract crystal settling, ensuring continuous suspension and reliable delivery of microcrystals into the droplet stream. (C) Integrated droplet microfluidic system with sedimentation system in operations, demonstrating uninterrupted crystal delivery and clog-free droplet generation.

5.3 N-Acetylglucosamine (GlcNac) binding to lysozyme, a proof-of-principle experiment for time-resolved mixing

To assess the performance of the droplet microfluidic device for time-resolved serial crystallography, N-Acetylglucosamine (GlcNac) bound to lysozyme was selected as a model system. This choice was informed by prior work employing a drop-on-demand sample delivery system to capture GlcNac binding at discrete timepoints ranging from 200 milliseconds to 2 seconds (148). Although, theoretical diffusion times for GlcNac into a $5 \times 5 \times 5 \mu\text{m}$ lysozyme crystal (based on a diffusion coefficient of $4.2 \times 10^{-6} \text{ cm}^2\text{s}^{-1}$ (295)) are approximately 2 milliseconds (181), experimental data revealed a significant delay in ligand occupancy. Specifically, GlcNac was absent at 200 milliseconds, partially visible at 600 milliseconds, and fully resolved only at the 2 second timepoint (Figure 78). This discrepancy between predicted and observed kinetics underscores the suitability of this system for benchmarking device performance and probing the temporal resolution of ligand binding events.

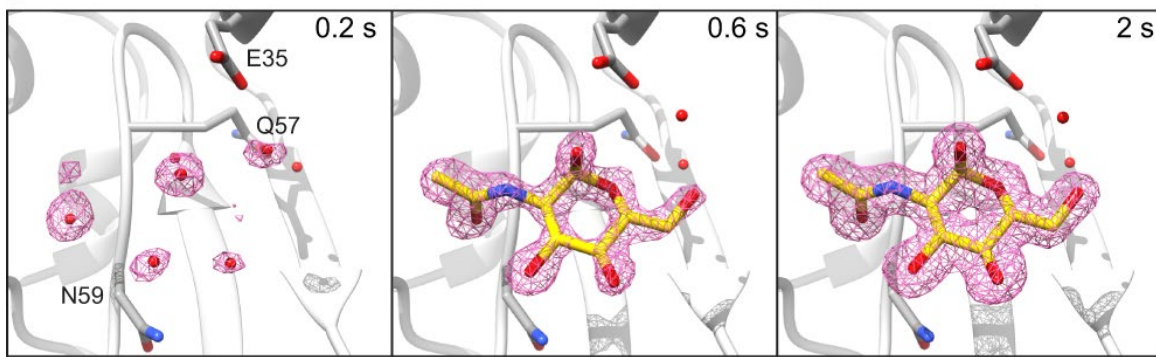


Figure 78. Time-resolved crystallographic snapshots of GlcNac binding to lysozyme using drop-on-demand sample delivery. 2F_o-F_c electron density maps illustrate ligand occupancy at 200 ms, 600 ms and 2 s following mixing of lysozyme microcrystal slurries with 50 mg/mL GlcNac. Image taken from Butrym *et al.* (148).

5.3.1 Validation of time-resolved GlcNac binding using a tapedrive-based sample delivery system

To confirm the reproducibility of GlcNac binding kinetics in lysozyme under time-resolved conditions, a series of experiments were conducted using a tapedrive-based sample delivery system at the ID29 beamline at ESRF (Figure 79A). This setup enabled co-flow mixing of microcrystals and ligand immediately prior to deposition onto a moving tape (Figure 79B). Microcrystal slurries and 50 mg/mL GlcNac solutions were loaded into syringe pumps and operated at a flow rate of 1 μ L/min (Figure 79C). To prevent sedimentation during data collection, an internal stirrer bead (NEMIX 50 syringe stirrer) maintained the crystal suspension (Figure 79C). Samples were transported through fused silica capillaries to a proprietary 3D-printed nozzle developed in-house at ESRF, where co-flow mixing took place (Figure 79D). The mixed stream was then ejected onto a 10 μ m thick hydrophilic polycarbonate membrane tape. Timepoints were defined by the distance between the nozzle and X-ray interaction region with a fixed tape speed of 30 mm/min. Using a Thorlab kinetic mount for precise distance calibration, mixing times of 500 millisecond (0.25 mm), 2 seconds (1.00 mm) and 5 seconds (2.5 mm) were achieved. Notably, because mixing occurs on the tape itself, the flow rates of crystal and ligand streams do not influence timepoint determination. This configuration enabled similar conditions under which delayed ligand occupancy was previously observed, providing a robust platform for benchmarking the temporal resolution of the droplet microfluidic device in subsequent experiments.

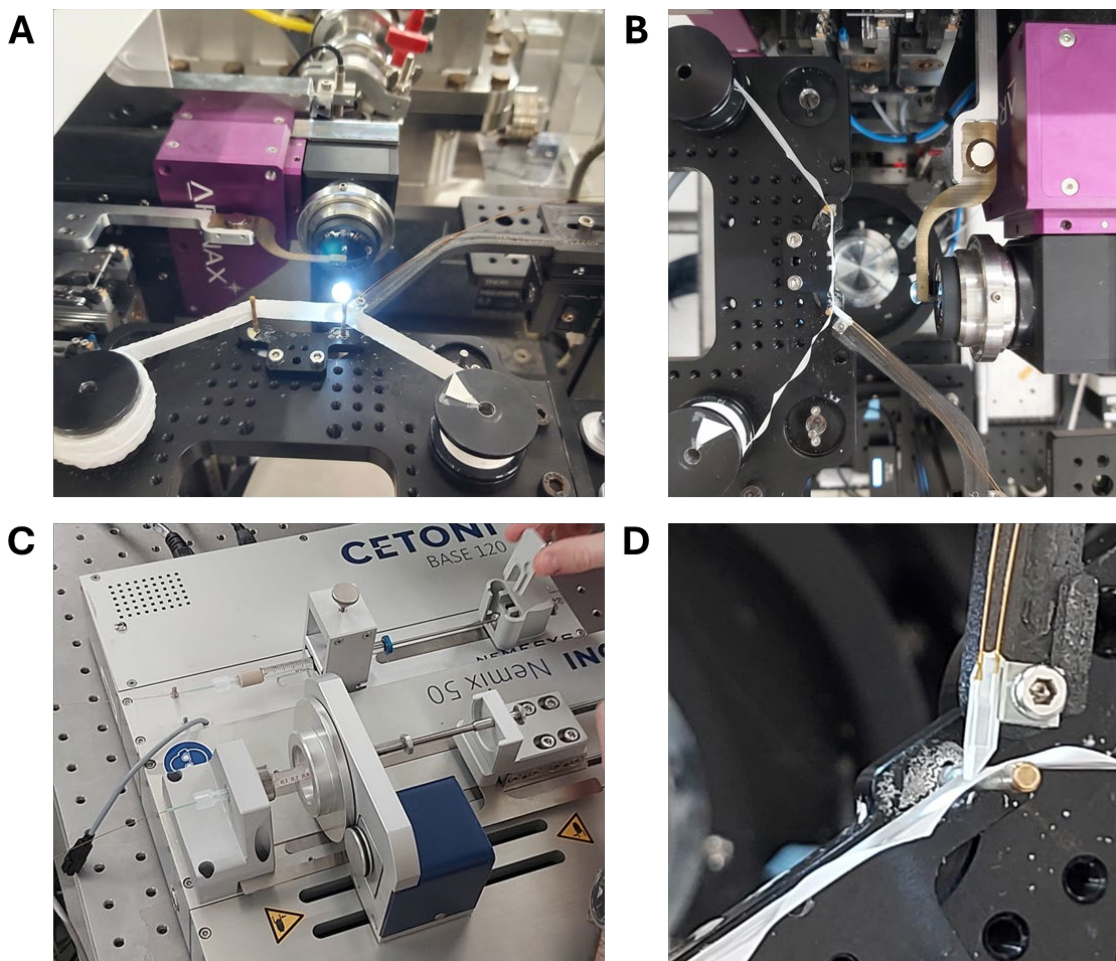


Figure 79. Experimental configuration of the tapedrive-based sample delivery system at ESRF ID29. (A) Front view of the tapedrive system with the nozzle approaching from the right. (B) Top-down view showing the nozzle entering from below, aligned for sample deposition. (C) Cetoni syringe pump setup with the upper syringe delivering GlcNac solution, while the lower syringe supplies crystal slurry. A built-in mixer prevents crystal sedimentation and ensure homogeneity. (D) Close up of the nozzle making contact with the tapedrive membrane tape, initiating sample deposition onto the moving tape.

To ensure reproducibility and compatibility with the tapedrive system, lysozyme microcrystal slurries were prepared using previously optimised batch conditions (163), yielding a narrow size distribution of 13 – 15 μm (Figure 80A). This uniformity facilitated synchronised reaction initiation and minimised the risk of clogging during sample delivery. As a baseline, an initial experiment was conducted without GlcNac to confirm the absence of ligand binding and to establish a reference dataset for subsequent time-resolved measurements. The resulting apo structure, resolved to 1.90 \AA (the current resolution limit of the tapedrive system at ESRF due to physical constraints and the detector distance of 150 mm from the sample), revealed water molecules occupying the canonical GlcNac binding site, flanked by residues E35, Q57 and N59 (Figure 80B). No GlcNac density was observed, as expected, validating the system's readiness for ligand mixing experiments. Time-resolved measurements were subsequently performed at three mixing intervals: 500 milliseconds (the shortest achievable timepoint with the ESRF tapedrive system), 2 seconds (to replicate prior data) and 5 seconds (to assess crystal integrity

at extended mixing times and maximise ligand occupancy). Polder and omit difference maps confirmed GlcNac binding at all three timepoints with minimal variation observed between them, likely attributable to the resolution limit of 1.90 Å (**Figure 80C**).

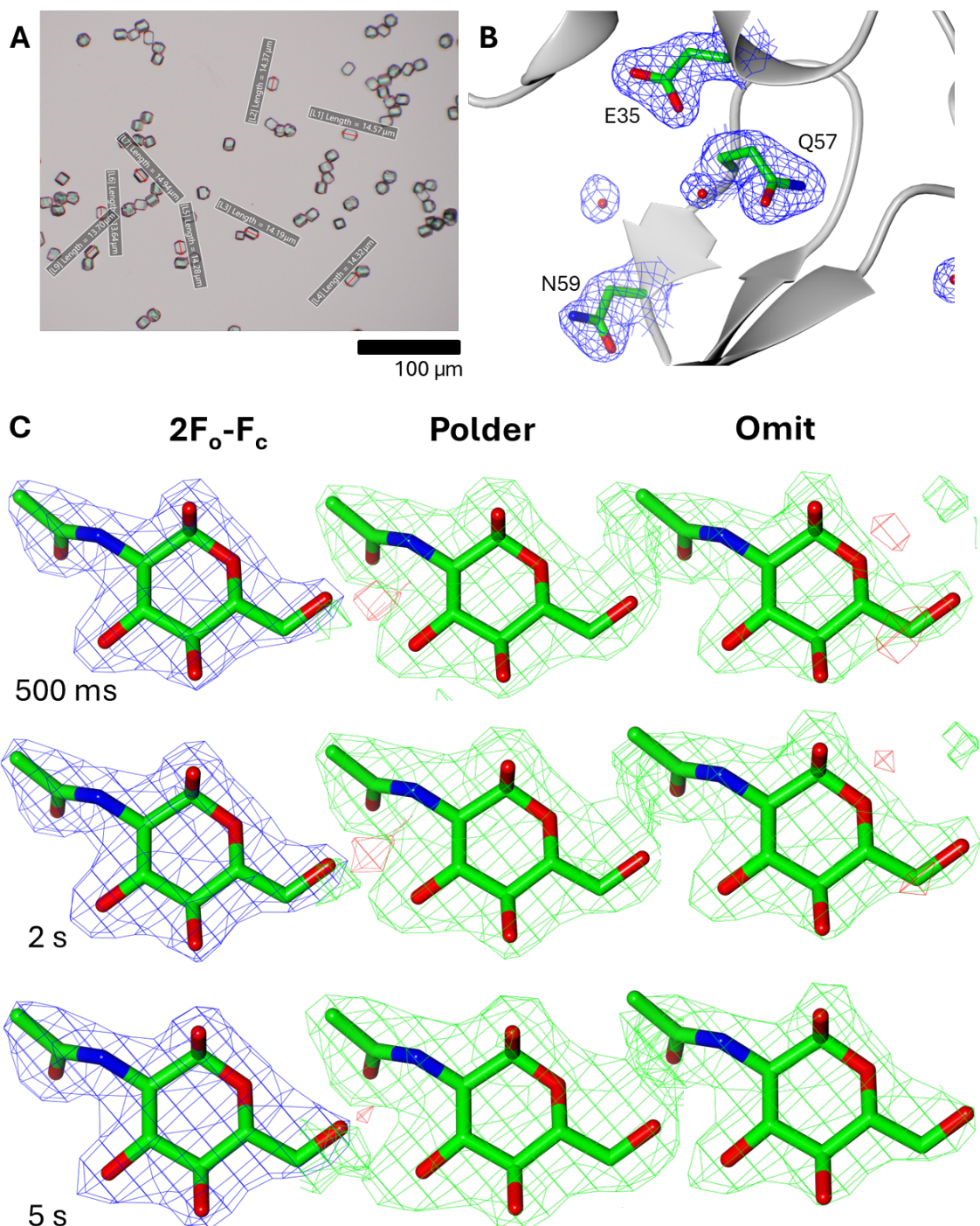


Figure 80. Time-resolved GlcNac binding via the ESRF tapedrive. (A) Lysozyme microcrystal slurries used during the experiment, measuring 13 – 15 μm . (B) Apo lysozyme with no GlcNac added confirming the presence of waters in the GlcNac binding site. (C) Electron density (contoured at 1 σ), polder and omit maps (contoured at 3 σ), for addition of 50 mg/mL GlcNac after 500 ms, 2 s and 5 s. Stick representation depicts carbon atoms as green, nitrogen atoms as blue and oxygen atoms as red.

5.3.2 Effect of GlcNac concentration on ligand occupancy

Building on the successful collection of time-resolved measurements of GlcNac binding to lysozyme microcrystals, the next focus was a variable that remains comparatively understudied in time-resolved crystallography: ligand concentration. In serial workflows, it is common practice to use an excess of ligand solution to maximise occupancy and enhance signal during time-resolved mixing experiments. However, the necessity of such high concentrations has not been systematically evaluated.

Inspired by a previous study which demonstrated that ligand binding constants could be directly measured within protein crystals (296), a series of equilibrium soaking experiments were designed to explore whether lower ligand concentrations could yield comparable occupancy. These experiments began with large single lysozyme crystals under cryogenic conditions, providing a simplified and controlled environment for evaluating binding behaviour. Crystals ranging from 200 – 300 μm were soaked in increasing concentrations of GlcNac for five minutes prior to cryo cooling in glycerol. An unsoaked crystal was also included as an apo reference. Each crystal underwent a 360 $^{\circ}$, 0.1 $^{\circ}$ fine-sliced rotation data collection strategy, yielding high-resolution datasets between 0.99 – 1.29 \AA . GlcNac molecules were modelled into the electron density maps for each concentration, followed by structural refinement and the generation of polder and omit maps, an approach previously established in earlier chapters to confirm the presence of ligands. As expected, the apo control structure showed no density for GlcNac, and similarly, the crystal soaked in 1 mg/mL GlcNac lacked discernible ligand density. In contrast, crystals soaked in concentrations ranging from 10 to 50 mg/mL exhibited clear electron density for GlcNac following refinement (**Figure 81**). Polder maps, and especially omit maps, revealed a progressive increase in difference density corresponding to the ligand, supporting concentration-dependent occupancy (**Figure 81**).

To extend the investigation of ligand concentration effects beyond cryogenic single crystal soaking, a parallel series of experiments was conducted using lysozyme microcrystal slurries under room-temperature conditions. This approach more closely mimics the environment of time-resolved serial crystallography experiments. Microcrystals slurries (13 – 15 μm) were allowed to settle before precipitant solution was entirely removed, leaving a concentrated crystal pellet, which was subsequently resuspended in GlcNac solutions ranging from 1 to 50 mg/mL (4.5 to 226 mM) for 5 minutes at room temperature. K_d would be inferred by measuring ligand occupancy in the crystal structure after soaking at known ligand concentrations. Assuming equilibrium conditions and constant ligand concentration, the degree of occupancy provides a basis for inferring binding affinity without requiring kinetic measurements.

Samples were loaded onto an SOSOS chip as before, followed by a directed-raster scanning strategy to collect diffraction data. This yielded high-resolution structures between 1.45 – 1.48 Å. The previous apo structure collected on the tapedrive system using the exact same microcrystal slurry was used as an apo reference dataset for comparison. Following refinement, GlcNAc molecules were modelled into the active site of lysozyme for each concentration. As with the cryogenic single crystal experiments, no ligand density was observed in the unsoaked or 1 mg/mL soaked slurry. Interestingly, the electron density, polder and omit maps from the microcrystal datasets revealed a less progressive build-up across the concentration series compared to the cryogenic single crystal experiments (Figure 82). Instead, high ligand occupancy was consistently observed from concentrations as low as 5 mg/mL, with relatively uniform density across the active site (Figure 82). This confirms that ligand diffusion into the microcrystals was both rapid and efficient, facilitated by reduced and homogenous crystal sizes (13 – 15 µm), along with increased mobility at room temperature. The absence of a steep concentration-dependent gradient in difference density implies that near-saturating occupancy was achieved within the five minute soaking window, even at modest ligand concentrations.

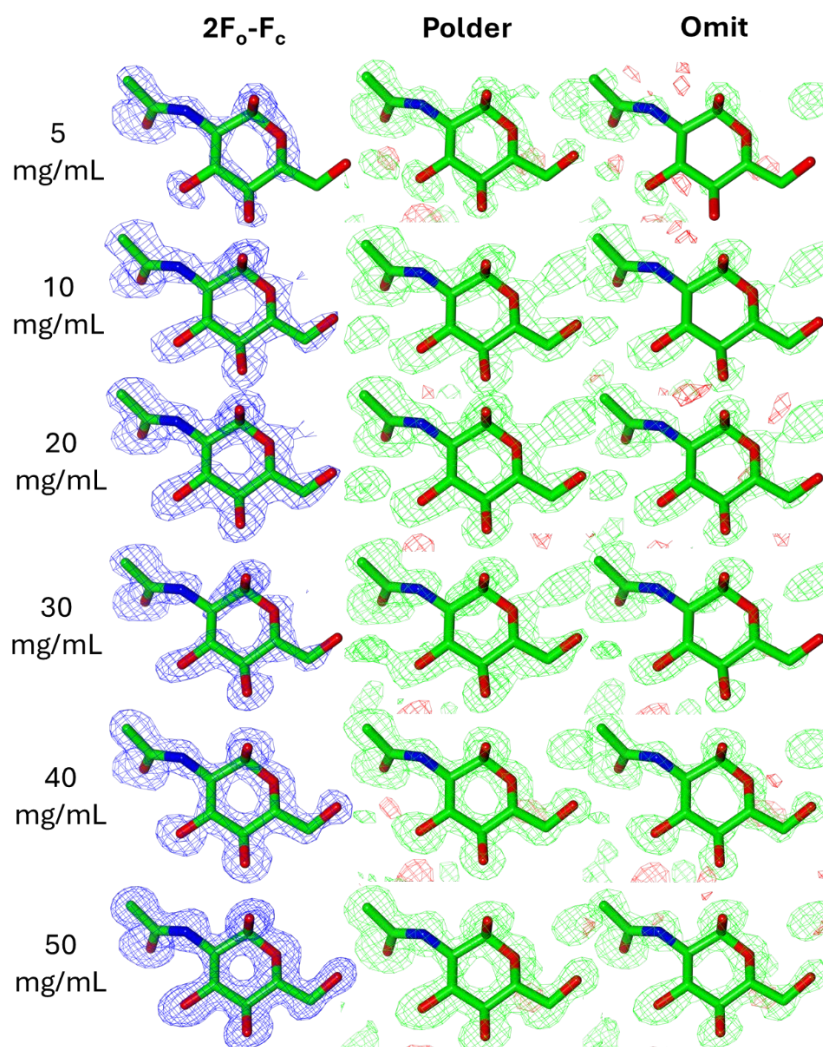


Figure 81. Electron density, polder, and omit maps of GlcNAc binding to single lysozyme crystals soaked with increasing ligand concentrations under cryogenic conditions. Electron

density maps (contoured at 1σ) and corresponding polder and omit maps (contoured at 3σ) are shown for lysozyme crystals soaked in GlcNac solution ranging from 5 to 50 mg/mL. Each map highlights the ligand-binding site following structural refinement. Together, these maps demonstrate a concentration-dependent increase in GlcNac occupancy within the lysozyme active site. Stick representation depicts carbon atoms as green, nitrogen atoms as blue and oxygen atoms as red.

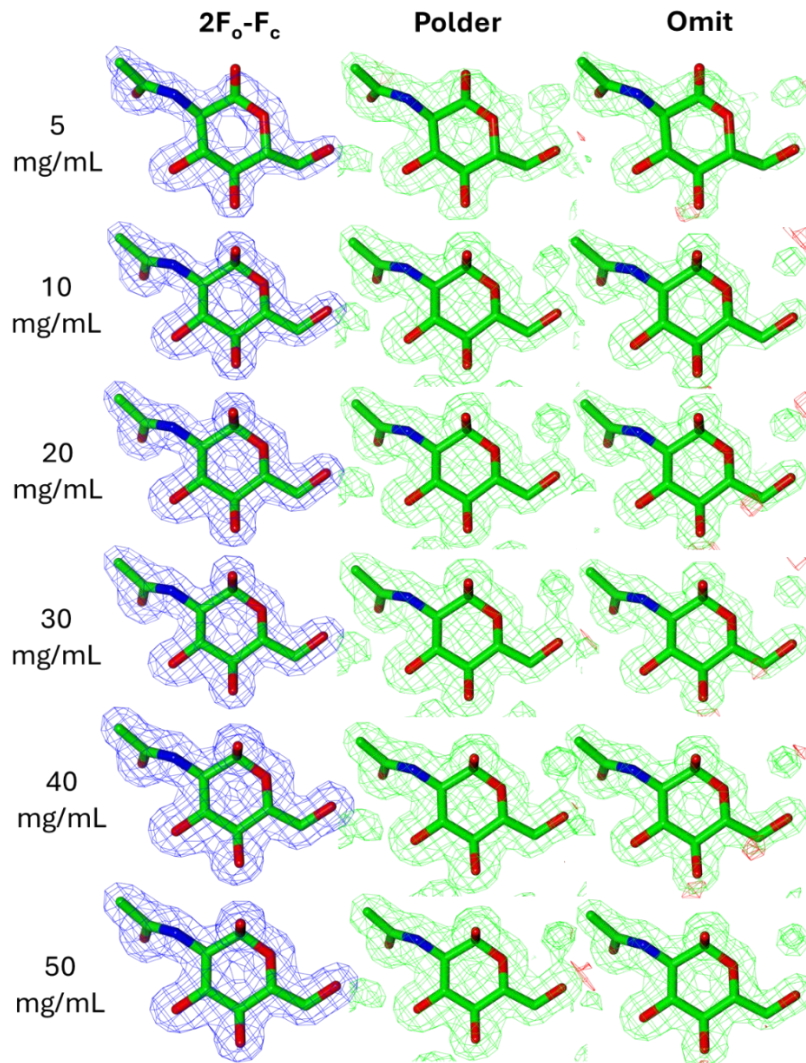


Figure 82. Electron density, polder, and omit maps of GlcNac binding to lysozyme microcrystal slurries soaked with increasing ligand concentrations under room temperature conditions. Electron density maps (contoured at 1σ) and corresponding polder and omit maps (contoured at 3σ) are shown for lysozyme microcrystal slurries soaked in GlcNac solution ranging from 5 to 50 mg/mL. Each map highlights the ligand-binding site following structural refinement. Stick representation depicts carbon atoms as green, nitrogen atoms as blue and oxygen atoms as red.

To quantitatively access ligand binding, occupancy refinement was performed in REFMAC for both rotation and serial datasets collected from lysozyme crystals soaked in GlcNac solutions ranging from 1 to 50 mg/mL. Refinement was carried out with restrained atomic coordinates and fixed B-factors for the protein backbone, allowing ligand occupancy to vary freely. Across both data collection modalities, refined occupancies generally increased with ligand concentration, consistent with a dose-dependent uptake of GlcNac into the lysozyme active site (Figure 83). However, the 30 mg/mL dataset deviated from this trend in both modalities, more prominently

in the rotation dataset. The likely cause of this is the variability in crystal size and ligand diffusion under cryogenic conditions, resulting in reduced ligand accumulation. Occupancy values in rotation datasets ranged from 0.75 at 5 mg/mL to 0.89 at 50 mg/mL, while serial datasets yielded slightly higher values, from 0.82 to 0.99 over the same concentration range. This modest elevation in occupancy for serial data may reflect improved ligand retention and reduced radiation damage under room-temperature conditions, facilitated by the serial approach. Together these experiments offer a framework for evaluating the tradeoffs between ligand concentration and occupancy across different crystallographic modalities. They also inform the design of future time-resolved mixing experiments, where optimising ligand delivery and minimising reagent consumption are critical for capturing transient states without compromising structural insights.

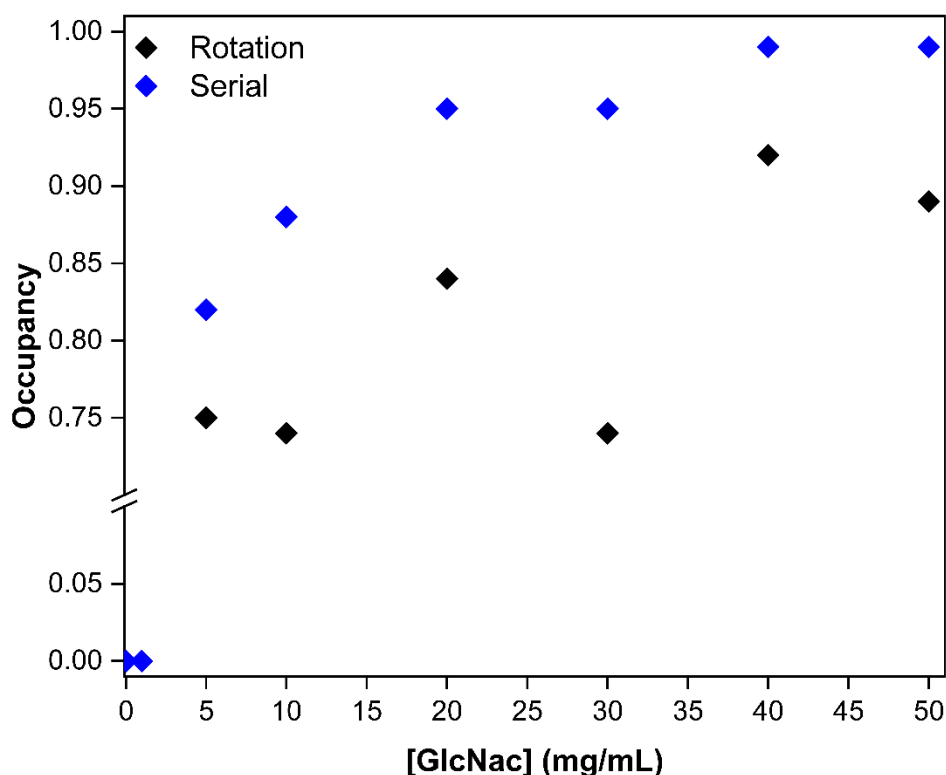


Figure 83. Refined GlcNac occupancy values across concentration and data collection modality. Occupancy values derived from REFMAC occupancy refinement plotted for lysozyme crystals soaked in GlcNac solutions ranging from 0 to 50 mg/mL. Rotation datasets (black) and serial datasets (blue) show a general increase in occupancy with ligand concentration, consistent with dose-dependent binding.

5.4 PDMS droplet microfluidic device commissioning beamtime

As part of ongoing efforts to develop modular microfluidic platforms for serial crystallography, the PDMS droplet microfluidic device was commissioned and installed at Diamond Light Source beamline I24. The microfluidic device was mounted in a 3D-printed holder and aligned on the beamline stage, with the droplet channel positioned to intersect the X-ray beam path (Figure

84A). The fluorinated oil, precipitant solution and lysozyme microcrystals were introduced into the device by tubing originating from plastic syringes held within the perpetual sedimentation system, continuously rotating to prevent crystal settling, and held above the sample interaction region on a dedicated table (**Figure 84B**). The experimental setup involved a laptop remotely operated outside the experimental hutch running the perpetual sedimentation system graphical user interface (position 1, **Figure 84C**) to move the sample syringes at the desired flow rates (position 2, **Figure 84C**) followed by the introduction of sample via tubing into the microfluidic device (position 3, **Figure 84C**), as well as tubing connecting the outlet of the device to a waste falcon tube situated adjacent to the sample interaction region (position 4, **Figure 84C**). This setup marked a successful integration of microfluidic hardware into a synchrotron beamline environment, establishing the foundation for future time-resolved experiments.

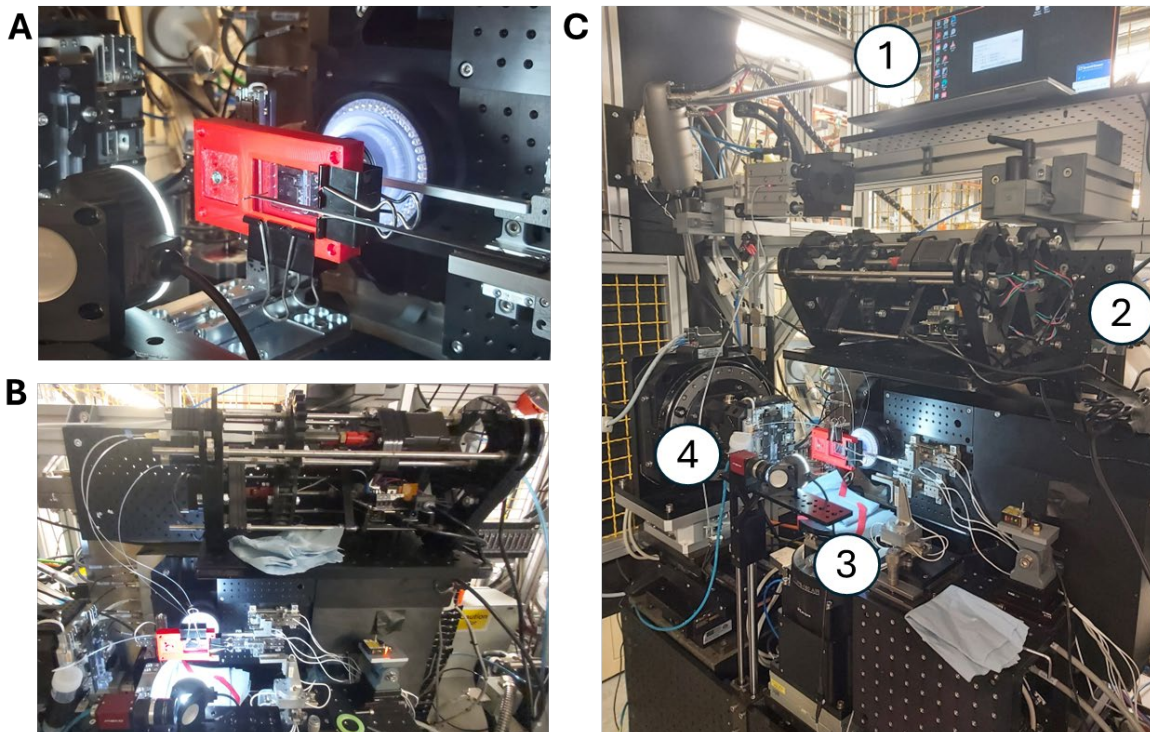


Figure 84. Integration of the PDMS droplet microfluidic device into the Diamond I24 beamline. (A) The PDMS device mounted in a custom 3D-printed holder and aligned on the beamline stage, with the droplet channel intersecting the X-ray beam path. (B) Sample delivery system comprising fluorinated oil, precipitant soliton and lysozyme microcrystals introduced via tubing from plastic syringes housed in a perpetual sedimentation system. The system was continuously rotating to prevent settling and positioned above the sample interaction region. (C) Schematic of the experimental workflow: (1) remote control laptop operating the sedimentation system graphical user interface; (2) syringe movement to regulate flow rate; (3) sample introduction into the microfluidic device; and (4) outlet tubing directing waste to a falcon tube adjacent to the interaction region.

Initial testing focused on evaluating the performance of the PDMS droplet microfluidic device under beamline conditions using a $7 \times 7 \mu\text{m}$ X-ray beam at 100% transmission and an X-ray energy of 20 keV. During early exposure, repeated irradiation at fixed X-ray interaction regions led to localised thermal degradation of the PDMS material (**Figure 85A**). This manifested as

visible burning and discolouration at the beam impact sites, compromising the material's integrity over time. Interestingly, while the damage was structurally evident, its impact on droplet flow was minimal, with only minor fluctuations observed in droplet trajectory and spacing. More critically, prolonged operation under continuous flow conditions induced expansion of the thin-film assembly, preventing crystal delivery to the droplets, likely due to a build-up of pressure within the microfluidic circuit (**Figure 85B**). Despite these setbacks, the widened channel at the X-ray interaction region significantly improved droplet contrast and facilitated reliable visualisation and alignment during data collection, representing a key design success (**Figure 85C**).

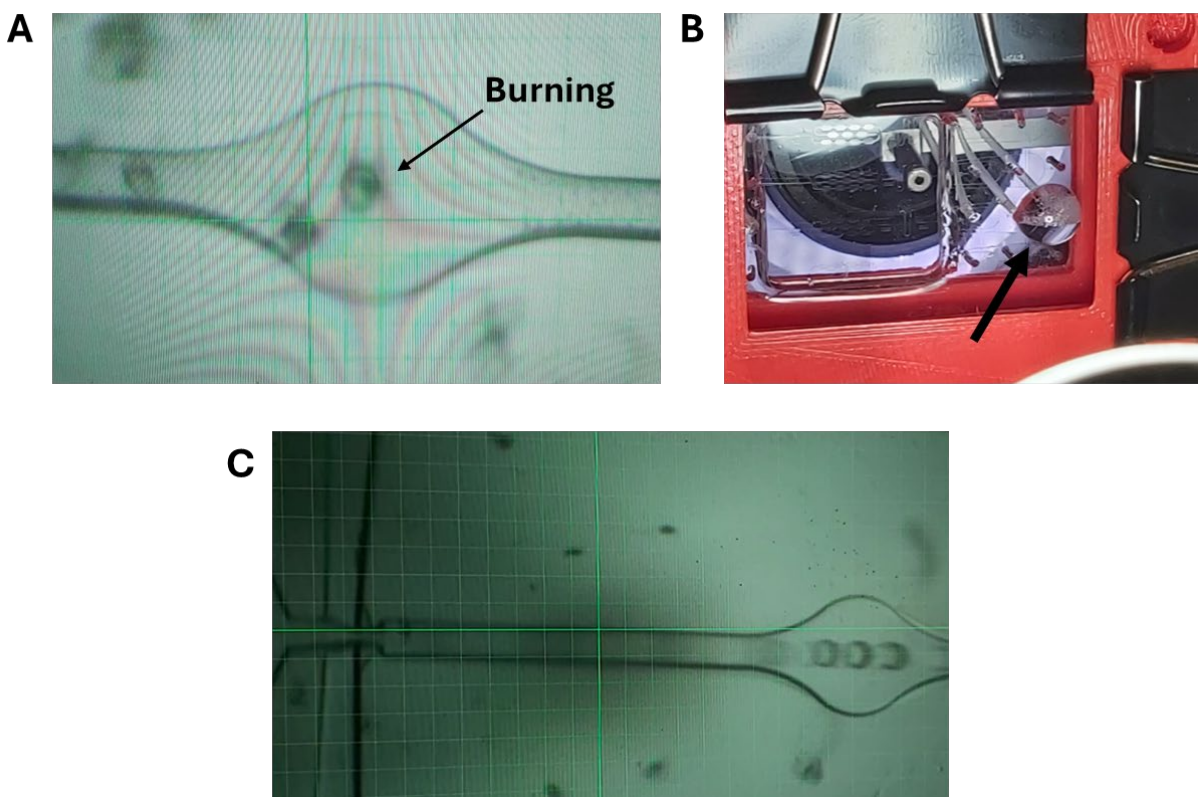


Figure 85. Evaluation of PDMS droplet microfluidic device performance under beamline conditions at I24. (A) Localised burning of the PDMS material following repeated exposure to a $7 \times 7 \mu\text{m}$ X-ray beam at 20 keV, indicating thermal degradation at fixed interaction regions. (B) Flow instability resulting from thin-film expansion (as depicted by the black arrow) during prolonged operation. (C) Improved droplet contrast and positional stability due to the presence of channel widening at the X-ray interaction region.

Given the limitations of dynamic flow under these conditions, a static approach was adopted to assess whether useable serial data could still be collected. The device was flooded with lysozyme microcrystals (13 – 15 μm) and subjected to raster grid scanning at 20 keV. For comparison, a mylar chipless chip was tested under identical conditions. Both experimental configurations and the grid-based scanning strategy are illustrated in **Figure 86**. The microfluidic datasets comprise collections from multiple PDMS devices with overall thicknesses ranging

from 600 to 850 μm . Notably, thickness non-uniformity across individual devices is expected to contribute to variation in background scattering levels.

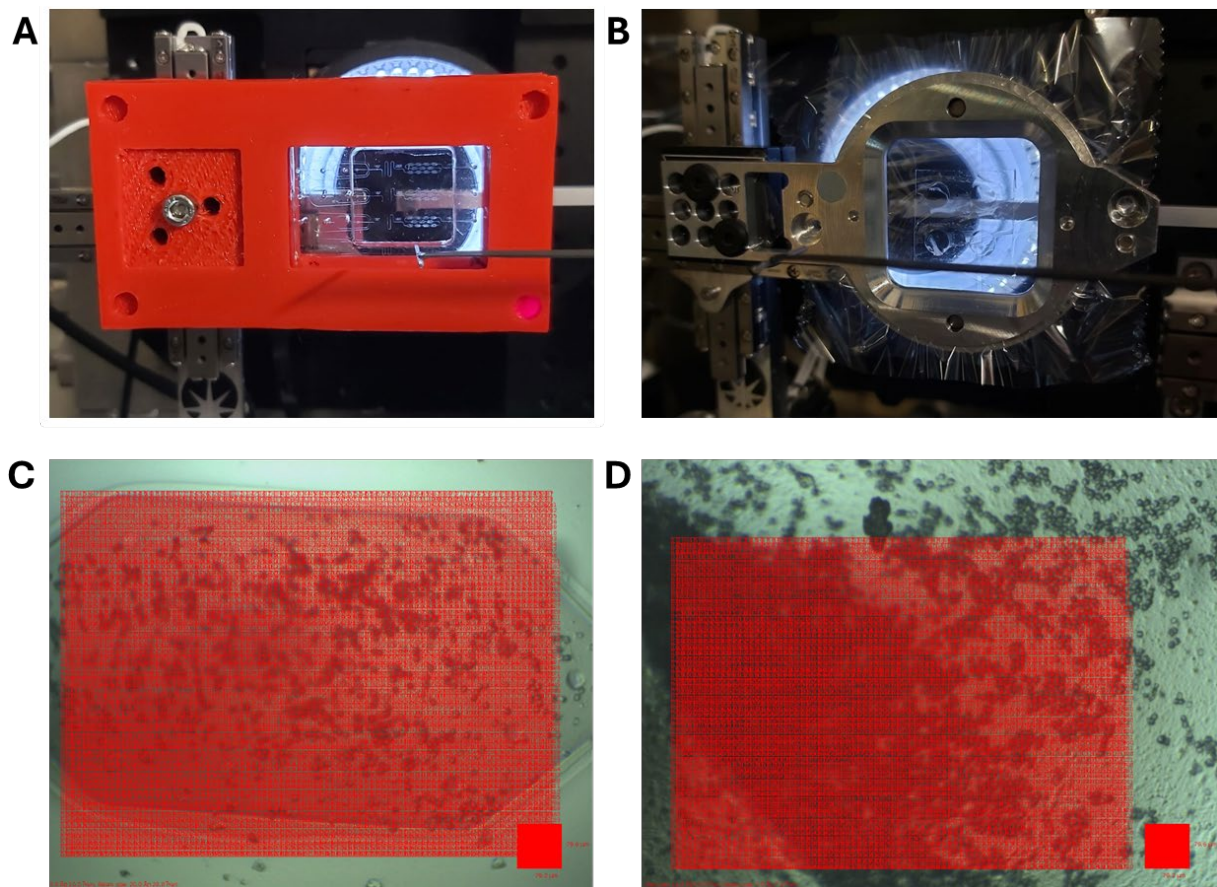


Figure 86. Static SSX data collection using PDMS microfluidic device and a mylar chipless chip. (A) PDMS microfluidic device mounted in a custom 3D-printed holder. (B) A mylar chipless chip mounted on the beamline with the integrated fixed-target holder mount. (C,D) Crystal-rich regions identified within each device, overlaid with a grid to guide a raster scanning data collection strategy, maximising hit rates.

Despite the absence of dynamic flow, useable serial data were successfully collected from the PDMS devices. Albeit with lower efficiency compared to the mylar control. A total of 97,717 images were processed from the microfluidic setup, yielding 20,207 hits, of which 3593 were indexed, resulting in 3376 integrated crystals (**Table 16**). In contrast, the mylar control produced 39,955 hits from 45,820 processed images, with 10,929 indexed images and 12,275 integrated crystals (**Table 16**).

Table 16. Data collection statistics for static SSX data collection of lysozyme microcrystals in the PDMS droplet microfluidic device and the mylar chipless chip.

	PDMS droplet microfluidic device	Mylar chipless chip
Processed images	97,717	45,820
Number of hits	20,207	39,955
Hit rate (%)	20.7	87.2
Number of indexed images	3593	10,929
Indexing rate (%)	17.8	27.4
Integrated crystals	3376	12,725
Merged lattices	3376	3376

Visual inspection of diffraction patterns revealed a distinct scattering ring at $\sim 7.5 \text{ \AA}$ in datasets collected using the PDMS droplet microfluidic device (Figure 87A). In contrast, no background scattering was observed in the mylar chipless chip datasets, consistent with expectations for low-scatter substrates. This elevated background in the PDMS device likely contributed to its lower indexing rate relative to the mylar control. Despite these differences, the final number of merged lattices was matched across both datasets, enabling a direct comparison of data quality. The $\text{CC}_{1/2}$ and SNR values were consistently lower for the PDMS device, in agreement with prior feasibility testing (Figure 87B). Nevertheless, a resolution cutoff of $\sim 2.0 \text{ \AA}$ was achieved using 13 – 15 μm lysozyme microcrystals in the PDMS device, compared to 1.8 \AA for the mylar chipless chip. These results demonstrate that, while background scattering impacts data quality, the PDMS device remains capable of delivering high-resolution structural data under static conditions.

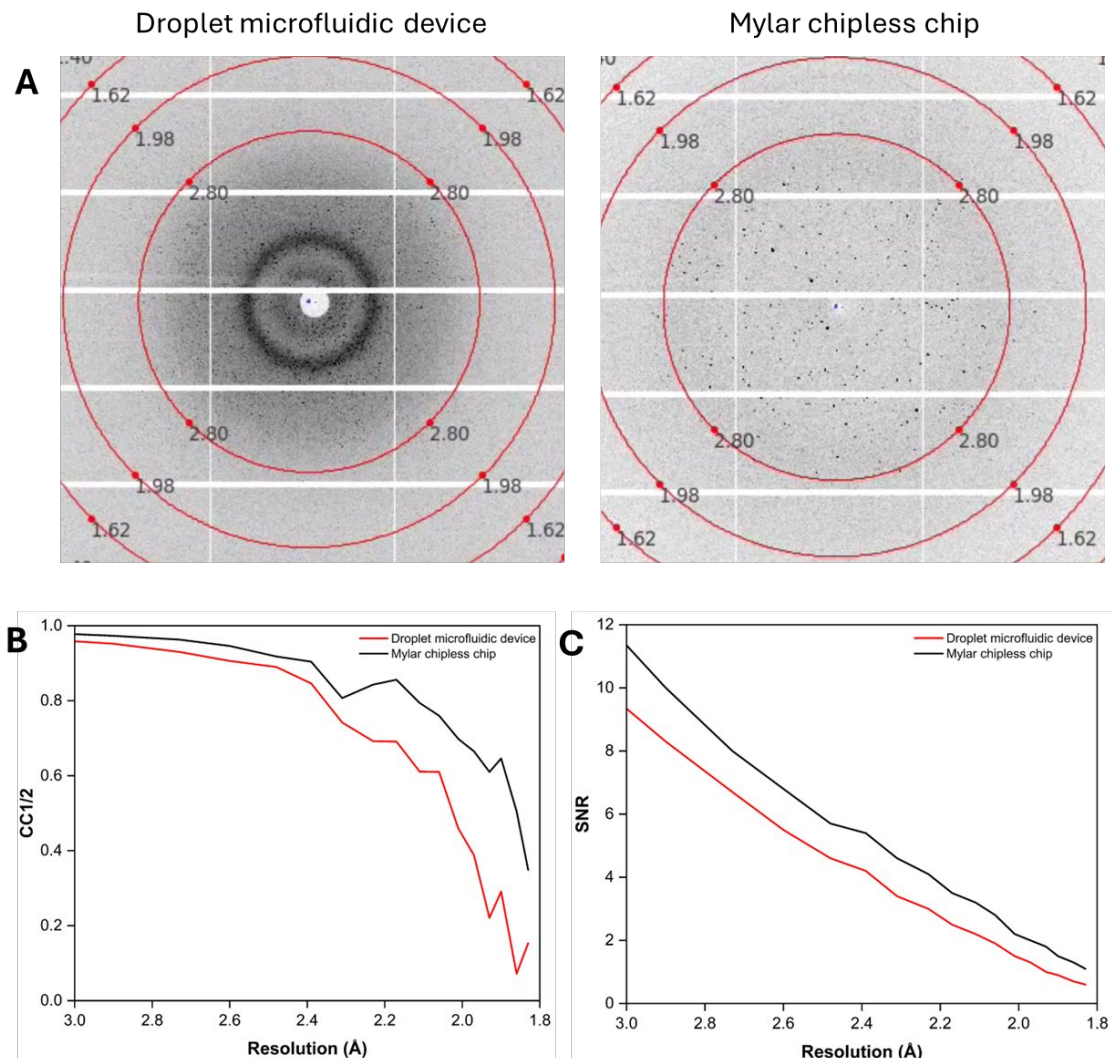


Figure 87. Comparison of diffraction quality between a PDMS droplet microfluidic device and a mylar chipless chip. (A) Representative diffraction pattern from the PDMS device showing a prominent scattering ring at $\sim 7.5 \text{ \AA}$, indicative of elevated background. No such scattering was observed in the mylar chipless chip. (B) $\text{CC}_{1/2}$ values plotted across resolution shells for both devices. (C) SNR comparisons across resolution bins.

While time-resolved mixing was not achieved during the commissioning beamtime, the ability to collect meaningful serial data from a flooded PDMS chip validates the platform's potential.

These results demonstrate that even early-stage prototypes can yield structurally informative datasets, and that static delivery modes offer a viable fallback when flow-base approaches are constrained. This final experiment closes the chapter with a pragmatic success, highlighting the resilience of the PDMS device, the value of iterative design, and the promise of microfluidic integration for future serial crystallography workflows.

5.5 Discussion

The work in this chapter outlines the development and validation of a droplet-based microfluidic platform for rapid micromixing and time-resolved serial crystallography. Motivated by the limitations of conventional co-flow mixers, namely high sample consumption, and limited temporal resolution, this work aimed to engineer a thin-film PDMS device capable of generating droplets with tuneable incubation times, minimal temporal blurring and direct X-ray compatibility.

A key outcome was the demonstration of robust mixing dynamics across a range of velocities and conditions. At 60 mm/s, mixing times remained at ~6 milliseconds regardless of crystal presence, indicating that lysozyme microcrystals do not perturb flow or homogenisation at these scales. The fastest mixing time, 1.73 milliseconds, was achieved using a 1:1 ligand-to-dye ratio. This enhancement is likely driven by entropy of mixing effects, where equal volumetric contributions maximise interfacial area and concentration gradients. Across the velocities from 60 to 300 mm/s, mixing times ranged from 1.85 to 6 milliseconds, confirming the platform's ability to match or exceed current benchmarks while offering modularity and reduced sample consumption. Although accurate mixing times are seldom reported in the literature, the sub-2 millisecond performance observed here is on par with high-velocity co-axial capillary mixers (183,297) and significantly outpaces alternatives strategies such as drop-on-drop sample delivery (148) or 3D-printed GVDN devices with integrated mixing blades, which typically achieve ~ 20 ms mixing times (298).

To assess the feasibility of integrating this droplet platform with X-ray interrogation, material testing was conducted to evaluate the impact of PDMS thickness on background scattering and data quality. Increasing PDMS thickness led to pronounced scattering artifacts, with rings observed at ~ 7.5 Å for 20 keV and ~ 6.5 Å for 12.4 keV, consistent with increased X-ray attenuation. These findings align with prior reports by Lyubimov *et al.* who observed similar ring artifacts in PDMS-based trap arrays (167), and by Lee *et al.* who demonstrated XFEL-induced degradation and hole formation in PDMS films (299). Elevating the beam energy to 20 keV dampened this effect, likely due to reduced photon-matter interaction cross-sections, as also noted by Ghazal *et al.* (300). However, thicker PDMS also correlated with diminished data quality, as reflected in lower CC_{1/2} and SNR values. Despite these limitations, useable diffraction data were still obtained from 20 – 25 µm lysozyme microcrystals, affirming the viability of PDMS-based device for *in situ* crystallographic applications when carefully optimised.

To support time-resolved studies, a compact microfluidic circuit was fabricated featuring a 60 $\mu\text{m} \times 40 \mu\text{m}$ droplet generation junction, serpentine incubation channels and eleven expanded incubation cells resulting in a temporal resolution range of 5 milliseconds to 5 seconds. Flow rates of 5, 10 and 25 $\mu\text{L}/\text{min}$ at a 4:1 oil-to-aqueous ratio yielded droplet diameters between 38 – 41 μm , with CV values from 1.37 – 3.01%. Manual tracking confirmed uniform residence times across droplets within the expanded incubation cells, aided by crystal presence within the flow. CV values for overall droplet residence time remained below 4%, ensuring reproducible timepoint assignment. The device was fabricated using a three-layer PDMS assembly: a 100 μm commercial thin film, a middle layer cast in a polyurethane mould (500 – 750 μm), and a top layer with a laser-cut aperture for beam access. Despite some non-uniformity in the middle layer, the device enabled stable droplet flow. A 3D-printed holder was developed to ensure efficient and reproducible device mounting at the beamline, along with a modified perpetual sedimentation system (173) to deliver lysozyme microcrystal slurries at densities up to 2 million crystals/mL. Continuous agitation prevented settling and preserved homogeneity, an issue that remains underrepresented in the literature despite its critical impact on hit rates and data quality. The anti-settling instrument developed by Lomb *et al.* for SFX highlights the importance of mechanical agitation (174), yet few studies have addressed this challenge.

To validate the system, the binding of GlcNac to lysozyme was selected as a model for time-resolved mixing. A control experiment using a tapedrive setup at ESRF confirmed ligand binding at 500 milliseconds, 2 seconds, and 5 seconds. The effect of GlcNac concentration on ligand occupancy was studied to establish whether lower ligand concentrations could achieve comparable occupancy values. Occupancy refinement across ligand concentrations revealed efficient binding even at low GlcNac concentrations (5 mg/mL), particularly in serial datasets. Rotation datasets showed occupancy values from 0.75 to 0.89, while serial datasets ranged from 0.82 to 0.99, suggesting enhanced diffusion kinetics in microcrystal slurries, due to increased surface area and reduced diffusion path lengths. Further investigation into the influence of ligand concentration in time-resolved mixing experiments is warranted. The observed sensitivity of occupancy to concentration indicates that serial crystallography could be harnessed not only for structural characterisation but also potentially for binding analysis. Notably, the high-throughput nature of serial data collection presents a compelling opportunity to determine binding affinities directly from diffraction data, echoing the pioneering work by Wu *et al.* (296) who achieved the first direct determination of a ligand binding constant within single protein crystals. Extending this approach to microcrystal slurries could enable systematic mapping of binding affinities across diverse ligand libraries, positioning serial crystallography as a transformative platform for structure-based drug discovery.

Commissioning beamtime at Diamond Light source beamline I24 confirmed the device's compatibility with synchrotron infrastructure, though challenges emerged during prolonged operation. Localised burning of the PDMS material was observed during repeated X-ray exposure likely due to thermal expansion, whilst flow instabilities arose from thin-film expansion under flow conditions. These effects mirror the findings of Lee *et al.* (299), who reported structural damage in PDMS under XFEL conditions, and underscore the need for more thermally resilient materials. Nonetheless, channel widenings improved droplet visualisation and enable efficient sample alignment and positioning prior to data collection. To mitigate degradation, a static raster-scanning approach was adopted at 20 keV. Compared to a mylar chipless chip, the PDMS device yielded lower $CC_{1/2}$ and SNR values and exhibited prominent scattering rings ($\sim 7.5\text{\AA}$), yet still produced high-resolution data with a cutoff of 2.0\AA (versus 1.8\AA for mylar).

These results contrast with the in-flow microfluidic platforms developed by Monteiro and colleagues (171,172), and the droplet injector system pioneered by the Ros Lab at ASU. Monteiro's devices employed polyimide and 3D-printed architecture for continuous sample delivery at synchrotron beamlines. Their flow-focusing device achieved stable in-flow diffraction with minimal sample consumption ($\sim 0.5\text{ }\mu\text{L/min}$), leveraging polyimide's superior X-ray transparency and thermal resilience. The 3D-MiXD platform further demonstrated rapid data acquisition and low background scattering, benefitting from rigid channels and optimised beamline integration. While Monteiro's systems support high-throughput continuous data collection, they lack the droplet-level temporal control and modularity demonstrated here. Similarly, Ros's suite of droplet injectors, including co-flow systems (143), segmented flow generators (144), and electrically stimulated injectors (145) prioritise sample conservation and XFEL compatibility. Their modular designs have enabled structural insights into conformational heterogeneity (147) and achieved up to 97% sample savings in time-resolved studies (146). Importantly, flow-focusing mixers, despite their widespread use, are prone to temporal blurring due to velocity gradients and axial dispersion. This inherent limitation compromises the precision of reaction timepoint assignment, particularly in fast kinetic regimes. In contrast, the PDMS droplet platform isolates reaction volumes and maintains uniform residence times, thereby improving confidence in time-resolved structural assignment.

These findings position the current platform within a broader continuum of X-ray compatible microfluidic technologies. While graphene-based devices reported by Sui *et al.* (294) offer ultra-thin architectures ($\sim 1\text{ }\mu\text{m}$) and near-zero background scattering, their fabrication complexity and fragility limit widespread adoption. Similarly, polyimide-based flow-focusing devices such as those developed by Monteiro *et al.* (171,172) demonstrate excellent X-ray transparency and mechanical resilience, but require specialised bonding techniques and lack droplet level

Chapter 5

temporal control. Recent advances in fixed-target microfluidics including COC chips and polymer-based platforms with moisture barriers and counter-diffusion crystallisation (158,160,162) have enabled room-temperature data collection, long-term crystal preservation, and scalable fabrication for automated workflows (159,163). These systems offer plug-and-play usability and low background scattering but are inherently static and do not support dynamic mixing or tuneable timepoint resolution. The present PDMS-based droplet platform bridges these approaches by combining modular fabrication, temporal precision, and synchrotron compatibility, albeit with trade-offs in scattering and thermal stability that future iterations must address.

Taken together, this work advances droplet-based microfluidics as a viable and versatile strategy for time-resolved serial crystallography. It addressed underexplored challenges such as crystal settling, temporal blurring, and material compatibility, while offering a modular framework for future integration with XFEL and synchrotron beamlines.

Chapter 6 Conclusions and future work

Time-resolved serial crystallography is poised to transform our understanding of biochemical processes by enabling structural snapshots of enzymatic reactions across timescales ranging from seconds to femtoseconds. As synchrotron and XFEL technologies continue to evolve, the field is shifting towards more physiologically relevant experiments, requiring not only rapid data collection but also precise control over reaction initiation, crystal delivery, and sample reproducibility. Despite its promise, widespread adoption remains limited by technical bottlenecks in microcrystal preparation, mixing fidelity, and the integration of biological relevance into experimental design.

This thesis addresses these challenges through a modular pipeline that integrates microcrystal engineering with droplet microfluidic technologies. The progression began with the optimisation of crystallisation conditions for *AtPdx1.3*, a PLP-dependent enzyme selected for its biological relevance and catalytic tractability. Initial efforts focused on transitioning from single crystal growth to reproducible microcrystal slurry generation. Phase diagram mapping under batch conditions, particularly via the microbatch-under-oil setup developed in this work, enabled efficient screening with minimal sample volumes and facilitated the identification of crystallisation regimes suitable for serial crystallography experiments. Microseeding strategies were essential for controlling nucleation and crystal morphology, yielding microcrystals compatible with static SFX data collection. However, variability in crystal size and uniformity underscored the need for more scalable and controllable approaches.

To overcome these limitations, a droplet-based crystallisation workflow was developed. This system enabled precise engineering of crystal size and uniformity, improving reproducibility and mitigating issues such as clogging during sample delivery. Successfully applied to SSX screening experiments, the workflow demonstrated its potential for high-throughput crystallisation. Importantly, the droplet format provided a scalable platform for producing microcrystals in volumes suitable for time-resolved studies, while maintaining control over nucleation and growth dynamics. Building on this foundation, a droplet microfluidic platform was implemented to enable rapid substrate mixing and controlled reaction initiation within an X-ray transmissible device. Leveraging the convective and diffusive nature of droplets, the system achieved sub-2 millisecond mixing times, on par with the current state-of-the-art mixing devices. The PDMS-based prototype was validated at a synchrotron source, demonstrating compatibility with existing beamline infrastructure, albeit with ongoing challenges that must be resolved in future iterations.

Future work will focus on refining each component of the pipeline to support broader adoption and expanded functionality. Material limitations of PDMS, including its X-ray attenuation and mechanical instability, must be addressed through the adoption of alternative materials such as COC or kapton. However, successful implementation will require careful attention to device bonding and iterative design to ensure fluidic integrity under beamline conditions. In parallel, scaling up crystal output remains a critical challenge. While droplet-based workflows offer precise control over nucleation, batch crystallisation remains the most accessible and widely adopted format. However, increasing batch volume often leads to broader crystal size distributions and reduced reproducibility. Future studies should systematically investigate how volume-dependent parameters influence crystal morphology and yield. Optimising these variables will be essential for producing high-quality microcrystals at scale, particularly for systems where droplet formats are impractical or unavailable. A time-resolved XFEL experiment on AtPdx1.3, informed by the timescales identified here, will serve as a critical validation of the pipeline. Additionally, the influence of ligand concentration on reaction progression and occupancy must be systematically explored to improve structural insights and reduce sample consumption. Finally, resolving crystal settling during sample delivery remains a key challenge. Initial efforts with the perpetual sedimentation system have been promising, but future designs must incorporate strategies to maintain slurry homogeneity and prevent sedimentation.

In conclusion, this thesis addresses several foundational challenges in time-resolved serial crystallography by developing modular workflows that combine droplet-based microfluidics with tailored microcrystallisation strategies. Through innovations in crystal size control, ligand delivery, and on-chip reaction initiation, this work establishes a reproducible framework for capturing transient enzymatic states under time-resolved conditions. By validating model systems, refining crystallisation protocols, and designing an X-ray transparent device for micromixing, this research lays the groundwork for more accessible, scalable, and biologically meaningful time-resolved studies. It contributes to the broader democratisation of serial crystallography and represents a significant step towards mechanistic interpretation of enzyme catalysis at atomic resolution.

Appendix A Supplementary crystallographic tables

Table 17. Data collection and initial refinement statistics for I320 cryo-trapping experiments.
Values in parentheses are for highest-resolution shell.

	30 s	2 mins	5 mins	7 mins	13 mins
Data Collection					
Space group	<i>H</i> 3				
<i>a, b, c</i> (Å)	179.00 179.00 116.70	178.20 178.20 115.50	178.40 178.40 114.8	177.90 177.90 115.20	177.80 177.80 114.70
α, β, γ (°)	90.0 90.0 120.0	90.0 90.0 120.0	90.0 90.0 120.0	90.0 90.0 120.0	90.0 90.0 120.0
Resolution (Å)	93.30 – 2.20 (2.24 – 2.20)	92.40 – 2.60 (2.64 – 2.60)	53.80 – 2.20 (2.24 – 2.20)	64.10 – 1.90 (1.94 – 1.90)	53.80 – 2.00 (2.04 – 2.00)
Completeness (%)	100.00 (100.00)	99.70 (97.90)	100.00 (99.40)	99.99 (97.90)	99.80 (95.40)
Multiplicity	5.3 (5.4)	5.3 (5.2)	5.3 (5.4)	5.3 (5.4)	5.3 (5.4)
SNR	7.6 (0.2)	5.7 (0.5)	7.0 (0.6)	9.0 (0.4)	7.7 (0.5)
CC _{1/2}	0.98 (0.25)	1.00 (0.20)	1.00 (0.30)	1.00 (0.30)	1.00 (0.30)
<i>R</i> _{merge}	14.8	20.9	18.3	10.7	17.3
Refinement					
Resolution (Å)	64.45 – 2.20	64.32 – 2.60	53.82 – 2.20	64.15 – 1.86	53.87 – 2.04
No. of reflections	71,217	43,544	64,564	114,086	86,077
<i>R</i> _{work}	0.232	0.250	0.289	0.259	0.254
<i>R</i> _{free}	0.269	0.300	0.331	0.309	0.282
Ramachandran favoured	1040 (95%)	951 (87%)	936 (85%)	1018 (92%)	1017 (93%)
Ramachandran allowed	43 (4%)	96 (9%)	112 (10%)	62 (6%)	67 (6%)
Ramachandran outliers	8 (1%)	44 (4%)	50 (5%)	18 (2%)	14 (1%)
Bond lengths (Å)	0.0066	0.0061	0.0050	0.0080	0.0072
Bond angles (°)	1.545	1.528	1.428	1.831	1.467

Table 18. Data collection and initial refinement statistics for PLP cryo-trapping experiments.
Values in parentheses are for highest-resolution shell.

	23 s	68 s	90 s	150 s
Data Collection				
Space group	<i>H</i> 3	<i>H</i> 3	<i>H</i> 3	<i>H</i> 3
<i>a, b, c</i> (Å)	179.30 179.30 116.90	178.60 178.60 116.00	177.80 177.80 116.00	178.10 178.10 115.40
α, β, γ (°)	90.0 90.0 120.0	90.0 90.0 120.0	90.0 90.0 120.0	90.0 90.0 120.0
Resolution (Å)	89.60 – 2.50 (2.54 – 2.50)	92.80 – 2.50 (2.54 – 2.50)	41.10 – 2.20 (2.24 – 2.20)	64.20 – 2.10 (1.86 – 1.83)
Completeness (%)	93.90 (94.30)	99.10 (95.70)	99.60 (100.00)	99.99 (100.00)
Multiplicity	2.4 (2.3)	5.4 (5.3)	3.7 (3.8)	5.5 (5.6)
SNR	3.7 (0.6)	5.4 (0.6)	6.2 (0.7)	5.4 (0.5)
CC _{1/2}	1.00 (0.20)	1.00 (0.20)	0.90 (0.30)	1.00 (0.30)
<i>R</i> _{merge}	18.2	26.6	17.3	20.6
Refinement				
Resolution (Å)	89.79 – 2.50	54.55 – 2.50	41.11 – 2.20	64.26 – 2.10
No. of reflections	45,584	46,795	72,933	80,504
<i>R</i> _{work}	0.229	0.230	0.218	0.224
<i>R</i> _{free}	0.278	0.281	0.276	0.264
Ramachandran favoured	980 (92%)	958 (90%)	999 (94%)	999 (94%)
Ramachandran allowed	62 (6%)	78 (8%)	48 (5%)	52 (5%)
Ramachandran outliers	16 (2%)	22 (2%)	11 (1%)	7 (1%)
Bond lengths (Å)	0.0060	0.0063	0.0078	0.0073
Bond angles (°)	1.569	1.672	1.802	1.741

Table 19. Data collection and initial refinement statistics for tapedrive experiments with lysozyme microcrystals and 50 mg/mL GlcNac. Values in parentheses are for highest-resolution shell.

	Apo	500 ms	2 s	5 s
Data Collection				
No. of collected images	2,000,000	2,000,000	2,000,000	500,000
No. of hits	32,032	69,388	53,768	15,204
Hit rate (%)	1.60	3.46	2.68	3.04
No. of indexed images	31,467	67,337	51,983	14,827
Indexing rate (%)	98.2	97.0	96.6	97.5
No. of integrated lattices	55,012	128,239	80,011	19,864
Space group	<i>P</i> 4 ₃ 212			
<i>a</i> , <i>b</i> , <i>c</i> (Å)	79.11, 79.72, 38.49	79.18, 79.50, 38.29	79.14, 79.49, 38.31	79.03, 79.53, 38.33
α, β, γ (°)	90, 90, 90	90, 90, 90	90, 90, 90	90, 90, 90
Resolution (Å)	79.42 – 1.90 (1.93 – 1.90)	79.34 – 1.90 (1.93 – 1.90)	79.31 – 1.90 (1.93 – 1.90)	79.28 – 1.97 (2.00 – 1.97)
No. of unique reflections	10,206 (497)	10,131 (498)	10,131 (498)	9112 (443)
Completeness (%)	100.00 (100.00)	100.00 (100.00)	100.00 (100.00)	100.00 (100.00)
Multiplicity	1557.72 (295.73)	2664.43 (515.19)	1882.10 (362.94)	635.17 (161.86)
SNR	14.2 (0.7)	19.1 (0.8)	15.5 (0.6)	9.5 (0.7)
CC _{1/2}	0.99 (0.43)	0.99 (0.55)	0.99 (0.49)	0.99 (0.32)
CC [*]	1.00 (0.78)	1.00 (0.84)	1.00 (0.81)	0.99 (0.70)
<i>R</i> _{split}	4.1 (135.7)	3.1 (104.4)	3.9 (130.9)	6.8 (147.5)
Wilson <i>B</i> -factor (Å ²)	39.99	39.26	39.65	39.00
Refinement				
Resolution (Å)	56.22 – 1.90	56.16 – 1.90	56.15 – 1.90	56.12 – 1.97
No. of reflections	10,170	10,094	10,095	9077
Reflections used for <i>R</i> _{free}	486	485	485	463
<i>R</i> _{work}	0.192	0.185	0.189	0.194
<i>R</i> _{free}	0.225	0.217	0.215	0.235
Ramachandran favoured	122 (96%)	121 (95%)	119 (93%)	122 (96%)

	Apo	500 ms	2 s	5 s
Ramachandran allowed	5 (4%)	6 (5%)	8 (7%)	5 (4%)
Ramachandran outliers	0 (0%)	0 (0%)	0 (0%)	0 (0%)
Bond lengths (Å)	0.0064	0.0062	0.0062	0.0066
Bond angles (°)	1.580	1.541	1.498	1.558

Table 20. Data collection and initial refinement statistics for static equilibrium soaks of lysozyme microcrystals with 1 to 20 mg/mL GlcNac on SOSOS chips at ESRF. Values in parentheses are for highest-resolution shell.

	1 mg/mL GlcNac	5 mg/mL GlcNac	10 mg/mL GlcNac	20 mg/mL GlcNac
Data Collection				
No. of collected images	240,000	240,000	240,000	240,000
No. of hits	77,370	81,540	82,898	90,413
Hit rate (%)	32.2	33.9	34.5	37.6
No. of indexed images	73,024	78,121	79,735	86,781
Indexing rate (%)	94.3	95.8	96.2	95.9
No. of integrated lattices	113,582	132,345	133,403	149,466
Space group	<i>P</i> 4 ₃ 2 ₁ 2			
<i>a</i> , <i>b</i> , <i>c</i> (Å)	79.27, 79.63, 38.57	79.31, 79.65, 38.46	79.39, 79.74, 38.44	79.38, 79.73, 38.42
α, β, γ (°)	90, 90, 90	90, 90, 90	90, 90, 90	90, 90, 90
Resolution (Å)	56.18 – 1.48 (1.51 – 1.48)	56.20 – 1.48 (1.51 – 1.48)	56.26 – 1.48 (1.51 – 1.48)	56.25 – 1.45 (1.48 – 1.45)
No. of unique reflections	21,187 (1018)	21,140 (1018)	21,168 (1016)	22,478 (1099)
Completeness (%)	100.00 (100.00)	100.00 (100.00)	100.00 (100.00)	100.00 (100.00)
Multiplicity	1644.81 (372.10)	1929.97 (438.17)	1964.76 (446.06)	2103.34 (377.18)
SNR	16.4 (0.3)	17.9 (0.5)	18.5 (0.5)	18.5 (0.4)
CC _{1/2}	0.99 (0.41)	0.99 (0.47)	0.99 (0.48)	0.99 (0.44)
CC [*]	1.00 (0.76)	1.00 (0.80)	1.00 (0.80)	1.00 (0.78)
<i>R</i> _{split}	3.3 (309.7)	3.1 (190.8)	3.1 (184.6)	3.0 (244.4)
Wilson <i>B</i> -factor (Å ²)	24.26	24.29	23.26	23.71
Refinement				
Resolution (Å)	56.24 – 1.48	56.26 – 1.48	56.32 – 1.48	56.32 – 1.45

	1 mg/mL GlcNac	5 mg/mL GlcNac	10 mg/mL GlcNac	20 mg/mL GlcNac
No. of reflections	21,133	21,083	21,111	22,422
Reflections used for R_{free}	1039	1031	1033	1112
R_{work}	0.190	0.188	0.166	0.168
R_{free}	0.198	0.198	0.196	0.209
Ramachandran favoured	119 (93%)	120 (94%)	120 (94%)	122 (95%)
Ramachandran allowed	8 (7%)	7 (6%)	7 (6%)	5 (5%)
Ramachandran outliers	0 (0%)	0 (0%)	0 (0%)	0 (0%)
Bond lengths (Å)	0.0087	0.0094	0.0084	0.0081
Bond angles (°)	1.781	1.844	1.673	1.659

Table 21. Data collection and initial refinement statistics for static equilibrium soaks of lysozyme microcrystals with 30 to 50 mg/mL GlcNac on SOSOS chips at ESRF. Values in parentheses are for highest-resolution shell.

	30 mg/mL GlcNac	40 mg/mL GlcNac	50 mg/mL GlcNac
Data Collection			
No. of collected images	240,000	240,000	240,000
No. of hits	73,817	78,502	75,005
Hit rate (%)	30.7	32.7	31.2
No. of indexed images	70,685	75,404	71,489
Indexing rate (%)	95.7	96.0	95.3
No. of integrated lattices	114,185	129,765	119,687
Space group	$P4_32_12$	$P4_32_12$	$P4_32_12$
a, b, c (Å)	79.44, 79.79, 38.40	79.44, 79.79, 38.38	79.45, 79.80, 38.35
α, β, γ (°)	90, 90, 90	90, 90, 90	90, 90, 90
Resolution (Å)	56.30 – 1.48 (1.51 – 1.48)	56.30 – 1.45 (1.48 – 1.45)	56.30 – 1.48 (1.51 – 1.48)
No. of unique reflections	21,178 (1020)	22,486 (1104)	21,166 (1032)
Completeness (%)	100.00 (100.00)	100.00 (100.00)	100.00 (100.00)
Multiplicity	1692.08 (382.86)	1844.84 (331.14)	1783.76 (405.42)
SNR	17.2 (0.4)	17.5 (0.4)	17.7 (0.5)

	30 mg/mL GlcNac	40 mg/mL GlcNac	50 mg/mL GlcNac
CC _{1/2}	0.99 (0.42)	0.99 (0.39)	0.99 (0.44)
CC*	1.00 (0.77)	1.00 (0.75)	1.00 (0.78)
R _{split}	3.3 (219.3)	3.1 (227.9)	3.3 (171.2)
Wilson B-factor (Å ²)	22.95	23.15	23.16
Refinement			
Resolution (Å)	56.36 – 1.48	56.36 – 1.45	56.37 – 1.48
No. of reflections	21,127	22,430	21,115
Reflections used for R _{free}	1031	1113	1033
R _{work}	0.168	0.166	0.165
R _{free}	0.200	0.208	0.194
Ramachandran favoured	118 (93%)	119 (94%)	119 (94%)
Ramachandran allowed	9 (7%)	8 (6%)	8 (6%)
Ramachandran outliers	0 (0%)	0 (0%)	0 (0%)
Bond lengths (Å)	0.0082	0.0079	0.0078
Bond angles (°)	1.675	1.672	1.665

Table 22. Data collection and initial refinement statistics for single crystal lysozyme GlcNac soaking experiments from 0 to 10 mg/mL. Values in parentheses are for highest-resolution shell.

	Apo	1 mg/mL GlcNac	5 mg/mL GlcNac	10 mg/mL GlcNac
Data Collection				
Space group	P4 ₃ 2 ₁ 2			
a, b, c (Å)	78.7, 78.7, 37.3	77.3, 77.3, 37.6	76.9, 76.9, 37.3	77.3, 77.3, 38.1
α, β, γ (°)	90.0, 90.0, 90.0	90.0, 90.0, 90.0	90.0, 90.0, 90.0	90.0, 90.0, 90.0
Resolution (Å)	39.3 – 1.10 (1.13 – 1.10)	38.6 – 1.20 (1.23 – 1.20)	38.5 – 1.10 (1.13 – 1.10)	77.3 – 1.30 (1.33 – 1.30)
Completeness (%)	99.5 (96.8)	91.3 (75.8)	100.0 (100.0)	99.5 (94.8)
Multiplicity	12.2 (11.5)	7.6 (5.3)	11.7 (11.2)	12.1 (12.1)
SNR	22.2 (1.2)	6.9 (0.3)	21.5 (1.8)	14.0 (1.1)
CC _{1/2}	1.00 (0.50)	1.00 (0.40)	1.00 (0.80)	1.00 (0.80)
R _{merge}	4.3 (143.9)	9.4 (158.7)	5.1 (94.4)	8.3 (122.5)
Refinement				

	Apo	1 mg/mL GlcNac	5 mg/mL GlcNac	10 mg/mL GlcNac
Resolution (Å)	35.21 – 1.05	34.59 – 1.17	38.48 – 1.15	54.72 – 1.29
No. of reflections	54,427	30,795	39,946	29,472
R_{work}	0.183	0.243	0.195	0.195
R_{free}	0.196	0.266	0.215	0.218
Ramachandran favoured	120 (94%)	120 (94%)	120 (94%)	120 (94%)
Ramachandran allowed	7 (6%)	7 (6%)	7 (6%)	7 (6%)
Ramachandran outliers	0 (0%)	0 (0%)	0 (0%)	0 (0%)
Bond lengths (Å)	0.0127	0.0078	0.0102	0.0106
Bond angles (°)	2.018	1.725	1.881	1.864

Table 23. Data collection and initial refinement statistics for single crystal lysozyme GlcNac soaking experiments from 20 to 50 mg/mL. Values in parentheses are for highest-resolution shell.

	20 mg/mL GlcNac	30 mg/mL GlcNac	40 mg/mL GlcNac	50 mg/mL GlcNac
Data Collection				
Space group	$P4_32_12$	$P4_32_12$	$P4_32_12$	$P4_32_12$
a, b, c (Å)	77.4, 77.4, 38.0	77.0, 77.0, 37.9	76.8, 76.8, 37.4	76.3, 76.3, 27.0
α, β, γ (°)	90.0, 90.0, 90.0	90.0, 90.0, 90.0	90.0, 90.0, 90.0	90.0, 90.0, 90.0
Resolution (Å)	38.70 – 1.10 (1.13 – 1.10)	77.00 – 1.00 (1.03 – 1.00)	38.40 – 1.10 (1.13 – 1.10)	76.30 – 1.20 (1.23 – 1.20)
Completeness (%)	100.0 (100.0)	97.6 (97.3)	99.7 (99.0)	98.4 (93.5)
Multiplicity	12.2 (11.3)	6.0 (5.1)	11.5 (10.6)	10.6 (7.8)
SNR	19.4 (1.2)	15.6 (0.9)	13.0 (1.1)	17.2 (1.0)
CC _{1/2}	1.00 (0.60)	1.00 (0.40)	1.00 (0.50)	1.00 (0.80)
R_{merge}	5.1 (174.2)	4.3 (95.3)	8.2 (120.4)	5.6 (85.2)
Refinement				
Resolution (Å)	38.71 – 1.15	34.47 – 0.99	38.44 – 1.08	34.14 – 1.17
No. of reflections	41,159	61,587	47,924	36,075
R_{work}	0.200	0.193	0.190	0.195
R_{free}	0.218	0.208	0.209	0.221

Chapter 6

	20 mg/mL GlcNac	30 mg/mL GlcNac	40 mg/mL GlcNac	50 mg/mL GlcNac
Ramachandran favoured	120 (94%)	120 (94%)	119 (93%)	121 (95%)
Ramachandran allowed	7 (6%)	7 (6%)	8 (7%)	6 (5%)
Ramachandran outliers	0 (0%)	0 (0%)	0 (0%)	0 (0%)
Bond lengths (Å)	0.0113	0.0155	0.0094	0.0095
Bond angles (°)	1.967	2.051	1.853	1.915

Appendix B Publication 1

Stubbs, J., Hornsey, T., Hanrahan, N., Esteban, L.B., Bolton, R., Malý, M., Basu, S., Orlans, J., De Sanctis, D., Shim, J., Shaw Stewart, P.D., Orville, A.M., Tews, I., West, J., 2024. Droplet microfluidics for time-resolved serial crystallography. *IUCrJ* 11, 237–248.

<https://doi.org/10.1107/S2052252524001799>

Publication is included overleaf for reference:



Received 12 January 2024

Accepted 23 February 2024

Edited by F. Maia, Uppsala University, Sweden

Keywords: droplet microfluidics; crystal miniaturization; micromixing; time-resolved serial crystallography.**PDB references:** lysozyme control, 8s2u; lysozyme droplet, 8s2v; Pdx1 control, 8s2w; Pdx1 droplet, 8s2x**Supporting information:** this article has supporting information at www.iucrj.org

Droplet microfluidics for time-resolved serial crystallography

Jack Stubbs,^{a,b*} Theo Hornsey,^a Niall Hanrahan,^{c,d} Luis Blay Esteban,^e Rachel Bolton,^{a,b} Martin Malý,^{a,d} Shibom Basu,^f Julien Orlans,^g Daniele de Sanctis,^g Jung-uk Shim,^h Patrick D. Shaw Stewart,ⁱ Allen M. Orville,^{b,j} Ivo Tews^{a,d} and Jonathan West^{d,k*}

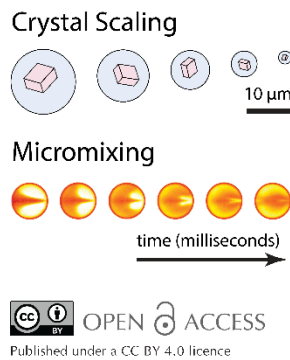
^aSchool of Biological Sciences, Faculty of Environmental and Life Sciences, University of Southampton, Southampton SO17 1BJ, United Kingdom, ^bDiamond Light Source, Harwell Science and Innovation Campus, Didcot, Oxfordshire OX11 0DE, United Kingdom, ^cSchool of Chemistry, Faculty of Engineering and Physical Sciences, University of Southampton, Southampton SO17 1BJ, United Kingdom, ^dInstitute for Life Sciences, University of Southampton, Southampton SO17 1BJ, United Kingdom, ^eUniversitat de València, Avenida de Cantaloch, 47, Sant Julià de Loria, Principat d'Andorra AD600, Spain, ^fEuropean Molecular Biology Laboratory, Grenoble Outstation, 71 Avenue des Martyrs, CS 90181, Grenoble 38042, Cedex 9, France, ^gEuropean Synchrotron Radiation Facility (ESRF), 71 Avenue des Martyrs, Grenoble 38042, Cedex 9, France, ^hFaculty of Engineering and Physical Sciences, University of Leeds, Leeds LS2 9JT, United Kingdom, ⁱDouglas Instruments Ltd, East Garston, Hungerford RG17 7HD, United Kingdom, ^jResearch Complex at Harwell, Harwell Science and Innovation Campus, Didcot, Oxfordshire OX11 0FA, United Kingdom, and ^kCancer Sciences, Faculty of Medicine, University of Southampton, Southampton SO17 1BJ, United Kingdom. *Correspondence e-mail: j.s1u21@soton.ac.uk, j.j.west@soton.ac.uk

Serial crystallography requires large numbers of microcrystals and robust strategies to rapidly apply substrates to initiate reactions in time-resolved studies. Here, we report the use of droplet miniaturization for the controlled production of uniform crystals, providing an avenue for controlled substrate addition and synchronous reaction initiation. The approach was evaluated using two enzymatic systems, yielding 3 µm crystals of lysozyme and 2 µm crystals of Pdx1, an *Arabidopsis* enzyme involved in vitamin B6 biosynthesis. A seeding strategy was used to overcome the improbability of Pdx1 nucleation occurring with diminishing droplet volumes. Convection within droplets was exploited for rapid crystal mixing with ligands. Mixing times of <2 ms were achieved. Droplet microfluidics for crystal size engineering and rapid micromixing can be utilized to advance time-resolved serial crystallography.

1. Introduction

Modern crystallography incorporates diffraction data collection at room temperature, providing a means to emulate physiological conditions whilst also observing the dynamic nature of proteins (Orville, 2020; Fraser *et al.*, 2011; Fischer, 2021). Challenges posed by elevated radiation damage (Holton, 2009; Garman, 2010; Garman & Weik, 2023) can be overcome by the collection of multiple datasets or the application of serial methods. No longer can optimal crystals be hand-picked, but instead large numbers of uniform microcrystals must be prepared. Advancements in instrumentation, including high-flux synchrotron sources and extreme-brilliance X-ray free-electron lasers (XFELs) (Chapman *et al.*, 2011; Chapman, 2019; Barends *et al.*, 2022), coupled with developments in automation, data processing, detector technologies (Förster *et al.*, 2019) and sample delivery, will ensure time-resolved experiments using serial methods will become routine in the near future.

Crystal size is a critical parameter for many reasons (Shoeman *et al.*, 2022); it should be tuned to the synchrotron or XFEL beam size [\sim 1–20 µm (Evans *et al.*, 2011)] for



OPEN ACCESS

Published under a CC BY 4.0 licence

IUCrJ (2024), 11, 237–248

<https://doi.org/10.1107/S2052252524001799> 237

research papers

improved signal-to-noise ratio in the X-ray diffraction pattern and efficient use of the protein sample. For time-resolved studies, the key advantages of small crystals are short substrate transport paths into the crystal lattice for rapid reaction triggering or short light paths for full penetration of exciting light. For illustration, substrate transport into the centre of a $2\text{ }\mu\text{m}$ crystal (*i.e.* $1\text{ }\mu\text{m}$ travel) is dependent on size (Schmidt, 2013) and several other factors, including the ligand diffusion coefficient, initial concentration, charge, mother liquor viscosity and crystal lattice packing, with time scales ranging from $400\text{ }\mu\text{s}$ for O_2 (32 Da) to 3.5 ms for larger ligands (*e.g.* ceftriaxone, 554 Da). Crystal uniformity is critically important, especially for synchronized reaction triggering, but also to avoid large crystals clogging capillaries used in many sample delivery systems. Ideal results will derive from monodisperse microcrystal slurries, robust sample delivery methods and reaction initiation strategies that exploit particular X-ray source characteristics and limit sample consumption.

Preparing large numbers of uniformly small crystals is an on-going challenge for the field. Although microcrystal showers are often the first hit in sparse matrix vapour diffusion screens, they typically need to be scaled-up by batch methods to produce the volumes required for serial crystallography experiments; this may reach millilitre volumes for time-course experiments with multiple time-point datasets (Tenboer *et al.*, 2014; Beale *et al.*, 2019; Stohrer *et al.*, 2021; Beale & Marsh, 2021; Shoeman *et al.*, 2022).

Crystal formation typically comprises a nucleation phase, followed by a growth phase. Under some crystallization conditions, nucleation occurs rapidly and, as crystals grow, they deplete protein in solution, and thereby prevent further nucleation. A popular strategy is to fragment crystals to make seeds to control crystal growth. Seeds effectively bypass nucleation, acting as nuclei to instantly initiate growth such that protein is shared throughout crystal growth (Stura & Wilson, 1990; D'Arcy *et al.*, 2007; Shaw Stewart *et al.*, 2011; Shoeman *et al.*, 2022). Nevertheless, this still results in crystal size variation, for example, if two seeds are in close proximity the competition for protein will result in a pair of smaller than average crystals. New approaches are therefore needed to compartmentalize single-crystal growth and produce uniformly sized crystals.

Microfluidics has attracted significant attention for crystallography as it can precisely control reaction environments (Li & Ismagilov, 2010; Puigmartí-Luis, 2014; Shi *et al.*, 2017; Sui & Perry, 2017). Initial efforts involved nanolitre environments enabling counter-diffusion for exploring phase diagrams (Hansen *et al.*, 2002; Zheng *et al.*, 2004; Li & Ismagilov, 2010), or dialysis to decouple and optimize nucleation separately from growth (Shim *et al.*, 2007a,b; Selimović *et al.*, 2009). Droplet microfluidic formats then allowed better control of crystal formation by negative feedback through protein depletion during crystal growth (Dombrowski *et al.*, 2007; Heymann *et al.*, 2014), defining crystal size by the available protein, *i.e.* droplet volume. Droplet microfluidic crystallizations have been demonstrated for lysozyme, glucose isomerase, trypsin, concanavalin A, D1D2 spliceosomal

snRNP particles (Heymann *et al.*, 2014; Akella *et al.*, 2014), sugar hydrolase and sialate O-acetylesterase (Babnigg *et al.*, 2022). Importantly, microfluidic droplets are highly monodisperse, which allows the protein supply to be exactly metered to achieve crystal uniformity. Studies to date have optimized droplet size to achieve single-crystal occupancy for the formation of large crystals suitable for obtaining synchrotron diffraction data *in situ*.

For time-resolved experiments there is also the challenge of rapidly triggering reactions with substrates and ligands (Echelmeier *et al.*, 2019). Mix-and-inject methods that first emerged (Weierstall *et al.*, 2012; Calvey *et al.*, 2016; Stagno *et al.*, 2017; Olmos *et al.*, 2018; Ishigami *et al.*, 2019; Dasgupta *et al.*, 2019; Pandey *et al.*, 2021; Murakawa *et al.*, 2022) involved coaxial flows with a core crystal stream. Hydrodynamic focusing results in stream-thinning to provide short paths for the transport of substrate molecules into the crystal prior to high-velocity injection into the beam using a gas dynamic virtual nozzle (GDVN) (DePonte *et al.*, 2008). As an efficient, high-hit-rate alternative, piezoelectric or acoustic drop-on-demand methods are gaining popularity for the delivery of substrate droplets onto crystals presented on fixed targets (Mehrabi *et al.*, 2019) or tape drives (Roessler *et al.*, 2016; Fuller *et al.*, 2017; Butrym *et al.*, 2021). Here, picolitre substrate volumes are dispensed onto individual crystals or crystals contained in nanolitre droplets (both within a humidified environment). Mixing initially occurs by impact-induced convection, followed by diffusion, then the registration of the crystal into the beam after a defined time delay (2 ms and upwards). These sample delivery methods and their considerations are captured in recent reviews (Schulz *et al.*, 2022; Barends *et al.*, 2022).

In this contribution, we explore droplet scaling from nanolitre volumes down to sub-picolitre volumes and demonstrate the ability to engineer crystal size and uniformity. Using *Arabidopsis thaliana* Pdx1, an enzyme involved in vitamin B6 biosynthesis (Rodrigues *et al.*, 2017, 2022), and lysozyme, we demonstrate crystal scaling to suitable dimensions and numbers for time-resolved serial crystallography. We show that with diminishing volumes, nucleation becomes improbable, but this can be countered by seeding. We go on to exploit droplets as convective environments for rapid micro-mixing, achieving mixing within 2 ms to support future strategies for understanding structural dynamics with high temporal resolution.

2. Material and methods

2.1. Protein expression, purification and crystallization

2.1.1. Lysozyme. Lysozyme (chicken egg white, Melford) was batch-crystallized using a ratio of one part 20 mg ml^{-1} lysozyme in 20 mM sodium acetate, pH 4.6 to four parts of mother liquor; 6%(*w/v*) PEG 6000 in 3.4 M NaCl and 1 M sodium acetate, pH 3.0; [adapted from previous conditions (Martin-Garcia *et al.*, 2017)]. The mixture was vortexed for 5 s and left to crystallize for 1 h at room temperature.

2.1.2. Trypsin. Trypsin (bovine pancreas, type I, Merck) needles were crystallized using seeded vapour diffusion conditions as previously described (Heymann *et al.*, 2014). Seed stocks were prepared by pooling crystals from many vapour diffusion drops, dilution in mother liquor [11–14% (w/v) PEG 4000, 15% ethylene glycol, 200 mM SiSO_4 , 100 mM MES, pH 6.5] and vortexing with a Hampton Seed Bead for 180 s by alternating between 30 s of vortexing and 30 s on ice followed by storage at -20°C . Seeded-batch trypsin crystallization involved one part 65 mg ml^{-1} trypsin in 3 mM CaCl_2 with benzamidine, one part mother liquor and one part seed prepared in mother liquor. The mixture was vortexed for 5 s and incubated at room temperature overnight.

2.1.3. Pdx1. Plasmid encoding wild-type Pdx1.3 (UniProt ID: Q8L940; EC: 4.3.3.6; Rodrigues *et al.*, 2017) was transformed into BL21 (DE3) competent *E. coli* cells, and grown to OD_{600} 0.6 at 37°C . After induction with 25% (w/v) lactose and growth for a further 16 h at 30°C , cells were harvested by centrifugation. Cells were resuspended in lysis buffer [50 mM Tris pH 7.5, 500 mM sodium chloride, 10 mM imidazole, 2% (v/v) glycerol] and sonicated on ice. The lysate was ultracentrifuged at 140 000*g* at 4°C for 1 h, filtered and immobilized on a metal ion affinity chromatography HisTrap HP column (GE Healthcare). Pdx1 was washed and eluted with lysis buffer, containing 50 mM and 500 mM imidazole, respectively, as well as 5% (v/v) glycerol. The eluted protein was buffer-exchanged into gel filtration buffer (20 mM Tris pH 8.0, 200 mM KCl), before centrifugal concentration with a 30 kDa cut-off (Vivaspin 20, Sartorius). Crystals for preparing seeds were produced by combining (1:1) \sim 12 mg ml^{-1} Pdx1 with mother liquor (600 mM sodium citrate, 100 mM HEPES pH 7) as 10 μl vapour diffusion drops in 24-well XRL plates (Molecular Dimensions). Crystals for seed stocks grew overnight and varied in size from 10 to 50 μm in length. Vortexing with a Hampton Seed Bead was carried out for a total of 180 s by alternating between 30 s of vortexing and 30 s on ice followed by storage at -20°C . Batch crystallization involved a 1:1:1 mixture of 12 mg ml^{-1} Pdx1, seed (10^5 – 10^7 ml^{-1}) and mother liquor. In droplets a 2:1 mixture of seeds (10^7 ml^{-1}) diluted in mother liquor with 12 mg ml^{-1} Pdx1 was used.

2.2. Droplet microfluidics

2.2.1. Device fabrication. Microfluidic devices (Whitesides, 2006) were replicated by soft lithography (Whitesides *et al.*, 2001) using SU-8 on silicon wafers. Fabrication protocols for the different SU-8 heights are described in the SU-8 2000 technical data sheet made available by Kayaku Advanced Materials. Poly(dimethylsiloxane) (PDMS, Sylgard 184) was cured on the SU-8 wafers at 60°C for 2 h, with the PDMS used to counter-mould polyurethane (Smooth-Cast 310) copies of the SU-8 wafers. Subsequent PDMS devices were cured in the polyurethane moulds for 2 h at 60°C . A range of different droplet microfluidic devices were used for the generation of nanolitre to femtolitre droplets. Droplet generation junction dimensions, flow rates and droplet characteristics for the different protein systems are documented in Tables S1–S3 (see

the CAD-file in the supporting information). Tubing ports were introduced using 1 mm-diameter Miltex biopsy punches (Williams Medical Supplies Ltd). Devices were bonded to glass microscope slides using a 30 s oxygen plasma treatment (Femto, Diener Electronic) followed by channel surface functionalization using 1% (v/v) trichloro(1H,1H,2H,2H-perfluoroctyl) silane (Merck) in HFE-7500 (3M Novec).

2.2.2. Microfluidic experimental setup. The experimental setup for droplet generation is shown in Fig. S1. The process involved the preparation of syringes containing protein, mother liquor and fluorinated oil (QX200, BioRad) which acts as the carrier phase. Pdx1 and trypsin I droplet preparations required the use of seeds within the mother liquor. Syringes were interfaced with 25 G needles (\sim 1.7 μl dead volume) for connecting to the microfluidic ports via polythene tubing (ID = 0.38 mm, OD = 1.09 mm, Smiths Medical). Syringe pumps (Fusion 100, Chemyx) were used to deliver reagents for droplet generation. Droplet generation was monitored using a Phantom Miro310 (Ametek Vision Research) high-speed camera mounted on an inverted microscope (CKX41, Olympus). Droplets were collected in microcentrifuge tubes and stored at room temperature for 2–3 days with a mineral oil overlay to prevent coalescence. Droplet dimensions and crystal occupancy were measured using a supervised *ImageJ* (NIH) process. Lambda (λ) is used to denote the average number of crystals per droplet.

2.2.3. Crystal retrieval and analysis. Crystals were retrieved from droplets by a procedure called ‘breaking the emulsion’. First, the QX200 oil is removed, then a tenfold volume (relative to emulsion volume) of mother liquor is added. Next, a volume of 1H,1H,2H,2H-perfluoro-1-octanol (PFO, Merck) is added to the emulsion with gentle pipetting used to break the emulsion. The PFO exchanges with the commercial surfactant surrounding the droplets, allowing the aqueous compartments of droplets to contact each other and coalesce. Finally, the single aqueous volume containing the crystals is removed for analysis by mounting on a coverslip for oil immersion imaging with a $60\times/1.4\text{NA}$ objective (Olympus). Crystal dimensions were measured using a custom MATLAB script (<https://github.com/luiblaes/Crystallography>) and manually validated.

2.3. Serial synchrotron crystallography

Lysozyme and Pdx1 crystals were concentrated by settling and applied to sheet-on-sheet (SOS) chips (Doak *et al.*, 2018). This involved removal of excess liquid and sandwiching 3–5 μl of the crystal slurry between two Mylar films and sealing inside a metal mount. A total of 81 800 images were collected per chip. Serial synchrotron crystallography (SSX) data for lysozyme and Pdx1 crystals grown in batch and within microfluidic droplets were collected on the new ID29 beamline at the European Synchrotron Radiation Facility (ESRF, France) using a $2 \times 4 \mu\text{m}$ ($V \times H$) beam of 11.56 keV X-rays, with a 90 μs pulse and 231.25 Hz repetition rate, and a 20 μm step movement between images. A JUNGFRAU 4M detector (Mozzanica *et al.*, 2018) with a sample-to-detector distance of

research papers

175 mm (1.8 Å in the corner) was used to collect diffraction patterns. Full information on data processing, structure determination and refinement are available in the supporting information.

2.4. Mixing in droplets and image analysis

Mixing of lysozyme crystals ($7 \times 2 \mu\text{m}$; grown by batch crystallization) with 25 mM sulfanilic acid azochromotrop (SAA, Merck, $\lambda_{\text{max}} = 505\text{--}510 \text{ nm}$), a highly absorbing red dye, was investigated using $30 \times 40 \mu\text{m}$ droplet-generation junctions with an oil:aqueous flow ratio of 2:1. The crystal:dye flow ratio was modulated along with total flow rates ranging from 7.5 to $45 \mu\text{l min}^{-1}$. To retain crystals in suspension for ensuring continuous crystal delivery to the microfluidic device, we used automated syringe rotation (Lane *et al.*, 2019). In an alternative setup, a droplet generator producing SAA droplets was positioned upstream of an inlet for the introduction of pre-formed $\sim 70 \mu\text{m}$ -diameter droplets containing lysozyme crystals. The lysozyme and SAA droplets were synchronized for one-to-one interception, followed by surfactant exchange with PFO for droplet fusion and ensuing circulation-driven micromixing. This experiment involved $12.5 \mu\text{l min}^{-1}$ 10% (v/v) QX200 in HFE7500, $4 \mu\text{l min}^{-1}$ lysozyme, $5 \mu\text{l min}^{-1}$ SAA dye and $4 \mu\text{l min}^{-1}$ PFO flow rates. For both strategies, diffusive-convective mixing of the SAA dye was captured by high-speed imaging (Phantom Miro310, Ametek Vision Research). Droplets were individually analysed to understand mixing with and without crystals. The coefficient of variation (CV) of the intensity of pixels defining each droplet was used as the mixing measure. CV approaches zero as the dye is homogenized throughout the droplet. The time from stream combination to a 5% pixel intensity CV value was used to define the mixing time. Mixing analysis was automated using a MATLAB script with 15 single droplet kymographs used to derive mixing time statistics.

3. Results

3.1. Experimental design

Droplet microfluidic designs incorporated aqueous inlets for protein, mother liquor, seed and another for the fluorinated oil with flow-focusing used for droplet generation [Fig. 1(a)]. Droplet generation junction dimensions were used to scale droplet volumes from ~ 750 to $\sim 1 \text{ pl}$ to investigate conditions for controlling lysozyme and Pdx1 crystal size and uniformity. To understand the effects of droplet confinement, the resulting crystals were compared with those grown under conventional batch conditions. Droplet microfluidics was then investigated as a means to rapidly mix crystals with substrates. Crystals were either encapsulated with substrate during droplet generation or crystal-containing droplets were fused with substrate-containing droplets.

3.2. Lysozyme crystallization in microfluidic droplets

Lysozyme is a well known standard that undergoes extremely fast nucleation (Forsythe *et al.*, 1999). Indeed, the

nucleation rate in our batch crystallization method is too fast to measure (Video S1 of the supporting information), but a resultant crystal density of $\sim 80 \text{ nl}^{-1}$ was observed ($\sim 80 \text{ M ml}^{-1}$). The rapid growth of lysozyme crystals introduces negative feedback to prevent later nucleation events. This aids length uniformity, producing crystals with an $8 \mu\text{m}$ average length and $\text{CV} \simeq 19\%$ [Fig. 1(c)].

Using batch crystallization as a benchmark we then sought to understand the effects of volume scaling by droplet confinement. Droplet microfluidics produced monodisperse ($\text{CV} < 4\%$) droplets ranging in size from 754 to 0.89 pl and crystal sizes ranging from 20 to $2 \mu\text{m}$ [Figs. 1(a) and 1(b)]. In the largest droplets [754 pl ($\phi 113 \mu\text{m}$)], crystals were too numerous to count, whereas smaller droplets showed a crystal occupancy ranging from an average of 15 crystals per droplet ($\lambda 15$) in 194 pl droplets to stochastically loaded 0.89 pl droplets with ~ 0.01 crystals per droplet ($\sim \lambda 0.01$) [Fig. 1(c)]. Multiple nucleation events within each droplet result in a high crystal size CV. As droplets are miniaturized, the mean occupancy falls below $\lambda 0.1$, giving rise to the majority of occupied droplets containing a single crystal. Confirming our expectations, single-crystal occupancy promotes uniformity, producing a crystal size CV of $\sim 15\%$ in 0.89 pl droplets. Importantly, single occupancy coupled with droplet volume control also confers crystal miniaturization, producing $\sim 3 \mu\text{m}$ long lysozyme crystals in the smallest 0.89 pl droplets [Fig. 1(c)].

Attaining single-crystal occupancy while aiming to reduce crystal size by limiting droplet volume becomes inefficient as a consequence of the nucleation density. Beyond this, other losses are apparent with droplet miniaturization [Fig. 1(f)], with the crystal density falling from $\sim 80 \text{ crystals nl}^{-1}$ for batch controls and 194 pl droplets to $\sim 7 \text{ crystals nl}^{-1}$ in the 0.89 pl droplets. Losses correlate with the increased surface area to volume ratio associated with droplet miniaturization [Fig. 1(f)], which may implicate the surfactant droplet interface as an inhibitory environment for crystal formation. In terms of throughput, losses are compensated by droplet generation frequency increasing with droplet miniaturization. In practice, droplet generation frequency increases 50-fold from 0.44 kHz with the 754 pl droplets to 23.5 kHz with the 0.89 pl droplets [Fig. 1(g)]. Such throughput with incubation off-chip allows the mass production of crystals which would otherwise be greatly limited by device size when undertaking on-chip crystallization.

3.3. Pdx1 crystallization in microfluidic droplets with seeding

We next sought to investigate whether the droplet approach could be applied to a protein with more typical crystallization behaviour than lysozyme. We used Pdx1, where nucleation rates are much lower, resulting in only a few crystals, which is inadequate for populating small droplets with crystals. To address this issue, we prepared Pdx1 seeds to substantially increase the crystal density and synchronize crystal growth initiation.

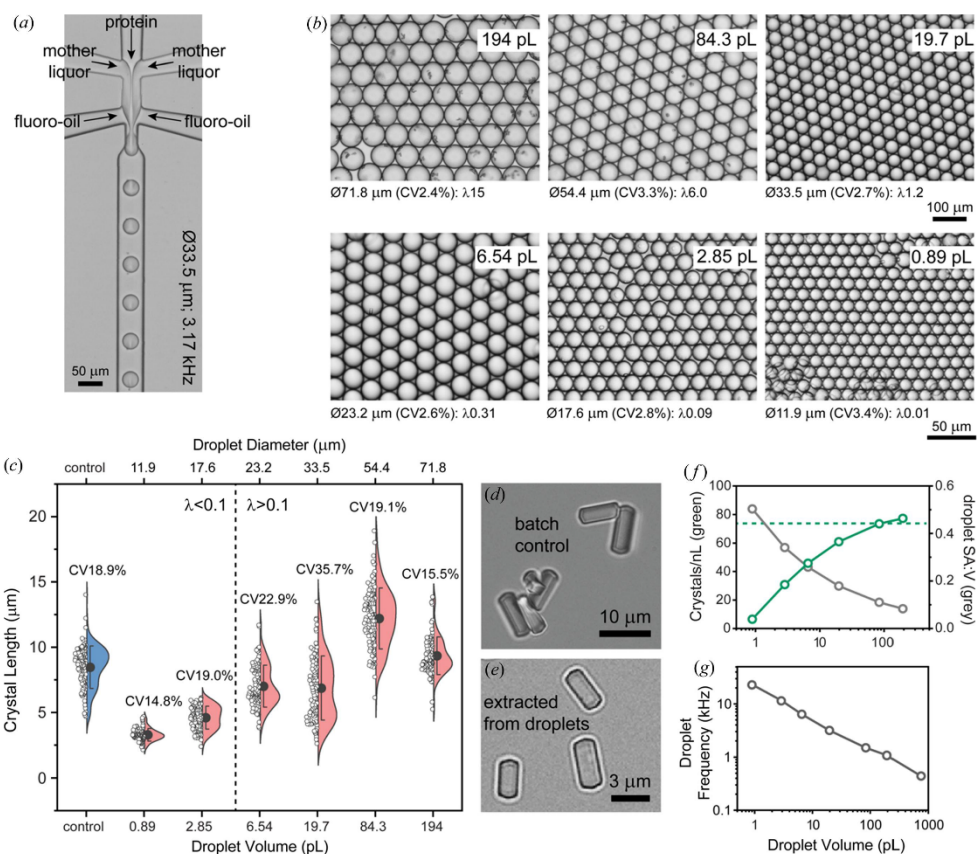


Figure 1
Lysozyme crystal size control by droplet volume scaling. (a) Protein crystallization droplets generated at kilohertz frequencies by combining streams of lysozyme, mother liquor and fluorinated oil. (b) Using different devices and flow rates (see Table S1 of the supporting information), monodisperse droplets ($CV < 4\%$) can be produced with picolitre to femtolitre volumes. (c) Lysozyme crystals produced under batch conditions (control, blue) were on average $8 \mu\text{m}$ long. The length of lysozyme crystals produced in droplets (salmon) correlates with the droplet volume, with $\sim 3 \mu\text{m}$ -long crystals produced in the smallest 0.89 pL droplets. Crystal uniformity emerges when the average number of crystals per droplet (λ) is ≤ 0.1 . (d) and (e) Visual comparison of lysozyme crystals prepared in batch (control) and extracted from 0.89 pL droplets by breaking the emulsion. (f) Droplet volume miniaturization is associated with reduced crystal density normalized to crystals per nanolitre (green) which correlates with increasing the surface area to volume (SA:V, grey) ratio. The batch crystal density value is denoted by the green dashed line. (g) Gains in droplet generation frequency scale with droplet volume reduction.

Under batch conditions, the addition of seeds produced a crystal density of 10^7 ml^{-1} with an average length of $\sim 11 \mu\text{m}$ [Fig. 2(a)]. Accordingly, tenfold seed dilution in mother liquor reduced the number of crystals while providing more protein per crystal, resulting in $\sim 18 \mu\text{m}$ -long crystals for 1/10 seed dilutions and $30 \mu\text{m}$ -long crystals for 1/100 seed dilutions [Fig. 2(a)]. In principle, seeding initiates crystal growth at the same time, providing equal access to protein throughout growth which results in same-sized crystals. In practice, crystals were variable in size, with a $\sim 25\%$ CV across the dilution series [Fig. 2(a)].

Translating the seeded crystallization of Pdx1 under batch conditions to droplet environments using 10^7 ml^{-1} seeds typically resulted in single-crystal occupancy to favour crystal length uniformity (CV 7–16%) across a 200-fold range of droplet volumes (1.1–219 pL) [Figs. 2(b) and 2(c)]. Droplet volume scaling with single-crystal occupancy allows the crystal size to be controlled, from $\sim 2 \mu\text{m}$ in length for the smallest 1.1 pL droplets, to $\sim 20 \mu\text{m}$ in length for the largest 219 pL droplets [Fig. 2(c)]. Overall, crystal size can be engineered by droplet volume while retaining uniformity, albeit with crystal occupancy decreasing with diminishing droplet volumes.

research papers

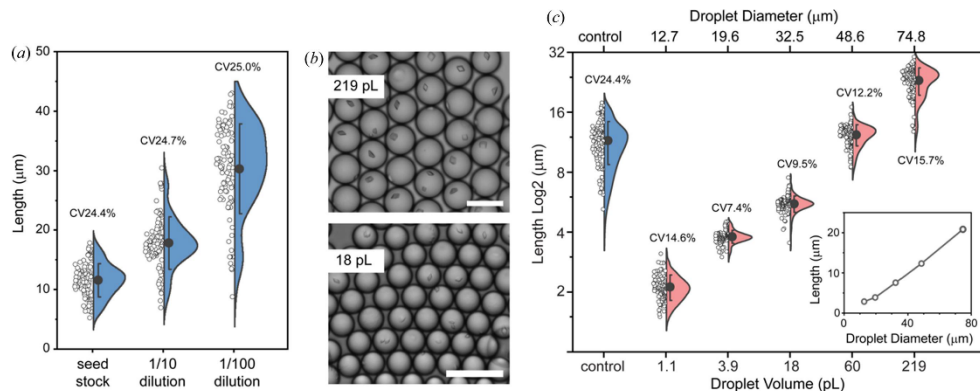


Figure 2

The effect of seeding under batch conditions compared with droplet conditions on Pdx1 crystal size. (a) Seeded batch Pdx1 crystallization involved a 1:1:1 mixture of Pdx1, seed (10^5 – 10^7 ml $^{-1}$) and mother liquor. The seed dilution affects crystal size (blue), but not crystal uniformity. (b) Pdx1 crystals were grown in droplets using a 2:1 mixture of seeds (10^7 ml $^{-1}$) in mother liquor with Pdx1. Pdx1 crystals grown in 219 and 18 pL monodisperse droplets typically have single occupancy (scale bars 100 μm). (c) Droplet miniaturization over a 200-fold range was used to control Pdx1 crystal length from ~20 to ~2 μm (salmon), with crystal length being proportional to droplet volume. (c, inset) Linear scaling of the crystal length with droplet diameter. Droplet confinement enables crystal-size uniformity (CVs 7.4–15.7%). Pdx1 crystals prepared in batch (control, blue) are large with low uniformity (CV 24.4%).

3.4. Considerations for crystallization in microfluidic droplets

3.4.1. Aspect ratio. The general applicability of droplets as environments for preparing a variety of different protein crystals is supported by previous work (Heymann *et al.*, 2014; Akella *et al.*, 2014; Babinigg *et al.*, 2022). To extend applicability, we sought to investigate the effect of droplet confinement on the growth of crystal needles. Using trypsin type I as a model needle system, it was evident that droplet diameters are insufficient to allow full elongation, resulting in a lower crystal axial ratio (l/w) or fragmentation into multiple small-needle crystals [Figs. S4(a) and S4(b)]. A similar effect is evident with parallelepiped-shaped lysozyme crystals, with the crystal axial ratio decreasing with droplet diameter [Fig. S4(c)]. This indicates that protein inclusion within the ends of elongated crystals is impeded within droplets.

3.4.2. Viscosity. Another consideration for the broader utility of droplet microfluidics for crystal preparation is the use of different crystallization mixtures. Precipitating agents such as poly(ethylene glycol) increase viscosity, which impacts the feasibility of producing stable droplet flows at sufficient throughput. To evaluate this effect, we prepared PEG 6000 solutions [0–25% (w/v)] ranging in viscosity from 1 to 21 mPa s and used these to observe the effect of viscosity on the generation of 50 μm-diameter droplets. Only an approximately threefold reduction in throughput was observed over these extremes (Fig. S5), indicating scope to apply droplet microfluidics to other crystallization conditions.

3.4.3. Minimum crystal size. The minimum crystal size is another consideration. Given that diffraction data can be obtained from sub-micrometre crystals (Gati *et al.*, 2017; Bücker *et al.*, 2020; Williamson *et al.*, 2023), and the 2–3 μm-long lysozyme and Pdx1 crystals prepared in ~1 pL droplets,

there is scope to further reduce droplet volumes. Though it is feasible to prepare monodisperse 5.4 μm-diameter droplets with a volume of 82 fL, the effect of greatly reduced seed occupancy and lower crystal formation frequency [Fig. 1(f)] prevented observable crystal formation [Fig. S6].

Smaller crystals are also harder to hit with a microfocus X-ray beam and impact sample delivery choice. For instance, small crystals will pass through 7 μm and larger apertures on fixed targets (Hunter *et al.*, 2014; Rödig *et al.*, 2015; Owen *et al.*, 2017; Mehrabi *et al.*, 2020), although smaller apertures are now emerging (Carrillo *et al.*, 2023). As an alternative, wells within fixed targets can be loaded by depositing 10–100s of picolitre droplets containing microcrystals using a piezoelectric injector. These droplets are larger than the aperture and held by surface tension to the well walls during data collection (Davy *et al.*, 2019).

3.5. Serial synchrotron crystallography

We tested the visually similar crystals of lysozyme and Pdx1 prepared in batch and droplets for diffraction quality, determining and comparing structures for the two scenarios. Though droplets can be directly dispensed on silicon fixed targets (Babinigg *et al.*, 2022), we opted to remove the fluorinated oil and surfactant to ensure optimal signal to noise. This can be achieved by a procedure called ‘breaking the emulsion’ [see Methods, compare Fig. S2].

SSX experiments were performed at the new ID29 serial beamline at ESRF. Data collection took 10 min with minimal sample consumption (3–5 μL volumes) using the ESRF sheet-on-sheet (SOS) chip sample holder (Doak *et al.*, 2018). A full dataset was achieved from a single chip of lysozyme with a microcrystal concentration of 10^8 ml $^{-1}$. However, Pdx1 required three chips to obtain complete data, owing to the

Table 1

Data collection and refinement statistics for lysozyme and Pdx1 crystals grown under batch conditions and in droplets.

Values in parentheses are for the high-resolution shell. For all datasets, the wavelength was 1.07 Å and the average crystal length was ~15 µm.

	Lysozyme control	Lysozyme droplet	Pdx1 control	Pdx1 droplet
Data collection				
No. of collected images	81800	81800	245400	245400
No. of hits	34032	22815	20268	20827
Hit rate (%)	41.6	27.9	8.2	8.5
Indexed images (single lattice)	29954	22304	19325	20635
Indexing rate (%)	88.0	97.7	95.3	99.0
Integrated patterns (including multiple lattices)	58984	51812	27581	25464
Space group	$P4_32_12$	$P4_32_12$	$H3$	$H3$
Unit-cell parameters				
$a = b$ (Å), c (Å)	79.0, 37.9	78.9, 37.9	177.9, 117.3	180.3, 119.2
α, β, γ (°)	90, 90, 90	90, 90, 90	90, 90, 120	90, 90, 120
Resolution (Å)	79.00–1.80 (1.83–1.80)	78.90–1.80 (1.83–1.80)	93.33–2.50 (2.54–2.50)	94.75–2.50 (2.54–2.50)
Total reflections	5096019 (26983)	5385630 (28772)	4534670 (215526)	4424291 (210986)
Unique reflections	11636 (669)	11607 (663)	47878 (4703)	50011 (4635)
Completeness (%)	100.0 (100.0)	100.0 (100.0)	100.0 (100.0)	100.0 (100.0)
Multiplicity	438.0 (47.67)	464.0 (51.94)	47.4 (45.18)	44.2 (41.83)
$\langle I/\sigma(I) \rangle$	13.5 (0.2)	17.2 (0.9)	4.4 (0.5)	5.0 (0.8)
$CC_{1/2}$	0.99 (0.49)	0.99 (0.44)	0.96 (0.17)	0.96 (0.27)
CC^*	0.99 (0.81)	0.99 (0.78)	0.99 (0.54)	0.99 (0.65)
R_{split}	5.2 (343.7)	4.9 (100.8)	19.6 (212.2)	17.1 (147.3)
Wilson B -factor (Å ²)	30.5	24.1	49.4	45.3
Refinement				
PDB entry	8S2U	8S2V	8S2W	8S2X
Resolution (Å)	55.92–1.80	55.85–1.80	64.47–2.50	65.40–2.50
No. of reflections	11597	11567	47873	50003
Reflections used for R_{free}	581	581	2316	2510
R_{work}	0.171	0.146	0.168	0.158
R_{free}	0.231	0.190	0.193	0.188
No. of atoms				
Protein	1023	1064	8081	8118
Ligand/ion	2	2	20	72
Water	59	66	181	186
Ramachandran favoured	127 (98%)	130 (98%)	1042 (98%)	1057 (99%)
Ramachandran allowed	2 (2%)	3 (2%)	25 (2%)	15 (1%)
Ramachandran outliers	0 (0%)	0 (0%)	0 (0%)	0 (0%)
Rama distribution Z-score†	-0.65 ± 0.70	-0.29 ± 0.68	-1.87 ± 0.22	-1.17 ± 0.23
Clashscore†	0.99	1.43	4.17	2.00
MolProbity score†	0.79	1.20	1.27	0.97
R.m.s deviations				
Bond lengths (Å)	0.0066	0.0080	0.0054	0.0062
Bond angles (°)	1.551	1.767	1.407	1.511

† As determined by MolProbity (Williams *et al.*, 2018).

lower microcrystal concentration of 10^7 ml⁻¹ and its lower symmetry $H3$ space group.

We used a similar number of integrated lattices to compare data quality and chose the same resolution cut-off (1.8 Å for lysozyme and 2.5 Å for Pdx1). Data between batch and droplet crystallization are equivalent for $CC_{1/2}$ and CC^* indices, whilst gains in $\langle I/\sigma(I) \rangle$ and R_{split} are observed for crystals grown in droplets [Table 1 and Fig. S3]. Refinement statistics showed that the R_{free} was, in both cases, lower for crystals grown from droplets, compared with batch; however, the difference is higher for lysozyme (0.04) compared with Pdx1 (0.005). We note that the signal-to-noise ratio in the highest-resolution shell was higher for crystals grown in droplets, compared with batch, which follows the trend in Wilson B for the data collected. For the two samples we tested, these observations suggest that droplet-grown crystals were more ordered than batch-grown samples, likely due to limited convection in the microscopic droplet environment, with

diffusion being the dominant mode of transporting protein to the growing crystal, resulting in slower crystal growth.

3.5.1. Mixing in droplets. Substrate-triggered time-resolved experiments require the mixing of crystal and substrate volumes. The median k_{cat} for enzymes is 13.7 s^{-1} (~70 ms reaction cycles) (Bar-Even *et al.*, 2011), requiring mixing and into-crystal transport (and binding) times of a few milliseconds to synchronize reactions and allow intermediates to be effectively resolved. However, mixing in conventional microfluidic systems is slow, limited by substrate diffusion into the crystal stream. In contrast, microfluidic droplets lend themselves to fast mixing (Song & Ismagilov, 2003). Here, the transport of droplets in microchannels introduces circulations within the droplet for rapid, convective-diffusive mixing (Fig. S7). We went on to explore the merits of two different droplet-based mixing approaches.

3.5.2. Mixing by droplet generation and transport. The first system involves mixing by droplet generation and transport.

research papers

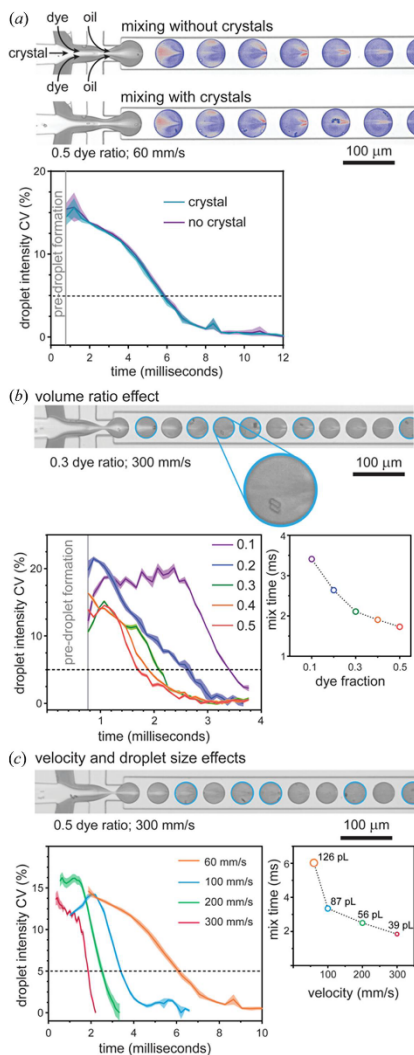


Figure 3

Mixing lysozyme crystals in droplets. (a) High-speed microscopy frame of mixing during droplet generation and transport along the channel (droplets are colour-enhanced to aid observation of mixing). The mixing rates with and without crystals are the same. Analysis involved 12 droplets with crystals and 10 droplets without. (b) Dye and crystal mixing in droplets at a ratio of 0.3 with a droplet velocity of 300 mm s^{-1} . Droplets containing crystals are highlighted with cyan circles. The mixing rate increases as the volume fraction of dye increases, with the optimal ratio being 0.5 (300 mm s^{-1} droplet velocity). The droplet pixel intensity CV is plotted as the mean \pm SD for 15 droplets. (c) Dye and crystal mixing in droplets at the optimal 0.5 ratio with a droplet velocity of 300 mm s^{-1} . The droplet pixel intensity CV is plotted as the mean \pm SD for 15 droplets. Increasing velocity increases convection (circulations within droplets) and shrinks droplet volumes to reduce diffusion paths, with both causing faster mixing.

Experiments involved the droplet encapsulation of a stream of pre-formed $\sim 7 \times 2 \mu\text{m}$ lysozyme crystals ($\sim 10^7 \text{ ml}^{-1}$) with a stream of red dye (SA A, 570 Da), comparable to a typical small-molecule substrate. Image analysis reveals that crystal and dye mixing during droplet generation occurs in a stepwise fashion: first, laminar streams converge with diffusion between streams initiating slow mixing, then droplet generation causes stream thinning (with short diffusion paths) for rapid mixing, followed by droplet transport with internal circulations driving mixing to completion [Fig. 3(a)]. Mixing begins upon flow convergence, with full mixing defined by a pixel intensity CV of 5%.

The presence of crystals within droplets did not affect mixing [Fig. 3(a)]. We next tested the 'entropy of mixing' theory (Ott & Boerio-Goates, 2000), which states that mixing is maximized when the volumes of initially separate liquids are equal. Indeed, at the same droplet velocity (300 mm s^{-1}), mixing times are reduced from 3.4 to 1.73 ms as the volume fraction of dye increases from 0.1 to 0.5 [Fig. 3(b)]. Taking this further, we investigated the effect of droplet velocity on mixing using the optimal 1:1 crystal:dye ratio. Increasing the velocity from 60 to 300 mm s^{-1} (droplet generation velocity limit) increased circulation speeds within droplets. Higher velocities also impart higher shear stresses during droplet generation, decreasing the droplet volume from 126 to 39 pL and producing shorter diffusion paths. Consequently, mixing times decrease from 6.0 ms at 60 mm s^{-1} to 1.85 ms at 300 mm s^{-1} [Fig. 3(c)], with faster mixing times anticipated using smaller and higher velocity droplets. Although mixing times are seldom reported, such fast mixing is equivalent to high-velocity co-axial capillary mixers (Calvey *et al.*, 2016), and exceeds mixing by drop-on-drop dispensing (Butrym *et al.*, 2021), or the ~ 20 ms mixing times reported for 3D-printed GDVN devices incorporating mixing blades (Knoška *et al.*, 2020).

3.5.3. Mixing initiated by droplet fusion. The ability to produce crystals in droplets affords an alternative strategy for mixing; protein crystals can be prepared in droplets by incubation (*e.g.* overnight) with droplets subsequently injected into a droplet device for fusion with substrate-containing droplets. This removes the need for breaking the emulsion, and moreover droplet-containment prevents crystal sedimentation within the syringe and channels being clogged. As a proof of principle, we developed a microfluidic circuit for generating 225 pL substrate droplets and synchronizing these with pre-formed 200 pL droplets containing crystals (Video S2). Synchronized droplet coupling was achieved by exploiting the size-dependent velocity differences between crystal-containing and substrate-containing droplets: the smaller, faster droplets approach and contact the larger droplets in readiness for fusion. A surfactant-exchange method was used for fusing droplets and initiating mixing (Mazutis *et al.*, 2009). Unlike mixing by droplet generation, this does not include the stream thinning effect for shortening diffusion paths. Reliable droplet fusion occurs at 100 mm s^{-1} , achieving mixing in ~ 7 ms (Video S3). Again, faster mixing is anticipated for smaller droplets. Note that into-crystal substrate transport can

occur earlier since convection within the droplet mobilizes the crystal throughout substrate-occupied regions before complete mixing is achieved. Nevertheless, the mixing times we report provide a conservative guide for the millisecond timescales that can be accessed, with the limiting step now being the into-crystal travel timescales of the substrate.

3.5.4. Droplets interfacing with the beam. To perform time-resolved experiments, mixing is followed by defined incubations and then crystal interaction with the beam. Importantly, droplets, and crystals within them, have the same transport velocity ensuring uniform incubation times. In contrast, conventional microfluidic transport suffers the effects of the parabolic velocity profile in which crystals in different streamlines are transported at different velocities (*i.e.* have different incubations). Periodic droplet generation with tuneable frequency (*e.g.* \sim 300 Hz to \sim 6 kHz in our reported mixing experiments) further offers potential for synchronization with beam repetition frequency to improve the hit rate. In practice, however, retaining periodicity during ejection into the beam introduces technical challenges which currently limit their potential (Echelmeier *et al.*, 2019, 2020; Doppler *et al.*, 2022; Sonker *et al.*, 2022). Droplet methods still exceed hit rates achieved using conventional GDVN methods, but now offer the benefits of faster micromixing for synchronized reaction triggering.

As an alternative to GDVN crystal injection into the beam, data collection can be achieved from within the microfluidic device, so-called *in situ* X-ray crystallography. Although PDMS is incompatible with X-rays due to high attenuation, it can nevertheless be used to analyse proteins with a spectral read-out. This enables experiment work-up in advance of visiting synchrotron or XFEL facilities. To exploit synchrotron capabilities and have broad utility, new challenges and technical possibilities emerge such as the fabrication of droplet microfluidic devices using thin-film materials (*e.g.* cyclic olefin co-polymer) that do not appreciably attenuate the X-ray beam (Sui *et al.*, 2016; Liu *et al.*, 2023). For much higher energy XFEL sources, the challenge of controlled ejection into the beam remains.

4. Conclusions

We have demonstrated droplet confinement and miniaturization for controlling crystal size and uniformity. At low picolitre and femtolitre scales, nucleation becomes improbable and can be bypassed using a seeding strategy for producing crystals only a few micrometres in length. The method was demonstrated with lysozyme and Pdx1, with crystals grown in droplets producing equivalent (if not better) diffraction data quality to those produced under batch conditions. Picolitre-scale droplet microfluidics also enables rapid, millisecond-scale micromixing to increase the temporal resolution of time-resolved experiments. Droplet microfluidic mixers can, in the future, be fabricated using thin-film, X-ray transparent materials for synchrotron experiments or coupled with beam injection methods to extend the approach to XFEL experi-

ments. In summary, droplet microfluidics methods offer great promise for improving time-resolved crystallography.

5. Related literature

The following references are cited in the supporting information: Agirre *et al.* (2023); Barty *et al.* (2014); Berman *et al.* (2003); Emsley *et al.* (2010); Gevorkov *et al.* (2019); Joosten *et al.* (2014); Monteiro *et al.* (2019); Murshudov *et al.* (2011); Potterton *et al.* (2018); Vagin & Teplyakov (2010); White (2019); White *et al.* (2012); Yefanov *et al.* (2015).

Acknowledgements

We thank Chris Holes for support with protein crystallization, ESRF for access to ID29 (under proposal Nos. MX2438 and MX2548) and Emma Beale for the adapted lysozyme crystallization conditions.

Funding information

The research was funded by a Diamond Doctoral Studentship Programme (studentship awarded to JS and RB); a South Coast Biosciences Doctoral Training Partnership (SoCoBio DTP) by the Biotechnology and Biological Sciences Research Council (BBSRC) (studentship No. BB/T008768/1 awarded to JS); BBSRC (studentship No. BB/S008470/1 awarded to IT); Science and Technology Facilities Council, Serial Data Processing and Analysis in CCP4i2 (awarded to IT and MM); Wellcome Investigator Award (award No. 210734/Z/18/Z awarded to AO); Royal Society Wolfson Fellowship (award No. RSWFR2 awarded to AO); NH acknowledges support from Engineering and Physical Sciences Research Council Impact Acceleration Account, EPSRC Transformative Healthcare Grant (grant No. EP/ T020997/1), and University of Southampton Seed Enterprise Development Fund; University of Southampton Seed Enterprise Development Fund (awarded to NH).

References

Agirre, J., Atanasova, M., Bagdonas, H., Ballard, C. B., Baslé, A., Beilsten-Edmands, J., Borges, R. J., Brown, D. G., Burgos-Mármol, J. J., Berriford, J. M., Bond, P. S., Caballero, I., Catapano, L., Chojnowski, G., Cook, A. G., Cowtan, K. D., Croll, T. I., Debreczeni, J. É., Devenish, N. E., Dodson, E. J., Drevon, T. R., Emsley, P., Evans, G., Evans, P. R., Fando, M., Foadi, J., Fuentes-Montero, L., Garman, E. F., Gerstel, M., Gildea, R. J., Hatti, K., Hekkelman, M. L., Heuser, P., Hoh, S. W., Hough, M. A., Jenkins, H. T., Jiménez, E., Joosten, R. P., Keegan, R. M., Keep, N., Krissinel, E. B., Kolenko, P., Kovalevskiy, O., Lamzin, V. S., Lawson, D. M., Lebedev, A. A., Leslie, A. G. W., Lohkamp, B., Long, F., Malý, M., McCoy, A. J., McNicholas, S. J., Medina, A., Millán, C., Murray, J. W., Murshudov, G. N., Nicholls, R. A., Noble, M. E. M., Oeffner, R., Pannu, N. S., Parkhurst, J. M., Pearce, N., Pereira, J., Perrakis, A., Powell, H. R., Read, R. J., Rigden, D. J., Rochira, W., Sammito, M., Sánchez Rodríguez, F., Sheldrick, G. M., Shelley, K. L., Simkovic, F., Simpkin, A. J., Skubak, P., Sobolev, E., Steiner, R. A., Stevenson, K., Tews, I., Thomas, J. M. H., Thorn, A., Valls, J. T., Uski, V., Usón, I., Vagin, A., Velankar, S., Vollmar, M., Walden, H., Waterman, D.,

research papers

Wilson, K. S., Winn, M. D., Winter, G., Wojdyr, M. & Yamashita, K. (2023). *Acta Cryst. D79*, 449–461.

Akella, S. V., Mowitz, A., Heymann, M. & Fraden, S. (2014). *Cryst. Growth Des.* **14**, 4487–4509.

Babnigg, G., Sherrell, D., Kim, Y., Johnson, J. L., Nocek, B., Tan, K., Axford, D., Li, H., Bigelow, L., Welk, L., Endres, M., Owen, R. L. & Joachimiak, A. (2022). *Acta Cryst. D78*, 997–1009.

Barends, T. R. M., Stauch, B., Cherezov, V. & Schlichting, I. (2022). *Nat. Rev. Methods Primers*, **2**, 1–24.

Bar-Even, A., Noor, E., Savir, Y., Liebermeister, W., Davidi, D., Tawfik, D. S. & Milo, R. (2011). *Biochemistry*, **50**, 4402–4410.

Barty, A., Kirian, R. A., Maia, F. R. N. C., Hantke, M., Yoon, C. H., White, T. A. & Chapman, H. (2014). *J. Appl. Cryst.* **47**, 1118–1131.

Beale, J. H., Bolton, R., Marshall, S. A., Beale, E. V., Carr, S. B., Ebrahim, A., Moreno-Chicano, T., Hough, M. A., Worrall, J. A. R., Tews, I. & Owen, R. L. (2019). *J. Appl. Cryst.* **52**, 1385–1396.

Beale, J. H. & Marsh, M. E. (2021). *J. V. E. J.* e61896.

Berman, H., Henrick, K. & Nakamura, H. (2003). *Nat. Struct. Mol. Biol.* **10**, 980–980.

Bücker, R., Hogan-Lamarre, P., Mehrabi, P., Schulz, E. C., Bultema, L. A., Gevorkov, Y., Brehm, W., Yefanov, O., Oberthür, D., Kassier, G. H. & Dwayne Miller, R. J. (2020). *Nat. Commun.* **11**, 996.

Butryn, A., Simon, P. S., Aller, P., Hinchliffe, P., Massad, R. N., Leen, G., Tooze, C. L., Bogacz, I., Kim, I.-S., Bhowmick, A., Brewster, A. S., Devenish, N. E., Brem, J., Kamps, J. J. A. G., Lang, P. A., Rabe, P., Axford, D., Beale, J. H., Davy, B., Ebrahim, A., Orlans, J., Storm, S. L. S., Zhou, T., Owada, S., Tanaka, R., Tono, K., Evans, G., Owen, R. L., Houle, F. A., Sauter, N. K., Schofield, C. J., Spencer, J., Yachandra, V. K., Yano, J., Kern, J. F. & Orville, A. M. (2021). *Nat. Commun.* **12**, 4461.

Calvey, G. D., Katz, A. M., Schaffer, C. B. & Pollack, L. (2016). *Struct. Dyn.* **3**, 054301.

Carrillo, M., Mason, T., Karpik, A., Martiel, I., Kepa, M., McAuley, K., Beale, J. & Padeste, C. (2023). *IUCrJ*, **10**, 678–693.

Chapman, H. N. (2019). *Annu. Rev. Biochem.* **88**, 35–58.

Chapman, H. N., Fromme, P., Barty, A., White, T. A., Kirian, R. A., Aquila, A., Hunter, M. S., Schulz, J., DePonte, D. P., Weierstall, U., Doak, R. B., Maia, F. R. N. C., Martin, A. V., Schlichting, I., Lomb, L., Coppola, N., Shoeman, R. L., Epp, S. W., Hartmann, R., Rolles, D., Rudenko, A., Foucar, L., Kimmel, N., Weidenspointner, G., Holl, P., Liang, M., Barthelmess, M., Caleman, C., Boutet, S., Bogan, M. J., Krzywinski, J., Bostedt, C., Bajt, S., Gumprecht, L., Rudek, B., Erk, B., Schmidt, C., Hörmke, A., Reich, C., Pietschner, D., Strüder, L., Hauser, G., Gorke, H., Ullrich, J., Herrmann, S., Schaller, G., Schopper, F., Soltau, H., Kühnel, K. U., Messerschmidt, M., Bozek, J. D., Hau-Riege, S. P., Frank, M., Hampton, C. Y., Sierra, R. G., Starodub, D., Williams, G. J., Hajdu, J., Timneanu, N., Seibert, M. M., Andreasson, J., Rocker, A., Jönsson, O., Svenda, M., Stern, S., Nass, K., Andritschke, R., Schröter, C. D., Krasniqi, F., Bott, M., Schmidt, K. E., Wang, X., Grotjohann, I., Holton, J. M., Barends, T. R. M., Neutze, R., Marchesini, S., Fromme, R., Schorb, S., Rupp, D., Adolph, M., Gorkhovet, T., Andersson, I., Hirsemann, H., Potdevin, G., Graaftsmma, H., Nilsson, B. & Spence, J. C. H. (2011). *Nature*, **470**, 73–77.

D'Arcy, A., Villard, F. & Marsh, M. (2007). *Acta Cryst. D63*, 550–554.

Dasgupta, M., Budday, D., de Oliveira, S. H. P., Madzelen, P., Marchany-Rivera, D., Seravalli, J., Hayes, B., Sierra, R. G., Boutet, S., Hunter, M. S., Alonso-Mori, R., Batyuk, A., Wierman, J., Lyubimov, A., Brewster, A. S., Sauter, N. K., Applegate, G. A., Tiwari, V. K., Berkowitz, D. B., Thompson, M. C., Cohen, A. E., Fraser, J. S., Wall, M. E., van den Bedem, H. & Wilson, M. A. (2019). *Proc. Natl. Acad. Sci. USA*, **116**, 25634–25640.

Davy, B., Axford, D., Beale, J. H., Butryn, A., Docker, P., Ebrahim, A., Leen, G., Orville, A. M., Owen, R. L. & Aller, P. (2019). *J. Synchrotron Rad.* **26**, 1820–1825.

DePonte, D. P., Weierstall, U., Schmidt, K., Warner, J., Starodub, D., Spence, J. C. H. & Doak, R. B. (2008). *J. Phys. D Appl. Phys.* **41**, 195505.

Doak, R. B., Nass Kovacs, G., Gorel, A., Foucar, L., Barends, T. R. M., Grünbein, M. L., Hilpert, M., Kloos, M., Roome, C. M., Shoeman, R. L., Stricker, M., Tono, K., You, D., Ueda, K., Sherrell, D. A., Owen, R. L. & Schlichting, I. (2018). *Acta Cryst. D74*, 1000–1007.

Dombrowski, R. D., Litster, J. D., Wagner, N. J. & He, Y. (2007). *Chem. Eng. Sci.* **62**, 4802–4810.

Doppler, D., Rabbani, M. T., Letrun, R., Cruz Villarreal, J., Kim, D. H., Gandhi, S., Egatz-Gomez, A., Sonker, M., Chen, J., Koua, F. H. M., Yang, J., Youssef, M., Mazalova, V., Bajt, S., Shelby, M. L., Coleman, M. A., Wiedorn, M. O., Knoska, J., Schön, S., Sato, T., Hunter, M. S., Hosseini, A., Kupitz, C., Nazari, R., Alvarez, R. C., Karpas, K., Zaare, S., Dobson, Z., Discianno, E., Zhang, S., Zook, J. D., Bielecki, J., de Wijn, R., Round, A. R., Vagovic, P., Kloos, M., Vakili, M., Ketawala, G. K., Stander, N. E., Olson, T. L., Morin, K., Mondal, J., Nguyen, J., Meza-Aguilar, J. D., Kodis, G., Vaiana, S., Martin-Garcia, J. M., Mariani, V., Schwander, P., Schmidt, M., Messerschmidt, M., Ourmazd, A., Zatsepin, N., Weierstall, U., Bruce, B. D., Mancuso, A. P., Grant, T., Barty, A., Chapman, H. N., Frank, M., Fromme, R., Spence, J. C. H., Botha, S., Fromme, P., Kirian, R. A. & Ros, A. (2022). *J. Appl. Cryst.* **55**, 1–13.

Echelmeier, A., Cruz Villarreal, J., Messerschmidt, M., Kim, D., Coe, J. D., Thifault, D., Botha, S., Egatz-Gomez, A., Gandhi, S., Brehm, G., Conrad, C. E., Hansen, D. T., Madsen, C., Bajt, S., Meza-Aguilar, J. D., Oberthür, D., Wiedorn, M. O., Fleckenstein, H., Mendez, D., Knoška, J., Martin-Garcia, J. M., Hu, H., Lisova, S., Allahgholi, A., Gevorkov, Y., Ayer, K., Aplin, S., Ginn, H. M., Graafsmma, H., Morgan, A. J., Greiffenberg, D., Klujev, A., Laurits, T., Poehlsen, J., Trunk, U., Mezza, D., Schmidt, B., Kuhn, M., Fromme, R., Sztuk-Dambietz, J., Raab, N., Hauf, S., Silenzi, A., Michelat, T., Xu, C., Danilevski, C., Parenti, A., Mekinda, L., Weinhausen, B., Mills, G., Vagovic, P., Kim, Y., Kirkwood, H., Bean, R., Bielecki, J., Stern, S., Giewekemeyer, K., Round, A. R., Schulz, J., Dörner, K., Grant, T. D., Mariani, V., Barty, A., Mancuso, A. P., Weierstall, U., Spence, J. C. H., Chapman, H. N., Zatsepin, N., Fromme, P., Kirian, R. A. & Ros, A. (2020). *Nat. Commun.* **11**, 4511.

Echelmeier, A., Sonker, M. & Ros, A. (2019). *Anal. Bioanal. Chem.* **411**, 6535–6547.

Emsley, P., Lohkamp, B., Scott, W. G. & Cowtan, K. (2010). *Acta Cryst. D66*, 486–501.

Evans, G., Axford, D. & Owen, R. L. (2011). *Acta Cryst. D67*, 261–270.

Fischer, M. (2021). *Q. Rev. Biophys.* **54**, e1.

Förster, A., Brandstetter, S. & Schulze-Briese, C. (2019). *Phil. Trans. R. Soc. A*, **377**, 20180241.

Forsythe, E. L. H., Snell, E., Malone, C. C. & Pusey, M. L. (1999). *J. Cryst. Growth*, **196**, 332–343.

Fraser, J. S., van den Bedem, H., Samelson, A. J., Lang, P. T., Holton, J. M., Echols, N. & Alber, T. (2011). *Proc. Natl. Acad. Sci. USA*, **108**, 16247–16252.

Fuller, F. D., Gul, S., Chatterjee, R., Burgie, E. S., Young, I. D., Lebrette, H., Srinivas, V., Brewster, A. S., Michels-Clark, T., Clinger, J. A., Andi, B., Ibrahim, M., Pastor, E., de Lichtenberg, C., Hussein, R., Pollock, C. J., Zhang, M., Stan, C. A., Kroll, T., Fransson, T., Weninger, C., Kubin, M., Aller, P., Lassalle, L., Bräuer, P., Miller, M. D., Amin, M., Koroidov, S., Roessler, C. G., Allaire, M., Sierra, R. G., Docker, P. T., Gownia, J. M., Nelson, S., Koglin, J. E., Zhu, D., Chollet, M., Song, S., Lemke, H., Liang, M., Sokaras, D., Alonso-Mori, R., Zouni, A., Messinger, J., Bergmann, U., Boal, A. K., Bollinger, J. M., Krebs, C., Högbom, M., Phillips, G. N., Vierstra, R. D., Sauter, N. K., Orville, A. M., Kern, J., Yachandra, V. K. & Yano, J. (2017). *Nat. Methods*, **14**, 443–449.

Garman, E. F. (2010). *Acta Cryst. D66*, 339–351.

Garman, E. F. & Weik, M. (2023). *Curr. Opin. Struct. Biol.* **82**, 102662.

Gati, C., Oberthuer, D., Yefanov, O., Bunker, R. D., Stellato, F., Chiu, E., Yeh, S.-M., Aquila, A., Basu, S., Bean, R., Beyerlein, K. R., Botha, S., Boutet, S., DePonte, D. P., Doak, R. B., Fromme, R., Galli, L., Grotjohann, I., James, D. R., Kupitz, C., Lomb, L., Messerschmidt, M., Nass, K., Rendek, K., Shoeman, R. L., Wang,

D., Weierstall, U., White, T. A., Williams, G. J., Zatsepin, N. A., Fromme, P., Spence, J. C. H., Goldie, K. N., Jehle, J. A., Metcalf, P., Barty, A. & Chapman, H. N. (2017). *Proc. Natl Acad. Sci. USA*, **114**, 2247–2252.

Gevorkov, Y., Yefanov, O., Barty, A., White, T. A., Mariani, V., Brehm, W., Tolstikova, A., Grigat, R.-R. & Chapman, H. N. (2019). *Acta Cryst. A*, **75**, 694–704.

Hansen, C. L., Skordalakes, E., Berger, J. M. & Quake, S. R. (2002). *Proc. Natl Acad. Sci. USA*, **99**, 16531–16536.

Heymann, M., Ophalage, A., Wierman, J. L., Akella, S., Szekely, D. M. E., Gruner, S. M. & Fraden, S. (2014). *IUCrJ*, **1**, 349–360.

Holton, J. M. (2009). *J. Synchrotron Rad.*, **16**, 133–142.

Hunter, M. S., Segelke, B., Messerschmidt, M., Williams, G. J., Zatsepin, N. A., Barty, A., Benner, W. H., Carlson, D. B., Coleman, M., Graf, A., Hau-Riege, S. P., Pardini, T., Seibert, M. M., Evans, J., Boutet, S. & Frank, M. (2014). *Sci. Rep.*, **4**, 6026.

Ishigami, I., Lewis-Ballester, A., Echelmeier, A., Brehm, G., Zatsepin, N. A., Grant, T. D., Coe, J. D., Lisova, S., Nelson, G., Zhang, S., Dobson, Z. F., Boutet, S., Sierra, R. G., Batyuk, A., Fromme, P., Fromme, R., Spence, J. C. H., Ros, A., Yeh, S.-R. & Rousseau, D. L. (2019). *Proc. Natl Acad. Sci. USA*, **116**, 3572–3577.

Joosten, R. P., Long, F., Murshudov, G. N. & Perrakis, A. (2014). *IUCrJ*, **1**, 213–220.

Knoška, J., Adriano, L., Awel, S., Beyerlein, K. R., Yefanov, O., Oberthuer, D., Peña Murillo, G. E., Roth, N., Sarrou, I., Villanueva-Perez, P., Wiedorn, M. O., Wilde, F., Bajt, S., Chapman, H. N. & Heymann, M. (2020). *Nat. Commun.*, **11**, 657.

Lane, S. I. R., Butement, J., Harrington, J., Underwood, T., Shrimpton, J. & West, J. (2019). *Lab Chip*, **19**, 3771–3775.

Li, L. & Ismagilov, R. F. (2010). *Annu. Rev. Biophys.*, **39**, 139–158.

Liu, Z., Gu, K. K., Shelyb, M. L., Gilbile, D., Lyubimov, A. Y., Russi, S., Cohen, A. E., Narayanasamy, S. R., Botha, S., Kupitz, C., Sierra, R. G., Poitevin, F., Gilardi, A., Lisova, S., Coleman, M. A., Frank, M. & Kuhl, T. L. (2023). *Acta Cryst. D*, **79**, 944–952.

Martin-Garcia, J. M., Conrad, C. E., Nelson, G., Stander, N., Zatsepin, N. A., Zook, J., Zhu, L., Geiger, J., Chun, E., Kissick, D., Hilgart, M. C., Ogata, C., Ishchenko, A., Nagaratanam, N., Roy-Chowdhury, S., Coe, J., Subramanian, G., Schaffer, A., James, D., Kettwala, G., Venugopalan, N., Xu, S., Corcoran, S., Ferguson, D., Weierstall, U., Spence, J. C. H., Cherezov, V., Fromme, P., Fischetti, R. F. & Liu, W. (2017). *IUCrJ*, **4**, 439–454.

Mazutis, L., Baret, J. C. & Griffiths, A. D. (2009). *Lab Chip*, **9**, 2665–2672.

Mehrabi, P., Müller-Werkmeister, H. M., Leimkoh, J.-P., Schikora, H., Ninkovic, J., Kriyokuca, S., Andrić, L., Epp, S. W., Sherrell, D., Owen, R. L., Pearson, A. R., Tellkamp, F., Schulz, E. C. & Miller, R. J. D. (2020). *J. Synchrotron Rad.*, **27**, 360–370.

Mehrabi, P., Schulz, E. C., Agthe, M., Horrell, S., Bourenkov, G., von Stetten, D., Leimkoh, J.-P., Schikora, H., Schneider, T. R., Pearson, A. R., Tellkamp, F. & Miller, R. J. D. (2019). *Nat. Methods*, **16**, 979–982.

Monteiro, D. C. F., Vakili, M., Harich, J., Sztucki, M., Meier, S. M., Horrell, S., Josts, I. & Trebbin, M. (2019). *J. Synchrotron Rad.*, **26**, 406–412.

Mozzanica, A., Andrá, M., Barten, R., Bergamaschi, A., Chirietti, S., Brückner, M., Dinapoli, R., Fröjd, E., Greiffenberg, D., Leonarski, F., Lopez-Cuenca, C., Mezza, D., Redford, S., Ruder, C., Schmitt, B., Shi, X., Thattil, D., Tinti, G., Vetter, S. & Zhang, J. (2018). *Synchrotron Radiat. News*, **31**, 16–20.

Murakawa, T., Suzuki, M., Fukui, K., Masuda, T., Sugahara, M., Tono, K., Tanaka, T., Iwata, S., Nango, E., Yano, T., Tanizawa, K. & Okajima, T. (2022). *Acta Cryst. D*, **78**, 1428–1438.

Murshudov, G. N., Skubák, P., Lebedev, A. A., Pannu, N. S., Steiner, R. A., Nicholls, R. A., Winn, M. D., Long, F. & Vagin, A. A. (2011). *Acta Cryst. D*, **67**, 355–367.

Olmos, J. L., Pandey, S., Martin-Garcia, J. M., Calvey, G., Katz, A., Knoska, J., Kupitz, C., Hunter, M. S., Liang, M., Oberthuer, D., Yefanov, O., Wiedorn, M., Heyman, M., Holl, M., Pande, K., Barty, A., Miller, M. D., Stern, S., Roy-Chowdhury, S., Coe, J., Nagaratanam, N., Zook, J., Verburg, J., Norwood, T., Poudyal, I., Xu, D., Koglin, J., Seaberg, M. H., Zhao, Y., Bajt, S., Grant, T., Mariani, V., Nelson, G., Subramanian, G., Bae, E., Fromme, R., Fung, R., Schwander, P., Frank, M., White, T. A., Weierstall, U., Zatsepin, N., Spence, J., Fromme, P., Chapman, H. N., Pollack, L., Tremblay, L., Ourmazd, A., Phillips, G. N. & Schmidt, M. (2018). *BMC Biol.*, **16**, 59.

Orville, A. M. (2020). *Curr. Opin. Struct. Biol.*, **65**, 193–208.

Ott, J. B. & Boero-Goates, J. (2000). *Chemical Thermodynamics: Principles and Applications*. Academic Press.

Owen, R. L., Axford, D., Sherrell, D. A., Kuo, A., Ernst, O. P., Schulz, E. C., Miller, R. J. D. & Mueller-Werkmeister, H. M. (2017). *Acta Cryst. D*, **73**, 373–378.

Pandey, S., Calvey, G., Katz, A. M., Malla, T. N., Koua, F. H. M., Martin-Garcia, J. M., Poudyal, I., Yang, J.-H., Vakili, M., Yefanov, O., Zieliński, K. A., Bajt, S., Awel, S., Doerner, K., Frank, M., Gelisio, L., Jernigan, R., Kirkwood, H., Kloos, M., Koliyadu, J., Mariani, V., Miller, M. D., Mills, G., Nelson, G., Olmos, J. L., Sadri, A., Sato, T., Tolstikova, A., Xu, W., Ourmazd, A., Spence, J. H. C., Schwander, P., Barty, A., Chapman, H. N., Fromme, P., Mancuso, A., Phillips, G. N., Bean, R., Pollack, L. & Schmidt, M. (2021). *IUCrJ*, **8**, 878–895.

Potterton, L., Agirre, J., Ballard, C., Cowtan, K., Dodson, E., Evans, P. R., Jenkins, H. T., Keegan, R., Krissinel, E., Stevenson, K., Lebedev, A., McNicholas, S. J., Nicholls, R. A., Noble, M., Pannu, N. S., Roth, C., Sheldrick, G., Skubak, P., Turkenburg, J., Uski, V., von Delft, F., Waterman, D., Wilson, K., Winn, M. & Wojdyr, M. (2018). *Acta Cryst. D*, **74**, 68–84.

Puigmartí-Luis, J. (2014). *Chem. Soc. Rev.*, **43**, 2253–2271.

Rodrigues, M. J., Giri, N., Royant, A., Zhang, Y., Bolton, R., Evans, G., Ealick, S. E., Begley, T. & Tews, I. (2022). *RSC Chem. Biol.*, **3**(2), 227–230.

Rodrigues, M. J., Windeisen, V., Zhang, Y., Guédez, G., Weber, S., Strohmeier, M., Hanes, J. W., Royant, A., Evans, G., Simning, I., Ealick, S. E., Begley, T. P. & Tews, I. (2017). *Nat. Chem. Biol.*, **13**, 290–294.

Roedig, P., Vartiainen, I., Duman, R., Panneerselvam, S., Stübe, N., Lorbeer, O., Warmer, M., Sutton, G., Stuart, D. I., Weckert, E., David, C., Wagner, A. & Meents, A. (2015). *Sci. Rep.*, **5**, 10451.

Roessler, C. G., Agarwal, R., Allaire, M., Alonso-Mori, R., Andi, B., Bachega, J. F. R., Bommer, M., Brewster, A. S., Browne, M. C., Chatterjee, R., Cho, E., Cohen, A. E., Cowan, M., Datwani, S., Davidson, V. L., Defever, J., Eaton, B., Ellson, R., Feng, Y., Ghislain, L. P., Glownia, J. M., Han, G., Hattne, J., Hellmich, J., Héroux, A., Ibrahim, M., Kern, J., Kuczewski, A., Lemke, H. T., Liu, P., Majlof, L., McClintock, W. M., Myers, S., Nelsen, S., Olechno, J., Orville, A. M., Sauter, N. K., Soares, A. S., Soltis, S. M., Song, H., Stearns, R. G., Tran, R., Tsai, Y., Uervirojanaengkorn, M., Wilmot, C. M., Yachandra, V., Yano, J., Yükl, E. T., Zhu, D. & Zouni, A. (2016). *Structure*, **24**, 631–640.

Schmidt, M. (2013). *Adv. Condens. Matter Phys.*, **2013**, 167276.

Schulz, E. C., Yorke, B. A., Pearson, A. R. & Mehrabi, P. (2022). *Acta Cryst. D*, **78**, 14–29.

Selimović, S., Jia, Y. & Fraden, S. (2009). *Cryst. Growth Des.*, **9**, 1806–1810.

Shaw Stewart, P. D., Kolek, S. A., Briggs, R. A., Chayen, N. E. & Baldock, P. F. M. (2011). *Cryst. Growth Des.*, **11**, 3432–3441.

Shi, H., Xiao, Y., Ferguson, S., Huang, X., Wang, N. & Hao, H. (2017). *Lab Chip*, **17**, 2167–2185.

Shim, J., Cristobal, G., Link, D. R., Thorsen, T. & Fraden, S. (2007a). *Cryst. Growth Des.*, **7**, 2192–2194.

Shim, J., Cristobal, G., Link, D. R., Thorsen, T., Jia, Y., Piattelli, K. & Fraden, S. (2007b). *J. Am. Chem. Soc.*, **129**, 8825–8835.

Shoeman, R. L., Hartmann, E. & Schlüting, I. (2022). *Nat. Protoc.*, **18**, 854–882.

Song, H. & Ismagilov, R. F. (2003). *J. Am. Chem. Soc.*, **125**, 14613–14619.

research papers

Sonker, M., Doppler, D., Egatz-Gomez, A., Zaare, S., Rabbani, M. T., Manna, A., Villarreal, J. C., Nelson, G., Ketawala, G. K., Karpas, K. & Alvarez, R. C. (2022). *Biophys. Rep.* **2**, 100081.

Stagno, J. R., Liu, Y., Bhandari, Y. R., Conrad, C. E., Panja, S., Swain, M., Fan, L., Nelson, G., Li, C., Wendel, D. R., White, T. A., Coe, J. D., Wiedorn, M. O., Knoska, J., Oberthuer, D., Tuckey, R. A., Yu, P., Dyba, M., Tarasov, S. G., Weierstall, U., Grant, T. D., Schwitters, C. D., Zhang, J., Ferré-D'Amaré, A. R., Fromme, P., Draper, D. E., Liang, M., Hunter, M. S., Boutet, S., Tan, K., Zuo, X., Ji, X., Barty, A., Zatsepин, N. A., Chapman, H. N., Spence, J. C. H., Woodson, S. A. & Wang, Y.-X. (2017). *Nature*, **541**, 242–246.

Stohrer, C., Horrell, S., Meier, S., Sans, M., von Stetten, D., Hough, M., Goldman, A., Monteiro, D. C. F. & Pearson, A. R. (2021). *Acta Cryst. D* **77**, 194–204.

Stura, E. A. & Wilson, I. A. (1990). *Methods*, **1**, 38–49.

Sui, S. & Perry, S. L. (2017). *Struct. Dyn.* **4**, 032202.

Sui, S., Wang, Y., Kolewe, K. W., Srajer, V., Henning, R., Schiffman, J. D., Dimitrakopoulos, C. & Perry, S. L. (2016). *Lab Chip*, **16**, 3082–3096.

Tenboer, J., Basu, S., Zatsepин, N., Pande, K., Milathianaki, D., Frank, M., Hunter, M., Boutet, S., Williams, G. J., Koglin, J. E., Oberthuer, D., Heymann, M., Kupitz, C., Conrad, C., Coe, J., Roy-Chowdhury, S., Weierstall, U., James, D., Wang, D., Grant, T., Barty, A., Yefanov, O., Scales, J., Gati, C., Seuring, C., Srajer, V., Henning, R., Schwander, P., Fromme, R., Ourmazd, A., Moffat, K., Van Thor, J. J., Spence, J. C. H., Fromme, P., Chapman, H. N. & Schmidt, M. (2014). *Science*, **346**, 1242–1246.

Vagin, A. & Teplyakov, A. (2010). *Acta Cryst. D* **66**, 22–25.

Weierstall, U., Spence, J. C. H. & Doak, R. B. (2012). *Rev. Sci. Instrum.* **83**, 035108.

White, T. A. (2019). *Acta Cryst. D* **75**, 219–233.

White, T. A., Kirian, R. A., Martin, A. V., Aquila, A., Nass, K., Barty, A. & Chapman, H. N. (2012). *J. Appl. Cryst.* **45**, 335–341.

Whitesides, G. M. (2006). *Nature*, **442**, 368–373.

Whitesides, G. M., Ostuni, E., Takayama, S., Jiang, X. & Ingber, D. E. (2001). *Annu. Rev. Biomed. Eng.* **3**, 335–373.

Williams, C. J., Headd, J. J., Moriarty, N. W., Prisant, M. G., Videau, L. L., Deis, L. N., Verma, V., Keedy, D. A., Hintze, B. J., Chen, V. B., Jain, S., Lewis, S. M., Arendall, W. B. III, Snoeyink, J., Adams, P. D., Lovell, S. C., Richardson, J. S. & Richardson, D. C. (2018). *Protein Sci.* **27**, 293–315.

Williamson, L. J., Galchenkova, M., Best, H. L., Bean, R. J., Munke, A., Awel, S., Pena, G., Knoska, J., Schubert, R., Dörner, K., Park, H.-W., Bideshi, D. K., Henkel, A., Kremling, V., Klopprogge, B., Lloyd-Evans, E., Young, M. T., Valerio, J., Kloos, M., Sikorski, M., Mills, G., Bielecki, J., Kirkwood, H., Kim, C., de Wijn, R., Lorenzen, K., Xavier, P. L., Rahmani Mashhour, A., Gelisio, L., Yefanov, O., Mancuso, A. P., Federici, B. A., Chapman, H. N., Crickmore, N., Rizkallah, P. J., Berry, C. & Oberthür, D. (2023). *Proc. Natl Acad. Sci. USA*, **120**, e2203241120.

Yefanov, O., Mariani, V., Gati, C., White, T. A., Chapman, H. N. & Barty, A. (2015). *Opt. Express*, **23**, 28459–28470.

Zheng, B., Tice, J. D., Roach, L. S. & Ismagilov, R. F. (2004). *Angew. Chem. Int. Ed.* **43**, 2508–2511.

Appendix C Publication 2

Tremlett, C.J.‡, Stubbs, J. ‡, Stuart, W.S., Stewart, P.D.S., West, J., Orville, A.M., Tews, I. and Harmer, N.J., 2025. Small but mighty: the power of microcrystals in structural biology. IUCrJ, 12(3), 262-279. <https://doi.org/10.1107/S2052252525001484>

Publication is included overleaf for reference:

feature articles



IUCr

ISSN 2052-2525

BIOLOGY | MEDICINE

Received 15 November 2024
Accepted 18 February 2025

Edited by F. Maia, Uppsala University, Sweden

† These authors made equal contributions.

Keywords: microcrystals; MicroED; serial crystallography; time-resolved studies; seeding; phase diagrams; sample preparation; sample delivery.

Small but mighty: the power of microcrystals in structural biology

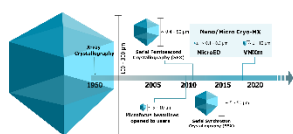
Courtney J. Tremlett,^{a,b*}‡ Jack Stubbs,^{c,d*}‡ William S. Stuart,^{a,b,e} Patrick D. Shaw Stewart,^f Jonathan West,^{g,h} Allen M. Orville,^{d,i} Ivo Tews^{c,g}‡ and Nicholas J. Harmer^{a,b}‡^aLiving Systems Institute, University of Exeter, Stocker Road, Exeter EX4 4QD, United Kingdom, ^bDepartment of Biosciences, University of Exeter, Stocker Road, Exeter EX4 4QD, United Kingdom, ^cSchool of Biological Sciences, Faculty of Environmental and Life Sciences, University of Southampton, Southampton SO17 1BJ, United Kingdom, ^dDiamond Light Source (United Kingdom), Harwell Science and Innovation Campus, Didcot OX11 0DE, United Kingdom, ^eDefence Science and Technology Laboratory, Porton Down, Salisbury SP4 0JQ, United Kingdom, ^fDouglas Instruments Ltd, East Garston, Hungerford RG17 7HD, United Kingdom, ^gInstitute for Life Sciences, University of Southampton, Southampton SO17 1BJ, United Kingdom, ^hCancer Sciences, Faculty of Medicine, University of Southampton, Southampton SO17 1BJ, United Kingdom, and ⁱResearch Complex at Harwell, Harwell Science and Innovation Campus, Didcot OX11 0FA, United Kingdom. *Correspondence e-mail: cjt212@exeter.ac.uk, jrs1u21@soton.ac.uk

Advancements in macromolecular crystallography, driven by improved sources and cryo cooling techniques, have enabled the use of increasingly smaller crystals for structure determination, with microfocus beamlines now widely accessible. Initially developed for challenging samples, these techniques have culminated in advanced beamlines such as VMXm. Here, an *in vacuo* sample environment improves the signal-to-noise ratio in X-ray diffraction experiments, and thus enables the use of submicrometre crystals. The advancement of techniques such as microcrystal electron diffraction (MicroED) for atomic-level insights into charged states and hydrogen positions, along with room-temperature crystallography to observe physiological states via serial crystallography, has driven a resurgence in the use of microcrystals. Reproducibly preparing small crystals, especially from samples that typically yield larger crystals, requires considerable effort, as no one singular approach guarantees optimal crystals for every technique. This review discusses methods for generating such small crystals, including mechanical crushing and batch crystallization with seeding, and evaluates their compatibility with microcrystal data-collection modalities. Additionally, we examine sample-delivery methods, which are crucial for selecting appropriate crystallization strategies. Establishing reliable protocols for sample preparation and delivery opens new avenues for macromolecular crystallography, particularly in the rapidly progressing field of time-resolved crystallography.

1. Introduction

Deciding on the optimal modality to address a biological question and prepare the corresponding sample is a challenge, with guidance scattered throughout the literature and across user experiences. In this review, we compile the resources to help resolve these choices and inform the experimental design to obtain static or time-resolved structures from microcrystals.

Microcrystals have played a pivotal role in developing microfocus beamlines at synchrotron facilities. Pioneering studies using microbeams at ID13 (Cusack *et al.*, 1998) at the European Synchrotron Radiation Facility (ESRF) paved the way for the construction of ID23-2, the first dedicated macromolecular microfocus beamline (Flot *et al.*, 2010). Today a growing number of microfocus beamlines are available, where data collection from microcrystals is possible, and an



OPEN ACCESS

Published under a CC BY 4.0 licence

overview of these facilities has been presented in a recent review by Chavas *et al.* (2024).

Microcrystals have been applied to room-temperature serial femtosecond crystallography (SFX) experiments at X-ray free-electron lasers (XFELs; Chapman *et al.*, 2011, 2014; Barends *et al.*, 2022). The first high-resolution structure from a slurry of microcrystals ($1 \times 1 \times 3 \mu\text{m}$) was published in 2012 (Boutet *et al.*, 2012). A second important development is crystal diffraction in cryo-electron microscopy (cryoEM), where appropriate sample preparation now enables data collection from submicrometre crystals/nanocrystals (micro/nano cryo-MX). A key application in this area is microcrystal electron diffraction (MicroED), where tilt-series data sets are acquired with minimal sample volumes (Shi *et al.*, 2013). Collectively, these methods have reduced the size of the crystal sizes that can be effectively studied by structural biologists from nanometre to micrometre scales (Fig. 1).

2. Microcrystal electron diffraction (MicroED)

MicroED uses a transmission electron microscope (TEM) to collect data sets from crystals with depths restricted to between 100 and 300 nm in all dimensions to reduce the possibility of multiple diffraction events from the lattice planes (Nannenga & Gonen, 2019; Martynowycz *et al.*, 2021). There are now ~ 150 structures in the PDB determined by MicroED (as of 31 October 2024). Of these, several could

not be obtained by other methods, including some membrane proteins (Zhu *et al.*, 2020; Gallenito & Gonen, 2022; Martynowycz *et al.*, 2023), hard-to-crystallize samples (Haymaker *et al.*, 2023) and radiation-sensitive samples (Martynowycz *et al.*, 2020). For crystals between 1 and 10 μm in one dimension, advanced nanofocus X-ray beamlines can be used to collect diffraction data utilizing the MicroED sample workflow (Beale, Waterman *et al.*, 2020; Crawshaw *et al.*, 2021; Warren *et al.*, 2024).

Electrons interact more strongly with biological matter compared with X-rays (Henderson, 1995), producing multiple diffraction planes and thus more comprehensive information per image through rotations. The considerably smaller electron wavelength at typical electron-microscope voltages leads to a larger Ewald sphere in comparison to X-rays, intersecting with more points in reciprocal space at a given time. However, this also results in the collected diffraction image lacking unit-cell information, so data from multiple crystals are merged and processed (Clabbers & Xu, 2021). Due to these characteristics, higher resolution structural information can be collected from smaller crystals with lower doses in multiple short exposures, providing higher signal to noise compared with X-ray methods (Henderson, 1992). Additionally, electrostatic potential maps are influenced by core and valence electron densities, allowing the bonding environment and oxidation states to be observed. However, this high interaction imposes an upper limit on MicroED crystal size to crystals

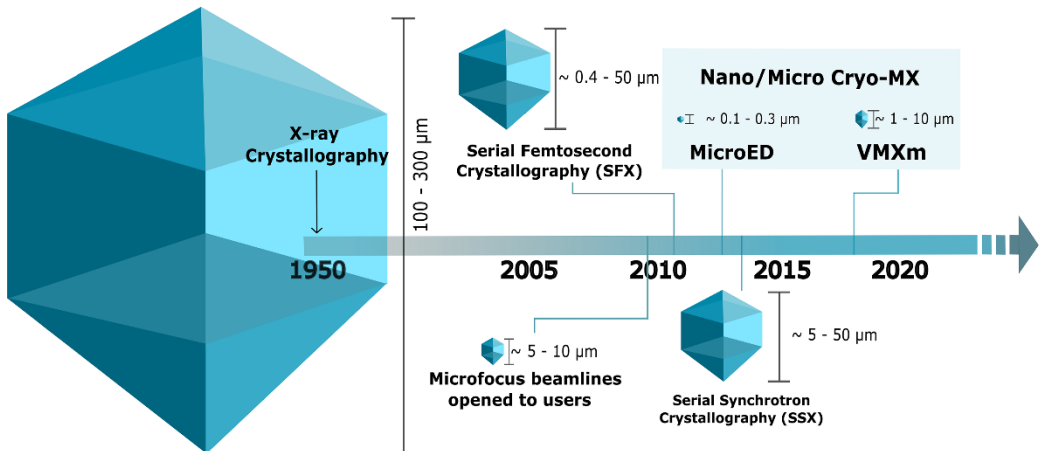


Figure 1

The evolution of macromolecular crystallography, told by size and method. Macromolecular X-ray crystallography (MX) gave rise to the first 3D protein structure, of myoglobin, determined by Kendrew and coworkers in 1957 (Kendrew *et al.*, 1958). Crystals for MX structure determination were required to have sizes greater than 100 μm in all dimensions to expose sufficient crystal lattice volumes to the beam (Smyth & Martin, 2000). Study of 5–10 μm crystals was made possible by the development of advanced instrumentation with dedicated microfocus beamlines such as ID23-2 at ESRF (Flot *et al.*, 2010). The advent of single-shot serial crystallography at XFELs opened up the opportunity to study samples (and/or reactions) at physiological temperatures. The first structure reported from this method was lysozyme (Boutet *et al.*, 2012). While serial methods were adopted by synchrotron sources, crystal sizes are typically larger and range between 10 and 50 μm , as seen for the first structure determined by this method (Gati *et al.*, 2014). Sample preparation using methods adapted from cryoEM include MicroED on one hand, with the first published structure in 2013 (Shi *et al.*, 2013), and X-ray crystallography on the other hand, with the VMXm beamline at the Diamond Light Source (Warren *et al.*, 2024), which are designed for the use of samples down to submicrometre sizes. Despite the plethora of methods, macromolecular crystallization currently remains a bottleneck for structural biologists.

feature articles

thinner than twice the mean free path of the incident electrons to limit multiple elastic scattering events. When this increases, the diffraction pattern will less reliably follow the expected structure-factor relationship, making data processing more challenging (Martynowycz *et al.*, 2021; Drevon *et al.*, 2023).

Improvements in sample preparation and continuous rotation data collection led to a 0.87 Å resolution structure of lysozyme, demonstrating the current capabilities of the technology and methodology (Martynowycz *et al.*, 2022). MicroED provides better definition of hydrogen atoms compared with X-ray data of similar resolution due to the improved contrast of hydrogens next to heavier atoms (Clabbers *et al.*, 2022). Most MicroED experiments are performed at 200–300 keV. However, ultra-low dose collections can routinely produce structures with resolutions below 3 Å (Lanza *et al.*, 2019). The TEM is partnered with one of two detector types: a direct electron detector (DED) or an indirect electron detector. DEDs provided a generational improvement on older detector technology (charge-coupled device detectors) by eliminating the requirement for light conversion and scintillation. These steps previously resulted in considerable background noise. The newest technology in DEDs offers higher precision by counting the electrons detected and offering advanced filtering to generate higher signal to noise. Detectors using electron counting offer higher resolution structures at lower doses from smaller crystals and minimize radiation damage (Martynowycz *et al.*, 2022), a feature that can be crucial when studying radiation-sensitive proteins. Electron counting mode is now the most widely used for MicroED, but many detectors also offer an integrating mode which can be used for less radiation-sensitive samples and faster data collection.

On the X-ray side, VMXm is an advanced nanofocus beamline that produces a stable $0.3 \times 2.3 \mu\text{m}$ (vertical \times horizontal) X-ray beam for diffraction data collection that is coupled with a very low sphere-of-confusion goniometer for sample rotation (Warren *et al.*, 2024). The tuneable X-ray energy (6–28 keV) allows data sets to be obtained at higher energy, prolonging the crystal lifetime in the beam using smaller samples, which together lead to gains from photo-electron escape (Storm *et al.*, 2020).

Both MicroED and data collection at VMXm are performed *in vacuo* to reduce noise as scattering from air. Additionally, the cryogenic conditions used for electron and X-ray diffraction help to reduce the effects of X-ray-induced photoelectric effects commonly referred to as 'radiation damage' (Henderson, 1995; Beale, Warren *et al.*, 2020; Warren *et al.*, 2024). Electron beams, like X-rays, cause ionizing radiation damage in biological macromolecules, posing challenges for MicroED studies. Evidence shows both global and site-specific radiation damage, with the average intensity of all reflections in proteinase K nanocrystals decreasing by 73% after $1 \text{ e}^- \text{ \AA}^{-2}$ exposure (Hattne *et al.*, 2018). This fluence corresponds to a dose of 4.5 MGy, which is much lower than the Garman limit of 30 MGy for X-ray cryo-MX, likely due to resolution differences (Baker & Rubinstein, 2010). Site-specific electron radiation damage has been observed below $1 \text{ e}^- \text{ \AA}^{-2}$ at sensitive sites, including metal centres, disulfide

bonds and acidic residues, mirroring X-ray cryo-MX findings (Hattne *et al.*, 2018). Fractionating the dose through serial approaches reduces radiation damage, akin to serial synchrotron crystallography (SSX) and serial femtosecond crystallography (SFX) (Bücker *et al.*, 2020). While MicroED and single-particle cryoEM typically report dose in $\text{e}^- \text{ \AA}^{-2}$, expressing it in grays would enable systematic comparisons across techniques. The RADDOSSE-3D GUI now facilitates the conversion from 'fluence weighted dose' to 'diffraction-decay weighted dose', enabling doses to be quoted in grays (Dickerson *et al.*, 2024).

In both MicroED and data collection at VMXm, crystals are pipetted onto one side of a glow-discharged carbon-coated grid, blotted to remove excess liquid in a humidity-controlled environment and then vitrified by rapidly plunging them into liquid ethane (Nannenga & Gonen, 2014). Reducing excess liquid around crystals and matching the sample to the beam size results in reduced background, thereby improving data quality (Warren *et al.*, 2015, 2024). Usually, data from fewer than ten deposited crystals on the grid are required to obtain a complete data set both for MicroED and at VMXm; however, settling on the grid can limit crystal lattice orientations, which consequently leads to missing cusps of the Ewald sphere. Ideally, crystals would fall randomly across the grid surface, providing access to all angles of rotation. However, this is often not the case with fixed methods and is particularly tricky with a plate-like crystal morphology. Frequently these crystals will lie on a preferred axis that has more surface-area contact with the grid (Gillman *et al.*, 2024). This can make a minimal impact on the data completeness if the crystal has high symmetry. For example, a crystal with a high-symmetry point group, such as cubic, would only require 45° of data. Comparatively, a monoclinic point group would require 180° of data around its unique axis for completeness. Therefore, the crystal symmetry can influence how many crystals are needed to obtain a complete data set. Common issues for users of the cryo-grid sample-preparation workflow are crystal loss during blotting, the observation of different thickness of the sample-embedding vitreous ice on the grid or crystal preferred orientation, creating a missing cone of data. Methods to troubleshoot and remedy these are covered in subsequent sections.

3. Serial crystallography

3.1. Overview of serial crystallography

In the purest sense, serial crystallography (SX) involves the collection of diffraction stills from randomly oriented crystals, merging multiple single exposures together to obtain a complete data set. Serial experiments can be performed at synchrotron sources (serial synchrotron crystallography, SSX) or at X-ray free-electron lasers (XFELs; serial femtosecond crystallography, SFX). A hybrid of serial and conventional methods involves the collection of multi-shot small-wedge data sets and is termed serial oscillation/rotation crystallography (SOX/SS-ROX/SF-ROX). Both SFX and SSX neces-

Table 1

Comparison of selected sample-delivery methods for serial crystallography.

Excluding drop-on-demand delivery directly into the X-ray beam with droplets of tens of picolitres to <5 nl in volume travelling at up to ~ 4 m s $^{-1}$ through the beam (see, for example, Roessler *et al.*, 2016; Mafuné *et al.*, 2016; Perrett *et al.*, 2024).

	Jets	Fixed targets	Tape drives	Microfluidics
Suitable crystal size (μm)	≤20 (GDVN) ≤50% of the internal diameter of capillary (GDVN/viscous jet)	~5–50 but aperture size-dependent (aperture-aligned) ≥1 μm (directed-raster)	~5–50	~3–25
Suitable sample volume† (μl)	≥500	50–200 (aperture-aligned) 5–10 (directed-raster)	50–500	100–500
Sample consumption‡	Tens of milligrams or more	Tens of micrograms (directed-raster) Hundreds of micrograms to several milligrams depending upon sample-loading method (aperture-aligned)	Hundreds to thousands of micrograms	Tens of micrograms
Sample-flow rate (μl min $^{-1}$)	~5–50 (GDVN) ~0.001–2 (viscous jet)	N/A	~1–10	~1
Sample velocity (through the interaction region) (m s $^{-1}$)	<200 (GDVN) <10 (viscous jet)	Approximately stationary	<10	<0.2
Data-acquisition rate	<4.5 MHz (GDVN) <200 Hz (viscous jet)	10–120 Hz	<500 Hz	<700 Hz
Technical difficulty	Moderate–high	Low–moderate	High	High
Compatibility with complementary data	X-ray emission spectroscopy	Electronic absorption spectroscopy	X-ray emission spectroscopy	Electronic absorption spectroscopy
Selected examples of biological case studies	Tpp49Aa1 (Williamson <i>et al.</i> , 2023) CTX-M-14 (Wiedorn <i>et al.</i> , 2018) Bacteriorhodopsin (Nogly <i>et al.</i> , 2015)	Fluoroacetate dehalogenase (Mehrabi, Schulz, Dsouza <i>et al.</i> , 2019) BEV2 (Roedig <i>et al.</i> , 2017) Myoglobin (Owen <i>et al.</i> , 2017)	Photosystem II (Bhownick <i>et al.</i> , 2023) Urate oxidase (Zielinski <i>et al.</i> , 2022) CTX-M-15 (Butryn <i>et al.</i> , 2021)	Cytochrome c oxidase (Ghosh <i>et al.</i> , 2023) Aspartate α -decarboxylase (Monteiro <i>et al.</i> , 2020) Lysozyme (Monteiro <i>et al.</i> , 2019)

† The required sample volume is highly dependent on the crystal density. ‡ Sample consumption is assuming a data set of ≥ 10 000 lattices.

sitate the collection of between 5000 and >100 000 crystal lattices, depending on the crystal system and method used, to obtain a complete data set (Mehrabi *et al.*, 2021). This extensive collection ensures high multiplicity, a critical factor during scaling to achieve optimal averaged intensities. This requirement becomes particularly important when a rocking curve is not captured and correlates with the higher *R* factors that are often observed in serial data sets. Most atomic models from serial data sets deposited in the PDB are based on 10 000–25 000 lattices.

Radiation damage remains a critical consideration in MX, SSX and SFX, with varying impacts across these techniques due to differences in exposure times, photon flux and experimental conditions (Garman & Weik, 2023). Thanks to the ‘diffraction-before-destruction’ principle enabled by the intense, ultrashort X-ray pulses (down to femtoseconds), SFX data are effectively free of radiation damage (Neutze *et al.*, 2000). However, specific radiation damage has been observed in cases where pulse lengths exceed 10 fs (Nass *et al.*, 2015; Lomb *et al.*, 2011), highlighting the importance of ultrafast exposures for achieving zero-dose conditions. In SSX, the limited photon flux necessitates much longer exposure times, making it impossible to fully avoid radiation damage. Radiation sensitivity is exacerbated by the typical room-temperature conditions of SSX experiments. Dose limits have

been inferred, with a half-diffraction dose of 380 kGy for lysozyme crystals at room temperature, although site-specific damage can occur at much lower doses (~ 80 kGy) and varies significantly between samples (de la Mora *et al.*, 2020; Leal *et al.*, 2013). Despite these challenges, radiation damage can be mitigated by distributing the absorbed dose over thousands of microcrystals or using low-dose exposures (Owen *et al.*, 2017). Radiation damage is less pronounced at cryogenic temperature, with a Garman limit of 30 MGy, but remains a key limiting factor in obtaining high-resolution structures (Owen *et al.*, 2006; Garman, 2010).

3.2. Sample delivery

There are multiple sample-delivery modalities for serial crystallography at room temperature. The four most commonly used are jets, fixed targets, tape drives and microfluidic devices (Fig. 2 and Table 1). These approaches are now commonplace at serial beamlines; however, the exact parameters vary depending on the synchrotron or XFEL facility being used. The array of sample-delivery approaches can achieve different experimental goals; selecting the correct one for the sample and experimental aim can be challenging. An extensive comparison of serial sample-delivery methods

feature articles

has previously been presented (Grünbein & Kovacs, 2019; Barends *et al.*, 2022).

3.2.1. Jets

Liquid jets are usually generated by a gas dynamic virtual nozzle (GDVN) through compression of a central stream of aqueous microcrystal slurry by a sheath gas flow (DePonte *et al.*, 2008). A small-diameter jet (typically 5 μm) ensures reduced background scatter and improved signal to noise, whilst the accompanying gas flow ensures that the jet deviation angle is minimal, ensuring that ice does not form and consequently plug the nozzle (Gañán-Calvo *et al.*, 2010). GDVNs are usually operated at flow rates of \sim 10–60 $\mu\text{l min}^{-1}$ (typical jet speeds of 10–50 m s^{-1} ; Schlichting, 2015). The subsequently developed double-flow focusing nozzle (DFFN) offers

flow rates as low as 5 $\mu\text{l min}^{-1}$, reducing the demand on sample. DFFN involves further focusing of the microcrystal slurry by an additional co-flowing solvent, resulting in a much finer liquid jet, eightfold lowered sample consumption, a further reduction in background scattering and improved reliability compared with the initial GDVN designs (Oberthuer *et al.*, 2017). However, manual fabrication of GDVNs is time-consuming and suffers inherent variability. 3D printing, based on two-photon polymerization, can reduce fabrication issues and increase the possible spatial resolution (Nelson *et al.*, 2016). Clogging in the GDVN is a potential failure point often mitigated by prior filtering of crystal size or limiting of the maximum crystal dimension to half the size of the nozzle internal diameter, ensuring a stable jet for prolonged periods.

Where the microcrystal slurry contains glycerol or PEG, the microfluidic electrokinetic sample holder (MESH) can be used

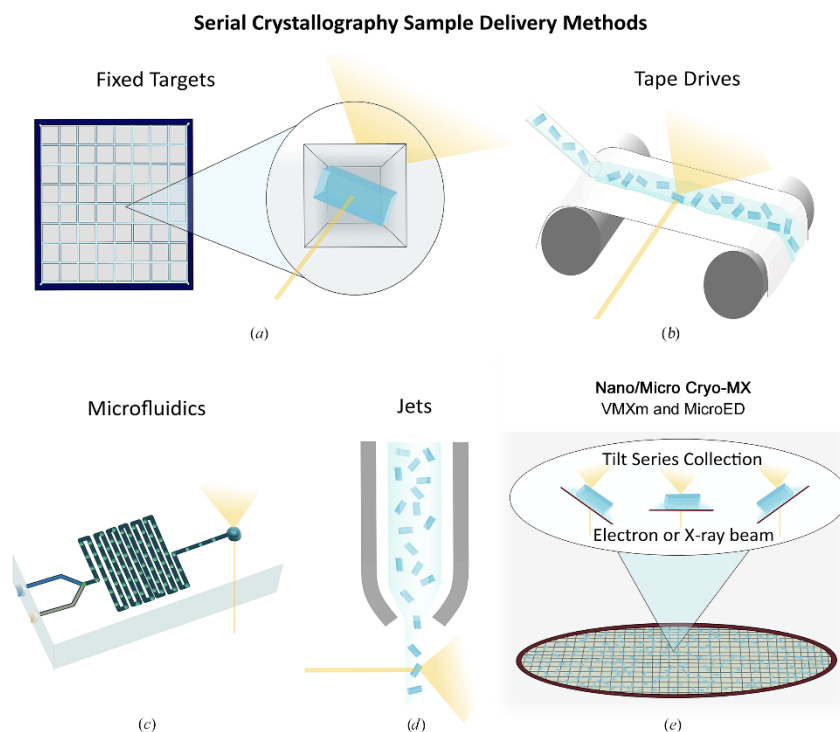


Figure 2
Overview of microcrystal sample-delivery methods in both serial and nano/micro cryo-MX techniques. (a) Fixed targets involve the immobilization of crystals in a chip with individual apertures that are rastered in a serial manner. These can be used in combination with droplet ejectors for time-resolved experiments. (b) Tape drives involve an X-ray-transparent tape where crystals are deposited as a stream or individual droplets. Time-resolved studies can be performed using a tape-drive strategy, with many facilities adapting systems to fit their setup. (c) Microfluidics can be used for *in situ* crystallization or time-resolved studies for rapid mixing experiments. (d) Jets provide a stream of microcrystal slurry to the beam and are the most sample-intensive method. (e) Nano/micro cryo-MX is an emerging field of microcrystallography currently containing MicroED and advanced beamlines such as VMXm at Diamond Light Source (Warren *et al.*, 2024). These involve the application of crystals to a carbon-coated cryoEM grid and collecting a tilt series around each crystal, making them distinct from other serial methods. Like the serial fixed targets, crystals are applied to a surface and excess solution is then blotted away to reduce background noise surrounding the sample. However, in nano/micro cryo-MX this is then vitrified to capture the crystals in amorphous ice, whereas fixed targets are collected at room temperature and crystals are captured in apertures within the solid support.

as an alternative sample injector. MESH employs an electric field to generate thin jets by electrospinning at a flow rate of $0.14\text{--}3.1\text{ }\mu\text{l min}^{-1}$, with the presence of glycerol/PEG extending the microjet length, delaying droplet formation and therefore stabilizing the focused liquid stream for longer durations (Sierra *et al.*, 2012). The requirement for glycerol or PEG in the condition was addressed through the development of the concentric-flow electrokinetic holder (coMESH) injector, where microcrystals are injected into a sheath liquid such as 2-methyl-2,4-pentanediol (MPD) for electrofocusing at a flow rate of $1\text{--}3\text{ }\mu\text{l min}^{-1}$ (Sierra *et al.*, 2016).

Structural determination of membrane proteins is often performed using a high-viscosity extruder (HVE), utilizing a $\sim 50\text{--}100\text{ }\mu\text{m}$ stream at typical flow rates of $1\text{--}300\text{ }\text{nl min}^{-1}$, thus providing a sample-efficient delivery system. Crystals are grown directly in or embedded within a high-viscosity carrier matrix, the choice of which depends on multiple factors including viscosity, flow properties, compatibility with the crystal system and background scattering. The initial injector design developed at Arizona State University involved the direct injection of membrane-protein crystals grown in lipidic cubic phase (LCP) into the X-ray beam (Weierstall *et al.*, 2014). Other carriers were subsequently introduced, including mineral-oil-based greases and hydrogels such as agarose, hydroxyethyl cellulose and high-molecular-weight polyethylene oxide (Botha *et al.*, 2015). The slow flow rates are well suited to synchrotron experiments and ensure that the exposed crystal is relatively still during the long exposure time (Weinert *et al.*, 2017; Nogly *et al.*, 2015; Martin-Garcia *et al.*, 2017). The HVE approach can also be applied to soluble proteins, however further factors should be considered: the effect of shear forces (produced from mechanical mixing of protein and high viscosity carrier matrix) on crystal stability, the compatibility of the crystallization condition with the high viscosity carrier matrix of choice and the crystal density, which directly correlates to hit rate (Fromme *et al.*, 2015).

3.2.2. Fixed targets

Fixed targets involve immobilization of crystals onto a solid support and subsequent scanning through the X-ray beam (Fig. 2). Hydrated crystals on fixed targets are protected with a Mylar film or kept within a humidity-controlled environment to prevent drying out (Roedig *et al.*, 2017; Oghbaei *et al.*, 2016; Mueller *et al.*, 2015; Doak *et al.*, 2024; Owen *et al.*, 2017). Depending on the fixed target used, two different methods of data collection are possible: aperture-aligned collection is used for crystals with defined locations and directed-raster methods are used where crystals are randomly distributed (Carrillo *et al.*, 2023). For fixed-target approaches, a volume of microcrystal slurry ($\sim 100\text{--}200\text{ }\mu\text{l}$) is pipetted onto a regular array of defined apertures (the smallest aperture currently available is $5\text{ }\mu\text{m}$; Carrillo *et al.*, 2023). Excess liquid is removed by applying a weak vacuum to the back of the chip. In the case of the Roadrunner setup, however, filter paper is used to back-blot the chip, analogous to MicroED grid preparation (Roedig *et al.*, 2017). The chip is aligned on the

beamline using imprinted fiducials, allowing efficient data collection utilizing translation stages (Sherrell *et al.*, 2015). A sealed fixed target also enables anaerobic serial data collection, when sample loading is performed in an anaerobic environment, enabling the observation of oxygen-dependent reactions within crystals (Rabe *et al.*, 2020). It is also possible to use a drop-on-demand strategy to load chips with picolitre volumes of crystal slurry at each well position without the need to pull a vacuum (Davy *et al.*, 2019).

Commonly used fixed targets for aperture-aligned data collection include the Oxford (Horrell *et al.*, 2021), HARE (Mehrabi *et al.*, 2020), MISP (Carrillo *et al.*, 2023) and Roadrunner (Roedig *et al.*, 2017) chips. The Oxford, HARE and Roadrunner chips are silicon nitride, whilst the MISP chip uses cyclic olefin copolymer (COC). Polymer approaches are now becoming the focus of fixed-target fabrication due to the cost-effectiveness and compatibility of materials such as Kapton (Bosman *et al.*, 2024). Chip design and layout vary between the three chips, with key parameters including fiducial spacing, aperture pitch and number of apertures (Owen *et al.*, 2023).

Crystal density in the slurry must be matched to the desired density of crystals per aperture: ideally one or two, or zero to one if substrates are to be added. If the crystal density is well optimized and the crystals do not show preferred orientations, two chips are generally required to obtain a complete data set. Crystals that are significantly elongated in one or two dimensions can more commonly sit in the apertures in one orientation, and in such cases more chips will be required. However, it is possible to overcome this issue by growing crystals directly on the chip through vapour diffusion (Norton-Baker *et al.*, 2021; Lieske *et al.*, 2019).

Aperture-less fixed targets involve crystal immobilization between two Mylar films held in a solid support that is directly rastered. Easy to prepare, sparing on sample (a minimum of $3\text{ }\mu\text{l}$ of crystal slurry) and comparatively quick to image ($\sim 10\text{ min per chip}$), they rarely show preferred crystal orientations and allow the collection of complete data from a single chip with an appropriate crystal density. The dominant designs are goniometer-based microgrids/micromeshes, where *MeshAndCollect* data collection is standard (Zarrine-Afsar *et al.*, 2012; Hirata *et al.*, 2014; Cohen *et al.*, 2014; Baxter *et al.*, 2016; Zander *et al.*, 2015), and Mylar sheet-on-sheet sandwiches (SOS/SOSOS chips; Doak *et al.*, 2024). Sometimes up to 100 000 images may be required as the hit rate is usually much lower than for aperture-aligned fixed targets due to the random crystal distribution. When performing a raster scan it is necessary to choose an appropriate raster spacing to avoid potential radiation-damage effects, dehydration or fouling of the film support that eventually impact data quality (Doak *et al.*, 2024).

3.2.3. Tape drives

Tape drives combine the advantages of fixed targets and on-demand delivery strategies of microcrystal slurries by using a thin X-ray-transparent tape that transfers the sample into the

feature articles

X-ray beam. The tape material is commonly Kapton (Fig. 2). The delivery onto tape can be in the form of a train of discrete droplets using synchronized acoustic droplet ejection (ADE; typically 2–3 nl per drop), piezoelectric droplet ejection (PDE; 50–200 pL per drop) (Roessler *et al.*, 2016; Fuller *et al.*, 2017; Butryn *et al.*, 2021) or a continuous stream using a capillary or an inkjet printing nozzle (Beyerlein *et al.*, 2017; Zielinski *et al.*, 2022). In the case of on-demand ADE and/or PDE strategies, it is possible to match droplet-injection rates with the X-ray source and/or detector repetition rates to reduce sample consumption and increase hit rates, making the method amenable to both synchrotron and XFEL facilities.

Due to the comparative simplicity of this arrangement, many XFEL and synchrotron beamlines have designed bespoke systems that are compatible with their instrument, each having unique advantages and disadvantages. Primary advantages of tape drives include one-dimensional synchronization of the droplet delivery into the X-ray interaction region (*i.e.* time, via tape velocity) compared with a four-dimensional synchronization search for on-the-fly droplet delivery [droplet position (x, y, z) plus time]. The tape drive also provides space to initiate reactions with different strategies that are offset from the interaction region and consequently allows a wide range of reaction time points (approximately microseconds or less to tens of seconds) to be probed, which is dictated by tape velocity and distance. When everything is optimized, tape-drive methods can be among the highest throughput and most sample-efficient for serial data collection. Tape-drive methods have also been exploited for time-resolved SFX and time-resolved X-ray emission spectroscopy from the same sample and X-ray pulse to provide correlated atomic and electronic information from metalloenzymes (Kamps *et al.*, 2024).

3.2.4. Microfluidics

Microfluidics allow data collection from static crystals in chambers (akin to fixed targets) or flowing crystals within a closed channel (Fig. 2), the latter of which has very specific needs in terms of materials and bonding, without which they are prone to leaking. Appreciable channel dimensions and flow rates for microfluidic devices drastically reduce sample consumption. Flow-focusing regimes align the sample to the X-ray interaction region, ensuring high hit rates (Monteiro *et al.*, 2019). In-flow serial data collection can be as simple as flowing microcrystals through a thin-walled glass capillary (Stellato *et al.*, 2014; Ghosh *et al.*, 2023) or can require microfabricated microfluidic chips with 3D-flow focusing geometries (Monteiro *et al.*, 2020). Samples within microfluidic devices have minimal exposure to the atmosphere, presenting the additional possibility of studying anaerobic samples or conditions provided that the device is manufactured with O₂ gas-impermeable materials. High flow rates will reduce the residency time of the sample in the X-ray beam, resulting in reduced hit rates, whilst slow flow rates are hampered by clogging of the microchannels (Monteiro *et al.*, 2020). Therefore, optimal flow rates must be carefully

balanced with the selected beam size, flux and detector rate during data collection.

Microcrystals in flow within a device are unlikely to show preferred orientation. Anti-settling devices will help to prevent potential clogging within the channel or sedimentation of crystals within the input syringe itself. The application of perpetual sedimentation via syringe rotation would allow continuous delivery of crystals in a suspended state, reducing crystal losses (Lane *et al.*, 2019). The issue of clogging can be addressed by utilizing microfluidic droplets in a segmented flow injector to synchronize the delivery of sample with the X-ray beam to minimize sample consumption (Echelmeier *et al.*, 2020). However, this approach still remains technically demanding and may yield low hit rates of ~1%, requiring lengthy data collection before a complete data set is collected (Doppler *et al.*, 2022).

4. Optimizing the sample for the experiment

As described, each method contains its own nuances of sample requirements based on the facility used, the experimental question being addressed and the sample-delivery modality chosen (Fig. 3). Therefore, the ability to tune the crystal system to obtain samples with suitable sizes, volume, density and uniformity is essential. Hence, no one singular approach will result in optimal crystals for every technique and system. The main strategies used when optimizing crystallization are phase diagrams, transitioning from vapour diffusion to batch and seeding.

4.1. Generating microcrystals from macrocrystals

Compared with time-resolved experiments, nano/micro cryo-MX techniques and ground-state serial structures do not require homogenous crystals. If larger crystals can be obtained, they can be crushed into suitably sized fragments (de La Cruz *et al.*, 2017). This often results in heterogeneous crystal sizes, increasing the likelihood of locating thin enough samples on cryo-grids. Additionally, this method was shown to be successful in preparing samples for tape drives, where Zielinski and coworkers vortexed 12 large urate oxidase (UOX) crystals to produce a slurry and then filtered to obtain suitable sub-20 µm crystals (Zielinski *et al.*, 2022). Although manual crystal disruption has been shown to be effective, if the parent crystal contains pathologies such as lattice defects, twinning, morphological irregularities or impurities, these will be transferred during seeding (de La Cruz *et al.*, 2017). In contrast, crystals grown to meet the size requirements may naturally contain variations between individual crystals. For most protein systems, a minimal crystal size is needed for high-resolution diffraction, and therefore protocols for fragmenting large crystals into microcrystals are essential. Large volumes of microcrystals can be produced by filtering crystals through stainless-steel filters using a HPLC pump (Shoeman *et al.*, 2023). This process achieves either ‘crystal sizing’, where large crystals are retained, or ‘crystal fragmentation’, where pressure breaks crystals apart (Shoeman *et al.*, 2023). Low crystal

density and low flow rates are ideal for sizing, while high flow rates generate the pressure needed for fragmentation. The uniformity of the resulting microcrystals depends heavily on the shape and softness of the crystal (Shoeman *et al.*, 2023).

For nano/micro cryo-MX, if larger crystals can be prepared on grids, focused ion beam (FIB) milling can be used to

produce suitably thin crystal lamellae (Duyvesteyn *et al.*, 2018; Zhou *et al.*, 2019; Bardin *et al.*, 2024; Noble & de Marco, 2024). This method is vastly more reproducible than manual crushing and results in an optimal crystal depth for nano/micro cryo-MX, but will inevitably be costly, labour-intensive and much lower throughput. Where large crystals cannot be manipulated

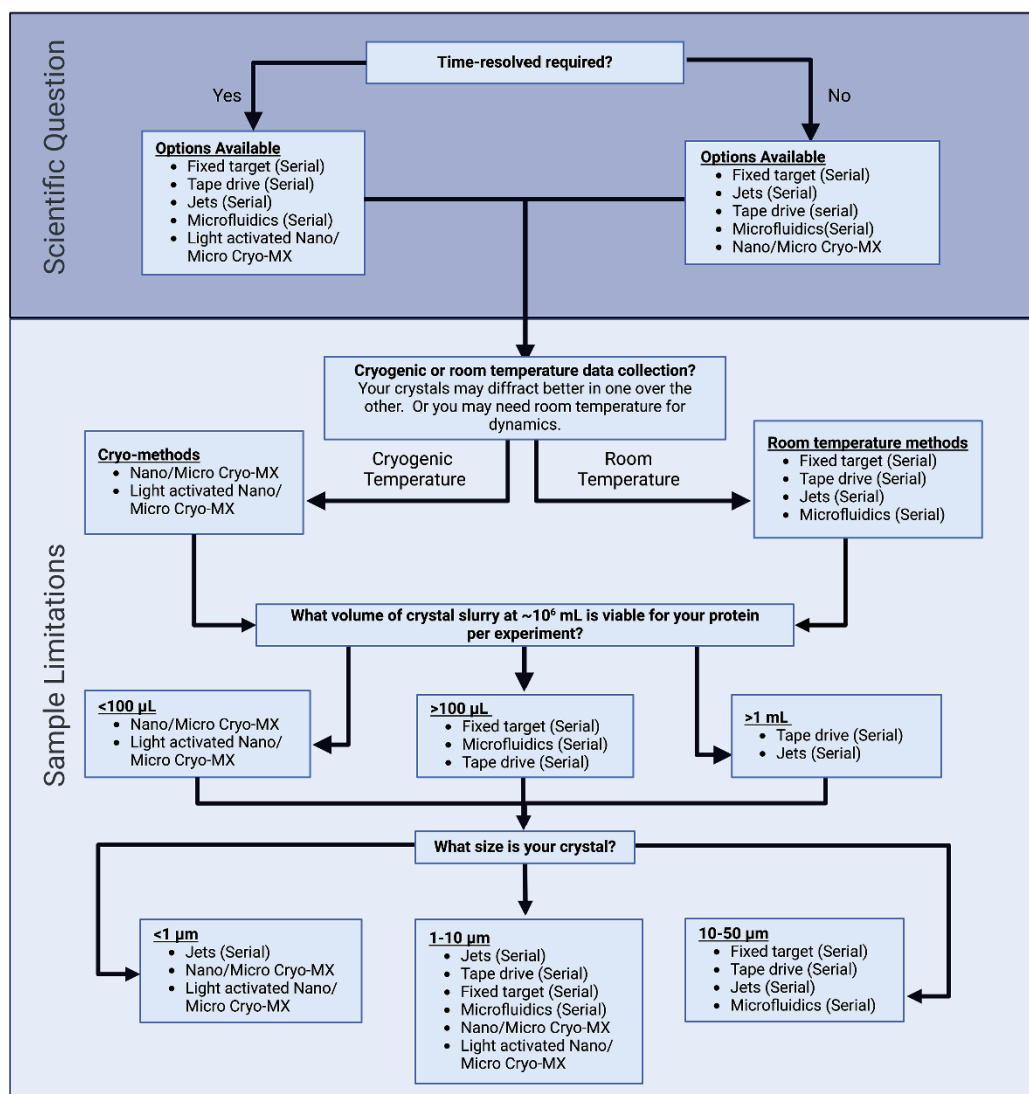


Figure 3

Decision flow chart to select the optimal microcrystal method for the scientific question (purple area) and the subsequent sample requirements (light blue area). This should be used as a guide for each method, taking into account the nuances of individual beamlines and equipment before attending beamtime.

feature articles

physically to meet method requirements, altering crystal size by manipulating the crystallization conditions is an alternative strategy.

4.2. Understanding your phase diagram

In most microcrystal projects an established crystallization condition already repeatedly yields the desired crystal form. Further fine-tuning via a combination of phase diagrams and seeding can be explored to increase the propensity of crystals with the appropriate size and distribution [Figs. 4(b) and 4(c)]. At this stage it is important to consider the final sample-delivery mode to minimize painful re-optimization later in the process. Notably, some of the modalities described are less amenable to highly viscous samples, such as nano/micro cryo-MX, jets and droplet-on-demand strategies. Therefore, options to reduce the viscosity would be preferable to minimize ice thickness, background noise or problems arising from sample delivery. Another factor is the risk of dehydration, which can occur during transit or within the crystallization condition itself, leading to crystal damage (Cheng, 2020). Tape drives and fixed targets are particularly prone to dehydration at longer time points, although some dehydration has been demonstrated to improve the crystal diffraction power (Russo Krauss *et al.*, 2012; Bowler *et al.*, 2015).

Once a condition has been decided, protein concentration and components of the mother liquor, such as pH, salt or precipitant, are changed in a stepwise fashion in either batch or vapour-diffusion crystallization experiments. Crystallization droplets are subsequently imaged, generating a visual representation and analysis of the phase diagram, allowing one to experimentally determine the undersaturated, metastable, nucleation and precipitation zones of the system. This method had been described for protein microcrystal growth before microfocus technologies had become readily available (Falkner *et al.*, 2005). By using the phase diagram, the size of the crystal and the crystal density may be tuned to meet the desired sample requirements. Additionally, the phase diagram provides a method to form a wide range of conditions to take to screening beamtime. Sometimes, crystals fail to meet the requirements for experimental data collection at this stage. To further optimize crystal density and quality, seeding methods are essential.

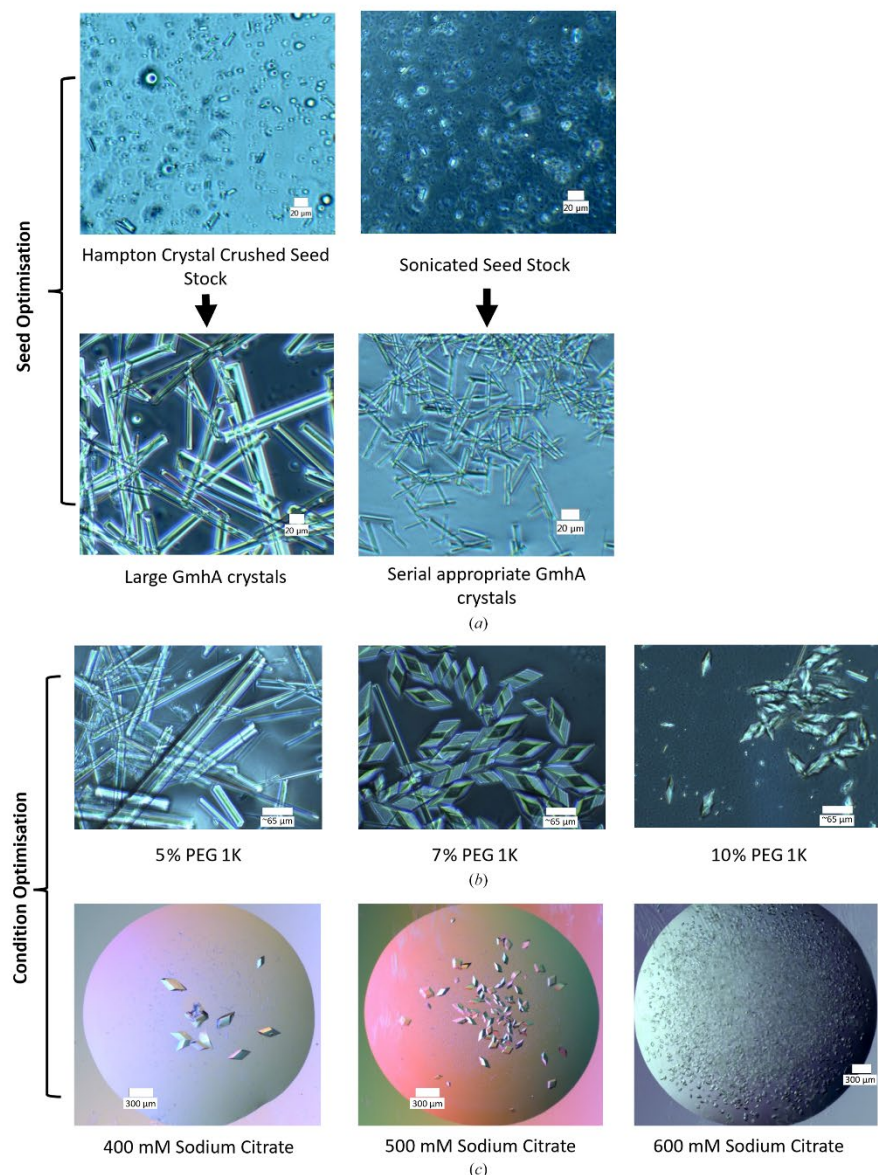
4.3. Seeding for microcrystals

Seeding, where crystalline nuclei are added to a crystallization solution to promote controlled growth in the metastable zone, was first developed in the 1980s (Thaller *et al.*, 1981). There are two forms of seeding: macroseeding and microseeding. Macroseeding uses already established single crystals as the nuclei. These are transferred to another protein solution, promoting crystal growth. Microseeding is the process of crushing previously grown crystals to form a suspension of nanocrystallites, which act as multiple nucleating points. In this section, we will be focusing on microseeding. Iterative seeding has been shown to increase crystal diffraction power and size under the original conditions

(Thaller *et al.*, 1985; Dods *et al.*, 2017) and to identify new crystallization hits, termed random microseed matrix screening (rMMS; Ireton & Stoddard, 2004). This evolved into the selection of microseeds for repetitive rounds of optimization, first demonstrated by D'Arcy *et al.* (2004), to improve crystal quality as judged by X-ray diffraction.

However, there has been debate on which methods produce the 'best' seeds (Khurshid *et al.*, 2014; He *et al.*, 2020; Obmolova *et al.*, 2014; Castro *et al.*, 2022) and it is likely that some methods will naturally work better with specific systems. In terms of microcrystal techniques, optimum seeds should be homogeneous in their size and geometry for reproducibility, scalability, simpler data processing and consistent ligand soaking (Parambil & Heng, 2017). Seeds are almost always heterogeneous, resulting in non-uniform crystal sizes [Fig. 4(a)]. Variations in crystal size and non-isomorphic unit-cell distributions can lead to the exclusion of valuable experimental data. Significant variations in crystal size can cause fluctuations in measured diffraction intensities, complicating the determination of optimal exposure times (White *et al.*, 2012). These inconsistencies hinder the reliable scaling and merging of data, often resulting in the exclusion of problematic data sets (White *et al.*, 2012). Crystal size heterogeneity may also result in the presence of poorly diffracting crystals, which can affect the hit rate and indexing success, and reduce overall diffraction quality, especially if the average crystal size does not match the beam size (Darmanin *et al.*, 2016).

Each method of seeding requires the selection of the best crystals that can be sacrificed from previous successful screening (D'Arcy *et al.*, 2004). The simplest approach is to add a physical agent (for example a silicone, steel, plastic or glass bead) and vortex the Eppendorf tube vigorously, followed by a set period of time on ice. Alternatively, mechanical force can be used, crushing the crystal(s) manually with a glass probe or capillary (D'Arcy *et al.*, 2014). Sonication applies ultrasonic sound waves to the solution, causing shock waves that induce sonofragmentation of the larger crystals into seeds (Zeiger & Suslick, 2011). In doing so, the solution will continue to warm up and changes in temperature can lead to the complete dissolution of protein crystals. However, depending on the crystal system, one method may give rise to smaller homogeneous seeds than others, resulting in more consistent crystals [Fig. 4(a)]. Heptose isomerase GmhA from *Burkholderia pseudomallei* provides a case study of a crystal system compatible with sonication (Harmer, 2010). This protein forms rod-like crystals that are thermostable to around 90°C, making it highly resistant to heating during sonication. This was selected over mechanical force methods due to the need to form much smaller seeds than could be generated by other methods. We observed here that the larger the size of the seed, the larger the resultant crystals [Fig. 4(a)]. Validating the seed stock by light microscopy, TEM or dynamic light scattering (DLS) is a way to check the success of the method employed for disrupting the crystal lattices effectively (Barnes *et al.*, 2016; Stevenson *et al.*, 2014; Kadima *et al.*, 1990).

**Figure 4**

Strategies for preparing microcrystals. (a) Heptose isomerase GmhA protein crystals from *Burkholderia pseudomallei* showing seed optimization for size control and homogeneity. The first seed stock was made using the Hampton Research Seed Bead and was combined with mother liquor and protein, resulting in non-optimal crystals for serial data collection. The same seed stock was then sonicated for 2 min at 60% amplification (20 s on and 20 s off) to produce smaller seeds. These produced much smaller crystals with the same conditions. The scale bar is 20 μ m. (b) Methylisocitrate lyase PrpB crystals from *Coxiella burnetii* optimized for serial data collection by increasing the concentration of PEG 1K (Stuart *et al.*, 2025). The crystals are shown to switch morphology upon increasing the PEG 1K concentration as well as reducing the crystal size. The scale bar is 65 μ m. (c) Pdx1, an *Arabidopsis* enzyme involved in vitamin B₆ biosynthesis, shows that an increase in salt concentration drastically reduces the crystal size and increases the number of nucleation events. The scale bar is 300 μ m.

feature articles

Once a seed stock has been made, it can be used at various concentrations to tune crystal nucleation, either by changing the seed concentration through phase diagrams (Fig. 4) or rMMS to obtain new conditions to optimize as above (D'Arcy *et al.*, 2014). It has been well documented that more concentrated seed stocks produce a higher concentration of smaller crystals by forming more nucleation points (Beale *et al.*, 2019). By systematically changing the protein and seed concentrations, one can often generate the desired crystal size. The optimized condition can then be scaled up as needed for particular synchrotron/XFEL applications or for nano/micro cryo-MX techniques, where the crystals can be directly applied to grids. Microcrystal techniques (especially for time-resolved studies) require multiple visits to the synchrotron or XFEL. It is therefore a requirement to produce a large stock of 'good' seeds, enabling reproducible methods to produce high-quality seed stock.

4.4. Scaling up from vapour diffusion to microbatch

For the nano/micro cryo-MX techniques, volumes up to 1 μ l from batch or vapour-diffusion experiments are sufficient to transfer directly onto cryo-grids. However, if a higher crystal density or larger volumes are required, the ability to scale up a crystal condition is important. Travel to a facility can include many forms of transportation, necessitating vessels to preserve samples in transit. Serial crystallography methods can require upwards of 100 μ l with a density of 10^7 – 10^8 crystals per millilitre. Scaled-up batch experiments that are easily transported to facilities in Eppendorf tubes are much more efficient for such experiments. These create a different environment to the typical crystallization plates and can lead to slight changes in the observed crystal size due to variation in evaporation conditions, altering the equilibration times between mixing and the onset of crystallization (Beale *et al.*, 2019).

The advantages of batch preparation have been outlined by Beale and coworkers, highlighting the increased control over the end result due to the removal of the transition zone between equilibration and nucleation (Beale *et al.*, 2019). Additionally, vapour-diffusion approaches are less scalable as the sample surface-area-to-volume ratio is reduced, resulting in less homogeneous crystal populations. When converting from vapour diffusion to batch, further considerations should be taken into account: precipitant and protein concentration are normally higher in vapour diffusion and equilibration occurs more slowly than in batch methods (Chayen, 1998). Precipitant concentration can be adjusted directly by increasing its concentration (typically 1.3–2 times higher in batch compared with vapour diffusion), enabling horizontal navigation of the phase diagram. Alternatively, it can be modified indirectly by varying the protein-to-precipitant ratio (commonly 1:1–1:3), resulting in a diagonal trajectory through the phase diagram. Both approaches extend the time spent in the nucleation zone, producing a greater number of small crystals and allowing fine-tuning of both crystal size and distribution (Stohrer *et al.*, 2021). Furthermore, the choice of crystallization condition will determine the rate of equilibration, as in general the more viscous PEG solutions will equilibrate more slowly than salt solutions.

In batch crystallization, rapid mixing of constituents creates a supersaturated solution, significantly enhancing nucleation. Agitating a standard batch crystallization setup, such as through microbatch mixing (MBM), has been shown to induce secondary nucleation points, facilitating the formation of microcrystals (Mahon *et al.*, 2016). However, optimizing the mixing speeds is crucial for each crystal system, as excessive agitation can compromise protein stability and reduce microcrystal yield. Rapid mixing can be combined with high-speed centrifugation to generate discrete layers of crystals, enabling the separation of crystals by size and subsequent concentration, increasing the crystal density (Tenboer *et al.*, 2014). Additionally, filtering the microcrystal slurry with appropriately sized filters allows the removal of excessively small or large crystals, ensuring a more uniform sample.

In principle, batch experiments can be scaled from nanolitre-sized droplets (in microbatch-under-oil setups) up to 200 μ l batches in Eppendorf tubes. However, further investigation is required to fully understand the effect of sample volume on the resulting crystal size, density and uniformity in batch methods. With each change in scale, iterative alterations to sample ratios may be required to maintain optimal conditions.

4.5. Optimization of grid-based sample delivery

For nano/micro cryo-MX techniques, commonly faced sample-preparation challenges are crystal preferred orientation and ice thickness. As discussed previously, some crystals will preferentially form more surface contacts with the grid along a particular face; this is commonly associated with plate or rod morphologies. Users can either re-optimize the system to select a different crystal morphology or use alternative strategies, such as on-grid crystallization. This method involves suspending the grid in the crystallization solution, vitrifying and then using FIB milling to optimize the sample thickness (Gillman *et al.*, 2023). Not only does this allow crystals to grow in random orientations, it reduces the likelihood of sample damage during grid application.

More commonly, the sample is taken from the crystallization droplet and applied using a pipette. After blotting, the crystals must remain in a layer of amorphous ice. Smaller crystals will form less surface contact with the glow-discharged sample grids, making them susceptible to removal during sample preparation by the blotting paper (Wolff *et al.*, 2020). Using a one-sided blotter can reduce this, although crystals can still migrate to the back side of the grid and be lost in the process. A more 'home-made' approach with a Büchner funnel applying a vacuum to one side of the grid has been shown to increase crystal density and match the ice quality achieved by semi-automated sample-vitrification robots (Zhao *et al.*, 2021). It is crucial the ice thickness is minimal, so that background noise is minimized. Manual blotting in a humidity-controlled environment has also been used, with lower reproducibility (Nicolas *et al.*, 2024). Samples with high viscosity (for example >20% PEG) are more susceptible to

thick ice as the filter paper absorption is reduced, resulting in longer blotting times, which can lead to sample dehydration. It is recommended to dilute the sample to reduce the viscosity and improve blotting (for example 5–10% PEG). Detailed grid optimization for MicroED has recently been compiled by experts in the field (Nicolas *et al.*, 2024).

4.6. Emerging crystallization strategies to control crystal size

Alternative approaches have been explored, including the application of microfluidics and nanotechnology. Microfluidics leverage compartmentalization for single-crystal growth and high crystal size uniformity. Droplet microfluidics have recently been harnessed, whereby the droplet acts as a controlled reaction environment, allowing the crystal size to be defined by the droplet volume. Through integration with seeding strategies, single-crystal occupancy can be achieved (Stubbs *et al.*, 2024). Similarly, complete control over the crystal system can be achieved by spatially confining the event of supersaturation to the tip of a single nanopipette (Yang *et al.*, 2023). Given the many challenges of crystallization, we can anticipate the ongoing emergence of new techniques for generating microcrystals.

5. Adding a fourth dimension: time-resolved approaches

The easy adoption of microcrystal strategies coincides with a paradigm shift in structural biology to observe the dynamic state(s) of macromolecules engaged in function (Orville, 2018). This is achieved, for instance, by time-resolved studies at room temperature using slurries of microcrystals, diffusing in substrates and then sampling at different time points across a reaction coordinate. These enzymatic states can then be combined into a stop-motion molecular movie with atomic spatial resolution at each time point. However, substrate transport into crystals can be a limiting factor, with traditional sized crystals (typically hundreds of micrometres in one dimension) resulting in long diffusion distances for ligands. This produces a gradient of reaction initiations across the crystal, yielding a distribution of states which significantly complicates the interpretation of electron-density maps, restricting the time points that can be studied (Schmidt, 2013). This results in overlooking earlier protein dynamics for many crystal systems. Enzymes react at approximately a factor of two slower in a crystal than in solution, as the crystal lattice limits normal-mode vibrations that are often critical to enzyme catalysis (Calvey *et al.*, 2020). Microcrystallography techniques enable us to effectively address issues related to substrate diffusion and state heterogeneity (Schmidt, 2013). It should be noted with respect to time-resolved experiments that a more viscous solution will also slow down the mixing, and ligand-diffusion times can extend collection time. Thus, further sample optimization may be necessary depending on the modality chosen.

While modern time-resolved methods emphasize room-temperature data collection, it is important not to overlook

classical cryotrapping approaches, which remain effective for many protein systems when the reaction occurs on a timescale that can be captured (Caramello & Royant, 2024). Cryogenic and room-temperature structure determination each offer distinct advantages and challenges, making the choice between them highly dependent upon the experimental goal. Room-temperature data collection can offer insights under closer to native biological conditions, providing a more accurate representation of conformational ensembles, allosteric communication and ligand-binding states (Fraser *et al.*, 2011; Fischer, 2021). It enables multi-conformer refinements and avoids the need for cryoprotectants, which can alter native solvent structures (Keedy *et al.*, 2015). However, room-temperature collection is more sensitive to radiation damage, limiting tolerable doses and often requiring larger crystal volumes or multiple crystals. Maintaining crystal hydration throughout the experiment is critical, as dehydration can lead to damage and non-isomorphism. Furthermore, thermal disorder increases, contributing to higher *B* factors, diffuse background scatter and reduced Bragg intensity at large scattering angles.

Cryogenic methods, by contrast, mitigate radiation damage, allowing higher doses and extended data collection from a single crystal. Cryogenic storage and transport simplify experimental logistics. However, cryogenic methods introduce artefacts, such as the need for cryoprotectants, which can perturb solvent structures or ligand interactions (Fraser *et al.*, 2011). Irreproducible cooling can introduce variability, and ice formation can damage crystals or interfere with diffraction data.

5.1. 4D and serial electron diffraction

4D MicroED has been suggested for time-resolved structures from microcrystals on femtosecond timescales by Du *et al.* (2023). The vitreous environment surrounding crystals can be locally melted with a laser to trigger protein dynamics, for example with a photocaged ligand or a rapid temperature jump. The reaction can then be trapped by removing the laser, causing rapid revitrification (Lorenz, 2024). While nanojoule energy levels are required for photoactivation, a higher energy in the microjoule range will be required for melting (Voss *et al.*, 2021).

Alternative data-collection methods for nano/micro cryosamples include serialED. Here, data are collected at specific grid positions in an automated manner, taking snapshots of crystals in random orientations and thereby eliminating the need for rotational data sets (Bücker *et al.*, 2020), a concept that evolved from serial crystallography. Currently, there are upcoming technological advancements that may lead to a convergence between MicroED and advanced microfocus beamlines (for example VMXm) with serial crystallography, such as the planned High-energy electron Xtallography Instrument (HeXI) at Diamond Light Source. Instrumentation akin to HeXI will provide both phase information and ultrafast time resolution for both large macromolecular and nanosized systems (<1 μm; Zhang *et al.*, 2021). Variations of

feature articles

energy may allow a greater range of sample sizes to maximize the quality of data collected (Shi & Huang, 2022) in a serial manner.

5.2. Time-resolved mix-and-inject serial crystallography (MISC)

A key application of serial crystallography is time-resolved experiments, for which microcrystals are ideal. The development of microfocus beamlines and the concurrent leaps in data processing have made this technique more widely accessible to non-expert users in the past few years. Experimental and data-processing workflows were first established at XFELs, which deliver short, extremely high-intensity X-ray pulses. SSX uses high-brilliance synchrotron radiation, typically with a narrow beam focus ($\sim 1\text{--}10\ \mu\text{m}$), collecting short millisecond exposures. SSX allows the observation of biochemical processes, including conformational rearrangements, enzyme catalysis and domain motion, all of which occur on microsecond-to-second timescales (Orville, 2018).

Mix-and-inject strategies rely upon the diffusion of a substrate into the channels of a crystal. Microcrystals allow short transport paths into the crystal to allow reaction synchrony for the interrogation of millisecond-regime dynamics (Schmidt, 2013). A variety of mixing setups are available. The most common setup is a GDVN or HVE injector placed upstream of a microfluidic mixer involving a co-flow or double-focusing strategy, where mixing is dominated by diffusion (Wang *et al.*, 2014; Calvey *et al.*, 2016; Doppler *et al.*, 2022; Vakili *et al.*, 2023). This scheme is also utilized by various tape drives, where crystals are applied in a narrow stream to an X-ray-compatible tape or in discrete droplets. The distance between mixing and X-ray-interaction regions together with the time travelled defines the ligand-mixing time point (Beyerlein *et al.*, 2017; Zielinski *et al.*, 2022). Drop-on-demand approaches utilize piezoelectric droplet ejectors (PDE) to dispense picolitre-sized droplets (50–200 pL) of substrate at high frequency on top of a train of crystal-containing droplets (2–5 nL) produced by acoustic droplet ejection (ADE), also on a moving tape at a defined distance (Butryn *et al.*, 2021). This approach involves droplet impact, whereby turbulent mixing is first dominated by convection and subsequently diffusion. The PDE approach can be applied to fixed targets, whereby picolitre volumes of substrate are ejected onto crystals maintained within apertures (LAMA; Mehrabi, Schulz, Agthe *et al.*, 2019). By combining this with a Hit-And-REturn (HARE) scheme, longer timescales of the order of seconds can be accessed (Schulz *et al.*, 2018). Finally, a hybrid BITS system (comBination of Inject-and-Transfer System) can use a mixture of crystal and substrate which is injected onto a polyimide fixed target that can be raster-scanned (Lee *et al.*, 2022). Droplet microfluidics provide a strong alternative to current mixing methods, with continuous convection and diffusion inside the droplet allowing mixing to approach single-millisecond timescales (Stubbs *et al.*, 2024). However, the remaining challenge for such an approach is

interfacing with the X-ray beam in a highly X-ray-transmissible device with low background noise.

5.3. Time-resolved pump–probe

Time-resolved strategies for light-activated systems generally involve an excitation laser pulse (pump) to illuminate the crystal, followed by an X-ray pulse (probe) to collect a diffraction pattern at a defined delay time. This allows access to a wide range of time regimes (subpicoseconds to seconds). If the system of interest is not naturally photoactivatable (only 0.5% are), an alternative is to use a photocaged substrate that is premixed with the crystals (Monteiro *et al.*, 2021). Upon light activation at a characteristic wavelength, the substrate will be released from the cage, subsequently diffusing into protein active sites. Photocages also allow perturbations such as pH jumps, a useful tool for investigating protonation states and observing intermediate states by halting reactions within pH-sensitive enzymes (Purohit *et al.*, 2024).

To ensure single-photon excitation and remove structural artefacts observed with multi-photon excitation, an appropriate pump laser fluence should be chosen, based upon a crystallographic power titration (Barends *et al.*, 2024). In addition, crystal thickness must be optimized, ensuring that it is smaller than the $1/e$ absorption depth of the pump laser at the designated wavelength of the excitation light, otherwise incomplete photoactivation may result (Grünbein *et al.*, 2020).

Liquid jets and high-viscosity extruders are commonly used to deliver photoactivatable samples, allowing a continuous laser illumination at the interaction region before interacting with X-rays in the probe region. Fixed targets, especially where crystals are maintained in a single aperture each, are well suited to laser experiments. These ensure that a single crystal is illuminated in the pump step. However, possible issues with unintended environmental pre-illumination or the accidental illumination of adjacent crystals with the pump laser should be considered (Gotthard *et al.*, 2024).

Finally, piezoelectric injectors in the drop-on-demand setup can be switched out for optical gates and lasers, allowing light-activated systems to be studied along with complementary data from X-ray emission spectroscopy (XES). This probes the redox and spin state of metals within the active site of metalloproteins (Fuller *et al.*, 2017).

6. Conclusions

Microcrystallography techniques hold great promise for tackling some of the most challenging questions in structural biology. By leveraging a range of crystal sizes and diverse methods for ligand delivery, researchers can tailor their approach to meet a wide variety of experimental needs. One persistent challenge, reproducibly growing crystals of adequate size and quality, is being met by strategically combining established crystallization methods. This review underscores the importance of choosing the optimal technique for each specific biological question, and it highlights the critical steps needed to optimize crystal quality for the chosen

experimental setup, significantly enhancing the likelihood of success. As time-resolved studies gain momentum, there is an even greater need for refined crystal optimization to address these emerging experimental demands effectively.

Acknowledgements

We thank Martin Malý for critical reading of the manuscript.

Funding information

This research was funded by a SWBio Doctoral Training Partnership (studentships awarded to CJT and WSS, studentship No. BB/M009122/1) by the BBSRC, the Diamond Doctoral Studentship Programme (studentship awarded to JS), a South Coast Biosciences Doctoral Training Partnership (SoCoBio DTP) by the BBSRC (studentship No. BB/T008768/1 awarded to JS), a Defence Science and Technology Laboratory studentship (DSTLX1000167246 awarded to WSS), BBSRC (BB/S008470/1 awarded to IT), Science and Technology Facilities Council, Serial Data Processing and Analysis in CCP4i2 (awarded to IT), a Wellcome Investigator Award (award No. 210734/Z/18/Z awarded to AMO) and a Royal Society Wolfson Fellowship (award No. RSWFR2 awarded to AMO).

References

Baker, L. A. & Rubinstein, J. L. (2010). *Methods Enzymol.* **481**, 371–388.

Bardin, A. A., Haymaker, A., Banihashemi, F., Lin, J. Y. S., Martynowycz, M. W. & Nannenga, B. L. (2024). *Ultramicroscopy*, **257**, 113905.

Barends, T. R. M., Gorel, A., Bhattacharyya, S., Schirò, G., Bacellar, C., Cirelli, C., Colletier, J.-P., Foucar, L., Grünbein, M. L., Hartmann, E., Hilpert, M., Holton, J. M., Johnson, P. J. M., Kloos, M., Knopp, G., Marekha, B., Nass, K., Nass Kovacs, G., Ozerov, D., Stricker, M., Weik, M., Doak, R. B., Shoeman, R. L., Milne, C. J., Huix-Rotllant, M., Cammarata, M. & Schlichting, I. (2024). *Nature*, **626**, 905–911.

Barends, T. R. M., Stauch, B., Cherezov, V. & Schlichting, I. (2022). *Nat. Rev. Methods Primers*, **2**, 59.

Barnes, C. O., Kovaleva, E. G., Fu, X., Stevenson, H. P., Brewster, A. S., DePonte, D. P., Baxter, E. L., Cohen, A. E. & Calero, G. (2016). *Arch. Biochem. Biophys.* **602**, 61–68.

Baxter, E. L., Aguila, L., Alonso-Mori, R., Barnes, C. O., Bonagura, C. A., Brehmer, W., Brunger, A. T., Calero, G., Caradoc-Davies, T. T., Chatterjee, R., Degrado, W. F., Fraser, J. M., Ibrahim, M., Kern, J., Kobilka, B. K., Kruse, A. C., Larsson, K. M., Lemke, H. T., Lyubimov, A. Y., Manglik, A., McPhillips, S. E., Norgren, E., Pang, S. S., Soltis, S. M., Song, J., Thomaston, J., Tsai, Y., Weis, W. I., Woldeyes, R. A., Yachandra, V., Yano, J., Zouni, A. & Cohen, A. E. (2016). *Acta Cryst. D72*, 2–11.

Beale, E. V., Warren, A. J., Trinção, J., Beilsten-Edmands, J., Crawshaw, A. D., Sutton, G., Stuart, D. & Evans, G. (2020). *IUCrJ*, **7**, 500–508.

Beale, E. V., Waterman, D. G., Hecksel, C., van Rooyen, J., Gilchrist, J. B., Parkhurst, J. M., de Haas, F., Buijsse, B., Evans, G. & Zhang, P. (2020). *Front. Mol. Biosci.* **7**, 179.

Beale, J. H., Bolton, R., Marshall, S. A., Beale, E. V., Carr, S. B., Ibrahim, A., Moreno-Chicano, T., Hough, M. A., Worrall, J. A. R., Tews, I. & Owen, R. L. (2019). *J. Appl. Cryst.* **52**, 1385–1396.

Beyerlein, K. R., Dierksmeyer, D., Mariani, V., Kuhn, M., Sarrou, I., Ottaviano, A., Awel, S., Knoska, J., Fuglerud, S., Jönsson, O., Stern, S., Wiedorn, M. O., Yefanov, O., Adriano, L., Bean, R., Burkhardt, A., Fischer, P., Heymann, M., Horke, D. A., Jungnickel, K. E. J., Kovaleva, E., Lorbeer, O., Metz, M., Meyer, J., Morgan, A., Pande, K., Panneerelvam, S., Seuring, C., Tolstikova, A., Lieske, J., Aplin, S., Roessle, M., White, T. A., Chapman, H. N., Meents, A. & Oberthürer, D. (2017). *IUCrJ*, **4**, 769–777.

Bhowmick, A., Hussein, R., Bogacz, I., Simon, P. S., Ibrahim, M., Chatterjee, R., Doyle, M. D., Cheah, M. H., Fransson, T., Chernev, P., Kim, I.-S., Makita, H., Dasgupta, M., Kaminsky, C. J., Zhang, M., Gätke, J., Haupt, S., Nangca, I. I., Keable, S. M., Aydin, A. O., Tono, K., Owada, S., Gee, L. B., Fuller, F. D., Batyuk, A., Alonso-Mori, R., Holton, J. M., Paley, D. W., Moriarty, N. W., Mamedov, F., Adams, P. D., Brewster, A. S., Dobbek, H., Sauter, N. K., Bergmann, U., Zouni, A., Messinger, J., Kern, J., Yano, J. & Yachandra, V. K. (2023). *Nature*, **617**, 629–636.

Bosman, R., Prester, A., Sung, S., von Soosten, L., Dibenedetto, S., Bartels, K., von Stetten, D., Mehrabi, P., Blatter, M., Lu, G., Suer, B., Wilmanns, M., Osbild, M. & Schulz, E. C. (2024). *Cell. Rep. Phys. Sci.* **5**, 101987.

Botha, S., Nass, K., Barends, T. R. M., Kabsch, W., Latz, B., Dworakowski, F., Foucar, L., Panepucci, E., Wang, M., Shoeman, R. L., Schlichting, I. & Doak, R. B. (2015). *Acta Cryst. D71*, 387–397.

Boutet, S., Lomb, L., Williams, G. J., Barends, T. R. M., Aquila, A., Doak, R. B., Weierstall, U., DePonte, D. P., Steinbrenner, J., Shoeman, R. L., Messerschmidt, M., Barty, A., White, T. A., Kassim, S., Kirian, R. A., Seibert, M. M., Montanez, P. A., Kenney, C., Herbst, R., Hart, P., Pines, J., Haller, G., Gruner, S. M., Philipp, H. T., Tate, M. W., Hromálik, M., Koerner, L. J., van Bakel, N., Morse, J., Ghonsalves, W., Arnlund, D., Bogan, M. J., Caleman, C., Fromme, R., Hampton, C. Y., Hunter, M. S., Johansson, L. C., Katona, G., Kupitz, C., Liang, M., Martin, A. V., Nass, K., Redecke, L., Stellato, F., Timneanu, N., Wang, D., Zatsepin, N. A., Schafer, D., Defever, J., Neutze, R., Fromme, P., Spence, J. C. H., Chapman, H. N. & Schlichting, I. (2012). *Science*, **337**, 362–364.

Bowler, M. W., Mueller, U., Weiss, M. S., Sanchez-Weatherby, J., Sorensen, T. L.-M., Thunissen, M. M. G. M., Ursby, T., Gobbo, A., Russi, S., Bowler, M. G., Brockhauser, S., Svensson, O. & Cipriani, F. (2015). *Cryst. Growth Des.* **15**, 1043–1054.

Bücker, R., Hogan-Lamarre, P., Mehrabi, P., Schulz, E. C., Bultema, L. A., Gevorkov, Y., Brehm, W., Yefanov, O., Oberthürer, D., Kassier, G. H. & Miller, R. J. D. (2020). *Nat. Commun.* **11**, 996.

Butrym, A., Simon, P. S., Aller, P., Hincliffe, P., Massad, R. N., Leen, G., Tooké, C. L., Bogacz, I., Kim, I.-S., Bhowmick, A., Brewster, A. S., Devenish, N. E., Brem, J., Kamps, J. J. A. G., Lang, P. A., Rabe, P., Axford, D., Beale, J. H., Davy, B., Ibrahim, A., Orlans, J., Storm, S. L. S., Zhou, T., Owada, S., Tanaka, R., Tono, K., Evans, G., Owen, R. L., Houle, F. A., Sauter, N. K., Schofield, C. J., Spencer, J., Yachandra, V. K., Yano, J., Kern, J. F. & Orville, A. M. (2021). *Nat. Commun.* **12**, 4461.

Calvey, G. D., Katz, A. M., Schaffer, C. B. & Pollack, L. (2016). *Struct. Dyn.* **3**, 054301.

Calvey, G. D., Katz, A. M., Zielinski, K. A., Dzikovski, B. & Pollack, L. (2020). *Anal. Chem.* **92**, 13864–13870.

Caramello, N. & Royant, A. (2024). *Acta Cryst. D80*, 60–79.

Carrillo, M., Mason, T., Karpik, A., Martiel, I., Kepa, M., McAuley, K., Beale, J. & Padeste, C. (2023). *IUCrJ*, **10**, 678–693.

Castro, F., Cunha, I., Ferreira, A., Teixeira, J. A. & Rocha, F. (2022). *Chem. Eng. Res. Des.* **178**, 575–582.

Chapman, H. N., Caleman, C. & Timneanu, N. (2014). *Philos. Trans. R. Soc. A*, **369**, 20130313.

Chapman, H. N., Fromme, P., Barty, A., White, T. A., Kirian, R. A., Aquila, A., Hunter, M. S., Schulz, J., DePonte, D. P., Weierstall, U., Doak, R. B., Maia, F. R. N. C., Martin, A. V., Schlichting, I., Lomb, L., Coppola, N., Shoeman, R. L., Epp, S. W., Hartmann, R., Rolles, D., Rudenko, A., Foucar, L., Kimmel, N., Weidenspointner, G., Holl, P., Liang, M., Barthelmess, M., Caleman, C., Boutet, S., Bogan, G.

feature articles

M. J., Krzywinski, J., Bostedt, C., Bajt, S., Gumprecht, L., Rudek, B., Erk, B., Schmidt, C., Hömke, A., Reich, C., Pietschner, D., Strüder, L., Hauser, G., Gorke, H., Ullrich, J., Herrmann, S., Schaller, G., Schopper, F., Soltau, H., Kühnel, K.-U., Messerschmidt, M., Bozek, J. D., Hau-Riege, S. P., Frank, M., Hampton, C. Y., Sierra, R. G., Starodub, D., Williams, G. J., Hajdu, J., Timneanu, N., Seibert, M. M., Andreasson, J., Rocker, A., Jönsson, O., Svenda, M., Stern, S., Nass, K., Andritschke, R., Schröter, C.-D., Krasniqi, F., Bott, M., Schmidt, K. E., Wang, X., Grotjohann, I., Holton, J. M., Barends, T. R. M., Neutze, R., Marchesini, S., Fromme, R., Schorb, S., Rupp, D., Adolph, M., Gorkhovet, T., Andersson, I., Hirsemann, H., Potdevin, G., Graafsma, H., Nilsson, B. & Spence, J. C. H. (2011). *Nature*, **470**, 73–77.

Chavas, L. M. G., Coulibaly, F. & Garriga, D. (2024). *IUCrJ*, **11**, 476–485.

Chayen, N. E. (1998). *Acta Cryst. D54*, 8–15.

Cheng, R. K. (2020). *Crystals*, **10**, 215.

Clabbers, M. T. B., Martynowycz, M. W., Hattne, J. & Gonen, T. (2022). *J. Struct. Biol. X*, **6**, 100078.

Clabbers, M. T. B. & Xu, H. (2021). *Acta Cryst. D77*, 313–324.

Cohen, A. E., Soltis, S. M., González, A., Aguilà, L., Alonso-Mori, R., Barnes, C. O., Baxter, E. L., Bremer, W., Brewster, A. S., Brunger, A. T., Calero, G., Chang, J. F., Chollet, M., Ehrenberger, P., Eriksson, T. L., Feng, Y., Hattne, J., Hedman, B., Hollenbeck, M., Holton, J. M., Keable, S., Kobilka, B. K., Kovaleva, E. G., Kruse, A. C., Lemke, H. T., Lin, G., Lyubimov, A. Y., Manglik, A., Mathews, I. I., McPhillips, S. E., Nelson, S., Peters, J. W., Sauter, N. K., Smith, C. A., Song, J., Stevenson, H. P., Tsai, Y., Uervorijnangkoorn, M., Vinetsky, V., Wakatsuki, S., Weis, W. I., Zadovnny, O. A., Zeldin, O. B., Zhu, D. & Hodgson, K. O. (2014). *Proc. Natl Acad. Sci. USA*, **111**, 17122–17127.

Crawshaw, A. D., Beale, E. V., Warren, A. J., Stallwood, A., Duller, G., Trincao, J. & Evans, G. (2021). *J. Vis. Exp.*, e62306.

Cruz, M. J. de la, Hattne, J., Shi, D., Seidler, P., Rodriguez, J., Reyes, F. E., Sawaya, M. R., Cascio, D., Weiss, S. C., Kim, S. K., Hinck, C. S., Hinck, A. P., Calero, G., Eisenberg, D. & Gonen, T. (2017). *Nat. Methods*, **14**, 399–402.

Cusack, S., Belrhali, H., Bram, A., Burghammer, M., Perrakis, A. & Riekel, C. (1998). *Nat. Struct. Mol. Biol.* **5**, 634–637.

D'Arcy, A., Bergfors, T., Cowan-Jacob, S. W. & Marsh, M. (2014). *Acta Cryst. F70*, 1117–1126.

D'Arcy, A., Mac Sweeney, A. & Habera, A. (2004). *J. Synchrotron Rad.* **11**, 24–26.

Darmanin, C., Strachan, J., Adda, C. G., Ve, T., Kobe, B. & Abbey, B. (2016). *Sci. Rep.* **6**, 25345.

Davy, B., Axford, D., Beale, J. H., Butrym, A., Docker, P., Ebrahim, A., Leen, G., Orville, A. M., Owen, R. L. & Aller, P. (2019). *J. Synchrotron Rad.* **26**, 1820–1825.

DePonte, D. P., Weierstall, U., Schmidt, K., Warner, J., Starodub, D., Spence, J. C. H. & Doak, R. B. (2008). *J. Phys. D Appl. Phys.* **41**, 195505.

Dickerson, J. L., McCubbin, P. T. N., Brooks-Bartlett, J. C. & Garman, E. F. (2024). *Protein Sci.* **33**, e5005.

Doak, R. B., Shoeman, R. L., Gorel, A., Niziński, S., Barends, T. R. M. & Schlichting, I. (2024). *J. Appl. Cryst.* **57**, 1725–1732.

Dods, R., Båth, P., Arnlund, D., Beyerlein, K. R., Nelson, G., Liang, M., Harimoorthy, R., Berntsen, P., Malmerberg, E., Johansson, L., Andersson, R., Bosman, R., Carabajo, S., Claesson, E., Conrad, C. E., Dahl, P., Hammarin, G., Hunter, M. S., Li, C., Lisova, S., Milathianaki, D., Robinson, J., Safari, C., Sharma, A., Williams, G., Wickstrand, C., Yefanov, O., Davidsson, J., DePonte, D. P., Barty, A., Brändén, G. & Neutze, R. (2017). *Structure*, **25**, 1461–1468.

Doppler, D., Rabbani, M. T., Letrun, R., Cruz Villarreal, J., Kim, D. H., Gandhi, S., Egatz-Gomez, A., Sonker, M., Chen, J., Koua, F. H. M., Yang, J., Youssef, M., Mazalova, V., Bajt, S., Shelby, M. L., Coleman, M. A., Wiedorn, M. O., Knoska, J., Schön, S., Sato, T., Hunter, M. S., Hosseiniyazadeh, A., Kuptitz, C., Nazari, R., Alvarez, R. C., Karpos, K., Zaare, S., Dobson, Z., Discianno, E., Zhang, S., Zook, J. D., Bielecki, J., de Wijn, R., Round, A. R., Vagovic, P., Kloos, M., Vakili, M., Ketawala, G. K., Stander, N. E., Olson, T. L., Morin, K., Mondal, J., Nguyen, J., Meza-Aguilar, J. D., Kodis, G., Vaiana, S., Martin-Garcia, J. M., Mariani, V., Schwander, P., Schmidt, M., Messerschmidt, M., Ourmazd, A., Zatsepin, N., Weierstall, U., Bruce, B. D., Mancuso, A. P., Grant, T., Barty, A., Chapman, H. N., Frank, M., Fromme, R., Spence, J. C. H., Botha, S., Fromme, P., Kirian, R. A. & Ros, A. (2022). *J. Appl. Cryst.* **55**, 1–13.

Drevon, T. R., Waterman, D. G. & Krissinel, E. (2023). *Acta Cryst. A79*, 180–191.

Du, D. X., Simjanoska, M. & Fitzpatrick, A. W. P. (2023). *J. Struct. Biol.* **215**, 107941.

Duyvesteyn, H. M. E., Kotecha, A., Ginn, H. M., Hecksel, C. W., Beale, E. V., de Haas, F., Evans, G., Zhang, F., Chiu, W. & Stuart, D. I. (2018). *Proc. Natl Acad. Sci. USA*, **115**, 9569–9573.

Echelmeier, A., Cruz Villarreal, J., Messerschmidt, M., Kim, D., Coe, J. D., Thifault, D., Botha, S., Egatz-Gomez, A., Gandhi, S., Brehm, G., Conrad, C. E., Hansen, D. T., Madsen, C., Bajt, S., Meza-Aguilar, J. D., Oberthür, D., Wiedorn, M. O., Fleckenstein, H., Mendez, D., Knoška, J., Martin-Garcia, J. M., Hu, H., Lisova, S., Allaghholi, A., Gevorkov, Y., Ayyer, K., Aplin, S., Ginn, H. M., Graafsmo, H., Morgan, A. J., Greiffenberg, D., Klujev, A., Laurus, T., Poehls, J., Trunk, U., Mezza, D., Schmidt, B., Kuhn, M., Fromme, R., Sztuk-Dambietz, J., Raab, N., Hauf, S., Silenzi, A., Michelat, T., Xu, C., Danilevski, C., Parenti, A., Mekinda, L., Weinhausen, B., Mills, G., Vagovic, P., Kim, Y., Kirkwood, H., Bean, R., Bielecki, J., Stern, S., Giewekemeyer, K., Round, A. R., Schulz, J., Dörner, K., Grant, T. D., Mariani, V., Barty, A., Mancuso, A. P., Weierstall, U., Spence, J. C. H., Chapman, H. N., Zatsepin, N., Fromme, P., Kirian, R. A. & Ros, A. (2020). *Nat. Commun.* **11**, 4511.

Falkner, J. C., Al-Somali, A. M., Jamison, J. A., Zhang, J., Adrianse, S. L., Simpson, R. L., Calabretta, M. K., Radding, W., Phillips, G. N. & Colvin, V. L. (2005). *Chem. Mater.* **17**, 2679–2686.

Fischer, M. (2021). *Q. Rev. Biophys.* **54**, e1.

Flot, D., Mairs, T., Giraud, T., Guijarro, M., Lesourd, M., Rey, V., van Brussel, D., Morawe, C., Borel, C., Hignette, O., Chavanne, J., Nurizzo, D., McSweeney, S. & Mitchell, E. (2010). *J. Synchrotron Rad.* **17**, 107–118.

Fraser, J. S., van den Bedem, H., Samelson, A. J., Lang, P. T., Holton, J. M., Echols, N. & Alber, T. (2011). *Proc. Natl Acad. Sci. USA*, **108**, 16247–16252.

Fromme, R., Ishchenko, A., Metz, M., Chowdhury, S. R., Basu, S., Boutet, S., Fromme, P., White, T. A., Barty, A., Spence, J. C. H., Weierstall, U., Liu, W. & Cherezov, V. (2015). *IUCrJ*, **2**, 545–551.

Fuller, F. D., Gul, S., Chatterjee, R., Burgie, E. S., Young, I. D., Lebrette, H., Srinivas, V., Brewster, A. S., Michels-Clark, T., Clinger, J. A., Andi, B., Ibrahim, M., Pastor, E., de Lichtenberg, C., Hussein, R., Pollock, C. J., Zhang, M., Stan, C. A., Kroll, T., Fransson, T., Weninger, C., Kubin, M., Aller, P., Lassalle, L., Bräuer, P., Miller, M. D., Amin, M., Koroidov, S., Roessler, C. G., Allaire, M., Sierra, R. G., Docker, P. T., Głownia, J. M., Nelson, S., Koglin, J. E., Zhu, D., Chollet, M., Song, S., Lenke, H., Liang, M., Sokaras, D., Alonso-Mori, R., Zouni, A., Messinger, J., Bergmann, U., Boal, A. K., Bollinger, J. M., Krebs, C., Högbom, M., Phillips, G. N., Vierstra, R. D., Sauter, N. K., Orville, A. M., Kern, J., Yachandra, V. K. & Yano, J. (2017). *Nat. Methods*, **14**, 443–449.

Gallenito, M. J. & Gonen, T. (2022). *Biochem. Soc. Trans.* **50**, 231–239.

Gañán-Calvo, A. M., DePonte, D. P., Herrada, M. A., Spence, J. C. H., Weierstall, U. & Doak, R. B. (2010). *Small*, **6**, 822–824.

Garman, E. F. (2010). *Acta Cryst. D66*, 339–351.

Garman, E. F. & Weik, M. (2023). *Curr. Opin. Struct. Biol.* **82**, 102662.

Gati, C., Bourenkov, G., Klinge, M., Rehders, D., Stellato, F., Oberthür, D., Yefanov, O., Sommer, B. P., Mogk, S., Duszenko, M., Betzel, C., Schneider, T. R., Chapman, H. N. & Redecke, L. (2014). *IUCrJ*, **1**, 87–94.

Ghosh, S., Zorić, D., Dahl, P., Bjelčić, M., Johannesson, J., Sandelin, E., Borjesson, P., Björling, A., Banacore, A., Edlund, P., Aurelius,

O., Milas, M., Nan, J., Shilova, A., Gonzalez, A., Mueller, U., Brändén, G. & Neutze, R. (2023). *J. Appl. Cryst.* **56**, 449–460.

Gillman, C., Bu, G., Danelius, E., Hattne, J., Nannenga, B. L. & Gonen, T. (2024). *J. Struct. Biol.* **X**, 9, 100102.

Gillman, C., Nicolas, W. J., Martynowycz, M. W. & Gonen, T. (2023). *IUCrJ*, **10**, 430–436.

Gotthard, G., Flores-Ibarra, A., Carrillo, M., Kepa, M. W., Mason, T. J., Stegmann, D. P., Olasz, B., Pachota, M., Dworkowski, F., Ozorov, D., Pedrini, B. F., Padeste, C., Beale, J. H. & Nogly, P. (2024). *IUCrJ*, **11**, 749–761.

Grünbein, M. L. & Nass Kovacs, G. (2019). *Acta Cryst. D* **75**, 178–191.

Grünbein, M. L., Stricker, M., Nass Kovacs, G., Kloos, M., Doak, R. B., Shoeman, R. L., Reinstein, J., Lecler, S., Haacke, S. & Schlichting, I. (2020). *Nat. Methods*, **17**, 681–684.

Harmer, N. J. (2010). *J. Mol. Biol.* **400**, 379–392.

Hattne, J., Shi, D., Glynn, C., Zee, C.-T., Gallagher-Jones, M., Martynowycz, M. W., Rodriguez, J. A. & Gonen, T. (2018). *Structure*, **26**, 759–766.

Haymaker, A., Bardin, A. A., Gonen, T., Martynowycz, M. W. & Nannenga, B. L. (2023). *Structure*, **31**, 1499–1503.

He, Y., Gao, Z., Zhang, T., Sun, J., Ma, Y., Tian, N. & Gong, J. (2020). *Org. Process Res. Dev.* **24**, 1839–1849.

Henderson, R. (1992). *Ultramicroscopy*, **46**, 1–18.

Henderson, R. (1995). *Q. Rev. Biophys.* **28**, 171–193.

Hirata, K., Shinzawa-Itoh, K., Yano, N., Takemura, S., Kato, K., Hatanaka, M., Muramoto, K., Kawahara, T., Tsukihara, T., Yamashita, E., Tono, K., Ueno, G., Hikima, T., Murakami, H., Inubushi, Y., Yabashi, M., Ishikawa, T., Yamamoto, M., Ogura, T., Sugimoto, H., Shen, J.-R., Yoshikawa, S. & Ago, H. (2014). *Nat. Methods*, **11**, 734–736.

Horrell, S., Axford, D., Devenish, N. E., Ebrahim, A., Hough, M. A., Sherrell, D. A., Storm, S. L. S., Tews, I., Worrall, J. A. R. & Owen, R. L. (2021). *J. Vis. Exp.*, e62200.

Ireton, G. C. & Stoddard, B. L. (2004). *Acta Cryst. D* **60**, 601–605.

Kadima, W., McPherson, A., Dunn, M. F. & Jurnak, F. A. (1990). *Biophys. J.* **57**, 125–132.

Kamps, J. J. A. G., Bosman, R., Orville, A. M. & Aller, P. (2024). *Methods Enzymol.* **709**, 57–103.

Keedy, D. A., Kenner, L. R., Warkentin, M., Woldeyes, R. A., Hopkins, J. B., Thompson, M. C., Brewster, A. S., Van Benschoten, A. H., Baxter, E. L., Uervirojanaengkorn, M., McPhillips, S. E., Song, J., Alonso-Mori, R., Holton, J. M., Weis, W. I., Brunger, A. T., Soltis, S. M., Lemke, H., Gonzalez, A., Sauter, N. K., Cohen, A. E., van den Bedem, H., Thorne, R. E. & Fraser, J. S. (2015). *eLife*, **4**, e07574.

Kendrew, J. C., Bodo, G., Dintzis, H. M., Parrish, R. G., Wyckoff, H. & Phillips, D. C. (1958). *Nature*, **181**, 662–666.

Khurshid, S., Saridakis, E., Govada, L. & Chayen, N. E. (2014). *Nat. Protoc.* **9**, 1621–1633.

Lane, S. I. R., Butement, J., Harrington, J., Underwood, T., Shrimpton, J. & West, J. (2019). *Lab Chip*, **19**, 3771–3775.

Lanza, A., Margheritis, E., Mugnaioli, E., Cappello, V., Garau, G. & Gemmi, M. (2019). *IUCrJ*, **6**, 178–188.

Leal, R. M. F., Bourenkov, G., Russi, S. & Popov, A. N. (2013). *J. Synchrotron Rad.* **20**, 14–22.

Lee, K., Kim, J., Baek, S., Park, J., Park, S., Lee, J.-L., Chung, W. K., Cho, Y. & Nam, K. H. (2022). *J. Appl. Cryst.* **55**, 813–822.

Lieske, J., Cerv, M., Kreida, S., Komadina, D., Fischer, J., Barthelmeß, M., Fischer, P., Pakendorf, T., Yefanov, O., Mariam, V., Seine, T., Ross, B. H., Crosas, E., Lorbeer, O., Burkhardt, A., Lane, T. J., Guenther, S., Bergtholdt, J., Schoen, S., Törnroth-Horsefield, S., Chapman, H. N. & Meents, A. (2019). *IUCrJ*, **6**, 714–728.

Lomb, L., Barends, T. R. M., Kassmeyer, S., Aquila, A., Epp, S. W., Erk, B., Foucar, L., Hartmann, R., Rudek, B., Rolles, D., Rudenko, A., Shoeman, R. L., Andreasson, J., Bajt, S., Barthelmeß, M., Barty, A., Bogan, M. J., Bostedt, C., Bozek, J. D., Caleman, C., Coffee, R., Coppola, N., DePonte, D. P., Doak, R. B., Ekeberg, T., Fleckenstein, H., Fromme, P., Gebhardt, M., Graafsma, H., Gumprecht, L., Hampton, C. Y., Hartmann, A., Hauser, G., Hirsemann, H., Holl, P., Holton, J. M., Hunter, M. S., Kabsch, W., Kimmel, N., Kirian, R. A., Liang, M., Maia, F. R. N. C., Meinhardt, A., Marchesini, S., Martin, A. V., Nass, K., Reich, C., Schulz, J., Seibert, M. M., Sierra, R., Soltau, H., Spence, J. C. H., Steinbrener, J., Stellato, F., Stern, S., Timneanu, N., Wang, X., Weidenspointner, G., Weierstall, U., White, T. A., Wunderer, C., Chapman, H. N., Ullrich, J., Strüder, L. & Schlichting, I. (2011). *Phys. Rev. B*, **84**, 214111.

Lorenz, U. J. (2024). *Curr. Opin. Struct. Biol.* **87**, 102840.

Mafuné, F., Miyajima, K., Tono, K., Takeda, Y., Kohno, J., Miyazaki, N., Kobayashi, J., Joti, Y., Nango, E., Iwata, S. & Yabashi, M. (2016). *Acta Cryst. D* **72**, 520–523.

Mahon, B. P., Kurian, J. J., Lomelino, C. L., Smith, I. R., Socorro, L., Bennett, A., Hendon, A. M., Chipman, P., Savin, D. A., Agbandje-McKenna, M. & McKenna, R. (2016). *Cryst. Growth Des.* **16**, 6214–6221.

Martin-Garcia, J. M., Conrad, C. E., Nelson, G., Stander, N., Zatsepin, N. A., Zook, J., Zhu, L., Geiger, J., Chun, E., Kissick, D., Hilgart, M. C., Ogata, C., Ishchenko, A., Nagaratnam, N., Roy-Chowdhury, S., Coe, J., Subramanian, G., Schaffer, A., James, D., Ketwala, G., Venugopal, N., Xu, S., Corcoran, S., Ferguson, D., Weierstall, U., Spence, J. C. H., Cherezov, V., Fromme, P., Fischetti, R. F. & Liu, W. (2017). *IUCrJ*, **4**, 439–454.

Martynowycz, M. W., Clabbers, M. T. B., Hattne, J. & Gonen, T. (2022). *Nat. Methods*, **19**, 724–729.

Martynowycz, M. W., Clabbers, M. T. B., Unge, J., Hattne, J. & Gonen, T. (2021). *Proc. Natl. Acad. Sci. USA*, **118**, e2108884118.

Martynowycz, M. W., Hattne, J. & Gonen, T. (2020). *Structure*, **28**, 458–464.

Martynowycz, M. W., Shiriaeva, A., Clabbers, M. T. B., Nicolas, W. J., Weaver, S. J., Hattne, J. & Gonen, T. (2023). *Nat. Commun.* **14**, 1086.

Mehrabi, P., Bücker, R., Bourenkov, G., Ginn, H. M., von Stetten, D., Müller-Werkmeister, H. M., Kuo, A., Morizumi, T., Eger, B. T., Ou, W.-L., Oghbaey, S., Sarracini, A., Besaw, J. E., Pare-Labrosse, O., Meier, S., Schikora, H., Tellkamp, F., Marx, A., Sherrell, D. A., Axford, D., Owen, R. L., Ernst, O. P., Pai, E. F., Schulz, E. C. & Miller, R. J. D. (2021). *Sci. Adv.* **7**, eabf1380.

Mehrabi, P., Müller-Werkmeister, H. M., Leimkoh, J.-P., Schikora, H., Ninkovic, J., Krivokuća, S., Andriček, L., Epp, S. W., Sherrell, D., Owen, R. L., Pearson, A. R., Tellkamp, F., Schulz, E. C. & Miller, R. J. D. (2020). *J. Synchrotron Rad.* **27**, 360–370.

Mehrabi, P., Schulz, E. C., Agthe, M., Horrell, S., Bourenkov, G., von Stetten, D., Leimkoh, J.-P., Schikora, H., Schneider, T. R., Pearson, A. R., Tellkamp, F. & Miller, R. J. D. (2019). *Nat. Methods*, **16**, 979–982.

Mehrabi, P., Schulz, E. C., Dsouza, R., Müller-Werkmeister, H. M., Tellkamp, F., Miller, R. J. D. & Pai, E. F. (2019). *Science*, **365**, 1167–1170.

Monteiro, D. C. F., Amoah, E., Rogers, C. & Pearson, A. R. (2021). *Acta Cryst. D* **77**, 1218–1232.

Monteiro, D. C. F., Vakili, M., Harich, J., Sztucki, M., Meier, S. M., Horrell, S., Josts, I. & Trebbin, M. (2019). *J. Synchrotron Rad.* **26**, 406–412.

Monteiro, D. C. F., von Stetten, D., Stohrer, C., Sans, M., Pearson, A. R., Santoni, G., van der Linden, P. & Trebbin, M. (2020). *IUCrJ*, **7**, 207–219.

Mora, E. de la Coquelle, N., Bury, C. S., Rosenthal, M., Holton, J. M., Carmichael, I., Garman, E. F., Burghammer, M., Colletier, J.-P. & Weik, M. (2020). *Proc. Natl. Acad. Sci. USA*, **117**, 4142–4151.

Mueller, C., Marx, A., Epp, S. W., Zhong, Y., Kuo, A., Balo, A. R., Soman, J., Schotte, F., Lemke, H. T., Owen, R. L., Pai, E. F., Pearson, A. R., Olson, J. S., Anfinrud, P. A., Ernst, O. P. & Miller, R. J. D. (2015). *Struct. Dyn.* **2**, 054302.

Nannenga, B. L. & Gonen, T. (2014). *Curr. Opin. Struct. Biol.* **27**, 24–31.

Nannenga, B. L. & Gonen, T. (2019). *Nat. Methods*, **16**, 369–379.

feature articles

Nass, K., Foucar, L., Barends, T. R. M., Hartmann, E., Botha, S., Shoeman, R. L., Doak, R. B., Alonso-Mori, R., Aquila, A., Bajt, S., Barty, A., Bean, R., Beyerlein, K. R., Bublitz, M., Drachmann, N., Gregersen, J., Jönsson, H. O., Kabsch, W., Kassemeyer, S., Koglin, J. E., Krumrey, M., Mattle, D., Messerschmidt, M., Nissen, P., Reinhard, L., Sitsel, O., Sokaras, D., Williams, G. J., Hau-Riege, S., Timneanu, N., Caleman, C., Chapman, H. N., Boutet, S. & Schlichting, I. (2015). *J. Synchrotron Rad.* **22**, 225–238.

Nelson, G., Kirian, R. A., Weierstall, U., Zatsepin, N. A., Faragó, T., Baumbach, T., Wilde, F., Niesler, F. B. P., Zimmer, B., Ishigami, I., Hikita, M., Bajt, S., Yeh, S.-R., Rousseau, D. L., Chapman, H. N., Spence, J. C. H. & Heymann, M. (2016). *Opt. Express*, **24**, 11515–11530.

Neutze, R., Wouts, R., van der Spoel, D., Weckert, E. & Hajdu, J. (2000). *Nature*, **406**, 752–757.

Nicolas, W. J., Gillman, C., Weaver, S. J., Clabbers, M. T. B., Shiriaeva, A., Her, A. S., Martynowycz, M. W. & Gonon, T. (2024). *Nat. Protoc.*, <https://doi.org/10.1038/s41596-024-01088-7>.

Noble, A. J. & de Marco, A. (2024). *Curr. Opin. Struct. Biol.* **87**, 102864.

Nogly, P., James, D., Wang, D., White, T. A., Zatsepin, N., Shilova, A., Nelson, G., Liu, H., Johansson, L., Heymann, M., Jaeger, K., Metz, M., Wickstrand, C., Wu, W., Båth, P., Berntsen, P., Oberthuer, D., Panneels, V., Cherezov, V., Chapman, H., Schertler, G., Neutze, R., Spence, J., Moraes, I., Burghammer, M., Standfuss, J. & Weierstall, U. (2015). *IUCrJ*, **2**, 168–176.

Norton-Baker, B., Mehrabi, P., Boger, J., Schönher, R., von Stetten, D., Schikora, H., Kwok, A. O., Martin, R. W., Miller, R. J. D., Redecke, L. & Schulz, E. C. (2021). *Acta Cryst. D77*, 820–834.

Oberthuer, D., Knoška, J., Wiedorn, M. O., Beyerlein, K. R., Bushnell, D. A., Kovaleva, E. G., Heymann, M., Gumprecht, L., Kirian, R. A., Barty, A., Mariani, V., Tolstikova, A., Adriano, L., Awel, S., Barthelmes, M., Dörner, K., Xavier, P. L., Yefanov, O., James, D. R., Nelson, G., Wang, D., Calvey, G., Chen, Y., Schmidt, A., Szczepak, M., Frielingsdorf, S., Lenz, O., Snell, E., Robinson, P. J., Šárler, B., Belšák, G., Maček, M., Wilde, F., Aquila, A., Boutet, S., Liang, M., Hunter, M. S., Scheerer, P., Lipscomb, J. D., Weierstall, U., Kornberg, R. D., Spence, J. C. H., Pollack, L., Chapman, H. N. & Bajt, S. (2017). *Sci. Rep.* **7**, 44628.

Obmolova, G., Malia, T. J., Tepliyakov, A., Sweet, R. W. & Gilliland, G. L. (2014). *Acta Cryst. F70*, 1107–1115.

Oghbaey, S., Sarracini, A., Ginn, H., Pare-Labrosse, O., Kuo, A., Marx, A., Epp, S. W., Sherrell, D. A., Eger, B. T., Zhong, Y., Loch, R., Mariani, V., Alonso-Mori, R., Nelson, S., Lemke, H. T., Owen, R. L., Pearson, A. R., Stuart, D. I., Ernst, O. P., Mueller-Werkmeister, H. M. & Miller, R. J. D. (2016). *Acta Cryst. D72*, 944–955.

Orville, A. M. (2018). *BMC Biol.* **16**, 55.

Owen, R. L., Axford, D., Sherrell, D. A., Kuo, A., Ernst, O. P., Schulz, E. C., Miller, R. J. D. & Mueller-Werkmeister, H. M. (2017). *Acta Cryst. D73*, 373–378.

Owen, R. L., de Sanctis, D., Pearson, A. R. & Beale, J. H. (2023). *Acta Cryst. D79*, 668–672.

Owen, R. L., Rudiño-Piñera, E. & Garman, E. F. (2006). *Proc. Natl. Acad. Sci. USA*, **103**, 4912–4917.

Parambil, J. V. & Heng, J. Y. Y. (2017). *Engineering Crystallography: From Molecule to Crystal to Functional Form*, edited by K. J. Roberts, R. Docherty & R. Tamura, pp. 235–245. Dordrecht: Springer.

Perrett, S., Fadini, A., Hutchison, C. D. M., Bhattacharya, S., Morrison, C., Turkot, O., Jakobsen, M. B., Grössler, M., Licon-Saláiz, J., Griese, F., Flewett, S., Valerio, J., Schulz, J., Biednov, M., Jiang, Y., Han, H., Yousef, H., Khakhulin, D., Milne, C., Barty, A. & van Thor, J. J. (2024). *Struct. Dyn.* **11**, 024310.

Purohit, V., Steussy, C. N., Rosales, A. R., Critchelow, C. J., Schmidt, T., Helquist, P., Wiest, O., Mescar, A., Cohen, A. E. & Stauffacher, C. V. (2024). *Biophys. J.* **123**, 622–637.

Rabe, P., Beale, J. H., Butrym, A., Aller, P., Dirr, A., Lang, P. A., Axford, D. N., Carr, S. B., Leissing, T. M., McDonough, M. A., Davy, B., Ebrahim, A., Orlans, J., Storm, S. L. S., Orville, A. M., Schofield, C. J. & Owen, R. L. (2020). *IUCrJ*, **7**, 901–912.

Roedig, P., Ginn, H. M., Pakendorf, T., Sutton, G., Harlos, K., Walter, T. S., Meyer, J., Fischer, P., Duman, R., Vartiainen, I., Reime, B., Warmer, M., Brewster, A. S., Young, I. D., Michels-Clark, T., Sauter, N. K., Kotecha, A., Kelly, J., Rowlands, D. J., Sikorsky, M., Nelson, S., Damiani, D. S., Alonso-Mori, R., Ren, J., Fry, E. E., David, C., Stuart, D. I., Wagner, A. & Meents, A. (2017). *Nat. Methods*, **14**, 805–810.

Roessler, C. G., Agarwal, R., Allaire, M., Alonso-Mori, R., Andi, B., Bachega, J. F. R., Bommer, M., Brewster, A. S., Browne, M. C., Chatterjee, R., Cho, E., Cohen, A. E., Cowan, M., Datwani, S., Davidson, V. L., Defever, J., Eaton, B., Ellison, R., Feng, Y., Ghislain, L. P., Glownia, J. M., Han, G., Hattne, J., Hellmich, J., Héroux, A., Ibrahim, M., Kern, J., Kuczewski, A., Lemke, H. T., Liu, P., Majolof, L., McClintock, W. M., Myers, S., Nelsen, S., Olechno, J., Orville, A. M., Sauter, N. K., Soares, A. S., Soltis, S. M., Song, H., Stearns, R. G., Tran, R., Tsai, Y., Uervirojnakorn, M., Wilmot, C. M., Yachandra, V., Yano, J., Yukl, E. T., Zhu, D. & Zouni, A. (2016). *Structure*, **24**, 631–640.

Russo Krauss, I., Sica, F., Mattia, C. A. & Merlini, A. (2012). *Int. Mol. Sci.* **13**, 3782–3800.

Schlichting, I. (2015). *IUCrJ*, **2**, 246–255.

Schmidt, M. (2013). *Adv. Condens. Matter Phys.* **2013**, 167276.

Schulz, E. C., Mehrabi, P., Müller-Werkmeister, H. M., Tellkamp, F., Jha, A., Stuart, W., Persch, E., De Gasparo, R., Diederich, F., Pai, E. F. & Miller, R. J. D. (2018). *Nat. Methods*, **15**, 901–904.

Sherrell, D. A., Foster, A. J., Hudson, L., Nutter, B., O’Hea, J., Nelson, S., Paré-Labrosse, O., Oghbaey, S., Miller, R. J. D. & Owen, R. L. (2015). *J. Synchrotron Rad.* **22**, 1372–1378.

Shi, D. & Huang, R. (2022). *Front. Mol. Biosci.* **9**, 988928.

Shi, D., Nannenga, B. L., Iadanza, M. G. & Gonon, T. (2013). *eLife*, **2**, e01345.

Shoeman, R. L., Hartmann, E. & Schlichting, I. (2023). *Nat. Protoc.* **18**, 854–882.

Sierra, R. G., Gati, C., Laksmono, H., Dao, E. H., Gul, S., Fuller, F., Kern, J., Chatterjee, R., Ibrahim, M., Brewster, A. S., Young, I. D., Michels-Clark, T., Aquila, A., Liang, M., Hunter, M. S., Koglin, J. E., Boutet, S., Junco, E. A., Hayes, B., Bogan, M. J., Hampton, C. Y., Puglis, E. V., Sauter, N. K., Stan, C. A., Zouni, A., Yano, J., Yachandra, V. K., Soltis, S. M., Puglis, J. D. & Demirci, H. (2016). *Nat. Methods*, **13**, 59–62.

Sierra, R. G., Laksmono, H., Kern, J., Tran, R., Hattne, J., Alonso-Mori, R., Lassalle-Kaiser, B., Glöckner, C., Hellmich, J., Schafer, D. W., Echols, N., Gildea, R. J., Grosse-Kunstleve, R. W., Sellberg, J., McQueen, T. A., Fry, A. R., Messerschmidt, M. M., Miahnahri, A., Seibert, M. M., Hampton, C. Y., Starodub, D., Loh, N. D., Sokaras, D., Weng, T.-C., Zwart, P. H., Glatzel, P., Milathianaki, D., White, W. E., Adams, P. D., Williams, G. J., Boutet, S., Zouni, A., Messinger, J., Sauter, N. K., Bergmann, U., Yano, J., Yachandra, V. K. & Bogan, M. J. (2012). *Acta Cryst. D68*, 1584–1587.

Smyth, M. S. & Martin, J. H. (2000). *Mol. Pathol.* **53**, 8–14.

Stellato, F., Oberthür, D., Liang, M., Bean, R., Gati, C., Yefanov, O., Barty, A., Burkhardt, A., Fischer, P., Galli, L., Kirian, R. A., Meyer, J., Panneerselvam, S., Yoon, C. H., Chervinskii, F., Speller, E., White, T. A., Betzel, C., Meents, A. & Chapman, H. N. (2014). *IUCrJ*, **1**, 204–212.

Stevenson, H. P., Makhov, A. M., Calero, M., Edwards, A. L., Zeldin, O. B., Mathews, I. I., Lin, G., Barnes, C. O., Santamaría, H., Ross, T. M., Soltis, S. M., Khosla, C., Nagarajan, V., Conway, J. F., Cohen, A. E. & Calero, G. (2014). *Proc. Natl. Acad. Sci. USA*, **111**, 8470–8475.

Stohrer, C., Horrell, S., Meier, S., Sans, M., von Stetten, D., Hough, M., Goldman, A., Monteiro, D. C. F. & Pearson, A. R. (2021). *Acta Cryst. D77*, 194–204.

Storm, S. L. S., Crawshaw, A. D., Devenish, N. E., Bolton, R., Hall, D. R., Tews, I. & Evans, G. (2020). *IUCrJ*, **7**, 129–135.

Stuart, W. S., Jenkins, C. H., Ireland, P. M., Isupov, M. N., Norville, I. H. & Harmer, N. J. (2025). *bioRxiv*, 2025.01.06.631558.

Stubbs, J., Hornsey, T., Hanrahan, N., Esteban, L. B., Bolton, R., Malý, M., Basu, S., Orlans, J., de Sanctis, D., Shim, J. U., Shaw Stewart, P. D., Orville, A. M., Tews, I. & West, J. (2024). *IUCrJ*, **11**, 237–248.

Tenboer, J., Basu, S., Zatsepin, N., Pande, K., Milathianaki, D., Frank, M., Hunter, M., Boutet, S., Williams, G. J., Koglin, J. E., Oberthuer, D., Heymann, M., Kupitz, C., Conrad, C., Coe, J., Roy-Chowdhury, S., Weierstall, U., James, D., Wang, D., Grant, T., Barty, A., Yefanov, O., Scales, J., Gati, C., Seuring, C., Srajer, V., Henning, R., Schwander, P., Fromme, R., Ourmazd, A., Moffat, K., Van Thor, J. J., Spence, J. C. H., Fromme, P., Chapman, H. N. & Schmidt, M. (2014). *Science*, **346**, 1242–1246.

Thaller, C., Eichele, G., Weaver, L. H., Wilson, E., Karlsson, R. & Janssonius, J. N. (1985). *Methods Enzymol.* **114**, 132–135.

Thaller, C., Weaver, L. H., Eichele, G., Wilson, E., Karlsson, R. & Janssonius, J. N. (1981). *J. Mol. Biol.* **147**, 465–469.

Vakili, M., Han, H., Schmidt, C., Wrona, A., Kloos, M., de Diego, I., Dörner, K., Geng, T., Kim, C., Koua, F. H. M., Melo, D. V. M., Rappas, M., Round, A., Round, E., Sikorski, M., Valerio, J., Zhou, T., Lorenzen, K. & Schulz, J. (2023). *J. Appl. Cryst.* **56**, 1038–1045.

Voss, J. M., Harder, O. F., Olshin, P. K., Drabbel, M. & Lorenz, U. J. (2021). *Struct. Dyn.* **8**, 054302.

Wang, D., Weierstall, U., Pollack, L. & Spence, J. (2014). *J. Synchrotron Rad.* **21**, 1364–1366.

Warren, A. J., Crawshaw, A. D., Trincao, J., Aller, P., Alcock, S., Nistea, I., Salgado, P. S. & Evans, G. (2015). *Acta Cryst. D71*, 2079–2088.

Warren, A. J., Trincao, J., Crawshaw, A. D., Beale, E. V., Duller, G., Stallwood, A., Lunnon, M., Littlewood, R., Prescott, A., Foster, A., Smith, N., Rehm, G., Gayadeen, S., Bloomer, C., Alianelli, L., Laundy, D., Sutter, J., Cahill, L. & Evans, G. (2024). *J. Synchrotron Rad.* **31**, 1593–1608.

Weierstall, U., James, D., Wang, C., White, T. A., Wang, D., Liu, W., Spence, J. C. H., Doak, R. B., Nelson, G., Fromme, P., Fromme, R., Grotjohann, I., Kupitz, C., Zatsepin, N. A., Liu, H., Basu, S., Wacker, D., Han, G. W., Katritch, V., Boutet, S., Messerschmidt, M., Williams, G. J., Koglin, J. E., Seibert, M. M., Klinker, M., Gati, C., Shoeman, R. L., Barty, A., Chapman, H. N., Kirian, R. A., Beyerlein, K. R., Stevens, R. C., Li, D., Shah, S. T. A., Howe, N., Caffrey, M. & Cherezov, V. (2014). *Nat. Commun.* **5**, 3309.

Weinert, T., Olieric, N., Cheng, R., Brüne, S., James, D., Ozerov, D., Gashi, D., Vera, L., Marsh, M., Jaeger, K., Dworkowski, F., Panepucci, E., Basu, S., Skopintsev, P., Doré, A. S., Geng, T., Cooke, R. M., Liang, M., Prota, A. E., Panneels, V., Nogly, P., Ermel, U., Schertler, G., Hennig, M., Steinmetz, M. O., Wang, M. & Standfuss, J. (2017). *Nat. Commun.* **8**, 542.

White, T. A., Kirian, R. A., Martin, A. V., Aquila, A., Nass, K., Barty, A. & Chapman, H. N. (2012). *J. Appl. Cryst.* **45**, 335–341.

Wiedorn, M. O., Oberthür, D., Bean, R., Schubert, R., Werner, N., Abbey, B., Aepfelbacher, M., Adriano, L., Allahgholi, A., Al-Qudami, N., Andreasson, J., Aplin, S., Awel, S., Ayer, K., Bajt, S., Barák, I., Bari, S., Bielecki, J., Botha, S., Boukhelef, D., Brehm, W., Brockhauser, S., Cheviakov, I., Coleman, M. A., Cruz-Mazo, F., Danilevski, C., Darmanin, C., Doak, R. B., Domaracky, M., Dörner, K., Du, Y., Fangohr, H., Fleckenstein, H., Frank, M., Fromme, P., Gafán-Calvo, A. M., Gevorkov, Y., Giewekemeyer, K., Ginn, H. M., Graafsma, H., Graceffa, R., Greiffenberg, D., Gumprecht, L., Göttlicher, P., Hajdu, J., Hauf, S., Heymann, M., Holmes, S., Horke, D. A., Hunter, M. S., Imlau, S., Kaukher, A., Kim, Y., Klyuev, A., Knoška, J., Kobe, B., Kuhn, M., Kupitz, C., Küpper, J., Lahey-Rudolph, J. M., Laurus, T., Le Cong, K., Letrun, R., Xavier, P. L., Maia, L., Maia, F. R. N. C., Mariani, V., Messerschmidt, M., Metz, M., Mezza, D., Michelat, T., Mills, G., Monteiro, D. C. F., Morgan, A., Mühlig, K., Munke, A., Münnich, A., Nette, J., Nugent, K. A., Nuguid, T., Orville, A. M., Pandey, S., Pena, G., Villanueva-Perez, P., Poehlsem, J., Previtali, G., Redecke, L., Riekehr, W. M., Rohde, H., Round, A., Safenreiter, T., Sarrou, I., Sato, T., Schmidt, M., Schmitt, B., Schönher, R., Schulz, J., Sellberg, J. A., Seibert, M. M., Seuring, C., Shelby, M. L., Shoeman, R. L., Sikorski, M., Silenzi, A., Stan, C. A., Shi, X., Stern, S., Sztuk-Dambietz, J., Szuba, J., Tolstikova, A., Trebbin, M., Trunk, U., Vagovic, P., Ve, T., Weinhausen, B., White, T. A., Wrona, K., Xu, C., Yefanov, O., Zatsepin, N., Zhang, J., Perbandt, M., Mancuso, A. P., Betzel, C., Chapman, H. & Barty, A. (2018). *Nat. Commun.* **9**, 4025.

Williamson, L. J., Galchenkova, M., Best, H. L., Bean, R. J., Munke, A., Awel, S., Pena, G., Knoska, J., Schubert, R., Dörner, K., Park, H.-W., Bideshi, D. K., Henkel, A., Kremling, V., Klopprogge, B., Lloyd-Evans, E., Young, M. T., Valerio, J., Kloos, M., Sikorski, M., Mills, G., Bielecki, J., Kirkwood, H., Kim, C., de Wijn, R., Lorenzen, K., Xavier, P. L., Rahmani Mashhour, A., Gelisio, L., Yefanov, O., Mancuso, A. P., Federici, B. A., Chapman, H. N., Crickmore, N., Rizkallah, P. J., Berry, C. & Oberthür, D. (2023). *Proc. Natl. Acad. Sci.* **120**, e2203241120.

Wolff, A. M., Young, I. D., Sierra, R. G., Brewster, A. S., Martynowycz, M. W., Nango, E., Sugahara, M., Nakane, T., Ito, K., Aquila, A., Bhowmick, A., Biel, J. T., Carbojo, S., Cohen, A. E., Cortez, S., Gonzalez, A., Hino, T., Im, D., Koralek, J. D., Kubo, M., Lazarou, T. S., Nomura, T., Owada, S., Samelson, A. J., Tanaka, T., Tanaka, R., Thompson, E. M., van den Bedem, H., Woldeyes, R. A., Yumoto, F., Zhao, W., Tono, K., Boutet, S., Iwata, S., Gonon, T., Sauter, N. K., Fraser, J. S. & Thompson, M. C. (2020). *IUCrJ*, **7**, 306–323.

Yang, R., Kvetny, M., Brown, W., Ogbonna, E. N. & Wang, G. (2023). *Anal. Chem.* **95**, 9462–9470.

Zander, U., Bourenkov, G., Popov, A. N., de Sanctis, D., Svensson, O., McCarthy, A. A., Round, E., Gordely, V., Mueller-Dieckmann, C. & Leonard, G. A. (2015). *Acta Cryst. D71*, 2328–2343.

Zarrine-Afsar, A., Barends, T. R. M., Müller, C., Fuchs, M. R., Lomb, L., Schlichting, I. & Miller, R. J. D. (2012). *Acta Cryst. D68*, 321–323.

Zeiger, B. W. & Suslick, K. S. (2011). *J. Am. Chem. Soc.* **133**, 14530–14533.

Zhang, Z., Yang, X., Huang, X., Li, J., Shaftan, T., Smaluk, V., Song, M., Wan, W., Wu, L. & Zhu, Y. (2021). *Sci. Rep.* **11**, 13890.

Zhao, J., Xu, H., Lebrette, H., Carroni, M., Taberman, H., Högbom, M. & Zou, X. (2021). *Nat. Commun.* **12**, 5036.

Zhou, H., Luo, Z. & Li, X. (2019). *J. Struct. Biol.* **205**, 59–64.

Zhu, L., Bu, G., Jing, L., Shi, D., Lee, M.-Y., Gonon, T., Liu, W. & Nannenga, B. L. (2020). *Structure*, **28**, 1149–1159.

Zielinski, K. A., Prester, A., Andaleeb, H., Bui, S., Yefanov, O., Catapano, L., Henkel, A., Wiedorn, M. O., Lorbeer, O., Crosas, E., Meyer, J., Mariani, V., Domaracky, M., White, T. A., Fleckenstein, H., Sarrou, I., Werner, N., Betzel, C., Rohde, H., Aepfelbacher, M., Chapman, H. N., Perbandt, M., Steiner, R. A. & Oberthuer, D. (2022). *IUCrJ*, **9**, 778–791.

Bibliography

1. Kendrew JC, Bodo G, Dintzis HM, Parrish RG, Wyckoff H, Phillips DC. A Three-Dimensional Model of the Myoglobin Molecule Obtained by X-Ray Analysis. *Nature*. 1958 Mar;181(4610):662–6.
2. Smyth MS, Martin JH. x ray crystallography. *Mol Pathol MP*. 2000 Feb;53(1):8–14.
3. Helliwell JR. The evolution of synchrotron radiation and the growth of its importance in crystallography. *Crystallogr Rev*. 2012 Jan 1;18(1):33–93.
4. Hendrickson WA. Synchrotron crystallography. *Trends Biochem Sci*. 2000 Dec 1;25(12):637–43.
5. Owen RL, Juanhuix J, Fuchs M. Current advances in synchrotron radiation instrumentation for MX experiments. *Arch Biochem Biophys*. 2016 Jul 15;602:21–31.
6. Chavas LMG, Coulibaly F, Garriga D. Bridging the microscopic divide: a comprehensive overview of micro-crystallization and in vivo crystallography. *IUCrJ*. 2024 Jul 1;11(4):476–85.
7. Genick UK, Borgstahl GEO, Ng K, Ren Z, Pradervand C, Burke PM, et al. Structure of a Protein Photocycle Intermediate by Millisecond Time-Resolved Crystallography. *Science*. 1997 Mar 7;275(5305):1471–5.
8. Moffat K. Time-Resolved Macromolecular Crystallography. *Annu Rev Biophys Biophys Chem*. 1989;18(1):309–32.
9. Šrajer V, Ren Z, Teng TY, Schmidt M, Ursby T, Bourgeois D, et al. Protein Conformational Relaxation and Ligand Migration in Myoglobin: A Nanosecond to Millisecond Molecular Movie from Time-Resolved Laue X-ray Diffraction. *Biochemistry*. 2001 Nov 1;40(46):13802–15.
10. Šrajer V, Teng T yi, Ursby T, Pradervand C, Ren Z, Adachi S ichi, et al. Photolysis of the Carbon Monoxide Complex of Myoglobin: Nanosecond Time-Resolved Crystallography. *Science*. 1996 Dec 6;274(5293):1726–9.
11. Chapman HN, Caleman C, Timneanu N. Diffraction before destruction. *Philos Trans R Soc B Biol Sci*. 2014 Jul 17;369(1647):20130313.
12. Neutze R, Wouts R, van der Spoel D, Weckert E, Hajdu J. Potential for biomolecular imaging with femtosecond X-ray pulses. *Nature*. 2000 Aug;406(6797):752–7.
13. Fischer M. Macromolecular room temperature crystallography. *Q Rev Biophys*. 2021;54:e1.
14. Fraser JS, van den Bedem H, Samelson AJ, Lang PT, Holton JM, Echols N, et al. Accessing protein conformational ensembles using room-temperature X-ray crystallography. *Proc Natl Acad Sci*. 2011 Sep 27;108(39):16247–52.
15. Chapman HN, Fromme P, Barty A, White TA, Kirian RA, Aquila A, et al. Femtosecond X-ray protein nanocrystallography. *Nature*. 2011 Feb;470(7332):73–7.

Bibliography

16. Spence JCH, Doak RB. Single Molecule Diffraction. *Phys Rev Lett.* 2004 May 12;92(19):198102.
17. Martynowycz MW, Clabbers MTB, Unge J, Hattne J, Gonen T. Benchmarking the ideal sample thickness in cryo-EM. *Proc Natl Acad Sci.* 2021 Dec 7;118(49):e2108884118.
18. Nannenga BL, Gonen T. The cryo-EM method microcrystal electron diffraction (MicroED). *Nat Methods.* 2019 May;16(5):369–79.
19. Henderson R. The potential and limitations of neutrons, electrons and X-rays for atomic resolution microscopy of unstained biological molecules. *Q Rev Biophys.* 1995 May;28(2):171–93.
20. Crawshaw AD, Beale EV, Warren AJ, Stallwood A, Duller G, Trincao J, et al. A Sample Preparation Pipeline for Microcrystals at the VMXm Beamline. *J Vis Exp JoVE.* 2021 Jun 17;(172):e62306.
21. Warren AJ, Trincao J, Crawshaw AD, Beale EV, Duller G, Stallwood A, et al. VMXm – A sub-micron focus macromolecular crystallography beamline at Diamond Light Source. *J Synchrotron Radiat.* 2024 Nov 1;31(6):1593–608.
22. Storm SLS, Crawshaw AD, Devenish NE, Bolton R, Hall DR, Tews I, et al. Measuring energy-dependent photoelectron escape in microcrystals. *IUCrJ.* 2020 Jan 1;7(1):129–35.
23. Tremlett CJ, Stubbs J, Stuart WS, Shaw Stewart PD, West J, Orville AM, et al. Small but mighty: the power of microcrystals in structural biology. *IUCrJ.* 2025 May 1;12(3):262–79.
24. Muybridge E, University of Pennsylvania. *Animal locomotion : an electro-photographic investigation of consecutive phases of animal movements : prospectus and catalogue of plates.* Philadelphia : Printed by J.B. Lippincott company; 1887
25. Caramello N, Royant A. From femtoseconds to minutes: time-resolved macromolecular crystallography at XFELs and synchrotrons. *Acta Crystallogr Sect Struct Biol.* 2024 Feb 1;80(2):60–79.
26. Orville AM. Entering an era of dynamic structural biology.... *BMC Biol.* 2018 May 31;16(1):55.
27. Aller P, Orville AM. Dynamic Structural Biology Experiments at XFEL or Synchrotron Sources. *Structural Proteomics: High-Throughput Methods. (Methods in Molecular Biology)* 2021. p. 203–28.
28. Stillman JDB (Jacob DB, Muybridge E. *The horse in motion as shown by instantaneous photography, with a study on animal mechanics founded on anatomy and the revelations of the camera, in which is demonstrated the theory of quadrupedal locomotion.* Boston, J. R. Osgood and company; 1882, 322 p.
29. Bijelic A, Rompel A. Polyoxometalates: more than a phasing tool in protein crystallography. *ChemTexts.* 2018 Oct 1;4(3):1–27.
30. Stan CV, Beavers CM, Kunz M, Tamura N. X-Ray Diffraction under Extreme Conditions at the Advanced Light Source. *Quantum Beam Sci.* 2018 Mar;2(1):4.
31. Leslie AGW. The integration of macromolecular diffraction data. *Acta Crystallogr D Biol Crystallogr.* 2006 Jan 1;62(1):48–57.

Bibliography

32. Boutet S, Lomb L, Williams GJ, Barends TRM, Aquila A, Doak RB, et al. High-Resolution Protein Structure Determination by Serial Femtosecond Crystallography. *Science*. 2012 Jul 20;337(6092):362–4.
33. Chapman HN. X-Ray Free-Electron Lasers for the Structure and Dynamics of Macromolecules. *Annu Rev Biochem*. 2019;88(1):35–58.
34. Barends TRM, Stauch B, Cherezov V, Schlichting I. Serial femtosecond crystallography. *Nat Rev Methods Primer*. 2022 Aug 4;2(1):1–24.
35. Nam KH. Hit and Indexing Rate in Serial Crystallography: Incomparable Statistics. *Front Mol Biosci*. 2022 Mar 25;9.
36. Brändén G, Neutze R. Advances and challenges in time-resolved macromolecular crystallography. *Science*. 2021 Aug 27;373(6558):eaba0954.
37. Bonifacio R, Pellegrini C, Narducci LM. Collective instabilities and high-gain regime in a free electron laser. *Opt Commun*. 1984 Jul 15;50(6):373–8.
38. Kondratenko AM, Saldin EL. Generating of coherent radiation by a relativistic electron beam in an undulator. Part Accel. 1980;10:207–16.
39. Huang N, Deng H, Liu B, Wang D, Zhao Z. Features and futures of X-ray free-electron lasers. *The Innovation*. 2021 May 28;2(2):100097.
40. Huang Z, Kim KJ. Review of x-ray free-electron laser theory. *Phys Rev Spec Top - Accel Beams*. 2007 Mar 12;10(3):034801.
41. Caleman C, Jares Junior F, Gränäs O, Martin AV. A Perspective on Molecular Structure and Bond-Breaking in Radiation Damage in Serial Femtosecond Crystallography. *Crystals*. 2020 Jul;10(7):585.
42. Lomb L, Barends TRM, Kassemeyer S, Aquila A, Epp SW, Erk B, et al. Radiation damage in protein serial femtosecond crystallography using an x-ray free-electron laser. *Phys Rev B*. 2011 Dec 20;84(21):214111.
43. Nass K. Radiation damage in protein crystallography at X-ray free-electron lasers. *Acta Crystallogr Sect Struct Biol*. 2019 Feb 1;75(2):211–8.
44. Nass K, Gorel A, Abdullah MM, V. Martin A, Kloos M, Marinelli A, et al. Structural dynamics in proteins induced by and probed with X-ray free-electron laser pulses. *Nat Commun*. 2020 Apr 14;11(1):1814.
45. Nass K, Foucar L, Barends TRM, Hartmann E, Botha S, Shoeman RL, et al. Indications of radiation damage in ferredoxin microcrystals using high-intensity X-FEL beams. *J Synchrotron Radiat*. 2015 Mar 1;22(2):225–38.
46. Williams LJ, Thompson AJ, Dijkstal P, Appleby M, Assmann G, Dworkowski FSN, et al. Damage before destruction? X-ray-induced changes in single-pulse serial femtosecond crystallography. *IUCrJ*. 2025 May 1;12(3):358–71.
47. Neutze R, Brändén G, Schertler GF. Membrane protein structural biology using X-ray free electron lasers. *Curr Opin Struct Biol*. 2015 Aug 1;33:115–25.

Bibliography

48. Colletier JP, Sawaya MR, Gingery M, Rodriguez JA, Cascio D, Brewster AS, et al. De novo phasing with X-ray laser reveals mosquito larvicide BinAB structure. *Nature*. 2016 Nov;539(7627):43–7.
49. Redecke L, Nass K, DePonte DP, White TA, Rehders D, Barty A, et al. Natively inhibited Trypanosoma brucei cathepsin B structure determined by using an X-ray laser. *Science*. 2013 Jan 11;339(6116):227–30.
50. Sawaya MR, Cascio D, Gingery M, Rodriguez J, Goldschmidt L, Colletier JP, et al. Protein crystal structure obtained at 2.9 Å resolution from injecting bacterial cells into an X-ray free-electron laser beam. *Proc Natl Acad Sci*. 2014 Sep 2;111(35):12769–74.
51. Williamson LJ, Galchenkova M, Best HL, Bean RJ, Munke A, Awel S, et al. Structure of the Lysinibacillus sphaericus Tpp49Aa1 pesticidal protein elucidated from natural crystals using MHz-SFX. *Proc Natl Acad Sci*. 2023 Dec 5;120(49):e2203241120.
52. Hedman B, Hodgson KO, Helliwell JR, Liddington R, Papiz MZ. Protein microcrystal diffraction and the effects of radiation damage with ultra-high-flux synchrotron radiation. *Proc Natl Acad Sci*. 1985 Nov;82(22):7604–7.
53. Stellato F, Oberthür D, Liang M, Bean R, Gati C, Yefanov O, et al. Room-temperature macromolecular serial crystallography using synchrotron radiation. *IUCrJ*. 2014 Jul 1;1(4):204–12.
54. Weinert T, Olieric N, Cheng R, Brünle S, James D, Ozerov D, et al. Serial millisecond crystallography for routine room-temperature structure determination at synchrotrons. *Nat Commun*. 2017 Sep 14;8(1):542.
55. Ebrahim A, Appleby MV, Axford D, Beale J, Moreno-Chicano T, Sherrell DA, et al. Resolving polymorphs and radiation-driven effects in microcrystals using fixed-target serial synchrotron crystallography. *Acta Crystallogr Sect Struct Biol*. 2019 Feb 1;75(2):151–9.
56. Rupp B. Origin and use of crystallization phase diagrams. *Acta Crystallogr Sect F*. 2015;71(3):247–60.
57. Falkner JC, Al-Somali AM, Jamison JA, Zhang J, Adrianse SL, Simpson RL, et al. Generation of Size-Controlled, Submicrometer Protein Crystals. *Chem Mater*. 2005 May 1;17(10):2679–86.
58. Beale JH, Bolton R, Marshall SA, Beale EV, Carr SB, Ebrahim A, et al. Successful sample preparation for serial crystallography experiments. *J Appl Crystallogr*. 2019 Dec 1;52(6):1385–96.
59. Bergfors T. Seeds to crystals. *J Struct Biol*. 2003 Apr 1;142(1):66–76.
60. Thaller C, Weaver LH, Eichele G, Wilson E, Karlsson R, Jansonius JN. Repeated seeding technique for growing large single crystals of proteins. *J Mol Biol*. 1981 Apr 15;147(3):465–9.
61. Lee DB, Kim JM, Seok JH, Lee JH, Jo JD, Mun JY, et al. Supersaturation-controlled microcrystallization and visualization analysis for serial femtosecond crystallography. *Sci Rep*. 2018 Feb 7;8(1):2541.
62. Ireton GC, Stoddard BL. Microseed matrix screening to improve crystals of yeast cytosine deaminase. *Acta Crystallogr D Biol Crystallogr*. 2004 Mar 1;60(3):601–5.

Bibliography

63. Luft JR, DeTitta GT. A method to produce microseed stock for use in the crystallization of biological macromolecules. *Acta Crystallogr D Biol Crystallogr*. 1999 May 1;55(5):988–93.
64. Till M, Robson A, Byrne MJ, Nair AV, Kolek SA, Shaw Stewart PD, et al. Improving the Success Rate of Protein Crystallization by Random Microseed Matrix Screening. *J Vis Exp* JoVE. 2013 Aug 31;(78):50548.
65. D'Arcy A, Villard F, Marsh M. An automated microseed matrix-screening method for protein crystallization. *Acta Crystallogr D Biol Crystallogr*. 2007 Apr 1;63(4):550–4.
66. D'Arcy A, Mac Sweeney A, Habera A. Modified microbatch and seeding in protein crystallization experiments. *J Synchrotron Radiat*. 2004 Jan 1;11(1):24–6.
67. Dods R, Båth P, Arnlund D, Beyerlein KR, Nelson G, Liang M, et al. From Macrocrystals to Microcrystals: A Strategy for Membrane Protein Serial Crystallography. *Structure*. 2017 Sep 5;25(9):1461-1468.e2.
68. Thaller C, Eichele G, Weaver LH, Wilson E, Karlsson R, Janssonius JN. Seed enlargement and repeated seeding. *Methods in Enzymology*, Academic Press; 1985. p. 132–5.
69. D'Arcy A, Bergfors T, Cowan-Jacob SW, Marsh M. Microseed matrix screening for optimization in protein crystallization: what have we learned? *Acta Crystallogr Sect F Struct Biol Commun*. 2014 Sep 1;70(9):1117–26.
70. Castro F, Cunha I, Ferreira A, Teixeira JA, Rocha F. Towards an enhanced control of protein crystallization: Seeded batch lysozyme crystallization in a meso oscillatory flow reactor. *Chem Eng Res Des*. 2022 Feb 1;178:575–82.
71. He Y, Gao Z, Zhang T, Sun J, Ma Y, Tian N, et al. Seeding Techniques and Optimization of Solution Crystallization Processes. *Org Process Res Dev*. 2020 Oct 16;24(10):1839–49.
72. Khurshid S, Saridakis E, Govada L, Chayen NE. Porous nucleating agents for protein crystallization. *Nat Protoc*. 2014 Jul;9(7):1621–33.
73. Obmolova G, Malia TJ, Teplyakov A, Sweet RW, Gilliland GL. Protein crystallization with microseed matrix screening: application to human germline antibody Fabs. *Acta Crystallogr Sect F Struct Biol Commun*. 2014 Aug 1;70(8):1107–15.
74. Zeiger BW, Suslick KS. Sonofragmentation of Molecular Crystals. *J Am Chem Soc*. 2011 Sep 21;133(37):14530–3.
75. Barnes CO, Kovaleva EG, Fu X, Stevenson HP, Brewster AS, DePonte DP, et al. Assessment of microcrystal quality by transmission electron microscopy for efficient serial femtosecond crystallography. *Arch Biochem Biophys*. 2016 Jul 15;602:61–8.
76. Stevenson HP, Makhov AM, Calero M, Edwards AL, Zeldin OB, Mathews II, et al. Use of transmission electron microscopy to identify nanocrystals of challenging protein targets. *Proc Natl Acad Sci U S A*. 2014 Jun 1;111(23):8470–5.
77. Kadima W, McPherson A, Dunn MF, Jurnak FA. Characterization of precrystallization aggregation of canavalin by dynamic light scattering. *Biophys J*. 1990 Jan 1;57(1):125–32.
78. Haupert LM, Simpson GJ. Screening of protein crystallization trials by second order nonlinear optical imaging of chiral crystals (SONICC). *Methods*. 2011 Dec 1;55(4):379–86.

Bibliography

79. Chayen NE. Comparative Studies of Protein Crystallization by Vapour-Diffusion and Microbatch Techniques. *Acta Crystallogr D Biol Crystallogr*. 1998 Jan 1;54(1):8–15.
80. Stohrer C, Horrell S, Meier S, Sans M, von Stetten D, Hough M, et al. Homogeneous batch micro-crystallization of proteins from ammonium sulfate. *Acta Crystallogr Sect Struct Biol*. 2021 Feb 1;77(2):194–204.
81. Mahon BP, Kurian JJ, Lomelino CL, Smith IR, Socorro L, Bennett A, et al. Microbatch Mixing: “Shaken not Stirred”, a Method for Macromolecular Microcrystal Production for Serial Crystallography. *Cryst Growth Des*. 2016 Nov 2;16(11):6214–21.
82. Tenboer J, Basu S, Zatsepin N, Pande K, Milathianaki D, Frank M, et al. Time-resolved serial crystallography captures high-resolution intermediates of photoactive yellow protein. *Science*. 2014 Dec 5;346(6214):1242–6.
83. Pearson AR, Mehrabi P. Serial synchrotron crystallography for time-resolved structural biology. *Curr Opin Struct Biol*. 2020 Dec 1;65:168–74.
84. Grünbein ML, Nass Kovacs G. Sample delivery for serial crystallography at free-electron lasers and synchrotrons. *Acta Crystallogr Sect Struct Biol*. 2019 Feb 1;75(2):178–91.
85. Martiel I, Müller-Werkmeister HM, Cohen AE. Strategies for sample delivery for femtosecond crystallography. *Acta Crystallogr Sect Struct Biol*. 2019 Feb 1;75(2):160–77.
86. Zhao FZ, Zhang B, Yan EK, Sun B, Wang ZJ, He JH, et al. A guide to sample delivery systems for serial crystallography. *FEBS J*. 2019;286(22):4402–17.
87. Jaho S, Axford D, Gu DH, Hough MA, Owen RL. Chapter Two - Use of fixed targets for serial crystallography. *Methods in Enzymology*. Academic Press; 2024 p. 29–55.
88. Doak RB, Shoeman RL, Gorel A, Nizinski S, Barends TRM, Schlichting I. Sheet-on-sheet fixed target data collection devices for serial crystallography at synchrotron and XFEL sources. *J Appl Crystallogr*. 2024 Dec 1;57(6):1725–32.
89. Doak RB, Nass Kovacs G, Gorel A, Foucar L, Barends TRM, Grünbein ML, et al. Crystallography on a chip – without the chip: sheet-on-sheet sandwich. *Acta Crystallogr Sect Struct Biol*. 2018 Oct 1;74(10):1000–7.
90. Hunter MS, Segelke B, Messerschmidt M, Williams GJ, Zatsepin NA, Barty A, et al. Fixed-target protein serial microcrystallography with an x-ray free electron laser. *Sci Rep*. 2014 Aug 12;4(1):6026.
91. Mueller C, Marx A, Epp SW, Zhong Y, Kuo A, Balo AR, et al. Fixed target matrix for femtosecond time-resolved and in situ serial micro-crystallography. *Struct Dyn*. 2015 Sep;2(5):054302.
92. Nam KH, Kim J, Cho Y. Polyimide mesh-based sample holder with irregular crystal mounting holes for fixed-target serial crystallography. *Sci Rep*. 2021 Jun 23;11(1):13115.
93. Oghbaey S, Sarracini A, Ginn HM, Pare-Labrosse O, Kuo A, Marx A, et al. Fixed target combined with spectral mapping: approaching 100% hit rates for serial crystallography. *Acta Crystallogr Sect Struct Biol*. 2016 Aug 1;72(8):944–55.
94. Owen RL, Axford D, Sherrell DA, Kuo A, Ernst OP, Schulz EC, et al. Low-dose fixed-target serial synchrotron crystallography. *Acta Crystallogr Sect Struct Biol*. 2017 Apr 1;73(4):373–8.

Bibliography

95. Roedig P, Ginn HM, Pakendorf T, Sutton G, Harlos K, Walter TS, et al. High-speed fixed-target serial virus crystallography. *Nat Methods*. 2017 Aug;14(8):805–10.
96. Roedig P, Vartiainen I, Duman R, Panneerselvam S, Stübe N, Lorbeer O, et al. A micro-patterned silicon chip as sample holder for macromolecular crystallography experiments with minimal background scattering. *Sci Rep*. 2015 May 29;5(1):10451.
97. Sherrell DA, Lavens A, Wilamowski M, Kim Y, Chard R, Lazarski K, et al. Fixed-target serial crystallography at the Structural Biology Center. *J Synchrotron Radiat*. 2022 Sep 1;29(5):1141–51.
98. Wierman JL, Paré-Labrosse O, Sarracini A, Besaw JE, Cook MJ, Oghbaey S, et al. Fixed-target serial oscillation crystallography at room temperature. *IUCrJ*. 2019 Mar 1;6(2):305–16.
99. Carrillo M, Mason TJ, Karpik A, Martiel I, Kepa MW, McAuley KE, et al. Micro-structured polymer fixed targets for serial crystallography at synchrotrons and XFELs. *IUCrJ*. 2023 Nov 1;10(6):678–93.
100. Davy B, Axford D, Beale JH, Butrym A, Docker P, Ebrahim A, et al. Reducing sample consumption for serial crystallography using acoustic drop ejection. *J Synchrotron Radiat*. 2019 Sep 1;26(5):1820–5.
101. Horrell S, Axford D, Devenish NE, Ebrahim A, Hough MA, Sherrell DA, et al. Fixed Target Serial Data Collection at Diamond Light Source. *JoVE J Vis Exp*. 2021 Feb 26;(168):e62200.
102. Bjelčić M, Sigfridsson Clauss KGV, Aurelius O, Milas M, Nan J, Ursby T. Anaerobic fixed-target serial crystallography using sandwiched silicon nitride membranes. *Acta Crystallogr Sect D*. 2023;79(11):1018–25.
103. Rabe P, Beale JH, Butrym A, Aller P, Dirr A, Lang PA, et al. Anaerobic fixed-target serial crystallography. *IUCrJ*. 2020 Sep 1;7(5):901–12.
104. Sherrell DA, Foster AJ, Hudson L, Nutter B, O’Hea J, Nelson S, et al. A modular and compact portable mini-endstation for high-precision, high-speed fixed target serial crystallography at FEL and synchrotron sources. *J Synchrotron Radiat*. 2015 Nov 1;22(6):1372–8.
105. Mehrabi P, Müller-Werkmeister HM, Leimkohl JP, Schikora H, Ninkovic J, Krivokuća S, et al. The HARE chip for efficient time-resolved serial synchrotron crystallography. *J Synchrotron Radiat*. 2020 Mar 1;27(2):360–70.
106. Owen RL, de Sanctis D, Pearson AR, Beale JH. A standard descriptor for fixed-target serial crystallography. *Acta Crystallogr Sect Struct Biol*. 2023 Aug 1;79(8):668–72.
107. Bosman R, Prester A, Sung S, von Soosten L, Dibenedetto S, Bartels K, et al. A systematic comparison of Kapton-based HARE chips for fixed-target serial crystallography. *Cell Rep Phys Sci*. 2024 Jun 19;5(6):101987.
108. Mehrabi P, Bücker R, Bourenkov G, Ginn HM, von Stetten D, Müller-Werkmeister HM, et al. Serial femtosecond and serial synchrotron crystallography can yield data of equivalent quality: A systematic comparison. *Sci Adv*. 2021 Mar 17;7(12):eabf1380.
109. Lieske J, Cerv M, Kreida S, Komadina D, Fischer J, Barthelmess M, et al. On-chip crystallization for serial crystallography experiments and on-chip ligand-binding studies. *IUCrJ*. 2019 Jul 1;6(4):714–28.

Bibliography

110. Norton-Baker B, Mehrabi P, Boger J, Schönherr R, von Stetten D, Schikora H, et al. A simple vapor-diffusion method enables protein crystallization inside the HARE serial crystallography chip. *Acta Crystallogr Sect Struct Biol*. 2021 Jun 1;77(6):820–34.
111. Baxter EL, Aguilal L, Alonso-Mori R, Barnes CO, Bonagura CA, Brehmer W, et al. High-density grids for efficient data collection from multiple crystals. *Acta Crystallogr Sect Struct Biol*. 2016 Jan 1;72(1):2–11.
112. Cohen AE, Soltis SM, González A, Aguilal L, Alonso-Mori R, Barnes CO, et al. Goniometer-based femtosecond crystallography with X-ray free electron lasers. *Proc Natl Acad Sci*. 2014 Dec 2;111(48):17122–7.
113. Hirata K, Shinzawa-Itoh K, Yano N, Takemura S, Kato K, Hatanaka M, et al. Determination of damage-free crystal structure of an X-ray–sensitive protein using an XFEL. *Nat Methods*. 2014 Jul;11(7):734–6.
114. Zarrine-Afsar A, Barends TRM, Mueller C, Fuchs MR, Lomb L, Schlichting I, et al. Crystallography on a chip. *Acta Crystallogr D Biol Crystallogr*. 2012 Mar 1;68(3):321–3.
115. Zander U, Bourenkov G, Popov AN, de Sanctis D, Svensson O, McCarthy AA, et al. MeshAndCollect: an automated multi-crystal data-collection workflow for synchrotron macromolecular crystallography beamlines. *Acta Crystallogr D Biol Crystallogr*. 2015 Nov 1;71(11):2328–43.
116. Axford D, Aller P, Sanchez-Weatherby J, Sandy J. Applications of thin-film sandwich crystallization platforms. *Acta Crystallogr Sect F Struct Biol Commun*. 2016 Apr 1;72(4):313–9.
117. DePonte DP, Weierstall U, Schmidt K, Warner J, Starodub D, Spence JCH, et al. Gas dynamic virtual nozzle for generation of microscopic droplet streams. *J Phys Appl Phys*. 2008 Oct 7;41(19):195505.
118. Rubio A, Montanero JM, Vakili M, Koua FHM, Bajt S, Chapman HN, et al. Superstability of micrometre jets surrounded by a polymeric shell. *J Appl Crystallogr*. 2025 Aug 1;58(4).
119. Vakili M, Vasireddi R, Gwozdz PV, Monteiro DCF, Heymann M, Blick RH, et al. Microfluidic polyimide gas dynamic virtual nozzles for serial crystallography. *Rev Sci Instrum*. 2020 Aug 7;91(8):085108.
120. Weierstall U, James D, Wang C, White TA, Wang D, Liu W, et al. Lipidic cubic phase injector facilitates membrane protein serial femtosecond crystallography. *Nat Commun*. 2014 Feb 14;5(1):3309.
121. Zahoor R, Bajt S, Šarler B. A numerical study of gas focused non-Newtonian micro-jets. *Int J Multiph Flow*. 2024 Jan 1;170:104628.
122. Gañán-Calvo AM, DePonte DP, Herrada MA, Spence J, Weierstall U, Doak RB. Liquid capillary micro/nanojets in free-jet expansion. *Small*. 2010 Apr 9;6(7):822–4.
123. Schlichting I. Serial femtosecond crystallography: the first five years. *IUCrJ*. 2015 Mar 1;2(2):246–55.
124. Oberthuer D, Knoška J, Wiedorn MO, Beyerlein KR, Bushnell DA, Kovaleva EG, et al. Double-flow focused liquid injector for efficient serial femtosecond crystallography. *Sci Rep*. 2017 Mar 16;7(1):44628.

Bibliography

125. Nelson G, Kirian RA, Weierstall U, Zatsepin NA, Faragó T, Baumbach T, et al. Three-dimensional-printed gas dynamic virtual nozzles for x-ray laser sample delivery. *Opt Express*. 2016 May 30;24(11):11515–30.
126. Paulson L, Narayanasamy SR, Shelby ML, Frank M, Trebbin M. Advanced manufacturing provides tailor-made solutions for crystallography with x-ray free-electron lasers. *Struct Dyn*. 2024 Feb 21;11(1):011101.
127. Vakili M, Bielecki J, Knoška J, Otte F, Han H, Kloos M, et al. 3D printed devices and infrastructure for liquid sample delivery at the European XFEL. *J Synchrotron Radiat*. 2022 Mar 1;29(2):331–46.
128. Sierra RG, Laksmono H, Kern J, Tran R, Hattne J, Alonso-Mori R, et al. Nanoflow electrospinning serial femtosecond crystallography. *Acta Crystallogr D Biol Crystallogr*. 2012 Nov 1;68(11):1584–7.
129. Sierra RG, Gati C, Laksmono H, Dao EH, Gul S, Fuller F, et al. Concentric-flow electrokinetic injector enables serial crystallography of ribosome and photosystem II. *Nat Methods*. 2016 Jan;13(1):59–62.
130. Botha S, Nass K, Barends TRM, Kabsch W, Latz B, Dworkowski F, et al. Room-temperature serial crystallography at synchrotron X-ray sources using slowly flowing free-standing high-viscosity microstreams. *Acta Crystallogr D Biol Crystallogr*. 2015 Feb 1;71(2):387–97.
131. Nogly P, James D, Wang D, White TA, Zatsepin N, Shilova A, et al. Lipidic cubic phase serial millisecond crystallography using synchrotron radiation. *IUCrJ*. 2015 Mar 1;2(2):168–76.
132. Sugahara M, Motomura K, Suzuki M, Masuda T, Joti Y, Numata K, et al. Viscosity-adjustable grease matrices for serial nanocrystallography. *Sci Rep*. 2020 Jan 28;10(1):1371.
133. Sugahara M, Nakane T, Masuda T, Suzuki M, Inoue S, Song C, et al. Hydroxyethyl cellulose matrix applied to serial crystallography. *Sci Rep*. 2017 Apr 6;7(1):703.
134. Sugahara M, Mizohata E, Nango E, Suzuki M, Tanaka T, Masuda T, et al. Grease matrix as a versatile carrier of proteins for serial crystallography. *Nat Methods*. 2015 Jan;12(1):61–3.
135. Shimazu Y, Tono K, Tanaka T, Yamanaka Y, Nakane T, Mori C, et al. High-viscosity sample-injection device for serial femtosecond crystallography at atmospheric pressure. *J Appl Crystallogr*. 2019 Dec 1;52(6):1280–8.
136. Berntsen P, Darmanin C, Balaur E, Flueckiger L, Kozlov A, Roque FG, et al. Stability, flow alignment and a phase transition of the lipidic cubic phase during continuous flow injection. *J Colloid Interface Sci*. 2022 Apr 1;611:588–98.
137. Berntsen P, Hadian Jazi M, Kusel M, Martin AV, Ericsson T, Call MJ, et al. The serial millisecond crystallography instrument at the Australian Synchrotron incorporating the “Lipidico” injector. *Rev Sci Instrum*. 2019 Aug;90(8):085110.
138. Martin-Garcia JM, Conrad CE, Nelson G, Stander N, Zatsepin NA, Zook J, et al. Serial millisecond crystallography of membrane and soluble protein microcrystals using synchrotron radiation. *IUCrJ*. 2017 Jul 1;4(4):439–54.
139. Fromme R, Ishchenko A, Metz M, Chowdhury SR, Basu S, Boutet S, et al. Serial femtosecond crystallography of soluble proteins in lipidic cubic phase. *IUCrJ*. 2015 Sep 1;2(5):545–51.

Bibliography

140. Roessler CG, Agarwal R, Allaire M, Alonso-Mori R, Andi B, Bachega JFR, et al. Acoustic Injectors for Drop-On-Demand Serial Femtosecond Crystallography. *Structure*. 2016 Apr 5;24(4):631–40.
141. Perrett S, Fadini A, Hutchison CDM, Bhattacharya S, Morrison C, Turkot O, et al. Kilohertz droplet-on-demand serial femtosecond crystallography at the European XFEL station FXE. *Struct Dyn*. 2024 Mar 1;11(2).
142. Mafuné F, Miyajima K, Tono K, Takeda Y, Kohno J, Miyauchi N, et al. Microcrystal delivery by pulsed liquid droplet for serial femtosecond crystallography. *Acta Crystallogr Sect Struct Biol*. 2016 Apr 1;72(4):520–3.
143. Doppler D, Rabbani MT, Letrun R, Cruz Villarreal J, Kim DH, Gandhi S, et al. Co-flow injection for serial crystallography at X-ray free-electron lasers. *J Appl Crystallogr*. 2022 Feb 1;55(1):1–13.
144. Echelmeier A, Cruz Villarreal J, Messerschmidt M, Kim D, Coe JD, Thifault D, et al. Segmented flow generator for serial crystallography at the European X-ray free electron laser. *Nat Commun*. 2020 Sep 9;11(1):4511.
145. Sonker M, Doppler D, Egatz-Gomez A, Zaare S, Rabbani MT, Manna A, et al. Electrically stimulated droplet injector for reduced sample consumption in serial crystallography. *Biophys Rep*. 2022 Dec 14;2(4):100081.
146. Doppler D, Grieco A, Koh D, Manna A, Ansari A, Alvarez R, et al. Minimized Sample Consumption for Time-Resolved Serial Crystallography Applied to the Redox Cycle of Human NQO1. *bioRxiv*; 2024.
147. Doppler D, Sonker M, Egatz-Gomez A, Grieco A, Zaare S, Jernigan R, et al. Modular droplet injector for sample conservation providing new structural insight for the conformational heterogeneity in the disease-associated NQO1 enzyme. *Lab Chip*. 2023;23(13):3016–33.
148. Butryn A, Simon PS, Aller P, Hinchliffe P, Massad RN, Leen G, et al. An on-demand, drop-on-drop method for studying enzyme catalysis by serial crystallography. *Nat Commun*. 2021 Jul 22;12(1):4461.
149. Fuller FD, Gul S, Chatterjee R, Burgie ES, Young ID, Lebrette H, et al. Drop-on-demand sample delivery for studying biocatalysts in action at X-ray free-electron lasers. *Nat Methods*. 2017 Apr;14(4):443–9.
150. Beyerlein KR, Dierksmeyer D, Mariani V, Kuhn M, Sarrou I, Ottaviano A, et al. Mix-and-diffuse serial synchrotron crystallography. *IUCrJ*. 2017 Nov 1;4(6):769–77.
151. Henkel A, Galchenkova M, Maracke J, Yefanov O, Klopprogge B, Hakanpää J, et al. JINXED: just in time crystallization for easy structure determination of biological macromolecules. *IUCrJ*. 2023 May 1;10(3).
152. Henkel A, Maracke J, Munke A, Galchenkova M, Mashhour AR, Reinke P, et al. Cfel tapedrive 2.0: a conveyor belt-based sample-delivery system for multi-dimensional serial crystallography. 33rd European Crystallographic Meeting, 2022.
153. Zielinski KA, Prester A, Andaleeb H, Bui S, Yefanov O, Catapano L, et al. Rapid and efficient room-temperature serial synchrotron crystallography using the CFEL TapeDrive. *IUCrJ*. 2022 Nov 1;9(6):778–91.

Bibliography

154. Kamps JJAG, Bosman R, Orville AM, Aller P. Sample efficient approaches in time-resolved X-ray serial crystallography and complementary X-ray emission spectroscopy using drop-on-demand tape-drive systems. *Methods in Enzymology*. Academic Press; 2024.
155. Maeki M, Tokeshi M. Microfluidic Technologies and Platforms for Protein Crystallography.. Applications of Microfluidic Systems in Biology and Medicine. Singapore: Springer Nature; 2024. p. 57–87.
156. Sui S, Perry SL. Microfluidics: From crystallization to serial time-resolved crystallography. *Struct Dyn*. 2017 May;4(3):032202.
157. Liu Z, Gu K, Shelby M, Roy D, Muniyappan S, Schmidt M, et al. In situ counter-diffusion crystallization and long-term crystal preservation in microfluidic fixed targets for serial crystallography. *J Appl Crystallogr*. 2024 Oct 1;57(5):1539–50.
158. Narayanasamy SR, Shelby ML, Chatterjee C, Zhou J, Rose S, Orlans J, et al. Novel polymer fixed-target microfluidic platforms with an ultra-thin moisture barrier for serial macromolecular crystallography. *bioRxiv*; 2025. p. 2025.07.13.663488.
159. Saha S, Chen Y, Russi S, Marchany-Rivera D, Cohen A, Perry SL. Scalable fabrication of an array-type fixed-target device for automated room temperature X-ray protein crystallography. *Sci Rep*. 2025 Jan 2;15(1):334.
160. Gilbile D, Shelby ML, Lyubimov AY, Wierman JL, Monteiro DCF, Cohen AE, et al. Plug-and-play polymer microfluidic chips for hydrated, room temperature, fixed-target serial crystallography. *Lab Chip*. 2021 Dec 7;21(24):4831–45.
161. Gu KK, Liu Z, Narayanasamy SR, Shelby ML, Chan N, Coleman MA, et al. All polymer microfluidic chips—A fixed target sample delivery workhorse for serial crystallography. *Biomicrofluidics*. 2023 Oct 13;17(5):051302.
162. Liu Z, Gu KK, Shelby ML, Gilbile D, Lyubimov AY, Russi S, et al. A user-friendly plug-and-play cyclic olefin copolymer-based microfluidic chip for room-temperature, fixed-target serial crystallography. *Acta Crystallogr Sect Struct Biol*. 2023 Oct 1;79(10):944–52.
163. Manna A, Sonker M, Koh D, Steiger M, Ansari A, Hu H, et al. Cyclic Olefin Copolymer-Based Fixed-Target Sample Delivery Device for Protein X-ray Crystallography. *Anal Chem*. 2024 Dec 31;96(52):20371–81.
164. de Wijn R, Rollet K, Olieric V, Hennig O, Thome N, Noûs C, et al. Crystallization and Structural Determination of an Enzyme:Substrate Complex by Serial Crystallography in a Versatile Microfluidic Chip. *J Vis Exp JoVE*. 2021 Mar 20;(169).
165. de Wijn R, Hennig O, Roche J, Engilberge S, Rollet K, Fernandez-Millan P, et al. A simple and versatile microfluidic device for efficient biomacromolecule crystallization and structural analysis by serial crystallography. *IUCrJ*. 2019 May 1;6(3):454–64.
166. Dhouib K, Malek CK, Pfleging W, Gauthier-Manuel B, Duffait R, Thuillier G, et al. Microfluidic chips for the crystallization of biomacromolecules by counter-diffusion and on-chip crystal X-ray analysis. *Lab Chip*. 2009;9(10):1412–21.
167. Lyubimov AY, Murray TD, Koehl A, Araci IE, Uervirojngankorn M, Zeldin OB, et al. Capture and X-ray diffraction studies of protein microcrystals in a microfluidic trap array. *Acta Crystallogr D Biol Crystallogr*. 2015 Apr 1;71(4):928–40.

Bibliography

168. Opara N, Martiel I, Arnold SA, Braun T, Stahlberg H, Makita M, et al. Direct protein crystallization on ultrathin membranes for diffraction measurements at X-ray free-electron lasers. *J Appl Crystallogr.* 2017;50(3):909–18.
169. Shelby ML, Gilbile D, Grant TD, Seuring C, Segelke BW, He W, et al. A fixed-target platform for serial femtosecond crystallography in a hydrated environment. *IUCrJ.* 2020 Jan 1;7(1):30–41.
170. Sui S, Mulichak A, Kulathila R, McGee J, Filiatreault D, Saha S, et al. A capillary-based microfluidic device enables primary high-throughput room-temperature crystallographic screening. *J Appl Crystallogr.* 2021 Aug 1;54(4):1034–46.
171. Monteiro DCF, Vakili M, Harich J, Sztucki M, Meier SM, Horrell S, et al. A microfluidic flow-focusing device for low sample consumption serial synchrotron crystallography experiments in liquid flow. *J Synchrotron Radiat.* 2019 Mar 1;26(2):406–12.
172. Monteiro DCF, von Stetten D, Stohrer C, Sans M, Pearson AR, Santoni G, et al. 3D-MiXD: 3D-printed X-ray-compatible microfluidic devices for rapid, low-consumption serial synchrotron crystallography data collection in flow. *IUCrJ.* 2020 Mar 1;7(2):207–19.
173. Lane SIR, Butement J, Harrington J, Underwood T, Shrimpton J, West J. Perpetual sedimentation for the continuous delivery of particulate suspensions. *Lab Chip.* 2019 Nov 5;19(22):3771–5.
174. Lomb L, Steinbrener J, Bari S, Beisel D, Berndt D, Kieser C, et al. An anti-settling sample delivery instrument for serial femtosecond crystallography. *J Appl Crystallogr.* 2012;45(4):674–8.
175. Ghosh S, Zorić D, Dahl P, Bjelčić M, Johannesson J, Sandelin E, et al. A simple goniometer-compatible flow cell for serial synchrotron X-ray crystallography. *J Appl Crystallogr.* 2023 Apr 1;56(2):449–60.
176. Banari A, Samanta AK, Munke A, Laugks T, Bajt S, Grünewald K, et al. Advancing time-resolved structural biology: latest strategies in cryo-EM and X-ray crystallography. *Nat Methods.* 2025 Jul;22(7):1420–35.
177. Barends TRM, Gorel A, Bhattacharyya S, Schirò G, Bacellar C, Cirelli C, et al. Influence of pump laser fluence on ultrafast myoglobin structural dynamics. *Nature.* 2024 Feb;626(8000):905–11.
178. Grünbein ML, Stricker M, Nass Kovacs G, Kloos M, Doak RB, Shoeman RL, et al. Illumination guidelines for ultrafast pump–probe experiments by serial femtosecond crystallography. *Nat Methods.* 2020 Jul;17(7):681–4.
179. Monteiro DCF, Amoah E, Rogers C, Pearson AR. Using photocaging for fast time-resolved structural biology studies. *Acta Crystallogr Sect Struct Biol.* 2021 Oct 1;77(10):1218–32.
180. Schmidt M. Reaction Initiation in Enzyme Crystals by Diffusion of Substrate. *Crystals.* 2020 Feb;10(2):116.
181. Schmidt M. Mix and Inject: Reaction Initiation by Diffusion for Time-Resolved Macromolecular Crystallography. *Adv Condens Matter Phys.* 2013 May 12;2013:e167276.
182. Calvey GD, Katz AM, Pollack L. Microfluidic Mixing Injector Holder Enables Routine Structural Enzymology Measurements with Mix-and-Inject Serial Crystallography Using X-ray Free Electron Lasers. *Anal Chem.* 2019 Jun 4;91(11):7139–44.

Bibliography

183. Calvey GD, Katz AM, Schaffer CB, Pollack L. Mixing injector enables time-resolved crystallography with high hit rate at X-ray free electron lasers. *Struct Dyn.* 2016 Sep;3(5):054301.
184. Vakili M, Han H, Schmidt C, Wrona A, Kloos M, De Diego I, et al. Mix-and-extrude: high-viscosity sample injection towards time-resolved protein crystallography. *J Appl Crystallogr.* 2023 Aug 1;56(4):1038–45.
185. Wang D, Weierstall U, Pollack L, Spence J. Double-focusing mixing jet for XFEL study of chemical kinetics. *J Synchrotron Radiat.* 2014 Nov;21(Pt 6):1364–6.
186. Zielinski KA, Pollack L. Advances in microfluidic mixers for time-resolved structural biology with X-rays. *Biophys Rev* [Internet]. 2025 May 23 [cited 2025 Jul 24]; Available from: <https://doi.org/10.1007/s12551-025-01321-x>
187. Mehrabi P, Schulz EC, Agthe M, Horrell S, Bourenkov G, von Stetten D, et al. Liquid application method for time-resolved analyses by serial synchrotron crystallography. *Nat Methods.* 2019 Oct;16(10):979–82.
188. Schulz EC, Mehrabi P, Müller-Werkmeister HM, Tellkamp F, Jha A, Stuart W, et al. The hit-and-return system enables efficient time-resolved serial synchrotron crystallography. *Nat Methods.* 2018 Nov;15(11):901–4.
189. Lee K, Kim J, Baek S, Park J, Park S, Lee JL, et al. Combination of an inject-and-transfer system for serial femtosecond crystallography. *J Appl Crystallogr.* 2022 Aug 1;55(4):813–22.
190. Barra ALC, Ullah N, Brognaro H, Gutierrez RF, Wrenger C, Betzel C, et al. Structure and dynamics of the staphylococcal pyridoxal 5-phosphate synthase complex reveal transient interactions at the enzyme interface. *J Biol Chem.* 2024 Jun 1;300(6).
191. Guédez G, Hipp K, Windeisen V, Derrer B, Gengenbacher M, Böttcher B, et al. Assembly of the Eukaryotic PLP-Synthase Complex from Plasmodium and Activation of the Pdx1 Enzyme. *Structure.* 2012 Jan 11;20(1):172–84.
192. Neuwirth M, Flicker K, Strohmeier M, Tews I, Macheroux P. Thermodynamic characterization of the protein-protein interaction in the heteromeric *Bacillus subtilis* pyridoxalphosphate synthase. *Biochemistry.* 2007;46.
193. Smith AM, Brown WC, Harms E, Smith JL. Crystal Structures Capture Three States in the Catalytic Cycle of a Pyridoxal Phosphate (PLP) Synthase *♦. *J Biol Chem.* 2015 Feb 27;290(9):5226–39.
194. Strohmeier M, Raschle T, Mazurkiewicz J, Rippe K, Sinning I, Fitzpatrick TB, et al. Structure of a bacterial pyridoxal 5'-phosphate synthase complex. *Proc Natl Acad Sci.* 2006 Dec 19;103(51):19284–9.
195. Ullah N, Andaleeb H, Mudogo CN, Falke S, Betzel C, Wrenger C. Solution Structures and Dynamic Assembly of the 24-Meric Plasmodial Pdx1–Pdx2 Complex. *Int J Mol Sci.* 2020 Jan;21(17):5971.
196. Zhu J, Burgner JW, Harms E, Belitsky BR, Smith JL. A New Arrangement of $(\beta/\alpha)8$ Barrels in the Synthase Subunit of PLP Synthase*♦. *J Biol Chem.* 2005 Jul 29;280(30):27914–23.

Bibliography

197. Burns KE, Xiang Y, Kinsland CL, McLafferty FW, Begley TP. Reconstitution and Biochemical Characterization of a New Pyridoxal-5'-Phosphate Biosynthetic Pathway. *J Am Chem Soc.* 2005 Mar 1;127(11):3682–3.
198. Hanes JW. Mechanistic studies on pyridoxal phosphate synthase: the reaction pathway leading to a chromophoric intermediate. *J Am Chem Soc.* 2008;130.
199. Raschle T, Amrhein N, Fitzpatrick TB. On the Two Components of Pyridoxal 5'-Phosphate Synthase from *Bacillus subtilis**. *J Biol Chem.* 2005 Sep 16;280(37):32291–300.
200. Barra ALC, Dantas L de OC, Morão LG, Gutierrez RF, Polikarpov I, Wrenger C, et al. Essential Metabolic Routes as a Way to ESKAPE From Antibiotic Resistance. *Front Public Health.* 2020 Feb 28;8:26.
201. Reeksting SB, Müller IB, Burger PB, Burgos ES, Salmon L, Louw AI, et al. Exploring inhibition of Pdx1, a component of the PLP synthase complex of the human malaria parasite *Plasmodium falciparum*. *Biochem J.* 2013 Jan 1;449(1):175–87.
202. Rodrigues MJ, Windeisen V, Zhang Y, Guédez G, Weber S, Strohmeier M, et al. Lysine relay mechanism coordinates intermediate transfer in vitamin B6 biosynthesis. *Nat Chem Biol.* 2017 Mar;13(3):290–4.
203. Robinson GC, Kaufmann M, Roux C, Fitzpatrick TB. Structural definition of the lysine swing in *Arabidopsis thaliana* PDX1: Intermediate channeling facilitating vitamin B6 biosynthesis. *Proc Natl Acad Sci.* 2016 Oct 4;113(40):E5821–9.
204. Robinson GC, Kaufmann M, Roux C, Martinez-Font J, Hothorn M, Thore S, et al. Crystal structure of the pseudoenzyme PDX1.2 in complex with its cognate enzyme PDX1.3: a total eclipse. *Acta Crystallogr Sect Struct Biol.* 2019 Apr 1;75(4):400–15.
205. Rodrigues MJ, Giri N, Royant A, Zhang Y, Bolton R, Evans G, et al. Trapping and structural characterisation of a covalent intermediate in vitamin B6 biosynthesis catalysed by the Pdx1 PLP synthase. *RSC Chem Biol.* 2022 Feb 9;3(2):227–30.
206. Shim Juk, Cristobal G, Link DR, Thorsen T, Fraden S. Using Microfluidics to Decouple Nucleation and Growth of Protein Crystals. *Cryst Growth Des.* 2007 Nov 1;7(11):2192–4.
207. Whitesides GM. The origins and the future of microfluidics. *Nature.* 2006 Jul;442(7101):368–73.
208. Bird RB, Stewart WE, Lightfoot EN. Transport phenomena. 2nd, Wiley international ed ed. New York: J. Wiley; 2002. 895 p.
209. Beebe DJ, Mensing GA, Walker GM. Physics and Applications of Microfluidics in Biology. *Annu Rev Biomed Eng.* 2002 Aug 1;4(Volume 4, 2002):261–86.
210. Ding Y, Howes PD, deMello AJ. Recent Advances in Droplet Microfluidics. *Anal Chem.* 2020 Jan 7;92(1):132–49.
211. Moragues T, Arguijo D, Beneyton T, Modavi C, Simutis K, Abate AR, et al. Droplet-based microfluidics. *Nat Rev Methods Primer.* 2023 Apr 20;3(1):1–22.
212. Teh SY, Lin R, Hung LH, P. Lee A. Droplet microfluidics. *Lab Chip.* 2008;8(2):198–220.
213. Song H, Tice JD, Ismagilov RF. A Microfluidic System for Controlling Reaction Networks in Time. *Angew Chem.* 2003;115(7):792–6.

Bibliography

214. Song H, Chen DL, Ismagilov RF. Reactions in Droplets in Microfluidic Channels. *Angew Chem Int Ed*. 2006;45(44):7336–56.

215. Tice JD, Song H, Lyon AD, Ismagilov RF. Formation of Droplets and Mixing in Multiphase Microfluidics at Low Values of the Reynolds and the Capillary Numbers. *Langmuir*. 2003 Oct 1;19(22):9127–33.

216. Aref H. Stirring by chaotic advection. In: *Hamiltonian Dynamical Systems*. CRC Press; 1987.

217. Ottino JM. *The Kinematics of Mixing: Stretching, Chaos, and Transport*. Cambridge University Press; 1989. 390 p.

218. Song H, Ismagilov RF. Millisecond Kinetics on a Microfluidic Chip Using Nanoliters of Reagents. *J Am Chem Soc*. 2003 Nov 1;125(47):14613–9.

219. Stroock AD, Dertinger SKW, Ajdari A, Mezić I, Stone HA, Whitesides GM. Chaotic Mixer for Microchannels. *Science*. 2002 Jan 25;295(5555):647–51.

220. Zhu P, Wang L. Passive and active droplet generation with microfluidics: a review. *Lab Chip*. 2016 Dec 20;17(1):34–75.

221. Baroud CN, Gallaire F, Dangla R. Dynamics of microfluidic droplets. *Lab Chip*. 2010;10(16):2032.

222. Dreyfus R, Tabeling P, Willaime H. Ordered and Disordered Patterns in Two-Phase Flows in Microchannels. *Phys Rev Lett*. 2003 Apr 11;90(14):144505.

223. Joanicot M, Ajdari A. Droplet Control for Microfluidics. *Science*. 2005 Aug 5;309(5736):887–8.

224. Link DR, Anna SL, Weitz DA, Stone HA. Geometrically Mediated Breakup of Drops in Microfluidic Devices. *Phys Rev Lett*. 2004 Feb 6;92(5):054503.

225. Whitesides GM, Ostuni E, Takayama S, Jiang X, Ingber DE. Soft Lithography in Biology and Biochemistry. *Annu Rev Biomed Eng*. 2001;3(1):335–73.

226. Xia Y, Whitesides GM. Soft Lithography. *Angew Chem Int Ed*. 1998;37(5):550–75.

227. Duffy DC, McDonald JC, Schueller OJA, Whitesides GM. Rapid Prototyping of Microfluidic Systems in Poly(dimethylsiloxane). *Anal Chem*. 1998 Dec 1;70(23):4974–84.

228. McDonald JC, Duffy DC, Anderson JR, Chiu DT, Wu H, Schueller OJA, et al. Fabrication of microfluidic systems in poly(dimethylsiloxane). *ELECTROPHORESIS*. 2000;21(1):27–40.

229. Sia SK, Whitesides GM. Microfluidic devices fabricated in Poly(dimethylsiloxane) for biological studies. *ELECTROPHORESIS*. 2003;24(21):3563–76.

230. Neves LB, Afonso IS, Nobrega G, Barbosa LG, Lima RA, Ribeiro JE. A Review of Methods to Modify the PDMS Surface Wettability and Their Applications. *Micromachines*. 2024 Jun;15(6):670.

231. Zhou J, Khodakov DA, Ellis AV, Voelcker NH. Surface modification for PDMS-based microfluidic devices. *ELECTROPHORESIS*. 2012;33(1):89–104.

232. Zhou J, Ellis AV, Voelcker NH. Recent developments in PDMS surface modification for microfluidic devices. *ELECTROPHORESIS*. 2010;31(1):2–16.

Bibliography

233. Bodas D, Khan-Malek C. Hydrophilization and hydrophobic recovery of PDMS by oxygen plasma and chemical treatment—An SEM investigation. *Sens Actuators B Chem.* 2007 Apr 10;123(1):368–73.

234. Chen IJ, Lindner E. The Stability of Radio-Frequency Plasma-Treated Polydimethylsiloxane Surfaces. *Langmuir.* 2007 Mar 1;23(6):3118–22.

235. Hwang SH, Gonzalez-Suarez AM, Stybayeva G, Revzin A. Prospects and Opportunities for Microsystems and Microfluidic Devices in the Field of Otorhinolaryngology. *Clin Exp Otorhinolaryngol.* 2020 Aug 11;14(1):29–42.

236. Lau BTC, Baitz CA, Dong XP, Hansen CL. A Complete Microfluidic Screening Platform for Rational Protein Crystallization. *J Am Chem Soc.* 2007 Jan 1;129(3):454–5.

237. Leng J, Salmon JB. Microfluidic crystallization. *Lab Chip.* 2009;9(1):24–34.

238. Li L, Ismagilov RF. Protein Crystallization Using Microfluidic Technologies Based on Valves, Droplets, and SlipChip. *Annu Rev Biophys.* 2010 Apr;39(1):139–58.

239. Hansen CL, Skordalakes E, Berger JM, Quake SR. A robust and scalable microfluidic metering method that allows protein crystal growth by free interface diffusion. *Proc Natl Acad Sci.* 2002 Dec 24;99(26):16531–6.

240. Puigmartí-Luis J. Microfluidic platforms: a mainstream technology for the preparation of crystals. *Chem Soc Rev.* 2014 Mar 10;43(7):2253–71.

241. Sauter C, Dhouib K, Lorber B. From Macrofluidics to Microfluidics for the Crystallization of Biological Macromolecules. *Cryst Growth Des.* 2007 Nov 1;7(11):2247–50.

242. Shi H huan, Xiao Y, Ferguson S, Huang X, Wang N, Hao H xun. Progress of crystallization in microfluidic devices. *Lab Chip.* 2017 Jun 27;17(13):2167–85.

243. Zheng B, Gerdts CJ, Ismagilov RF. Using nanoliter plugs in microfluidics to facilitate and understand protein crystallization. *Curr Opin Struct Biol.* 2005 Oct 1;15(5):548–55.

244. Zheng B, Tice JD, Roach LS, Ismagilov RF. A Droplet-Based, Composite PDMS/Glass Capillary Microfluidic System for Evaluating Protein Crystallization Conditions by Microbatch and Vapor-Diffusion Methods with On-Chip X-Ray Diffraction. *Angew Chem Int Ed.* 2004;43(19):2508–11.

245. Zheng B, Roach LS, Ismagilov RF. Screening of Protein Crystallization Conditions on a Microfluidic Chip Using Nanoliter-Size Droplets. *J Am Chem Soc.* 2003 Sep 1;125(37):11170–1.

246. Yadav MK, Gerdts CJ, Sanishvili R, Smith WW, Roach LS, Ismagilov RF, et al. In situ data collection and structure refinement from microcapillary protein crystallization. *J Appl Crystallogr.* 2005;38(6):900–5.

247. Hansen CL, Classen S, Berger JM, Quake SR. A Microfluidic Device for Kinetic Optimization of Protein Crystallization and In Situ Structure Determination. *J Am Chem Soc.* 2006 Mar 1;128(10):3142–3.

248. Heymann M, Ophalage A, Wierman JL, Akella S, Szebenyi DME, Gruner SM, et al. Room-temperature serial crystallography using a kinetically optimized microfluidic device for protein crystallization and on-chip X-ray diffraction. *IUCrJ.* 2014 Sep 1;1(Pt 5):349–60.

Bibliography

249. Zheng B, Ismagilov RF. A Microfluidic Approach for Screening Submicroliter Volumes against Multiple Reagents by Using Preformed Arrays of Nanoliter Plugs in a Three-Phase Liquid/Liquid/Gas Flow. *Angew Chem Int Ed*. 2005;44(17):2520–3.

250. Li L, Mustafi D, Fu Q, Tereshko V, Chen DL, Tice JD, et al. Nanoliter microfluidic hybrid method for simultaneous screening and optimization validated with crystallization of membrane proteins. *Proc Natl Acad Sci*. 2006 Dec 19;103(51):19243–8.

251. Selimović Š, Jia Y, Fraden S. Measuring the Nucleation Rate of Lysozyme using Microfluidics. *Cryst Growth Des*. 2009 Apr 1;9(4):1806–10.

252. Shim Juk, Cristobal G, Link DR, Thorsen T, Jia Y, Piattelli K, et al. Control and Measurement of the Phase Behavior of Aqueous Solutions Using Microfluidics. *J Am Chem Soc*. 2007 Jul 1;129(28):8825–35.

253. Gerdts CJ, Tereshko V, Yadav MK, Dementieva I, Collart F, Joachimiak A, et al. Time-Controlled Microfluidic Seeding in nL-Volume Droplets To Separate Nucleation and Growth Stages of Protein Crystallization. *Angew Chem Int Ed*. 2006;45(48):8156–60.

254. Dombrowski RD, Litster JD, Wagner NJ, He Y. Crystallization of alpha-lactose monohydrate in a drop-based microfluidic crystallizer. *Chem Eng Sci*. 2007 Sep 1;62(17):4802–10.

255. Maeki M, Teshima Y, Yoshizuka S, Yamaguchi H, Yamashita K, Miyazaki M. Controlling Protein Crystal Nucleation by Droplet-Based Microfluidics. *Chem – Eur J*. 2014;20(4):1049–56.

256. Yamaguchi H, Maeki M, Yamashita K, Nakamura H, Miyazaki M, Maeda H. Controlling one protein crystal growth by droplet-based microfluidic system. *J Biochem (Tokyo)*. 2013 Apr 1;153(4):339–46.

257. Akella SV, Mowitz A, Heymann M, Fraden S. Emulsion-Based Technique To Measure Protein Crystal Nucleation Rates of Lysozyme. *Cryst Growth Des*. 2014 Sep 3;14(9):4487–509.

258. Babnigg G, Sherrell D, Kim Y, Johnson JL, Nocek B, Tan K, et al. Data collection from crystals grown in microfluidic droplets. *Acta Crystallogr Sect Struct Biol*. 2022 Aug 1;78(8):997–1009.

259. Tambasco-Studart M, Titiz O, Raschle T, Forster G, Amrhein N, Fitzpatrick TB. Vitamin B6 biosynthesis in higher plants. *Proc Natl Acad Sci*. 2005 Sep 20;102(38):13687–92.

260. Martiel I, Beale JH, Karpik A, Huang CY, Vera L, Olieric N, et al. Versatile microporous polymer-based supports for serial macromolecular crystallography. *Acta Crystallogr Sect Struct Biol*. 2021 Sep 1;77(9):1153–67.

261. Beale JH, Marsh ME. Optimizing the Growth of Endothiapepsin Crystals for Serial Crystallography Experiments. *JoVE J Vis Exp*. 2021 Feb 4;(168):e61896.

262. Orlans J, Rose SL, Ferguson G, Oscarsson M, Homs Puron A, Beteva A, et al. Advancing macromolecular structure determination with microsecond X-ray pulses at a 4th generation synchrotron. *Commun Chem*. 2025 Jan 7;8(1):1–12.

263. White TA, Kirian RA, Martin AV, Aquila A, Nass K, Barty A, et al. CrystFEL: a software suite for snapshot serial crystallography. *J Appl Crystallogr*. 2012 Apr 1;45(2):335–41.

Bibliography

264. Agirre J, Atanasova M, Bagdonas H, Ballard CB, Baslé A, Beilsten-Edmands J, et al. The CCP4 suite: integrative software for macromolecular crystallography. *Acta Crystallogr Sect Struct Biol*. 2023 Jun 1;79(6):449–61.

265. Vagin A, Teplyakov A. Molecular replacement with MOLREP. *Acta Crystallogr D Biol Crystallogr*. 2010 Jan 1;66(1):22–5.

266. Schaffner I, Mlynek G, Flego N, Pühringer D, Libiseller-Egger J, Coates L, et al. Molecular Mechanism of Enzymatic Chlorite Detoxification: Insights from Structural and Kinetic Studies. *ACS Catal*. 2017 Nov 3;7(11):7962–76.

267. Emsley P, Lohkamp B, Scott WG, Cowtan K. Features and development of Coot. *Acta Crystallogr D Biol Crystallogr*. 2010 Apr 1;66(4):486–501.

268. Murshudov GN, Skubák P, Lebedev AA, Pannu NS, Steiner RA, Nicholls RA, et al. REFMAC5 for the refinement of macromolecular crystal structures. *Acta Crystallogr D Biol Crystallogr*. 2011 Apr;67(Pt 4):355–67.

269. Potterton L, Agirre J, Ballard C, Cowtan K, Dodson E, Evans PR, et al. CCP4i2: the new graphical user interface to the CCP4 program suite. *Acta Crystallogr Sect Struct Biol*. 2018 Feb 1;74(2):68–84.

270. Joosten RP, Long F, Murshudov GN, Perrakis A. The PDB_REDQ server for macromolecular structure model optimization. *IUCrJ*. 2014 Jul 1;1(4):213–20.

271. Berman H, Henrick K, Nakamura H. Announcing the worldwide Protein Data Bank. *Nat Struct Mol Biol*. 2003 Dec;10(12):980–980.

272. Williams CJ, Headd JJ, Moriarty NW, Prisant MG, Videau LL, Deis LN, et al. MolProbity: More and better reference data for improved all-atom structure validation. *Protein Sci*. 2018;27(1):293–315.

273. Barty A, Kirian RA, Maia FRNC, Hantke M, Yoon CH, White TA, et al. Cheetah: software for high-throughput reduction and analysis of serial femtosecond X-ray diffraction data. *J Appl Crystallogr*. 2014 Jun 1;47(3):1118–31.

274. Stubbs J, Hornsey T, Hanrahan N, Esteban LB, Bolton R, Malý M, et al. Droplet microfluidics for time-resolved serial crystallography. *IUCrJ*. 2024 Mar 1;11(2):237–48.

275. Shoeman RL, Hartmann E, Schlichting I. Growing and making nano- and microcrystals. *Nat Protoc*. 2022 Nov 30;1–29.

276. Ibrahim M, Chatterjee R, Hellmich J, Tran R, Bommer M, Yachandra VK, et al. Improvements in serial femtosecond crystallography of photosystem II by optimizing crystal uniformity using microseeding procedures. *Struct Dyn*. 2015 Jul;2(4):041705.

277. De Zitter E, Coquelle N, Oeser P, Barends TRM, Colletier JP. Xtrapol8 enables automatic elucidation of low-occupancy intermediate-states in crystallographic studies. *Commun Biol*. 2022 Jun 29;5(1):640.

278. Fadini A, Apostolopoulou V, Lane TJ, Thor JJ van. Denoising Reveals Low-Occupancy Populations in Protein Crystals. *bioRxiv*; 2024. p. 2024.11.06.622276.

279. Bourgeois D, Royant A. Advances in kinetic protein crystallography. *Curr Opin Struct Biol*. 2005 Oct 1;15(5):538–47.

Bibliography

280. Bourgeois D, Weik M. Kinetic protein crystallography: a tool to watch proteins in action. *Crystallogr Rev.* 2009 Apr 1;15(2):87–118.

281. Mehrabi P, Sung S, von Stetten D, Prester A, Hatton CE, Kleine-Döpke S, et al. Millisecond cryo-trapping by the spitrobot crystal plunger simplifies time-resolved crystallography. *Nat Commun.* 2023 Apr 25;14(1):2365.

282. Spiliopoulou M, Hatton CE, Kollewe M, Leimkoh JP, Schikora H, Tellkamp F, et al. SPITROBOT-2 advances time-resolved cryo-trapping crystallography to under 25 ms. *bioRxiv*; 2025. p. 2025.05.23.655289.

283. Clinger JA, Moreau DW, McLeod MJ, Holyoak T, Thorne RE. Millisecond mix-and-quench crystallography (MMQX) enables time-resolved studies of PEPCK with remote data collection. *IUCrJ.* 2021 Sep 1;8(5):784–92.

284. Indergaard JA, Mahmood K, Gabriel L, Zhong G, Lastovka A, McLeod MJ, et al. Instrumentation and methods for efficient time-resolved X-ray crystallography of biomolecular systems with sub-10 ms time resolution. *IUCrJ.* 2025 May 1;12(3):372–83.

285. Caramello N, Adam V, Pearson AR, Royant A. The *in crystallo* optical spectroscopy toolbox. *J Appl Crystallogr.* 2025 Jun 1;58(3):1068–78.

286. Evans G, Axford D, Owen RL. The design of macromolecular crystallography diffraction experiments. *Acta Crystallogr D Biol Crystallogr.* 2011 Apr 1;67(4):261–70.

287. Forsythe EL, H. Snell E, Malone CC, Pusey ML. Crystallization of chicken egg white lysozyme from assorted sulfate salts. *J Cryst Growth.* 1999 Jan;196(2–4):332–43.

288. Schaffner I, Hofbauer S, Krutzler M, Pirker KF, Bellei M, Stadlmayr G, et al. Dimeric chlorite dismutase from the nitrogen-fixing cyanobacterium *Cyanothece* sp. PCC7425. *Mol Microbiol.* 2015;96(5):1053–68.

289. Ildefonso M, Revalor E, Punniar P, Salmon JB, Candoni N, Veesler S. Nucleation and polymorphism explored via an easy-to-use microfluidic tool. *J Cryst Growth.* 2012 Mar 1;342(1):9–12.

290. Tice JD, Lyon AD, Ismagilov RF. Effects of viscosity on droplet formation and mixing in microfluidic channels. *Anal Chim Acta.* 2004 Apr;507(1):73–7.

291. Li Y, Ward KR, Burns MA. Viscosity Measurements Using Microfluidic Droplet Length. *Anal Chem.* 2017 Apr 4;89(7):3996–4006.

292. Bar-Even A, Noor E, Savir Y, Lieberman W, Davidi D, Tawfik DS, et al. The Moderately Efficient Enzyme: Evolutionary and Physicochemical Trends Shaping Enzyme Parameters. *Biochemistry.* 2011 May 31;50(21):4402–10.

293. Ott JB, Boerio-Goates J. Chemical thermodynamics: principles and applications. London, UK ; San Diego: Academic Press; 2000. 664 p.

294. Sui S, Wang Y, Kolewe KW, Srajer V, Henning R, Schiffman JD, et al. Graphene-based microfluidics for serial crystallography. *Lab Chip.* 2016 Aug 2;16(16):3082–96.

295. Zhong Y, Bauer BA, Patel S. Solvation properties of N-acetyl- β -glucosamine: Molecular dynamics study incorporating electrostatic polarization. *J Comput Chem.* 2011;32(16):3339–53.

Bibliography

296. Wu S ying, Dornan J, Kontopidis G, Taylor P, Walkinshaw MD. The First Direct Determination of a Ligand Binding Constant in Protein Crystals. *Angew Chem.* 2001;113(3):602–6.
297. Zielinski KA, Dolamore C, Dalton KM, Smith N, Termini J, Henning R, et al. Resolving DJ-1 Glyoxalase Catalysis Using Mix-and-Inject Serial Crystallography at a Synchrotron. *bioRxiv*. 2024 Jul 20;2024.07.19.604369.
298. Knoška J, Adriano L, Awel S, Beyerlein KR, Yefanov O, Oberthuer D, et al. Ultracompact 3D microfluidics for time-resolved structural biology. *Nat Commun.* 2020 Jan 31;11(1):657.
299. Lee K, Lee D, Baek S, Kim J, Park J, Lee SJ, et al. Radiation Damage of Polydimethylsiloxane and Polyimide by X-ray Free-Electron Laser. *Appl Sci.* 2022 Jan;12(17):8431.
300. Ghazal A, Lafleur JP, Mortensen K, Kutter JP, Arleth L, Jensen GV. Recent advances in X-ray compatible microfluidics for applications in soft materials and life sciences. *Lab Chip.* 2016 Nov 1;16(22):4263–95.